From the holdings of the Department of Special Collections , Princeton University Library, Princeton, NJ

These documents are either in the public domain, or can only be used for educational and research purposes (Fair use) as per U.S. Copyright law (text below). By accessing this file, all users agree that their use falls in the public domain or within fair use as defined by the copyrightlaw. We do not charge any permission or usage fees for the publication of images of material inour collections, including those provided by Princeton University Library, via our website, catalog, or directly from staff.For more information regarding copyright, credit, and citation please review the information onthe Copyright, Credit and Citation Guidelines page of our website.
https://library.princeton.edu/special-collections/policies/copyright-credit-and-citation-guidelines. If you have any questions, including how to order higher-quality images from the collection, contact Special Collections Public Services via our Ask Us! Form. https://library.princeton.edu/special-collections/ask-us

Doctoral Dissertations, 2011-2026

Astrophysical Sciences

2018

Simulating Dispersal of Protoplanetary Disks and Planetary Atmospheres with Consistent Radiation and Thermochemistry

Wang, Lile

Princeton, NJ : Princeton University

http://arks.princeton.edu/ark:/88435/dsp013t945t53n

U.S. Copyright law: The copyright law of the United States (Title 17, §108, United States Code) governs the making of photocopies or other reproductions of copyrighted material. Under certain conditions specified in the law, libraries and archives are authorized to furnish a photocopy or other reproduction. One of these specified conditions is that the photocopy or reproduction is not to be used for any purpose other than private study, scholarship, or research. If a user makes a request for, or later uses, a photocopy or reproduction for purposes in excess of fair use that user may be liable for copyright infringement. This institution reserves the right to refuse to accept a copying order if, in its judgment, fulfillment of the order would involve a violation of copyright law. https://www.copyright.gov/title17/title17.pdf

Simulating Dispersal of Protoplanetary Disks and Planetary Atmospheres with Consistent Radiation and Thermochemistry

Lile Wang

A Dissertation
Presented to the Faculty
of Princeton University
in Candidacy for the Degree
of Doctor of Philosophy

Recommended for Acceptance
by the Department of
Astrophysical Sciences
Adviser: Professor Jeremy Goodman

September 2018

© Copyright by Lile Wang, 2018.
All rights reserved.

Abstract

This thesis focuses on combining (magneto-)hydrodynamic (HD/MHD) simulations with consistent radiation and thermochemistry. We implement a simulation code, an extensions of the Godunov HD/MHD solver `Athena++`, that co-evolves radiation and thermochemistry with HD/MHD (Chapter 2). A stoichiometry-compatible scheme for advection of chemical species is proposed that has lower computation costs than conventional schemes. Radiative transfer and thermochemistry solvers are optimized for graphics processing units (GPUs), showing considerable acceleration.

Chapter 3 simulates unmagnetized photoevaporation in protoplanetary disks (PPDs) with this code. Most models have a three-layer structure: a cold mid-plane, warm intermediate layer, and hot wind, the last having typical speeds ~ 40 km s^{-1} and mass-loss rates $\sim 10^{-9}\ M_\odot$ yr^{-1} when driven primarily by ionizing UV radiation. H_2O molecules re-form in the intermediate layer and survive at relatively high wind temperatures due to reactions being out of equilibrium. Wind mass loss rates are sensitive to the treatment of both the hydrodynamics and the thermochemistry.

We use the code specifically on hydrostatic grids to study the puzzle of transitional disks, which have inner cavities in gas and dust but mostly signs of accretion (Chapter 4). Results indicate that gas near the mid-plane has a dimensionless ambipolar parameter in the right general range for wind solutions to drive transonic accretion in the predominantly neutral mid-plane.

Chapter 5 carries out global MHD simulations of magnetized PPD, thus combining magnetic acceleration with photoevaporation, and linking outflow (winds) to inflow (accretion). When magnetization is sufficient to drive accretion rate $\sim 10^{-8}\ M_\odot$ yr^{-1}, as is typically observed, the mass loss rates in the winds are comparable. Models lacking EUV photons feature warm magnetized winds at typical poloidal speeds $\gtrsim 4$ km s^{-1}. Mass loss rate are subtly affected by ionization due to UV and X-ray radiation near wind bases. EUV photons yields the three-layer structure of photoevaporation, whereas the warm intermediate layer, which remains bound to the star in the magnetized models of Chapter 3, becomes a magneto-thermal wind.

The code is also used to investigate the photoevaporation of primordial planetary atmospheres (Chapter 6). EUV photons are most important in launching the photoevaporative wind, while the EUV photospheres sensitively depend on the entropy and mass in the convective layer. We then find the photoevaporation model capable to reproduce the observed bimodal radius distribution of sub-Neptune Kepler planets semi-quantitatively.

Acknowledgements

I would like to thank my thesis advisor Jeremy Goodman who has been supporting and helping me on my research and my life. His passion and insight in science constantly inspire me.

Thanks to the members on my thesis committee: Bruce Draine, Eve Ostriker, James Stone and Phillip Armitage (thesis reader), who have provided inspiring advices throughout the route to this thesis. Thanks to Xue-Ning Bai, Kengo Tomida, Jiming Shi, Zhaohuan Zhu, Fei Dai, James Owen, and Wendy Ju, for helpful discussions and suggestions.

Special thanks to Renyue Cen and Jenny Greene who offered me hand-on-hand helps at the beginning of my doctoral study. I shall also thank Gillian Knapp, Renyue Cen and Jenny Greene for the help when I was having troubles in my life.

Relation to Published Work

Chapter 2 is based on a forthcoming paper in preparation to be submitted to the Astrophysical Journal.

Chapter 3 is based on a publication written in collaboration with Jeremy Goodman, *Hydrodynamic Photoevaporation of Protoplanetary Disks with Consistent Thermochemistry*, in the Astrophysical Journal, Volume 847 Issue , article id. 11 (2017).

Chapter 4 is based on a publication written in collaboration with Jeremy Goodman, *Wind-driven Accretion in Transitional Protostellar Disks*, in the Astrophysical Journal, Volume 835 Issue 1, article id. 59 (2017).

Chapter 5 is based on a forthcoming paper written in collaboration with Xue-Ning Bai and Jeremy Goodman, *Global Simulations of Protoplanetary Disk Outflows with Coupled Non-ideal Magnetohydrodynamics and Consistent Thermochemistry*, to be submitted to the Astrophysical Journal.

Chapter 6 is based on a publication written in collaboration with Fei Dai, *Evaporation of Low-Mass Planet Atmospheres: Multidimensional Hydrodynamics with Consistent Thermochemistry*, in the Astrophysical Journal, Volume 860 Issue 2, article id. 175 (2018).

Contents

Abstract . . . iii
Acknowledgements . . . iv
Relation to Published Work . . . v
List of Tables . . . x
List of Figures . . . xi

1 Introduction **1**
1.1 Dispersal of Protoplanetary Disks . . . 1
1.1.1 Photoevaporative Winds . . . 1
1.1.2 Magnetized Winds . . . 2
1.1.3 Consistent Combination of Dynamics and Microphysics: the New Challenge . . . 4
1.2 Photoevaporation of Planetary Atmospheres . . . 5

2 Methods: HD/MHD with Consistent Microphysics **7**
2.1 Athena++ and Its Modifications . . . 7
2.1.1 Conservation of Chemicals in Fluid Advection . . . 7
2.1.2 Interacting with Athena++ via API . . . 10
2.2 Radiation . . . 11
2.2.1 Direct Ray Tracing . . . 11
2.2.2 Scattered Radiation . . . 12
2.3 Thermochemistry . . . 15
2.3.1 Thermochemical Evolution . . . 16
2.3.2 GPU-Optimized Algorithm . . . 18
2.4 Examples of Code Verification . . . 21
2.4.1 Advection of Chemical Species . . . 21
2.4.2 Diffusion of Radiation . . . 22
2.4.3 Comprehensive Test of Coupled Dynamics and Thermochemistry . . . 23

3 Photoevaporation of Protoplanetary Disks **28**
3.1 Microphysics in Photoevaporating PPDs . . . 28
3.1.1 Radiative Transfer . . . 28
3.1.2 Chemistry and Thermodynamics in General . . . 29
3.2 Fiducial Model . . . 30
3.2.1 Fiducial Model Setup . . . 30

3.2.2 Results . . . 32
3.3 Exploring the Parameter Space . . . 38
3.3.1 Setup of Models . . . 38
3.3.2 Results of Various Models . . . 39
3.4 Discussion . . . 41
3.4.1 Roles of Different Bands of Radiation . . . 41
3.4.2 Comparison with GH09 . . . 42
3.4.3 Comparison with OECA10 . . . 46
3.5 Chapter Summary . . . 47
Appendices . . . 48
Appendix 3.A Details of Key Thermochemical Processes . . . 48
3.A.1 FUV induced reactions of H_2 . . . 48
3.A.2 FUV induced reactions of H_2O and OH . . . 49
3.A.3 Dust and PAH . . . 49
3.A.4 Other Molecular and Atomic Cooling Processes . . . 51

4 Transitional PPDs: Chemistry and Accretion 53
4.1 The Accretion Puzzle in TDs . . . 53
4.1.1 TD Accretion in General . . . 53
4.1.2 Inflow Speed of TD Accretion . . . 54
4.1.3 Radial Advection of Magnetic Flux . . . 56
4.2 Physical State of the Cavity Gas . . . 57
4.2.1 Model Setup . . . 57
4.2.2 Results . . . 58
4.3 Discussion . . . 60
4.4 Chapter Summary . . . 62

5 Magnetized Wind of PPDs 64
5.1 MHD with Magnetic Diffusivities . . . 64
5.1.1 Radiative Transfer and Thermochemistry . . . 65
5.1.2 Non-ideal MHD Diffusivities . . . 66
5.1.3 Diagnostics of MHD Wind Models . . . 67
5.2 Fiducial Model Setup . . . 69
5.2.1 Geometries of the Simulation Domain . . . 69
5.2.2 Central Protostar and Radiation Sources . . . 69
5.2.3 Initial and Boundary Conditions . . . 70
5.2.4 Simulation Run . . . 71
5.3 Fiducial Model Results . . . 71
5.3.1 Magnetohydrodynamics of Disk and Wind . . . 74
5.3.2 Thermochemistry and Radiation . . . 79
5.4 Parameter Study . . . 82
5.4.1 Setup of Models . . . 82
5.4.2 Verification of the Fiducial Model . . . 85
5.4.3 Heating, ionization, diffusivity and dynamics . . . 85
5.4.4 EUV Hybrid Wind . . . 86

5.4.5 Disk Magnetization . . . 90
5.4.6 Dust: Chemistry and MHD Instability . . . 90
5.5 Discussions . . . 91
5.5.1 Comparison with B17 . . . 91
5.5.2 Comparison with Chapter 3 . . . 92
5.5.3 Implications of Observables . . . 93
5.6 Chapter Summary . . . 93
Appendices . . . 94
Appendix 5.A Additional Details in Radiation and Thermochemistry . . . 94
5.A.1 Ionization by Diffuse High Energy Photons and Radioactive Decay . . . 94
5.A.2 Self-/Cross-Shielding and Absorption of FUV Photons . . . 95
5.A.3 Pre-absorption of Radiation at the Inner Radial Boundary . . . 95

6 Photoevaporation of Planetary Atmosphere 97
6.1 Hydrostatics of Planet Atmosphere . . . 97
6.1.1 Convective (Adiabatic) Interior . . . 98
6.1.2 Radiative (Isothermal) Exterior and Model Calibration . . . 99
6.1.3 Mass Loss with Unbalanced Ambient Pressure . . . 100
6.2 Fiducial Model . . . 102
6.2.1 Fiducial Model Setup . . . 105
6.2.2 Fiducial Model Results . . . 106
6.3 Exploring the Parameter Space . . . 109
6.3.1 Stellar Wind Ram Pressure and the Effects of Multidimensions 109
6.3.2 Different Bands of Radiation . . . 113
6.3.3 Configuration of Atmospheres . . . 114
6.3.4 Envelope Mass Fraction and the Planet Core . . . 115
6.3.5 High Energy Photon Flux and "Cooling Limited" . . . 115
6.4 Discussions . . . 115
6.4.1 Grid Data of Photoevaporative Model and Evaporation Timescale 115
6.4.2 Scaling Relations of the Mass Loss Rate . . . 117
6.4.3 Mass and Radius Evolution of Planet Atmosphere . . . 118
6.5 Chapter Summary . . . 121
Appendices . . . 122
Appendix 6.A Semi-analytic Models . . . 122
6.A.1 Governing physics and equations . . . 122
6.A.2 Critical and boundary conditions . . . 123
6.A.3 Steady versus static: Caveats and necessity of a consistent model 124
Appendix 6.B Additional Details of Thermochemistry . . . 125
6.B.1 Precipitation of PAH . . . 125

7 Conclusions 126
7.1 Future Works . . . 126
7.1.1 Extensions on Disk Wind Models . . . 127
7.1.2 Photoevaporative Planetary Atmospheres: One Dimension Up 128

Bibliography **129**

List of Tables

3.1 Properties of the fiducial model 34
3.2 Models exploring parameter space 39
3.3 Approximate line luminosity 41

4.1 Properties of the fiducial model 59

5.1 Properties of the fiducial model 73
5.2 Mass loss rate in different species for Model 0. 82
5.3 Various models for parameter study 84
5.4 Mass loss rate in different species for Model 5. 90

6.1 Properties of the fiducial model 102
6.2 Characteristic radii of the fiducial model 107
6.3 Models exploring the parameter space 109

List of Figures

2.1 Schematic diagram of linear (upper panel) and asynchronous (lower panel) computation scheme for thermochemistry evolution. 20

2.2 Test results of different advection schemes (see §2.4.1), showing results of advection at $t = 1$ code time for all four species, in code units. Note that the curves for uncorrected, CMA, and stoichiometry-compatible results overlap each other in the first two rows. The first two rows also have a black solid curve showing the exact result. 22

2.3 Test results of Monte Carlo ray tracing on the GPU. Left panel shows the meridional plot for $n_{\rm ph}c$ (photon number density times the speed of light), while the right column compares the results along $\theta \in \{0.2,\ 0.4,\ 0.6\}$ radial lines with theoretical predictions (see §2.4.2). All quantities are shown in code units. 24

2.4 Layout of one-dimensional hydrodynamics test problem coupled with thermodynamics and chemistry. 24

2.5 Example of comparing the analytic solution to simulations. As the initial condition, $x_e = 0$ for all x at $t = 0$, hence the $t = 0$ curve is not shown in the logarithmic plot in the lower-right panel. The $t = 11$ yr curves are not visible since they perfectly overlap with the analytic solution. 27

3.1 Meridional plots for the fiducial model (§3.2), averaged through the final 100 yr of the simulation. **Top row**: basic hydrodynamic profiles; left panel: mass density in units of 10^{-24} g cm^{-3}; middle panel: temperature in Kelvin; right panel: radial velocity in km s^{-1}. Panels in the top row are overlapped by streamlines (white solid lines), separated by $10^{-10}\ M_\odot$ yr^{-1} wind mass loss rate (see §3.2.2 for details), and the locations of sonic points (white dashed line). **Bottom row**: relative abundance of different species [in units of $n({\rm X})/n_{\rm H}$]; left panel: H_2; middle panel: CO; right panel: H_2O. 33

3.2 Cooling/heating rates (left ordinate) and fluid properties (right ordinate) along streamlines. $n_{\rm H}$ is the number density of hydrogen nuclei. In right column, horizontal axis is arc length (λ) measured from the wind base [where $\mathcal{B} = 0$, eq. (3.1)]. Vertical dotted line marks sonic point. Left column present the profile *vertically below* wind base (i.e. $z - z_{\rm base}$). Vertical dashed line indicates wind base as defined by GH09. Upper row: streamline rooted at $R_0 = 5$ AU. Lower row: $R_0 = 15$ AU. 35

3.3 Ratio of local effective radiation flux (in $n_{\rm ph}c$) of Lyα to $h\nu = 7$ eV soft FUV, given that the luminosities in these two bands are identical. 36
3.4 Variation of mass-loss rate measured at the $r = 100$ AU outer boundary of the fiducial model (Model 0). The dashed horizontal line shows the average of mass-loss rate over the last 200 yr. 36
3.5 Distribution functions of key molecular species for the fiducial model in the two-dimensional space of $\{\log_{10} T\} \times \{v_r\}$ (common logarithm of temperature and radial velocity). The mass distribution function is normalized as $\mathrm{d}^2 m/[\mathrm{d}\log_{10}(T/\mathrm{K})\mathrm{d}(v_r/\mathrm{km\ s^{-1}})]$, i.e. mass of the species per dex-temperature per $(v_r/\mathrm{km\ s^{-1}})$. 38
3.6 Selected plots of streamlines (based on 100 yr average), overlaid on density colormaps, that are relevant to the discussions in §3.3.2. The black curves, showing the streamlines, are separated by $10^{-10}\ M_\odot\ \mathrm{yr}^{-1}$ each. The white curves denote the location of sonic point of all streamlines plotted. Note that, for clearer presentation, the radial coordinates in all panels are $\log_{10}(r/\mathrm{AU})$. 40
3.7 Profiles of heating mechanisms, in units of erg $\mathrm{cm}^{-3}\ \mathrm{s}^{-1}$, at $R = 15$ AU, for all models involved in this chapter. Heating mechanisms are distinguished by line shape and color as marked in the legend at the upper left. 43
3.8 Same as Fig. 3.7, but shows profiles of different cooling mechanisms at $R = 15$ AU. 44
3.9 Radial profiles of the differential wind mass loss rate, $(2\pi R^2 \dot{\Sigma})$, for the time-averaged fiducial simulation. Dashed curve is calculated by applying GH09's prescription to the density and temperature structure of our simulation, whereas solid curve is our actual mass-loss rate. . . 45
3.10 Distribution function of gas in the space spanned by $\{\log_{10} T\} \times \{\log_{10} \xi_{\rm X-ray}\}$, measured for the fiducial model. X-ray ionization parameter $\xi_{\rm X-ray}$ is defined as $F_X/n_{\rm H}$, viz. photon number flux density divided by the number density of hydrogen nuclei. Heavy white curve indicates the $\log_{10}\xi$–$\langle\log_{10} T\rangle$ relation based on our colormap histogram (the average of $\log_{10} T$ is weighted by the mass of gas), while the thin white curves indicate the hydrostatic ξ–T relations adopted in OECA10 (solid: inner-hole disks; dashed: primordial disks; note that the definition of ξ is different in OECA10, which is converted here to the defintion in this chapter). 47

4.1 Relative abundance of significant neutral $(n/n_{\rm H} > 10^{-5})$ and ionic $(n/n_{\rm H} > 10^{-8})$ species at the midplane. The relative abundance of electrons is shown by the heavy black curve; other species as noted in the legend. 58
4.2 Ambipolar parameter Am vs. cylindrical radius r and latitude θ. Each panel corresponds to one of the models in Table 4.1, as marked. White curves are loci of constant gaussian scale height: h (solid), and $2h$ (dashed). 59

4.3 Example of a WK93-type wind. Physical quantities are plotted in dimensionless forms (note that here $c_s = 1.4$ km s^{-1}, $n_0 = 6.4 \times 10^9$ cm^{-3}, and $B_0 = 4.45 \times 10^{-2}$ G) against vertical coordinate z in units of thermal scale height $h_p \equiv c_s r/v_K = 0.13$ AU. The model is shown from the midplane through the sonic point. Wind base is at $z/h_p \simeq 1.5$, where v_r changes its direction. Physical quantities are marked by line color and shapes (as indicated in the legend). Note that velocities v_z and v_r pertain to the *neutral* component. β is the plasma beta, viz. the ratio of gas pressure to magnetic pressure. Intersection of solid red and horizontal dotted line marks $B_r/B_0 = 1/\sqrt{3}$, the critical field inclination for launching a cold BP82 wind from the midplane. . 61

5.1 Meridional plots for the fiducial model (Model 0; §5.2), showing the innermost 50 AU averaging through the final 50 yr of the simulation. **Top row** presents basic hydrodynamic profiles: left panel: mass density in units of 10^{-24} g cm^{-3}; middle panel: temperature in Kelvin; right panel: poloidal velocity in units of km s^{-1}. **Bottom row** shows MHD-related profiles: left panel: plasma β (dimensionless); middle panel: toroidal magnetic field in units of Gauss; right panel: ambipolar Elsasser number Am (dimensionless). Panels are overlapped by poloidal streamlines separated by 10^{-9} $M_\odot$ yr^{-1} wind mass loss rate (top row, in black solid lines) or poloidal magnetic field lines (bottom row, in white solid lines). In addition, the locations of poloidal Alfvenic points (in white dashed line), and wind bases (in magenta solid line) are overlaid on all panels. 72

5.2 MHD profiles of the fiducial model (Model 0), showing the results averaging through the final 50 yr of simulation. The profiles are plotted along three different magnetic field lines, which intercept the equatorial plane at cylindrical radii $R_0 = 3$ AU (left column), $R_0 = 10$ AU (middle column), and $R_0 = 30$ AU (right column), respectively. Detailed descrption of this figure is found in §5.3. 75

5.3 For Model 0 (averaged throught the final 50 yr), decomposed poloidal specific forces along the field line anchoring the equatorial plane at $R_0 = 10$ AU, showing the contributions of gas pressure gradient $f_{\rm gas}$, magnetic pressure gradient $f_{\rm mag}$, and net inertial force $f_{\rm ine}$ (see eq. 5.9). All forces are normalized to $f_0 \equiv p_{\rm mid}/(R_0\rho_{\rm mid})$. Vertical dotted and dashed lines in black indicate the locations of wind base and the poloidal Alfvenic point, respectively. 76

5.4 Three diagnostic quantities along the field line anchoring the disk at $R_0 = 10$ AU (k, ω and l, with normalizations k_0, ω_0 and l_0; see eq. 5.11) of Model 0 (averaged throught the final 50 yr). Vertical dotted and dashed lines in black indicate the locations of wind base and the poloidal Alfvenic point, respectively. 77

5.5 Radial profiles of mass dispersal rates of the fiducial model (Model 0; averaged throught the final 50 yr). Accretion rates contributed by wind and laminar Maxwell stress are estimated by eq. (5.13). The radial profile of Shakura-Sunyaev α parameter for radial angular momentum transport (see eq.5.14) is also presented as $10^{-5}\alpha$ for reference. 78
5.6 Vertical profile of local mass flux [in $M_\odot$ yr^{-1} per (z/R)] at $R = 2$ AU and $R = 10$ AU of Model 0 (averaged throught the final 50 yr), plotted below the wind bases. Blue and red colors indicate accretion and decretion/outflow, respectively. Solid lines are measured directly from the simulation, while dashed curves are values predicted by taking vertical gradients of $T_{z\phi}$ magnetic stress. Vertical dash-dotted line in black indicates the locations of $h_{\rm mid}$, the scale height at the mid-plane. . . . 79
5.7 For Model 0 (averaged throught the final 50 yr), along the field line anchoring the disk at $R_0 = 10$ AU. **Upper panel**: Heating/cooling timescales, normalized by the Keplerian angular velocity $\Omega_{\rm K}$ at $R_0 = 10$ AU, due to different heating/cooling mechanisms ("Γ" and "Λ" are the heating/cooling terms in eq. 2.17). A black solid line, showing the flow timescale along the current field line (eq. 5.17), is plotted for reference. **Lower panel**: Local radiation flux in (photon cm^{-2} s^{-1}). Vertical dotted and dashed lines in black indicate the locations of wind base and the poloidal Alfvenic point, respectively. 80
5.8 In Model 0 (averaged throught the final 50 yr), distribution of key species: H_2O/OH, CO, O (atomic oxygen), C (atomic carbon), C^+ (ionized carbon), and S^+ (ionized sulfur). Top two rows show their spatial distribution, while bottom two row presents their distribution funtions in the two-dimensional space subtended by poloidal velocity magnitude $v_{\rm p}$ and logarithm of temperature $\log_{10}(T/{\rm K})$. The mass distribution function is normalized as ${\rm d}^2m/[{\rm d}\log_{10}(T/{\rm K}){\rm d}(v_{\rm p}/{\rm km\ s^{-1}})]$, i.e. mass of the species (in g) per dex-temperature per $(v_{\rm p}/{\rm km\ s^{-1}})$. Stream lines, wind bases and Alfvenic surfaces are indicated in the top two rows in the same way as Figure 5.1. 83
5.9 Ambipolar Elsasser number (top panel) and inverse of heating times scale (bottom panel) of Models 0, 2, 3, 4, plotted along the field lines anchoring the equatorial plane at $R_0 = 10$ AU in each model. Vertical dotted and dashed lines in black indicate the locations of wind base and the poloidal Alfvenic point of Model 0, respectively. 86
5.10 Same as Figure 5.1, but plotted for Model 5. 87
5.11 Decomposition of force along the field line emanating from $R_0 = 5$ AU, for Model 5 (averaged throught the final 50 yr). Denotations of lines are the same as Figure 5.3. 87
5.12 Same as Figure 5.8 but for Model 5. Note that the ranges of distribution in temperature and velocity are different. 88

5.13 Meridional plots of Model 7 for $(\beta/\beta_{\min} - 1)$ (upper panel, see eq. 5.8) and $|T_{r\phi}/(\rho v_r v_\phi)|$ (lower panel, see eq. 5.18), showing a snapshot immediately after instabilities are developed ($t \sim 60$ yr). Denotations of overlaid lines are identical to Figure 5.1. 91

6.1 Radius of the radiative-convective boundary $r_{\rm rcb}$, which roughly resembles the *observed* radius of planets, presented as a function of solid core mass M_c and envelope mass fraction characterized by $M_{\rm ad}/M_c$ ($M_{\rm ad}$ is the mass of the adiabatic atmosphere). The white curve overlaid indicates the limit at which the ambient pressure can marginally confine a hydrostatic atmosphere. The region on its upper left consists of models that would rapidly disperse their envelopes due to Parker wind. Note the critical core mass that occurs at $M_c \sim 3\ M_\oplus$, which depends logarithmically on the luminosity of the host star, the core composition, and the ambient pressure. 100

6.2 Meridional slice plot of the fiducial model at steady state, averaged through the final 0.05 yr of the fiducial simulation. The top row presents fluid properties, including mass density ρ (upper left panel; colormap saturated for $\rho > 10^{-10}$ g cm^{-3} to present the wind better), magnitude of velocity $|v|$ (upper middle), and temperature T (upper right). The bottowm row exhibits the relative abundances of important chemical species, including electons (lower left), neutral hydrogen (lower middle), and water (lower right). The streamlines (white solid curves; separated by $2 \times 10^{-11}\ M_\oplus$ yr^{-1} mass loss rate) and transonic surface (black dashed curve) are overlaid in the density panel. Regarding the way of presentation in this figure, rays for radiative transfer are injected from the left, and all rays travel horizontally across the simulation domain. Note the hydrostatic "tail" on the night side over the planet; see §6.2.2. 103

6.3 Radial profiles at $\theta = 0.4$ of the time-averaged fiducial model. Fluid mechanics profiles (ρ, v_r and T, upper left panel), radiation flux in four energy bins (lower left), inverse cooling timescale ($\tau_{\rm cool}^{-1}$, upper right), and inverse heating timescale ($\tau_{\rm heat}^{-1}$, lower right) in four panels, respectively. Denotation of curve shapes and colors are indicated in each individual panel. Vertical solid lines show the wind base, while vertical dotted lines indicate the sonic point. 104

6.4 Meridional slice plot of the $p_{\rm ram} = 10^{-3}$ dyn cm^{-2} case in Models W (left panel: mass density ρ; middle panel: magnitude of velocity $|v|$; right panel: temperature T), where a strong stellar wind ram pressure is included. The colormap exhibits the mass density ρ, showing the time-averaged results for the final 10^{-2} yr of quasi-steady states. The denotation of overlays in this figure are identical to the upper left panel of Figure 6.2. See §6.3.1 for the details of simulation setup. 110

6.5 Scattered plots showing the $\dot{M}$-$R_{\rm EUV}$ relations for Models E, G, KH, TE, and C, as well as the fiducial model. Makers of each model series are indicated by the legend. The simple relation $\dot{M} \propto R_{\rm EUV}^2$ is shown by a dashed line. 111
6.6 Simulation results of model serieses X (varying envelope mass fraction; left block), M (varying core mass; central block), and F (varying high energy flux, right block). Each data point, representing a model in its quasi-steady state, is indicted by a cross ("×"). In some panels, dashed or dotted lines present simple power-laws (indicated by legends in the panels) to help the reader recognize the general trend of variation. Panels related to $R_{\rm EUV}$ are not shown for model series F as $R_{\rm EUV}$ does not vary appreciably in the series. y-axes of the panels on the top-row all present $\dot{E}_k$ (the kinetic energy carried by the outflow, in erg s^{-1}), while those of the bottom-row panels present $\dot{M}$ (the mass loss rate, in $M_\oplus$ yr^{-1}). 112
6.7 Evaporation timescale of planet atmosphere. The heavy white curve is the critical curve above which the isothermal layer pressure cannot be balanced by the ambient ($p_\infty < p_{\rm amb}$, see §6.1.3), and the white dashed curve indicates $\rho_\infty \simeq 10^{-13}$ g cm^{-3}, above which the pressure balance by outflow is no longer valid (see also discussions in §6.4.1). $t_{\rm evap}$ in the region with unbalanced ambient pressure above the solid white white curve is calculated with eqs. (6.12) and (6.13), which should read the blue-green color map indicated on the top. $t_{\rm evap}$ based on simulation results, presented by the region below the critical curve, should read the purple-yellow color map on the right. 116
6.8 Evolution of model planet atmospheres, resembling the conditions of the two planets in Kepler-36, showing $r_{\rm rcb}$ and envelope mass fraction. Note that the two planets start from the same initial envelope mass fraction, but the less massive one (corresponding to Kepler-36b) has already evaporated most of its envelope via Parker wind before $t = 10^6$ yr. See §6.4.3 for detailed discussions. 119
6.9 Bimodal distribution of evolved model planets. Scattered white dots present a sub-sample of simulated planet atmosphere evolution results (10^3 out of 10^4; for clearer presentation). The color-mapped contour is the estimated distribution function with Gaussian kernel, scaled to frequency per $\{\log_{10} P \times \log_{10} R_p\}$ (upper panel), and $\{\log_{10} M_{\rm ad}/M_c \times \log_{10} R_p\}$ (lower panel), using the results of the whole ensemble. . . . 120
6.10 The radial profile of various quantities in the spherically symmetric analytical solution of a 5 $M_\oplus$, 10^{-2} envelope mass fraction at 0.1 AU, presented in §6.A.1. Mass density ρ, radial velocity u, temperature T, and neutral fraction $(1 - x_e)$ profiles are presented in different line styles, which are indicated in the legend. The vertical thin dotted line indicates the location where the flow is transonic. 123

Chapter 1

Introduction

1.1 Dispersal of Protoplanetary Disks

A protostar newly spawned is usually surrounded by a gaseous disk, which is believed to be the birthplaces of planets, namely a protoplanetary disk (PPD hereafter). PPDs disperse, on a timescale $\sim 10^{6-7}$ yr lifespan (e.g. Zuckerman et al., 1995; Haisch et al., 2001) in three ways: (1) forming planets; (2) accreting onto the central protostar; (3) launching outflows (see Williams & Cieza 2011; Armitage 2011 for reviews). This thesis discusses dispersal of PPDs via (2), and especially (3).

Two mechanisms are believed to drive disk winds. *Photoevaporative winds* are driven by the heat injected by ultraviolet (UV)/X-ray photons. *Magnetized winds* accelerate along magnetic lines via $\vec{J} \times \vec{B}$ force. We review these two scenarios respectively in this section.

1.1.1 Photoevaporative Winds

In absence of magnetic fields, PPD winds are considered to be launched primarily by photoevaporation. High energy photons heat up the gas by photoionization, photodissociation and photoelectric effect, depositing energy into gas particles. On a single photoionization/photodissociation/photoelectric event, the energy deposition is roughly $(h\nu - I)$, where $h\nu$ denotes the photon energy and I is the energy of activation (ionization/dissociation/work function). Such energy is always compared to the depth of stellar gravitation potential well,

$$|\varepsilon_{\rm grav}| = \frac{GM_*}{2r} \sim 5 \text{ eV}/m_p \times \left(\frac{M_*}{M_\odot}\right)\left(\frac{r}{\rm AU}\right)^{-1} , \tag{1.1}$$

where M_* is the stellar mass, to assess whether the irradiated gas is able to escape. Equivalently, one can also compare the local radius to the gravitational radius (e.g. Hollenbach et al., 1994a), $r_g \equiv GM_*/c_s^2$, where c_s is the speed of sound in the irradiate gas, to estimate whether the heated gas at some location is gravitationally unbound. Some simulations suggested that there could still be outflow of gas at $r \sim 0.1 r_g$ due

to hydrodynamic interactions (e.g. Font et al., 2004), though, the mass loss rate of outflow is considerably suppressed at small radii $r \ll r_g$.

There are two kinds of sources of high energy photons for PPD photoevaporation: (1) the young stellar object surrounded by the disk, and (2) other young stellar objects in the same stellar cluster. Case (2) is usually referred to as "external photoevaporation", and indeed shares approximately the same set of microphysical processes as the former [1] . This thesis focuses on case (1) nonetheless.

Hard photons that have sufficient energy to irradiate the gas on disk surfaces can be classified in different energy bands, which experience different microscopic physics and have differing effects on PPDs. In this thesis, we use the term "far-UV (FUV)" for photon energies 6 eV $< h\nu <$ 13.6 eV, "extreme-UV (EUV)" for 13.6 eV $< h\nu <$ 0.1 keV, and "X-ray" for $h\nu >$ 0.1 keV. Pioneering works in central-star photoevaporation, e.g. Font et al. (2004); Alexander et al. (2006a,c), modeled EUV photoevaporation in hydrodynamic simulations with minimal thermochemistry, as it was generally believed that all EUV irradiated gas has similar temperature $T \gtrsim 10^4$ K, and is insensitive to complicated thermochemical processes. On the other hand, calculations with detailed thermochemistry, e.g. Gorti & Hollenbach (2008, 2009) (hereafter GH08, GH09), discussed the possibility of FUV and X-ray irradiated photoevaporation. GH09 suggested that detailed microphysics, especially in collisional excitations of atoms and molecules that result in cooling, and in dust-related processes, may still dramatically impact the dynamics of outflow by affecting the thermodynamics of the gas near the altitude of wind launching. GH08 and GH09 adopt semi-analytic prescriptions for the wind mass-loss rate rather than simulate multidimensional hydrodynamics. Some recent works conducted hydrodynamic simulations with interpolation tables of gas temperature drawn from hydrostatic calculations in thermochemical equilibrium (e.g. Owen et al. 2010a, in which cooling processes by collisional excitation of atoms/molecules are ignored). All those works aforementioned had to sacrifice at least one aspect in the combination of time-dependent dynamics and consistent microphysics for affordable computations.

1.1.2 Magnetized Winds

Pure photoevaporative winds, without magnetic fields, carry their own angular momentum only, hence are not directly relevant to disk accretion. This subsection discusses magnetized disk wind, which is considered to drive accretion efficiently.

Conventionally, magnetized disk accretion is considered to be dominated by turbulent viscosity of magnetorotational instability (MRI, Balbus & Hawley 1991). Nevertheless, recent works have demoted MRI from this key position. For example, if the field is strong enough to drive accretion at typically observed rate, it will be too

[1] External photoevaporation is thoroughly discussed in e.g. Johnstone et al. (1998); Armitage (2000); Adams et al. (2004); Fatuzzo & Adams (2008). More recently, Haworth & Harries (2012), Haworth et al. (2016), and Haworth et al. (2017) have progressed even further by coupling hydrodynamics with thermochemistry in simulations of externally irradiated disks and pre-stellar cores. These simulations has special geometry, and features relatively more complicated thermochemistry for ionization equilibrium.

strong for MRI turbulence (e.g. Bai & Goodman, 2009; Bai, 2011a). Also, MRI could also be vulnerable to non-ideal MHD effects (see Turner et al. 2014 for a review). Simulations found that through the inner region of a PPD (with cylindrical radii $R \lesssim 15$ AU) MRI is suppressed when ambipolar diffusion comes into action (see also Bai & Stone, 2013a; Lesur et al., 2014; Gressel et al., 2015a). In the outer region, ambipolar diffusion can still damp MRI substantially (e.g. Simon et al., 2013a,c).

Compared to MRI that could be insufficient in driving accretion, wind-driven accretion is nowadays believed to be a promising candidate mechanism: once magnetized with a large-scale poloidal magnetic field threading the disk, magnetic fields mediate angular momentum transport between the bulk disks and outflows. The advantage of wind launching accretion over MRI in the efficiency of driving accretion can be interpreted as a matter of angular momentum conservation, and eventually, of geometry. Consider an annular control volume $(R, \phi, z) \in [R_1, R_2] \times [0, 2\pi] \times [-h, +h]$ in cylindrical coordinates aligned with the disk, which has half thickness $\sim h \ll R_1$. We assume axisymmetry within this volume. Integrating the mass flux $\rho\mathbf{v}$ and angular-momentum flux $R(\rho v_\phi \mathbf{v} - B_\phi \mathbf{B}/4\pi)$ over all surfaces surrounding this control volume, we read the conservation of angular momentum,

$$\left[\dot{M}_{\rm acc} j + \frac{R}{2}\int_{-h}^{h} {\rm d}z\ B_R B_\phi\right]_{R=R_1}^{R=R_2} = \int_{R_1}^{R_2} {\rm d}R \left\{ \frac{{\rm d}\dot{M}_{\rm wind}}{{\rm d}R} j - \frac{R^2}{2}\left[\frac{B_\phi B_z}{2}\right]_{z=-h}^{z=h} \right\} \ , \quad (1.2)$$

where $\dot{M}_{\rm acc}$ is the total accretion mass flow, $\dot{M}_{\rm wind}$ is the total outflow of the wind from the disk surfaces ($z = \pm h$) within radius R, and $j = Rv_\phi \simeq (GM_* R)^{1/2}$ estimates the specific angular momentum. Noting that ${\rm d}\dot{M}_{\rm acc}/{\rm d}R = {\rm d}\dot{M}_{\rm wind}/{\rm d}R$ in steady state and taking the limit $R_2 \to R_1$ (i.e. taking the differential of both sides in eq. 1.2), we obtain

$$\frac{\dot{M}_{\rm acc}}{R}\frac{{\rm d}j}{{\rm d}R} = -h\langle B_R B_\phi\rangle_z - \frac{R}{2}\left[B_z B_\phi\right]_{z=-h}^{z=h} \ , \quad (1.3)$$

where $\langle\cdot\rangle_z$ indicates a vertical average over the range $-h < z < h$. Eq. 1.3 reveals, by geometry, that winds could overwhelm MRI turbulence in the efficiency of driving accretion: around a cylindrical volume that contains the disk, the wind stress $B_z B_\phi$ acts on a "top/bottom" surface area $\sim \pi R^2$, while the $B_R B_\phi$ stress (effectively the "viscosity") acts on the "side" surface area $\sim 2\pi R h$. If the B_R and B_z components of the magnetic field have comparable strength, then the wind stress exert a torque larger than the turbulent viscosity by a factor $\sim R/h \sim \Omega R/c_{\rm s} \gg 1$. In fact, according to some recent simulation explorations [e.g. Bai & Stone (2017), Bai (2017) (**B17**)], the inequality $|B_R| < |B_z|$ almost always holds within steady-state disks due to magnetic diffusivities, further enhancing the advantage of wind stress over turbulence viscous stress.

Regarding the details in launching mechanism, magnetized winds can be further classified into roughly two types, as is clarified in e.g. Bai (2017): (1) magneto-centrifugal wind, whose poloidal fields are strong enough to enforce corotation near the wind base, driving an outflow centrifugally (e.g. Blandford & Payne, 1982); (2) magneto-thermal wind, whose poloidal fields are weak and the outflow is driven by

the gradient of pressure, combining magnetic pressure of toroidal fields and gas thermal pressure. Modeling of global wind kinematic suggests the second case (Bai et al., 2016; Bai, 2016a)

Similar to photoevaporation, co-evolution of radiation, thermochemistry and non-ideal MHD for global disk models has been proposed for years but computational costs are still the hurdle. In early days, self-similar global solutions of magnetized outflows were calculated with ideal MHD (e.g. Blandford & Payne, 1982; Li, 1995; Ferreira, 1997), to which local solutions that considered non-ideal MHD are matched (e.g. Wardle & Königl, 1993; Königl et al., 2010; Salmeron et al., 2011). Global simulations on magnetized disks (may be more generic and not necessarily specific to PPDs) have been also conducted: some mainly focus on the ideal MHD regime (e.g. Krasnopolsky et al., 2003; Pudritz et al., 2006), while e.g. Zanni et al. (2007a); Tzeferacos et al. (2009a) studied the effect of magnetic diffusivities by parameterization them with global constants. According to detailed thermochemical calculations such as Bai & Goodman (2009) and Xu & Bai (2016), however, magnetic diffusivity profiles vary considerably along both radial and vertical directions in PPDs. To date, most existing works on magnetized PPD wind launching with more realistic magnetic diffusivities have mostly been carried out locally (e.g. Bai & Stone, 2013a; Bai, 2013), or at least locally in one dimension (e.g. Gressel et al., 2015a). Recently Bai & Stone (2017) and B17 constructed global magnetized wind solutions with axisymmetry, where the thermodynamics used a prescribed temperature profile, and the conditions of magnetic diffusivity were approximated by a pre-calculated interpolation table.

1.1.3 Consistent Combination of Dynamics and Microphysics: the New Challenge

In order to model photoevaporative and/or magnetized wind of PPDs, one is required to take the richness of the microphysics into account, as well as its interaction with the HD/MHD system. Such requirements raise a new flag of challenge to researchers working on PPDs.

As can be recognized in the discussions in §1.1.1 and §1.1.2, magnetized wind launching mechanisms are indeed closely related to the physics behind photoevaporation: photoionization and photoelectric effect yield free electrons, whose abundance is crucial for MHD, and even if much of the acceleration is attributed to magnetic fields, thermal pressure has a role in initiating the wind and determining its mass flux. Prescribing the profiles of temperature and magnetic diffusivities, instead of calculating those physics consistently, takes the risk of giving unphysical results.

Over the years, young stellar objects are observed to constrain the dynamics of PPD outflows, with forbidden atomic lines such as [Ne II] 12.8 μm, [O I] 6300 Å, [O I] 5577 Å (e.g. Hartigan et al., 1995; Pascucci et al., 2007; Pascucci & Sterzik, 2009; Rigliaco et al., 2013; Simon et al., 2016), and with molecular features (e.g. Pontoppidan et al., 2008; Carr & Najita, 2008; Bast et al., 2011; Pontoppidan et al., 2011). Contemporary works bridging theories/simulations to such observations are usually done by post-processing with steady-states in thermochemistry (e.g. Owen et al.,

2011; Ádámkovics et al., 2014; Ercolano & Owen, 2016)). However, recent discoveries emphasize the necessity of coupling consistent time-dependent thermochemistry and radiative transfer with HD/MHD simulations to yield accurate theoretical models, as the timescales of thermochemical reactions could well be comparable to the timescales of wind kinematics (e.g. Turner et al. (2007); Ilee et al. (2011, 2017); see also R. Xu et al., in preparation).

To better understand PPD dispersal, in a grid-based simulation, a suitable thermochemical network must be evolved in each grid zone. Thermochemistry calculations usually suffer from excessive computation costs brought by the stiffness of thermochemical systems, and hence are typically done on static grids only (e.g. GH08, GH09, and `ProDiMo` as described by Woitke et al. 2009, 2016). Transport of photons, especially infrared (e.g. Kuiper et al., 2010), X-ray (see Igea & Glassgold, 1999), and Lyα (Bethell & Bergin, 2011) photons, subject to scattering and re-emission processes, is another difficulty. Almost all previous works lack either consistent hydrodynamics/magnetohydrodynamics (HD/MHD) or thermochemistry: these have not been consistently accomplished simultaneously. Existing computation codes that claim possession of the research frontier nowadays, on the other hand, always have at least one of these issues: (1) restricted availability and/or copyright limitations, (2) incapability to be integrated with HD/MHD calculations (more often than not, due to lack of efficiency), and (3) reliability and accuracy being not under control.

This thesis, which has just witnessed the soar of computations on unconventional architectures (e.g. graphics processing units, GPU), pursues a more comprehensive understanding towards the photoevaporation problem by attempting to write a code that combines time-dependent thermochemistry with hydrodynamics consistently, assisted by those updated technologies in computation. We will present the description of such code in Chapter 2. One of the applications is the simulations of photoevaporative winds (Chapter 3). We also use this microphysics system on hydrostatic grids to investigate the transitional disk puzzle (Chapter 4) as a precursor, before the schemes are further applied to non-ideal MHD simulations of generic magnetized PPD winds (Chapter 5).

1.2 Photoevaporation of Planetary Atmospheres

As one of the direct products of PPD evolution, primordial atmospheres of planets are possible to be modeled and discussed within the same framework of combined dynamics, radiation and thermochemistry (e.g. Owen & Jackson, 2012; Owen & Wu, 2016).

When the planet gravitational potential well is not too deep ($M \lesssim 60\ M_\oplus$), incident high energy photons are able to irradiate the primordial planetary atmospheres and cause photoevaporation. (see also Lammer et al., 2003; Yelle, 2004; Tian et al., 2005; Lecavelier Des Etangs, 2007; Sanz-Forcada et al., 2011). Direct evidences of planet photoevaporation have been reported. These include "hot Jupiters" (e.g. Vidal-Madjar et al., 2003, 2004; Sanz-Forcada et al., 2011), and sub-Neptune planets (e.g. Ehrenreich et al., 2015). In addition, recent observation showing bimodal

distribution of transiting planet radii (Fulton et al., 2017; Dong et al., 2017). This bimodality has been predicted by Owen & Wu (2013) and Lopez & Fortney (2013) as a consequence of photoevaporation, and further discussed by e.g. Owen & Wu (2017) and Jin & Mordasini (2017).

Models with hydrodynamics and microphysics have been constructed to understand the physics of evaporating planet atmosphere. Murray-Clay et al. (2009) constructed semi-analytic models of photoevaporation, assuming spherical symmetry, for "hot Jupiters". This scenario is extended to more complicated dynamics by including X-ray in Owen & Jackson (2012). The influence of magnetic fields was explored analytically and with simulations by Owen & Adams (2014). Both Schneiter et al. (2016) and Tripathi et al. (2015) simulated the evaporation of a model hot Jupiter in three dimensions, featuring the dynamics of photoevaporation outflow and interactions with orbital motion. Two-dimensional simulation in Christie et al. (2016) focused on the interaction with the ram pressure of stellar wind. Carroll-Nellenback et al. (2017) studied on the eventual fate of the outflow as an evaporating planet orbits around the central star. Due to the prohibitive computational costs to evolve a complete thermochemical network, those models consist only of a minimal set of reactions, i.e. photoionization/photodissociation of atomic hydrogen and Lyα cooling, or simply uses a one-to-one mapping of gas temperature to local ionization parameter by radiation.

We expect the combination of consistent thermochemistry with hydrodynamics to shed more light on the problem. Similar to PPD winds, costly calculations can be finished within a reasonable "wall-clock time" by utilizing the power of GPUs with methods stated in Chapter 2. We present our explorations and discussions in Chapter 6, with which we expect to achieve better understanding of the microphysics and hydrodynamics relevant to photoevaporation, and probably yield predictions and/or explanations to observables.

Chapter 2

Methods: HD/MHD with Consistent Microphysics

Comprehensive computation of PPD dispersal requires consistent combination of these three important modules: (1) Hydrodynamics (HD) or magnetohydrodynamics (MHD); (2) Radiation; (3) Thermochemistry (chemistry, heating & cooling, and ionization). This chapter describes implementations and verification of those modules.

2.1 Athena++ and Its Modifications

We base our (magneto-)hydrodynamic calculations on `Athena++`, a grid-based higher-order Godunov MHD code (White et al. 2016; J. Stone et al., in preparation). `Athena++` works on various kinds of coordinate systems to solve HD/MHD problems in conservative form; it conserves mass, energy, (angular) momentum and magnetic flux to machine precision.

To incorporate desired microphysics into `Athena++`, consistent modifications to the code are necessary, since `Athena++` solves only the HD/MHD equations themselves. There is one functionality that must involve direct modifications to `Athena++` itself: advection of chemical species (§2.1.1). Other modifications can be implemented via the API `UserWorkInLoop` (§2.1.2) without touching the infrastructures of `Athena++`. We will discuss these two types of modifications in the rest of this section.

2.1.1 Conservation of Chemicals in Fluid Advection

A plethora of applications of `Athena++`, including all computations discussed within this thesis, utilize piecewise linear method (PLM) for reconstruction and HLLC/HLLD Riemann solver. This combination provides sufficiently good accuracy at reasonable computation costs. Hence this subsection is dedicates to the advection of chemical species with PLM and HLLC/HLLD methods.

Unless nuclear reactions are involved, all processes must strictly conserve the abundance of chemical elements. In particular, this applies to the advection of fluid. Advection in `Athena++`, as a Godunov solver, generally consists of three steps: (1)

Reconstruction of values at interfaces for variables; (2) Calculating fluxes with a Riemann solver; (3) Adding the divergences of fluxes to the variables. Conservation of chemicals is naturally guaranteed in step (3) if the first two steps are implemented correctly.

Without loss of generality, we discuss problems with one spatial dimension only; all schemes can be easily generalized to three dimensional cases. In general, the flux of the sth chemical species at the $i-1/2$ surface (left surface of the ith cell),

$$\mathcal{F}^s_{i-1/2} = x^s_{i-1/2}\mathcal{F}^\rho_{i-1/2} \ ; \quad x^s_{i-1/2} \equiv \left[\frac{n^s}{\rho}\right]_{i-1/2} \ , \tag{2.1}$$

where $[n^s/\rho]_{i-1/2}$ is the ratio of the number density of the sth species to mass density at the $i-1/2$ surface, $F^s_{i-1/2}$ and $\mathcal{F}^\rho_{i-1/2}$ are the fluxes of the sth species in molecule numbers and mass density at the $i-1/2$ surface, respectively.

Bottom line: Element conservation

It is straightforward to write down the condition of element conservation for fluxes of chemical species at cell surfaces, for each element indexed by ν,

$$\sum_s \mathcal{N}_{\nu,s}\mathcal{F}^s_{i-1/2} = \frac{1}{\alpha}X_\nu \mathcal{F}^\rho_{i-1/2} \ , \tag{2.2}$$

where s runs through all species, $\mathcal{N}_{\nu,s}$ stands for the number of atoms of the νth element in the sth species, X_ν the relative abundance by nucleus number of the νth element, and $\alpha \equiv \sum_\nu X_\nu m_\nu$ the mean *atomic* mass. Eq. (2.2) is generally an incomplete constraint whenever the number of species is greater than the number of elements. Note that this condition is well-defined only when element abundances are constants, which formally reads,

$$\sum_s \mathcal{N}_{\nu,s} n^s_i = \frac{1}{\alpha}X_\nu \rho_i \ , \quad \forall \ i \ . \tag{2.3}$$

It is easily proven that feeding the absolute or relative abundances into the machine and let the reconstructor and/or Riemann solver work on each individual species independently is *not* an option: because higher order methods (e.g. PLM) reconstruct the values at cell surfaces with non-linear functions, conservation of elements indicated by eq. 2.2 is almost certainly violated.

Consistent multifluid advection (CMA)

In order to keep the elemental abundances correct, the authors of Plewa & Müller (1999), and especially Glover et al. (2010), proposed the concept of "consistent multifluids advection" (CMA), in which the reconstruction of the relative abundances of chemical species that are used in eq. (2.1), $\{x^s_{i-1/2}\}$, is determined based on the

originally reconstructed relative abundances $\{\tilde{x}^s_{i-1/2}\}$, with a set of coefficients $\{\eta_\nu\}$,

$$x^s_{i-1/2} = \sum_\nu \frac{\mathcal{N}_{\nu,s}}{\mathcal{N}_{\mathrm{tot},s}} \eta_\nu \tilde{x}^s_{1-1/2} \ , \tag{2.4}$$

(where $\mathcal{N}_{\mathrm{tot},s}$ is the total number of nuclei in the molecule of species s) such that,

$$\sum_s \mathcal{N}_{\mu,s} x^s_{i-1/2} \equiv \sum_\nu \mathcal{M}_{\mu,\nu}\eta_\nu = \frac{X_\mu}{\alpha} \ ; \quad \mathcal{M}_{\mu,\nu} \equiv \sum_s \mathcal{N}_{\mu,s} \frac{\mathcal{N}_{\nu,s}}{\mathcal{N}_{\mathrm{tot},s}} \tilde{x}^s_{i-1/2} \ . \tag{2.5}$$

The set of $\{\eta_\nu\}$ is hence obtained by solving the linear system in eq. (2.5), whose dimension equals to the number of elements. Note that an individual set of $\{\eta_\nu\}$ should be solved for every cell surface. The resulting spatial order of accuracy regarding such reconstructed $\{x^s_{i-1/2}\}$ is the same as the original reconstruction scheme for $\{\tilde{x}^s_{i-1/2}\}$.

Donor-cell-like reconstruction: Conservation first, fast

One straightforward way to determine $\{x^s_{i-1/2}\}$ has a simple and clear physical picture: HLLC and HLLD capture the contact discontinuity, across which no species should be advected (mixture between waves through two different surfaces is prevented by the CFL condition). As a result, the relative abundance of a chemical species in the flow across a cell surface should strictly equal its relative abundance in the cell on the left-/right-hand side, depending on which way the contact surface moves. Hence a "donor-cell-like" scheme can be adopted, which evaluates $x^s_{i-1/2}$ as,

$$x^s_{i-1/2} = \left(\frac{n^s_{i-1}}{\rho_{i-1}}\right) \Theta(\mathcal{F}^\rho_{i-1/2}) + \left(\frac{n^s_i}{\rho_i}\right) \Theta(-\mathcal{F}^\rho_{i-1/2}) \ , \tag{2.6}$$

where Θ denotes the Heaviside Theta function. Given globally constant element abundance (eq. 2.3), one finds the condition (2.2) to be naturally satisfied. One merit of this scheme is that the computation cost is minimal. It can also be applied to the cases in which element abundances are *not* global constants, which is impossible with the original CMA scheme. We also note that, although this scheme is first order in space (as $x^s_{i-1/2}$ is constructed at zeroth order), since the fluxes of chemical species strictly follow the mass flux (see eq. 2.1), it is not as diffusive as other advection schemes of the same order in case that the fluid is mostly static.

Stoichiometry-compatible reconstruction: Matrix inversion avoided

We hereby propose another scheme which can achieve a higher order of spatial accuracy than the donor-cell-like method but avoids matrix inversions in the CMA procedure. An important concept is the stoichiometric space $\mathcal{S}$, defined as the null space of the matrix $\mathcal{N}_{\nu,s}$. By definition, if we have a vector of chemical species abundances n^s, for all $\Delta n^s \in \mathcal{S}$, $n^s \to (n^s + \Delta n^s)$ keeps element abundances the same as n^s. The orthonormal bases of $\mathcal{S}$ are used to construct the projection matrix to $\mathcal{S}$, denoted as $\mathcal{P}$ in what follows.

Without any modifications, the reconstructed cell surface states $x^s_{i-1/2}$ can be formally written as,

$$x^s_{i-1/2,l} = x^s_{i-1} + \chi^s_{i-1/2,l} \ , \quad x^s_{i-1/2,r} = x^s_i + \chi^s_{i-1/2,r} \ , \tag{2.7}$$

where $\chi^s_{i-1/2,l/r}$ includes all higher order terms for the reconstructed $x^s_{i-1/2,l/r}$. With PLM reconstruction, $\chi^s_{i-1/2,l/r}$ should be given by,

$$\begin{aligned} \chi^s_{i-1/2,l} &= \phi(\partial x^s_{i-1,f}, \partial x^s_{i-1,b}, c_{i-i,f}, c_{i-1,b})\ (\xi_{i-1/2} - \langle\xi\rangle_{i-1})(\xi_{i-1/2} - \langle\xi\rangle_{i-1}) \ , \\ \chi^s_{i-1/2,r} &= \phi(\partial x^s_{i,f}, \partial x^s_{i,b}, c_{i,f}, c_{i,b})\ (\xi_{i-1/2} - \langle\xi\rangle_{i})(\xi_{i-1/2} - \langle\xi\rangle_{i}) \ , \end{aligned} \tag{2.8}$$

where ξ is the coordinate variable, $\xi_{i-1/2}$ is the location of the surface, $\langle\cdot\rangle_{i-1}$ is the volume-averaged cell-center value in the $(i-i)$th cell, and

$$\begin{aligned} \partial x^s_{i-1,f} &\equiv \frac{\langle x\rangle^s_i - \langle x\rangle^s_{i-1}}{\langle\xi\rangle_i - \langle\xi\rangle_{i-1}} \ , \quad \partial x^s_{i-1,b} \equiv \frac{\langle x\rangle^s_{i-1} - \langle x\rangle^s_{i-2}}{\langle\xi\rangle_{i-1} - \langle\xi\rangle_{i-2}} \ ; \\ c_{i-1,f} &\equiv \frac{\langle\xi\rangle_i - \langle\xi\rangle_{i-1}}{\xi_{i-1/2} - \langle\xi\rangle_{i-2}} \ , \quad c_{i-1,b} \equiv \frac{\langle\xi\rangle_{i-1} - \langle\xi\rangle_{i-2}}{\langle\xi\rangle_{i-1} - \xi_{i-3/2}} \end{aligned} \tag{2.9}$$

(similar definitions for the $x^s_{1-1/2,r}$ expression are omitted). Function ϕ is usually called "slope-limited derivative". For `Athena++`, the slope-limited derivative used by its PLM reconstruction is the modified van Leer type, proposed by Mignone (2014).

In general, the slope limited derivative is not a linear function of the reconstructed quantity, causing problems in chemical species and/or element conservation. With the help of projection matrix $\mathcal{P}$ onto the stoichiometric space, however, we can recast eq. (2.7) as,

$$x^s_{i-1/2,l} = x^s_{i-1} + \sum_r \mathcal{P}^s_r \ \chi^r_{i-1/2,l} \ , \tag{2.10}$$

(similar expression for $x^s_{i-1/2,r}$ omitted), and eventually,

$$x^s_{i-1/2} = x^s_{i-1/2,l}\Theta(\mathcal{F}^\rho_{i-1/2}) + x^s_{i-1/2,r}\Theta(-\mathcal{F}^\rho_{i-1/2}) \ . \tag{2.11}$$

Obviously reconstructed $\{x^s_{i-1/2}\}$ by eqs. (2.10), (2.11) are fully consistent with the donor-cell-like scheme eq. 2.6, regarding the abundance of elements. In the same time, introducing the slope-limited derivative gives the scheme higher order of accuracy. Compared to the original CMA scheme, in addition to the ability to deal with varying abundances of elements, this method has another merit: the computational cost is significantly lower—for one simulation, the projection matrix $\mathcal{P}$ is obtained once and for all (typically calculated using singular value decomposition).

2.1.2 Interacting with Athena++ via API

Time integration of HD/MHD problems in `Athena++` is conducted cycle by cycle, moving forward by an increment in time δt. At the end of each cycle, the overloaded callback function `UserWorkInLoop` is executed once. The interface through which the

microphysics module interacts with the HD/MHD integrator requires no more access than this API.

During the execution of `UserWorkInLoop`, the following operations are carried out:

- Direct ray-tracing and absorption along each ray (§2.2.1); CPU-based calculation of diffuse radiation is also carried out if necessary.
- Evolution of a thermochemical network for time δt (§2.3). Before integrating this network, the advected abundance of chemical species (§2.1.1) and gas internal energy are read from each cell, and some pre-processing steps are conducted. Thermochemical integration results are post-processed before writing the evolved chemical abundances and gas internal energy back to the HD/MHD solver for next step of advection.
- If GPU-based radiative transfer routines (§2.2.2) are utilized, their operations start at the end of an API call. A thread in the background will monitor those GPU computations during CPU-based HD/MHD integration. At the beginning of the next `UserWorkInLoop` call, GPU computation results are collected if the jobs are done (if not, the thread tells the code to wait until they are done), and then used for the corresponding cycle of thermochemical calculations.

2.2 Radiation

Radiation shapes the thermal and chemical conditions of fluids: it is one of the important inputs to thermochemical calculations. For discussion purposes, we roughly divide the method that we solve radiation problems into two categories: direct ray-tracing, and diffuse radiation.

2.2.1 Direct Ray Tracing

If scattering is negligible, the path of a photon is a straight ray until it is absorbed. Calculating the path for a ray is a geometry problem. In order to trace a ray consistently, we must know the exact points at which this ray enters and leaves all cells on its way. In three-dimensional problems, a cell has 6 (six) surfaces, formally described by $\{S_i(\mathbf{x}) = 0\}$ where $i = 1, \cdots, 6$ and $\mathbf{x}$ represents the spatial coordinates. We denote the point at which the ray enters this cell $\mathbf{x}_0$, and the unit vector along the direction of this ray by $\mathbf{r}$. The set of six equations,

$$S_i(\mathbf{x}_0 + l_i\mathbf{r}) = 0 \ ; \quad i = 1 \ , \cdots \ , 6 \ , \tag{2.12}$$

are solved for $\{l_i\}$. If the number of dimensions is less than three in the problem, or some cell surfaces have zero area (e.g. polar wedge cells in spherical polar grids), fewer equations in (2.12) are solved; but the vectors $\mathbf{x}_0$ and $\mathbf{r}$ should still be considered in three dimensions. Note that some of the equations may have multiple roots (most commonly, in cylindrical and spherical coordinate grids, whose equations for cell surfaces can be quadratic); these roots with multiplicity should also be considered.

The index i' for *smallest positive* $\{l_i\}$ (denoted as $l_{\rm min}$) is then found: the ray then leaves this cell at $\mathbf{x}_0 + l_{\rm min}\mathbf{r}$ through the i'th surface–this is the starting point for solving the path in the next cell. Such steps of propagation are repeated until the ray leaves the domain.

Once the path of a ray is obtained, this path will not change, and is stored for re-use at each time step: the indices of all cells on its path, including $\{\mathbf{x}_0, l_{\rm min}\}$ in each cell, are stored to save the cost of calculation. When the mesh is refined or corasened, re-calculating the geometry of rays is necessary. In every cycle, every ray is treated as being assigned to an individual directional emitter that shines different number of photons $N_{\rm ph,init}(h\nu)$ at different photon energy $h\nu$ into this ray. In general this number of photons in the ray can be arbitrary numbers.

One special but commonly met situation is that an isotropic point source is desired, in which case the number of photons assigned to one ray at photon energy $h\nu$ is,

$$N_{\rm ph,init}(h\nu) = L_*(h\nu)\frac{\Delta\Omega}{4\pi}\delta t \ , \tag{2.13}$$

where $L_*(h\nu)$ is the luminosity of the source at photon energy $h\nu$, $\Delta\Omega$ is the solid angle that the current ray represents, and δt is the current timestep.

During the propagation inside a cell, the absorption mean free path for photon energy $h\nu$, $\lambda_{\rm abs}(h\nu)$, is calculated, and the effective photon flux inside this cell is estimated by averaging absorbed flux along the path within the cell,

$$\begin{aligned} F_{\rm ph,eff}(h\nu) &\simeq N_{\rm ph,in}(h\nu)\left(\frac{l_{\rm min}}{\delta V\delta t}\right)\left(\int_{\rm in}^{\rm out}{\rm d}s\right)^{-1}\int_{\rm in}^{\rm out}{\rm d}s\,\exp[-l_{\rm min}/\lambda_{\rm abs}(h\nu)] \\ &= N_{\rm ph,in}\left(\frac{l_{\rm min}}{\delta V\delta t}\right)\left\{\frac{1-\exp[-l_{\rm min}/\lambda_{\rm abs}(h\nu)]}{l_{\rm min}/\lambda_{\rm abs}}\right\} \ , \end{aligned} \tag{2.14}$$

where δV is the volume of this cell. It is straightforward to verify that $F_{\rm ph} \to N_{\rm ph,in}l_{\rm min}/(\delta V\delta t)$ at the optically thin limit ($l_{\rm min}/\lambda_{\rm abs} \to 0$); at high optical depths, $F_{\rm ph} \propto (l_{\rm min}/\lambda_{\rm abs})^{-1}$. If more than one ray propagate through the cell, equivalent fluxes are calculated for every ray using eq. (2.14), and then accumulated for each energy bin to obtain the total equivalent flux. On leaving this cell, the number of photons that the current ray carries is reduced due to absorption,

$$N_{\rm ph,out}(h\nu) = N_{\rm ph,in}(h\nu)\exp[-l_{\rm min}/\lambda_{\rm abs}(h\nu)] \ . \tag{2.15}$$

In addition, the accumulated column density of every chemical species it has passed through since emission is also registered: some thermochemical reaction rates will need these data.

2.2.2 Scattered Radiation

The direct ray tracing method alone is only suitable for cases where scattering is negligible. If not, another module must be introduced to deal with this situation.

This subsection discusses the Monte-Carlo method that deals with those scattered photons.

General scheme of Monte Carlo ray tracing

A Monte Carlo calculation of scattered radiation starts by generating a number of photon packets. To each packet, an initial direction of propagation and a number of photons are assigned. There are two types of photon creation processes that we most commonly encounter:

- A radiation source. In this case, the distribution of locations, directions and photon numbers of packets should obey the properties of the source.
- Photons scattered during the propagation of rays (§2.2.1). In this case, the locations of created photon packets should be distributed in the cells along the ray, and the distributions of photon numbers and directions should follow the differential cross section of relevant scattering processes. The number of photons scattered should be subtracted from the photon number in the ray.

After a photon packet is created, a random number $\tau_{\rm sca}$ (namely the scattering optical depth) that has exponential probability distribution function $f(\tau_{\rm sca}) = \exp(-\tau_{\rm sca})$ $(0 \leq \tau_{\rm sca} < \infty)$ is generated. The photon packet then travels along a straight line across cells (with the scheme described in 2.2.1); in each cell, the scattering optical depth is calculated as $\Delta\tau_{\rm sca} = l_{\rm min}/\lambda_{\rm sca}$, where $l_{\rm min}$ is the line segment length of photon packet propagation and $\lambda_{\rm sca}$ the scattering mean free path within the current cell. In the mean time, the number of photons in the packet is also reduced by eq. (2.15). The effective flux (which is indeed $n_{\rm ph}c$, the photon number density times the speed of light) that the photon packet contributes to the cell is estimated by eq. (2.14). Such $\Delta\tau_{\rm sca}$'s are accumulated until the sum exceeds $\tau_{\rm sca}$ when the ray leaves a cell–the current trip ends in this cell. The exact end point is calculated as,

$$l_{\rm end} = \lambda_{\rm sca}\left(\tau_{\rm sca} - \sum_{\rm before}\Delta\tau_{\rm sca}\right) \;\; ; \quad \mathbf{x}_{\rm end} = \mathbf{x}_0 + l_{\rm end}\mathbf{r} \; . \tag{2.16}$$

In eq. the sum goes through the path before the photon packet enters the current cell, $\mathbf{r}$ is the unit direction vector of photon propagation, and $\mathbf{x}_0$ is the point at which the photon enters the current cell. At $\mathbf{x}_{\rm end}$, the original photon packet is destroyed, and $N_{\rm split}$ "split" new photon packets are created. The directions and photon numbers of these new photon packets are assigned with random number generators, whose distribution functions should follow the differential cross section of scattering. If we mark the pre-split photon packet as level L, then the $N_{\rm split}$ new photon packets are marked by level $(L+1)$. Note that there should be a maximum photon packet level $L_{\rm max}$: when the level reaches $L_{\rm max}$, a photon packet should not be split any more (equivalently, $N_{\rm split}$ is set to 1 for $L = L_{\rm max}$) photons, so that the total time and memory consumption of computation does not explode.

Such procedures are taken for every photon packet, until at least one of the three stopping conditions is satisfied: (1) the photon packet leaves the simulation domain

(note that we need to set reflective boundaries in some cases, through which the photon packet does not actually escape, e.g. on the polar axis and at the mid-plane of a spherical coordinate grid); (2) the number of photons in this packet is lower than a threshold $N_{\rm ph,min}$; (3) total number of scattering events reaches a threshold. Generally speaking, more scattering events and higher photon packet level limit $L_{\rm max}$ yield better results (with less sampling noise and better convergence), but the computation costs in time and memory space are usually major limits.

The Monte Carlo scheme of photon packet tracing is straightforward to implement, but virtually impossible to be utilized with HD/MHD simulation in real-time, due to excessive computation costs. Therefore, CPU-based Monte Carlo photon packet tracing is mostly used for post-processing, and seldom for simulations themselves.

GPU-accelerated Monte Carlo

With the power of graphics processing units (GPUs), however, photon packet tracing can be finished within acceptable computation costs. The architecture of GPUs may vary with manufacturer and/or version of hardware, but in general they have some common features.

A GPU has scores of streaming multiprocessors (SMs). Each SM is equivalent to a single-instruction-multiple-threads (SIMT, similar but subtly different from the concept of single-instruction-multiple-data, SIMD) machine: it has multiple cores sharing the same instruction cache. Threads are organized by thread bundles (bundles for short hereafter). In addition to individual memory space, all threads within one bundle have shared access to a memory space that is held locally by the SM–this *shared memory* space is usually small (to date, such shared memory is usually no more than 96 kilobytes per bundle). A bundle is assigned to an SM and will generally stay until computation tasks are finished for this bundle. In one clock cycle, those threads are executed simultaneously on their assigned SM with identical instructions but on different sets of data. All SMs also have access to a global graphics memory. Such global graphics memory is relatively big, but the latency is high–it takes an SM many (~ 100) clock cycles to retrieve data from it. SMs also have very fast but read-only access to another relatively small patch of memory, usually called texture memory or *constant memory*, which is only writable by pertinent commands on the CPU side.

In order to utilize the features of a GPU for Monte Carlo ray tracing, we generally adopt the following scheme of calculation:

1. The simulation domain is split into multiple subdomains, as the shared memory on an SM is unlikely to be sufficient for the grid data, i.e. grid structures and scattering mean free path profiles, of the whole domain. In `Athena++`, the whole domain (the *mesh*) is usually divided into many subdomains (*meshblocks*); such meshblocks are naturally the units of domain splitting.

2. A number of "initial" photon packets are generated and assigned to meshblocks.

3. Photon packets are dispatched to thread bundles with grid data. Each bundle has a copy of the grid data of a meshblock as well as a number of photons on

the meshblock. Note that, for better load balancing, it is generally beneficial to assign one meshblock to multiple bundles, each of which holds the same copy of grid data but different sets of photon packets. The number of bundles assigned for one meshblock is generally proportional to the number of photon packets times the approximate optical depth across this meshblock (estimated by the typical size of the meshblock divided by the typical mean free path therein).

4. Photon packets are evolved on the meshblock, in virtually the same way as the CPU version. In a bundle, each thread evolves one photon packet. Photon packets, excluding those that are paused, are evolved simultaneously. If some photon packets leave the current meshblock, they are paused and put into background. Newly created photon packets due to splitting are also paused currently and put into background. This step is repeated until the number of repeats reaches some upper limit, or a certain fraction of photon packets are paused.

5. Steps 3 and 4 combined are called a cycle, and are executed repeatedly until the desired stopping conditions are met (e.g. maximum cycle number, maximum photon packet number, etc.). At the beginning of each cycle, the paused packets are started at current locations.

6. Finally, accumulated equivalent flux $n_{\rm ph}c$ in each cell is summarized in the global graphics memory, and then transferred to the CPU.

2.3 Thermochemistry

In each zone of the simulation domain, a coupled set of ordinary differential equations (ODEs) is solved to update the abundances of chemical species $\{n^i\}$ and internal energy density ϵ. These equations read, nominally,

$$\begin{aligned} \frac{{\rm d}n^i}{{\rm d}t} &= \mathcal{A}^i_{\ jk} n^j n^k + \mathcal{B}^i_{\ j} n^j \ ; \\ \frac{{\rm d}\epsilon}{{\rm d}t} &= \Gamma - \Lambda \ ; \end{aligned} \tag{2.17}$$

in which the terms involving $\{\mathcal{A}^i_{\ jk}\}$ describe those most commonly encountered two-body reactions, while those in $\{\mathcal{B}^i_{\ j}\}$ represent one-body processes, such as photoionization/photodissociation, spontaneous decay/disintegration, etc. Γ and Λ are the heating and cooling rates per unit volume, respectively. $\{\mathcal{A}^i_{\ jk}\}$, $\{\mathcal{B}^i_{\ j}\}$, Γ and Λ are usually functions of temperature T, calculated from the thermal energy density $\epsilon = c_V(\{n^i\})T$, where c_V is the heat capacity of the gas at constant volume: thermochemistry and HD/MHD are solved in separate steps, hence we use c_V instead of c_P here. During the process of ODE solving (e.g. in the internal cycles of an ODE solver), the temperature is updated along with changes in ϵ and c_V.

2.3.1 Thermochemical Evolution

The thermochemical ODEs, eq. (2.17), are usually very stiff, and hence numerically difficult to solve. This subsection discusses the method that we use for solving this ODE system.

Reaction rates and Jacobian matrices

Integrating thermochemical ODEs requires us to obtain reaction rates. In terms of the method in numerical evaluation of rate coefficients, the reaction can be re-categorized into three types:

1. *Two-body reactions* (along with their corresponding heating/cooling processes) that have modified Arrhenius type of rate coefficients, $k = k_0(T/T_0)^\beta \exp(-T/T_0)$, where k_0, T_0 and β are parameters that are tabulated in astrochemical databases, especially the `UMIST` database (McElroy et al., 2013).

2. *Photoreactions*. The most important parameter is the absorption cross section of a reaction. We specifically note that, as the chemical abundances evolve, the effective flux given by eq. (2.14) must be adjusted accordingly.

3. *Reactions with interpolated rates*. A lot of reactions and cooling/heating processes have reaction rates that are functions of temperature that cannot easily be expressed analytically; they can also depend on thermochemical conditions of the current cell (e.g. escape probability of cooling photons). These reactions require interpolation tables to evaluate rate coefficients when the ODEs are solved. Different tables are usually generated for each cell; they are one-dimensional (in temperature), since the total mass density and elemental abundances of a cell are assumed to be fixed during a thermochemical step.

As themochemical ODEs are usually stiff, Jacobian matrices of the reaction rates are required by (semi-)implicit methods of integration. Once we have a way to obtain the reaction rates, in principle, the Jacobians can be obtained by taking partial derivatives numerically. Nevertheless, numerical derivatives for Jacobians can be costly to calculate (as the reaction rates are calculated repeatedly), while the Jacobians themselves do not have to be exact. In order to lower the costs of computation, we actually estimate them by the approximate method stated below:

- The derivatives of the mass action law with respect to the abundances of reactants are taken trivially. For example, $[\partial(\mathcal{A}^i_{jk} n^j n^k)/\partial n^j]_{\mathcal{A}} = \mathcal{A}^i_{jk} n^k$ $(j \neq k)$.

- Derivatives with respect to thermal energy density are obtained by taking the derivatives of temperature first and dividing the results by c_V. Note that temperature derivatives for reactions of types 1 and 3 can be taken analytically. The dependence of c_V on $\{n^i\}$ can generally be ignored in practice.

- The derivatives of effective radiation fluxes $F_{\rm ph,eff}$ with respect to $\{n^i\}$ can be obtained by $\partial(\lambda^{-1}_{\rm abs})/\partial n^i = \sigma^i_{\rm abs}$, where $\sigma^i_{\rm abs}$ is the absorption cross section of

the ith species. As $\partial F_{\rm ph,eff}/\partial(\lambda_{\rm abs}^{-1})$ is obtained analytically, $\partial F_{\rm ph,eff}/\partial n^i$ is easily calculated. In practice, however, it is safe to only consider the species that has maximum contribution to $\lambda_{\rm abs}^{-1}$ in the current cell as a proxy of all $\partial(\lambda_{\rm abs}^{-1})/\partial n^i$. If we take this simplification, $\partial(\lambda_{\rm abs}^{-1})/\partial n^i$ must be re-scaled accordingly.

Pre-processing

The ODEs are solved as initial value problem; the initial values are taken from the step of HD/MHD evolution that has just been finished. Note that `Athena++` uses total energy density for its Godunov solver; the thermal energy density ϵ is obtained by subtracting kinetic and magnetic (in MHD simulations) energy densities from the total.

Before inserting the advected chemical abundances into the initial values of the ODEs, the consistency of those abundances must be checked: during the HD/MHD step, the density floor (numerical lower limit of mass density) might be reached, which raises the mass density without doing anything to the chemical abundances. If consistency problems are actually found, simple rescaling of all species will generally solve them. Similarly, the combination of numerical floors in mass density and gas pressure may cause some cells to have unphysical internal energy density; such issues should also be identified and fixed by resetting the internal energy density so that the corresponding gas temperature is not below the floor or beyond the cap (such floor and cap should be set by the user depending on the physical processes of interest in the simulation).

This pre-processing step is also responsible for preparing the evaluation of reaction rates and Jacobians, in each cell: (1) generating interpolation tables of reaction rates based on the thermochemical environments of the cell; (2) finding the species that has maximum contribution to $\lambda_{\rm abs}^{-1}$.

Selectable ODE backends

As we already have the method of calculating reaction rates and estimating the Jacobians, solving the thermochemical ODEs becomes relatively straightforward. We standardize the interface of reaction rates and Jacobian evaluation so that the users can select their preferred ODE solver as the backend, including:

- `CVODE`, the standard and widely used ODE solver library (see Hindmarsh et al., 2005). `CVODE` is believed to be sufficiently reliable, but it has inappropriate designs in memory access, and sacrifices a lot of efficiency for better generality.
- CPU-based implicit Rosenbrock solver with adaptive step size control and error estimator (see also Press et al., 2002, chapter 16 section 6).
- GPU-based solver (see §2.3.2).

Users can also write their own solvers if necessary. In general, the solver should have the functionality to report failures in convergence, and must be (semi-)implicit to deal with the stiffness of our ODEs.

Post-processing

Before writing the thermochemically evolved abundances and thermal energy density into the code for the next step of HD/MHD evolution, some post-processing procedures must be carried out for every cell, so that unphysical outcomes of some thermochemcial calculations are eliminated before they spoil the whole simulation.

For one cell, if the ODE solver reports an error (usually failures in convergence) about solving the thermochemical ODEs, or some results are apparently unphysical (e.g. "not-a-number" abundances, or abundances that are seriously negative, or the conservation in chemical elements is significantly violated), a retry in solving thermochemical ODEs is conducted, with the same initial condition but smaller initial step size and more stringent step size control. If the retry fails again, an error report is generated and presented to the user, while the user should already have decided in the initialization file that, in this situation, the code will continue by reverting the current step of thermochemical calculation (i.e. take the abundances and thermal energy density before this step of thermochemical evolution as the evolved results) for this cell, or simply abort the whole simulation.

More often than not, some tiny but acceptable issues in evolved thermochemical systems occur. The two most common issues are, (1) element conservation is always slightly violated due to rounding errors (this is a more significant issue with the GPU-based solver, as a GPU usually works with single precision float point numbers), and (2) abundances of some species becomes slightly negative because of numerical errors. These issues are addressed with a regularization procedure that consists of the following steps:

1. If some species have negative abundances, their abundances are set to zero.

2. Abundances of elements are calculated for the initial and final states of thermochemical evolution. In the final state, the abundances in the single-element species are adjusted to compensate the differences. This step corrects the violation in element abundances brought by step 1.

3. If step 2 causes negative abundances in some single-element species, the most abundant compound species is disintegrated into elements just sufficiently to correct this.

In case that there are still negative abundances after this procedure, an error flag will be raised, and the current cell will enter the retry step, described by the previous paragraph.

2.3.2 GPU-Optimized Algorithm

The thermochemical ODEs are always costly to solve, but embarassingly parallel among cells. In order to accelerate our calculations, we port the solvers to GPUs. In this substep, the thermochemical evolution of each cell is assigned to a thread bundle. Because of the special architecture of GPUs (see also §2.2.2), the algorithms

should be adjusted to optimize their performances on a GPU, especially by utilizing the SIMT architecture.

Reaction rates and Jacobian matrices

Evaluating reaction rates and Jacobians is relatively straightforward to optimize for SIMT. Each type of the three kinds of reactions (§2.3.1) is calculated simultaneously by all threads in the bundle; each thread calculates the rate (and the contribution to the Jacobian if necessary) of one reaction, so that the threads share the same set of instructions. If there are more reactions than threads, such SIMT operation is repeated to cover all reactions. Sometimes some threads are idle as there are fewer reactions to calculate. When a thread finishes calculation, it writes the contribution of its reaction to the rates and the Jacobian on the memory shared by the bundle. Since this memory space is shared, such writing must be done via atomic operation routines to avoid race conditions.

Solving linear systems: LU decomposition on SIMT

No matter what kind of (semi-)implicit ODE solver is adopted, solving linear systems is always the most necessary and costly stage throughout the whole working cycle. What is needed by thermochemistry evolution is solving small scale (corresponding to the number of chemical species; usually $\sim 20 - 30$ in this thesis) in large batches (corresponding tot he number of cells in the simulation, usually $> 10^4$) concurrently: existing GPU routines are all optimized for solving large dense/sparse matrices *one at a time*, hence are *not* suitable for our purposes.

We found that the Crout's algorithm for LU decomposition with row pivoting (see also Press et al., 2002) is a good choice to be implemented on the SIMT architecture of GPUs to solve big batches of small matrices concurrently. We present the pseudo code in Algorithm 1. All steps listed in Algorithm 1 are executed by all threads; each thread holds its own thread index i, but all threads share the instructions and the access to the matrix a_{ij} and vector v_i. Due to data dependency, all threads computing the same matrix must be synchronized at lines 5, 8 and 11. Once the LU-decomposed matrix with the permutation vector is obtained, the back-substitution procedures for the final solution are trivial.

Asynchronous scheme: Hiding pre-/post-processing behind computation

Although we have already ported the most computation intensive part of thermochemistry calculations—the ODE solver—to GPUs, pre-/post-processing steps are still most easily done on the CPU because of considerations of flexibility and complexity, requiring communication between CPUs and GPUs. If we naively organize all the tasks linearly, a considerable amount of wall-clock time will be wasted: one task will have to wait until the previous one is fully completed, causing unnecessary idling of devices. Instead, we utilize the feature of modern GPUs programming, that can execute tasks asynchronously: after the CPU finishes pre-processing for a relatively

Algorithm 1: LU decomposition of a matrix on a SIMT unit.

Data : Matrix to be decomposed a_{ij} (size $N \times N$)
Result: LU-decomposed a_{ij}; Permutation vector p_i.

$i \leftarrow$ thread index $(0 \leq i \leq N-1)$;
$v_i \leftarrow$ maximum absolute value in the ith row of a_{ij}
for $j \leftarrow 0$ **to** $N-1$ **do**
    `/* Compute U and unrescaled L */`
    for $k \leftarrow 0$ **to** $\min\{i-1, j-1\}$ **do** $a_{ij} \leftarrow a_{ij} - a_{ik}a_{kj}$;
    `/* Pivoting: diagonal holds greatest possible abs value */`
    synchronize threads;
    if $i \geq j$ **then** $t_i \leftarrow |a_{ij}|/v_i$;
    $i_{\max} \leftarrow$ index for the maximum t_i with $i \geq j$;
    synchronize threads;
    if $j \neq i_{\max}$ **then** swap$(a_{i_{\max},i}, a_{ji})$;
    if i is 0 **then** swap$(v_{i_{\max}}, v_j)$, $p_i \leftarrow i_{\max}$;
    `/* Rescale L */`
    synchronize threads;
    if $j < i$ **then** $a_{ij} \leftarrow a_{ij}/a_{jj}$;
end

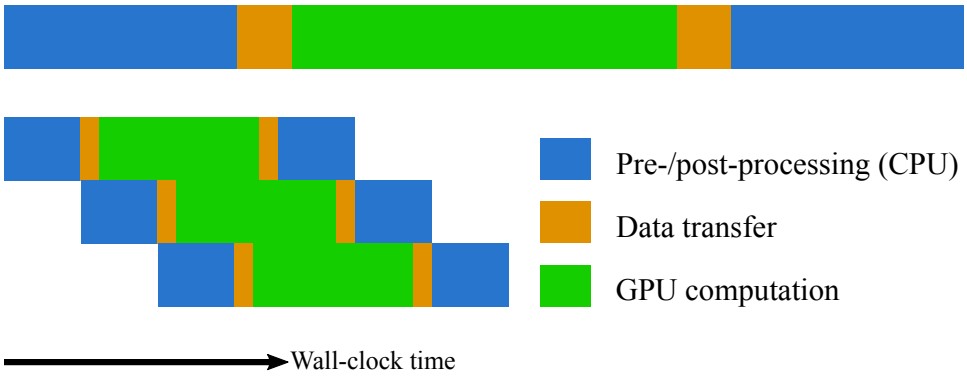


Figure 2.1 Schematic diagram of linear (upper panel) and asynchronous (lower panel) computation scheme for thermochemistry evolution.

small chunk of cells, it sends the pre-processed data to the data bus. It then immediately continues to work on the next chunk of pre-processing, while data transfer and subsequent GPU computation are carried out in the background simultaneously. In the mean time, the GPU will automatically distribute its tasks: if a new batch of tasks comes before the slowest ones in the previous batch have finished, the GPU will dispatch some new tasks to the computation resources (e.g. SMs) that have already finished their jobs for the previous batch. This also minimizes idling within the GPU itself.

Figure 2.1 compares the naive linear scheme to the asynchronous one, illustrating the advantage of the latter.

2.4 Examples of Code Verification

2.4.1 Advection of Chemical Species

In order to test the algorithms discussed in §2.1.1, we present one of the test problems we constructed to examine those algorithms, in order to illustrate their capabilities clearly. All quantities discussed in this subsection are in code units and are presented dimensionlessly.

We construct a one-dimensional simulation within domain $\xi \in [-0.5,\ 0.5]$, which is evenly divided into 64 zones. Periodic boundary conditions are set at both $\xi = \pm 0.5$ boundaries. The mass density $\rho = 1$ and energy density $\epsilon = 1$ are constants in the simulation domain, and moves at a constant velocity $v = 1$ from left to right. Four chemical species A, A_2, AB, B, consisting of two elements A and B, are advected passively with the fluid; no chemical reactions are calculated in this test. At $t = 0$, the initial profiles of species abundances are (for fair comparison with CMA, element abundances are constants throughout the domain),

$$\begin{aligned} n_{\rm A} &= 0.49\Theta(-x) + 0.05\Theta(x) + 0.2x \ ; \\ n_{\rm A_2} &= 0.20\Theta(-x) + 0.40\Theta(x) - 0.1x \ ; \\ n_{\rm AB} &= 0.01\Theta(-x) + 0.05\Theta(x) \ ; \\ n_{\rm B} &= 0.09\Theta(-x) + 0.05\Theta(x) \ . \end{aligned} \tag{2.18}$$

The test case is evolved until $t = 1$, which takes 374 steps to finish with CFL number 0.3. Ideally at $t = 1$ the profiles should be identical to those that $t = 0$, due to the periodic conditions. In Figure 2.2, we present the advected profiles in the first two rows (compared to the exact result), and show the violation of element conservation in the bottom row. Curves marked as "Uncorrected" indicates the result when the PLM reconstruction scheme is directly applied to $\{x^s_{i-1/2}\}$ without any correction regarding element/species conservation. We have, from the figure, these observations:

- Advection results are much less diffusive with PLM reconstruction, with or without correction, compared to the donor-cell-like scheme.
- All results conserve element B, up to an acceptable truncation error. The profiles of abundances in species AB and B are initially piecewise constants, which minimizes the impact of non-linear slope-limited derivatives even for the uncorrected scheme (eq. 2.8).
- The scheme with uncorrected PLM reconstruction shows considerable violation of element conservation in A, within only 374 steps. Such errors accumulate: after only $\sim 10^5$ steps, they will eventually rise to $\sim 10^{-1}$, which is unacceptable for thermochemcial calculations. Donor-cell-like and corrected PLM reconstruction schemes conserve the species abundances rather well.

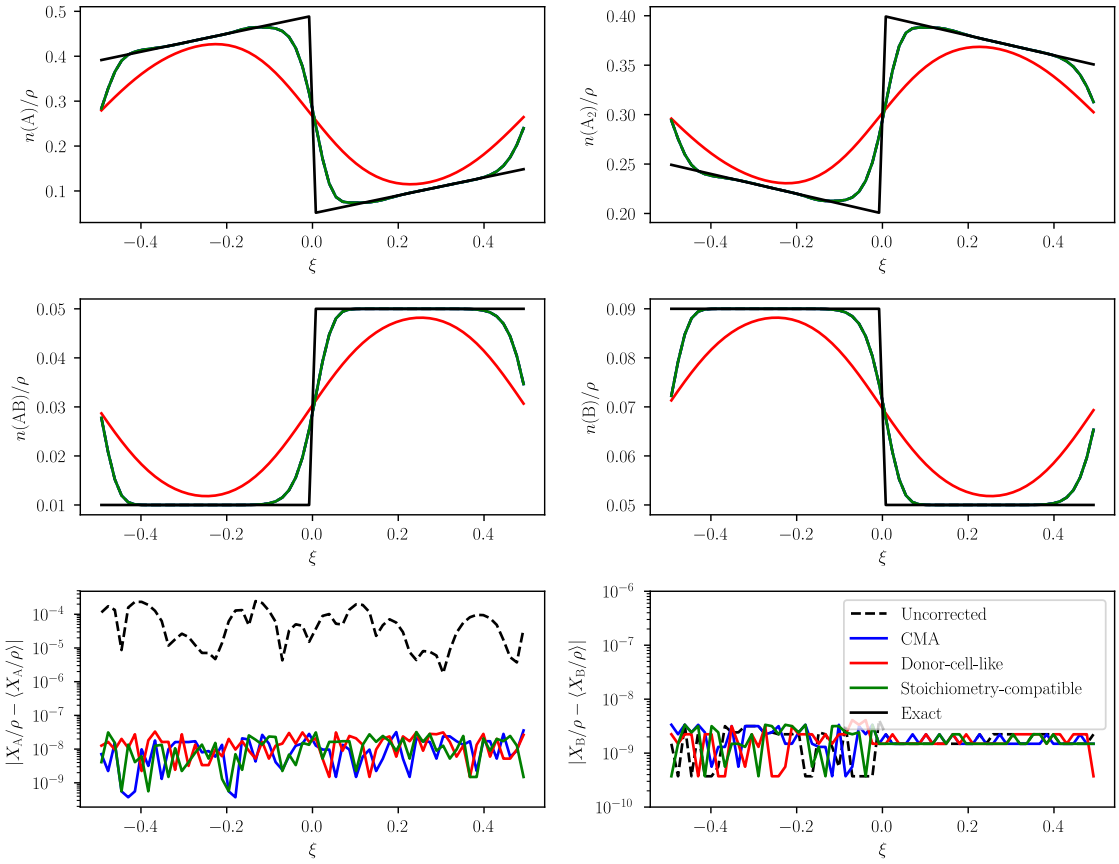


Figure 2.2 Test results of different advection schemes (see §2.4.1), showing results of advection at $t = 1$ code time for all four species, in code units. Note that the curves for uncorrected, CMA, and stoichiometry-compatible results overlap each other in the first two rows. The first two rows also have a black solid curve showing the exact result.

2.4.2 Diffusion of Radiation

This subsection tests the Monte Carlo ray tracing scheme on the GPU, and also our geometric ray-tracing, which is shared by the CPU version of the algorithm.

We setup a unit test that has a point source in a medium with scattering and absorption. If the medium is relatively opaque, the behavior of the radiation field can be approximately described by a diffusion equation. A monochromatic point source is located at $\mathbf{x}_s$ with luminosity L (in photons per unit time). The diffusion equation for photon number density n_ph, in steady states ($\partial_t n_\mathrm{ph} = 0$), reads

$$\frac{c}{3}\lambda_\mathrm{sca}\nabla^2 n_\mathrm{ph} - c\lambda_\mathrm{abs}^{-1} n_\mathrm{ph} + 4\pi L\delta(\mathbf{x} - \mathbf{x}_s) = \partial_t n_\mathrm{ph} = 0 \ , \tag{2.19}$$

where λ_sca and λ_abs are photon mean free paths respectively, $\mathbf{x}$ denotes the spatial coordinates, and δ is the Dirac delta function. Solving eq. (2.19) by Fourier transform

we obtain the Yukawa-type result,

$$n_{\rm ph} = \frac{3L}{c\lambda_{\rm sca}|\mathbf{x}-\mathbf{x}_s|}\exp\left[-\left(\frac{3}{\lambda_{\rm sca}\lambda_{\rm abs}}\right)^{1/2}|\mathbf{x}-\mathbf{x}_s|\right] . \tag{2.20}$$

For the simulation, we setup a uniform medium on a spherical polar grid with axisymmetry about the polar axis (hence $\partial_\phi = 0$). The grid spans a spatial domain with radial range $r \in [1, 10]$ and colatitude range $\theta \in [0, \pi/2]$, and has resolution $N_r \times N_\theta = 128 \times 128$; radial zones are spaced logarithmically and latitudinal zones evenly. Here the only reasonable places to put a point source in this domain are on the polar axis; locating the source elsewhere creates a radiating ring because of axisymmetry, which does not yield simple and clear analytic solution for us to compare with. We set the source at $\mathbf{x}_s = 5\hat{\mathbf{z}}$, with luminosity $L = 1$. The mean free paths for scattering and absorption are set to $\lambda_{\rm sca} = 0.5$ and $\lambda_{\rm abs} = 10$, respectively. 10^4 photons are injected into the system from the point source, and we allow $N_{\rm split} = 2$ photon packet splitting with maximum level $L_{\rm max} = 2$. These photons are allowed to evolve 50 cycles, each cycle allows every photon to travel through 64 cells on the same meshblock (see §2.2.2).

We present the results in the steady state in Figure 2.3, where the left panel shows the $n_{\rm ph}c$ profile and the right column compares the profiles along $\theta \in \{0.2,\ 0.4,\ 0.6\}$ radial lines with the analytic solution in eq. (2.20). Almost perfect overlaps are observed for all those radial profiles. The relative error of Monte Carlo ray tracing is $\lesssim 1$ % for the $\theta = 0.2$ case. The $\theta = 0.6$ profile shows more shot noise as the number of photon packet reaching there is less. It is worth noting that the Monte Carlo results shown is generated within 10^{-1} s wall-clock time on a NVIDIA GTX 1080 GPU, while the same computation cannot be finished on a CPU core within 10 s.

2.4.3 Comprehensive Test of Coupled Dynamics and Thermochemistry

This subsection features a comprehensive verification of many modules discussed earlier in this chapter. We construct a test problem that combines hydrodynamics and radiation-related thermochemistry.

The geometry of our test problem is simple: it has one-dimensional plane-parallel geometry with translational symmetry along y and z-axis (viz. $\partial_y = \partial_z = 0$; we also assume that the fluid motion goes along x-axis only, viz. $\mathbf{u} = u\hat{\mathbf{x}}$). The layout is sketched in Figure 2.4.

Thermochemistry: Minimum but enough

We aim to compare simulations to analytic results. To simplify the (semi-)analytic solutions, only three basic chemical species are involved in this section: H, H^+, and

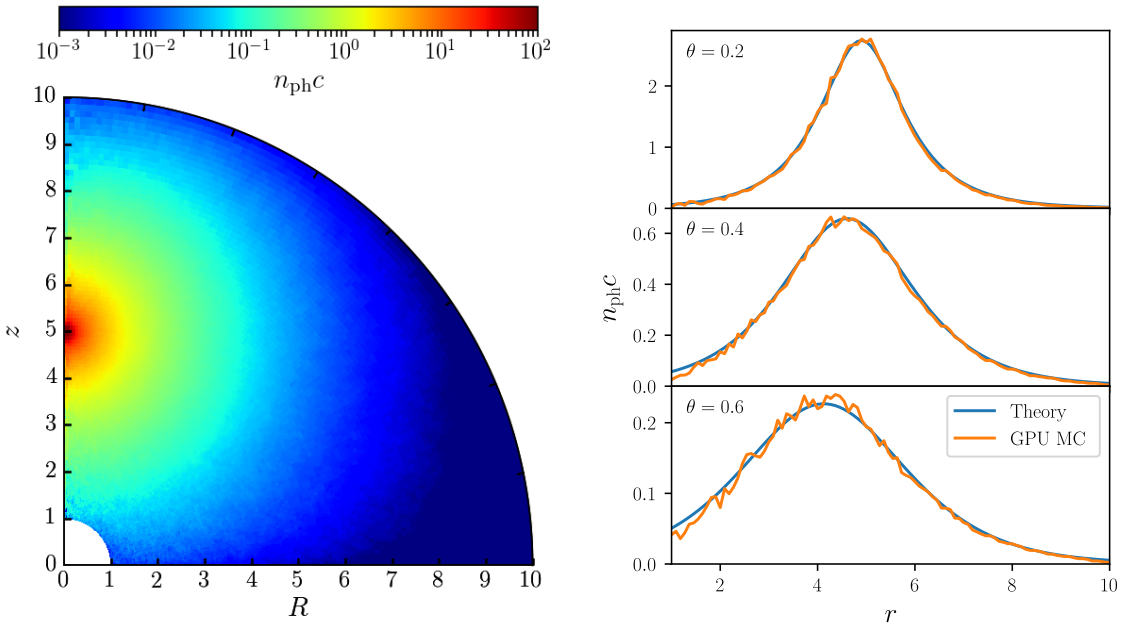


Figure 2.3 Test results of Monte Carlo ray tracing on the GPU. Left panel shows the meridional plot for $n_{\rm ph}c$ (photon number density times the speed of light), while the right column compares the results along $\theta \in \{0.2,\ 0.4,\ 0.6\}$ radial lines with theoretical predictions (see §2.4.2). All quantities are shown in code units.

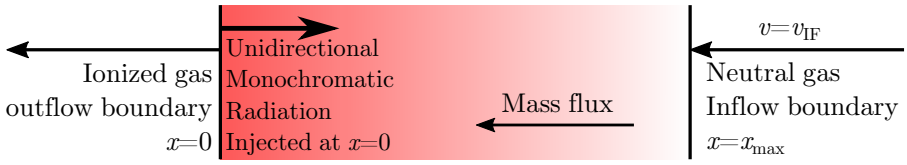


Figure 2.4 Layout of one-dimensional hydrodynamics test problem coupled with thermodynamics and chemistry.

e^-, with photoionization and radiative recombination reactions,

$$\mathrm{H} + h\nu \rightarrow \mathrm{H}^+ + e^- \ ; \quad \mathrm{H}^+ + e^- \rightarrow \mathrm{H} + h\nu \ . \tag{2.21}$$

For simplicity, we only apply monochromatic radiation to the system, and assume that the photons re-emitted in the second reaction get out of the system without any reactions (hence a type-B recombination coefficient is applied). Basic heating and cooling processes corresponding to two reactions are also introduced, including photoelectric heating with $\langle E_{\rm pe}\rangle = h\nu - I_e$ ($I_e = 13.6$ eV is the ionization threshold of atomic hydrogen) for each hydrogen atom ionized, and recombination cooling $\langle E_{\rm rr}\rangle = 3k_{\rm B}T/2$ for each hydrogen atom reformed ($k_{\rm B}$ is the Boltzmann constant). In e.g. Draine (2011a), calculations suggest that $\langle E_{\rm rr}\rangle$ is smaller than $3k_{\rm B}T/2$ ($\langle E_{\rm rr}\rangle \sim [0.684 - 0.0416\ln(T_4/Z^2)]k_{\rm B}T$, $T_4 \equiv (T/10^4\ {\rm K})$ where Z is nucleus charge number), since the electrons with lower kinetic energy are more easily to be captured by ions. However, if recombination captures a significant fraction of free electrons, the preference for lower electron energy does not apply. Here we assume $\langle E_{\rm rr}\rangle = 3k_{\rm B}T/2$ for clarity.

Guiding equations of the system

Here we use x and t as the variables for the spatial and temporal coordinates (not to be confused with local electron fraction x_e). The hydrodynamic equations in this case read,

$$\begin{aligned} &0 = \partial_t\rho + \partial_x(\rho u) \ ; \ 0 = \rho(\partial_t u + u\partial_x u) + \partial_x p \ ; \ 0 = \partial_x F + F\sigma n_{\rm H}(1-x_e) \ , \\ &S_E = \partial_t\left(E + \frac{1}{2}\rho u^2\right) + \partial_x\left[u\left(E + \frac{1}{2}\rho u^2 + p\right)\right] \ ; \end{aligned} \tag{2.22}$$

Here ρ is the mass density, u is the velocity component along x-axis, p is the gas pressure, $E = p/(\gamma - 1)$ is the internal energy density (note that the gas in our test problem always has $\gamma = 5/3$), and F is the photon number flux. The energy source term S_E is given by,

$$S_E = F\sigma n_{\rm H}(1-x_e)(h\nu - I_e) - \alpha_{\rm B} n_{\rm H}^2 x_e^2 \langle E_{\rm rr}\rangle \ . \tag{2.23}$$

σ is the absorption cross section of atomic hydrogen at photon energy $h\nu$, $n_{\rm H} \simeq \rho/m_p$ the number density of hydrogen in all forms (H and H^+ combined; we ignore the difference between the proton mass m_p and the mass of the hydrogen atom $m_{\rm H}$ in this subsection), and $\alpha_{\rm B}$ the type-B recombination rate at local temperature T. For simplicity, we adopt the `UMIST` version $\alpha_{\rm B} = 3.5 \times 10^{-12}\ {\rm cm^3\ s^{-1}} (T/300\ {\rm K})^{-0.75}$. In order to evaluate the ionized fraction x_e, we write,

$$(\partial_t + u\partial_x)x_e = S_I \ , \quad S_I \equiv F\sigma(1-x_e) - \alpha_{\rm B} n_{\rm H} x_e^2 \ . \tag{2.24}$$

It is straightforward to verify that these governing equations are invariant under Galileo transformations.

Steady state solutions

For steady state solutions (traveling wave solution, etc.), we apply operator and variable substitutions $\partial_t \to (-v_{\rm IF}\partial_x)$ and $u \to w + v_{\rm IF}$, where $v_{\rm IF} = F/n_{\rm H}$ is the propagation speed of the ionization front. These substitutions are equivalent to a transform to a new frame of reference, where the ionization front is static in steady state. We then solve the linear set of equations with respect to $\partial_x\rho$, $\partial_x w$, $\partial_x E$ and $\partial_x x_e$, to obtain,

$$\begin{aligned} &\partial_x\rho = (w\Delta)^{-1}(\gamma-1)S_E \ ; \quad \partial_x w = (-\rho\Delta)^{-1}(\gamma-1)S_E \ ; \\ &\partial_x E = \Delta^{-1} w S_E \ ; \quad \partial_x x_e = (w n_{\rm H})^{-1} S_I \ ; \quad \Delta \equiv w^2 - c_s^2 \ , \end{aligned} \tag{2.25}$$

where $c_s \equiv \gamma p/\rho$ is the local speed of sound. We then recast those equations into dimensionless form. First, by specifying reference dimensional variables l_0 (dimension of length), ρ_0 (density at $x = x_{\rm max}$), c_{s0} (speed of sound at $x = x_{\rm max}$; $c_{s0}^2 = \gamma k_{\rm B} T_0/m_p$), E_0 [energy density at $x = x_{\rm max}$; $E_0 = n_0 k_{\rm B} T_0/(\gamma-1)$], and F_0 (the photon number flux density at $x = 0$), the following equalities define the dimensionless parameters:

$$\begin{aligned} &\lambda \equiv \frac{x}{l_0} \ , \ \varrho \equiv \frac{\rho}{\rho_0} \ , \ \Theta \equiv \frac{T}{T_0} \ , \ \mu \equiv \frac{w}{c_{s0}} \ , \ \delta \equiv \frac{\Delta}{c_{s0}^2} = \mu^2 - \epsilon\varrho^{-1} \ , \\ &\xi_0 \equiv \frac{\langle E_{\rm rr}\rangle_{T=T_0}}{k_{\rm B}T_0} = \frac{3}{2} \ , \ \zeta_0 \equiv \frac{h\nu - I_e}{I_e} \ , \ \tau_0 \equiv \frac{\sigma\rho_0 l_0}{m_p} \ , \ \epsilon \equiv \frac{E}{E_0} \ , \ \varphi \equiv \frac{F}{F_0} \ , \\ &C_1 \equiv \frac{F_0\sigma I_e l_0}{c_{s0}^3 m_p} \ , \ C_2 \equiv \alpha_0 \left(\frac{\rho_0}{m_p}\right)^2 \left(\frac{k_{\rm B}T_0 l_0}{\rho_0 c_{s0}^3}\right) \ , \ C_3 \equiv \frac{F_0\sigma l_0}{c_{s0}} \ , \ C_4 \equiv \frac{\alpha_0 l_0 \rho_0}{c_{s0} m_p} \ . \end{aligned} \tag{2.26}$$

Then the equations are re-written in dimensional forms,

$$\begin{aligned} &\partial_\lambda\varrho = (\mu\delta)^{-1}(\gamma-1)\Sigma_E \ ; \quad \partial_\lambda\mu = (-\varrho\delta)(\gamma-1)\Sigma_E \ ; \\ &\partial_\lambda\epsilon = \gamma(\gamma-1)\delta^{-1}\mu\Sigma_E \ ; \quad \partial_\lambda x_e = \mu^{-1}\Sigma_I \ ; \quad \partial_\lambda\varphi = -\tau_0\varrho(1-x_e)\varphi \ ; \\ &\Sigma_E \equiv C_1\varphi\varrho(1-x_e)\zeta_0 - C_2\Theta^{\kappa+1}x_e^2\varrho^2\xi_0 \ ; \quad \Sigma_I \equiv C_3\varphi(1-x_e) - C_4\Theta^\kappa x_e^2\varrho \ . \end{aligned} \tag{2.27}$$

These of equations are actually ODEs rather than PDEs, and ∂_λ is indeed $({\rm d}/{\rm d}\lambda)$.

We set the reference variables (other than F_0) according to the gas-feeding flow at $x = x_{\rm max}$, hence the boundary condition there is simply $\varrho = 1$, $\mu = (-v_{\rm IF}/c_{s0})$, $\epsilon = 1$, and $x_e = 0$. "Shooting" procedures are then taken: we adjust the value of $\ln\varphi$ at $x = x_{\rm max}$ before integrating down to $x = 0$, so that $\ln\varphi = 0$ (hence $\varphi \equiv F/F_0 = 1$) at $x = 0$.

In Figure 2.5, we show an example that compares our simulation with an analytic solution discussed in this subsection. The model has $F_0 = 10^{11}$ cm^{-2} s^{-1}, $\rho_0 = 10^4 m_p$ cm^{-3}, and $T_0 = 100$ K. The injected photons have energy $h\nu = 20$ eV, at which $\sigma = 2.211 \times 10^{-18}$ cm^2. The range of x that the simulation solves is $0 < x < x_{\rm max} = 30$ AU. The speed of the ionization front is $v_{\rm IF} = 10^2$ km s^{-1}. The simulation is run on a one-dimensional grid with 64 cells along x-direction.

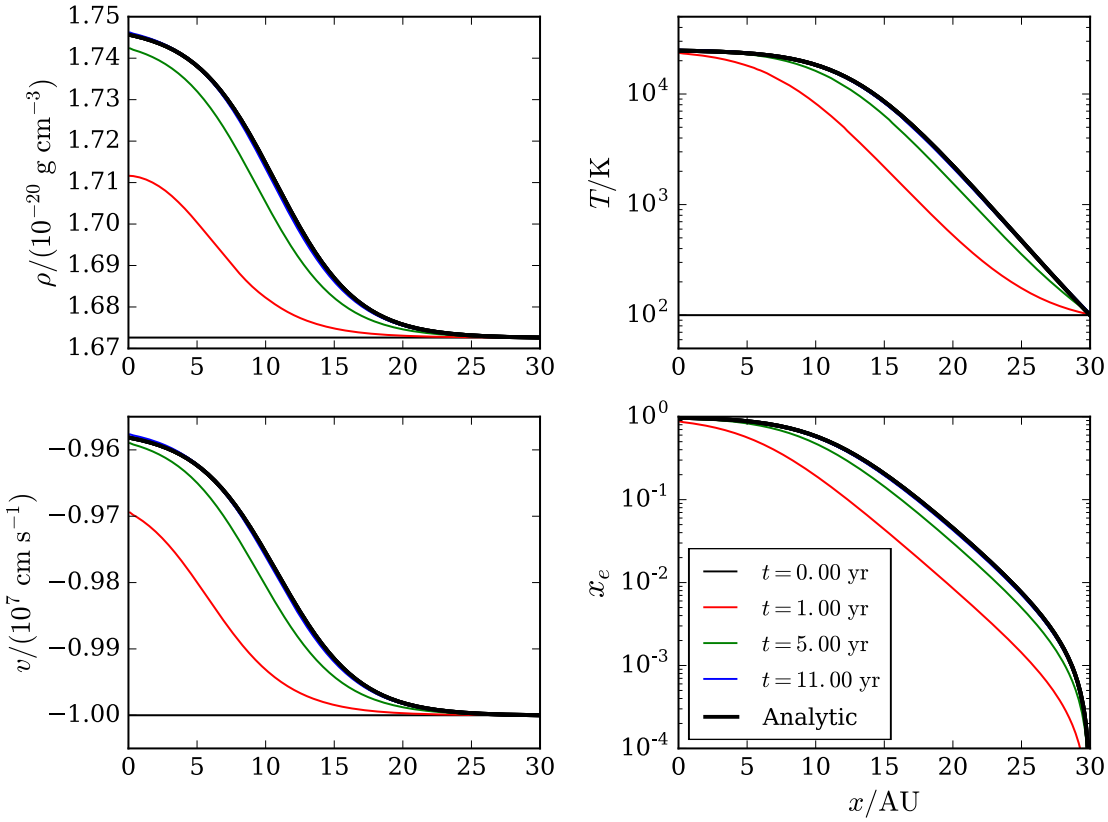


Figure 2.5 Example of comparing the analytic solution to simulations. As the initial condition, $x_e = 0$ for all x at $t = 0$, hence the $t = 0$ curve is not shown in the logarithmic plot in the lower-right panel. The $t = 11$ yr curves are not visible since they perfectly overlap with the analytic solution.

Chapter 3

Photoevaporation of Protoplanetary Disks

This chapter discusses the pure photoevaporation processes of PPDs, with no magnetic fields. While the overall simulation method is a combination of modules in Chapter 2, physical approximations and thermochemical network setup are briefly summarized in §3.1. §3.2 introduces the parameter choices underlying our fiducial model and its simulation results. For several other models that differ from the fiducial one in one or more parameters, §with the goal of exploring the effects of these parameters on gross properties of the flow, especially the mass-loss rate. In §3.4, we discuss the role that different bands of radiation play, and also compare and contrast our results with some existing works. §3.5 concludes and summarizes this chapter. The Appendix 3.A provides details on key thermochemical processes.

3.1 Microphysics in Photoevaporating PPDs

3.1.1 Radiative Transfer

In general, the scheme of radiative transfer in this chapter follows §2.2.1. We notice that absorption processes dominate scattering for most of the radiation that we consider: FUV, EUV, and 1 keV X-rays (Draine, 2011b; Verner et al., 1996). An exception would be Lyα photons, which may dominate the FUV luminosity, and whose scattering into nonradial directions might allow them to penetrate more deeply into the disk (e.g. Bethell & Bergin, 2011). We find, however, that unscattered soft FUV photons penetrate the intermediate layer anyway, and more deeply than Lyα . With a post-processing scheme based on §2.2.1, we will calculate the spacial profile of Lyα once the fiducial model results are obtained (see §3.2.2).

Like Lyα , these photons dissociate H_2O and OH, which can be important coolants, but not H_2 or CO (e.g. Shull, 1978). The scattering of harder X-rays can be important for ionization and hence magnetic coupling of the upper layers of the disk (e.g. Igea & Glassgold, 1999; Bai & Goodman, 2009), but we are neglecting magnetic fields here.

Therefore, in this chapter, scattering is neglected, and radiative transfer consists only of radial ray tracing, the sources of all hard photons being assumed to lie at the origin ($r = 0$).

3.1.2 Chemistry and Thermodynamics in General

Guided by GH08, GH09, and our own numerical experiments, we adopt 24 species that are most relevant to heating and cooling processes involved in PPD photoevaporation: e^- (free electrons), H^+, H, H_2, $H_2{}^*$ (using the $v = 6$ vibrational state as a proxy for H_2 in all excited states, see §3.A.1 and TH85), He, He^+, O, O^+, O^* (the ^1D state of atomic oxygen as a proxy for all neutral excited states, see §3.A.2), OH, H_2O, C, C^+, CO, S, S^+, Si, Si^+, Fe, Fe^+, Gr, Gr^+, Gr^-. Here Gr and $Gr^\pm$ denote neutral and singly-charged dust grains, respectively.

Standard two-body reactions

We extract the reactions involving these species from the `UMIST` astrochemistry database (McElroy et al., 2013). However, the interstellar radiation fields and matter densities to which the standard `UMIST` database is usually applied are rather different from those of PPDs. We therefore exclude all reactions involving photons and dust grains in the `UMIST` library; instead, we evaluate those reaction rates separately.

Photoreactions

Photoionization and photodissociation are critical mechanisms that affect photoevaporation. At each photon energy, the ionization cross section of each atomic species is evaluated using the data in Verner & Yakovlev (1995); Verner et al. (1996). For molecular species that can react with FUV photons, namely H_2, CO, OH, and H_2O here, we adopt the FUV-induced photochemcial reaction rate based on Tielens & Hollenbach (1985, hereafter TH85) for H_2, Visser et al. (2009) for CO (note that this photodissociation cross section is $\sim 10\times$ the value in TH85), and Ádámkovics et al. (2014, hereafter AGN14) for H_2O and OH. The photochemical processes related to H_2, C and CO may be subject to considerable self-shielding and cross-shielding. Using the radial column density data that are obtained by integrating along radial rays, we evaluate the impact of the self-/cross-shielding by adopting the analytic formulae in Visser et al. 2009 (for CO) and TH85 (for C), and Draine & Bertoldi (1996) (for H_2). It is worth noting that the FUV-induced processes in parallel with photodissociation of H_2, H_2O and OH, e.g. FUV pumping of H_2 onto its excited states and its subsequent effects, can have considerable thermodynamic effects. We discuss those key reactions in details in §3.A.1 §3.A.2.

Heating and cooling

Heating and cooling processes are directly associated with chemical reactions. While the amount of energy deposited into and removed from the gas by photoionization and recombination can be estimated straightforwardly (see Draine, 2011b, eqs. 27.3,

27.23), the thermodynamic effects of other chemical reactions need elaboration. Details are provided in § 3.A.1 through §3.A.3. There are other radiative mechanisms that remove energy from the gas, especially collisionally pumped ro-vibrational transitions of molecules and fine-structure transitions of atoms. We briefly summarize those mechanisms and our method for evaluating them in §3.A.4.

Dust reactions

Dust grains are usually crucial in PPD photoevaporation. Following the arguments in GH08, as well as Geers et al. (2006, 2007); Perez-Becker & Chiang (2011b), polycyclic aromatic hydrocarbons (PAHs) dominate dust grains of other sizes in the following effects, thanks to their dominant contribution to total dust surface area: photoelectric heating of gas, dust-gas collisional energy transfer, recombination with free electrons, dust-assisted molecular hydrogen formation, and neutralization of positive ions. We include the processes listed above as outlined in §3.A.3.

3.2 Fiducial Model

This section presents the setup and results of our fiducial model, whose main properties are listed in Table 6.1. Other models, each differing from the fiducial in one parameter, are described in §3.3.

3.2.1 Fiducial Model Setup

Grid layout

The simulation domain is axisymmetric, extending from 2 AU to 100 AU in radius (r) and 0 to $\pi/2$ in colatitude (θ). All models are presumed to be symmetric about the equatorial plane, so that, for example, quoted mass-loss rates include outflows at $\theta > \pi/2$. All dependence on the azimuthal coordinate (ϕ) is ignored. Outflow boundary conditions with a radial flow limiter are imposed at $r = 2$ AU and $r = 100$ AU, and reflecting boundary conditions at $\theta = 0$ and $\theta = \pi/2$. Our standard resolution is 256 radial by 128 latitudinal zones, the radial zones being logarithmically spaced, and the latitudinal zones equally spaced.

Central young star

The gravitational field is that of a 1 $M_\odot$ star located at the origin. The disk, whose self-gravity is neglected, is initialized in hydrostatic and centrifugal balance, except for slight imbalances due to numerical discretization. The disk density and temperature profile follow the steady state solution in Nelson et al. (2013), in which we set the midplane density as $n = 10^{10}$ cm^{-3} and temperature $T = 20$ K at $r = 10^2$ AU, with radial power index being (-2.25) for density and (-0.5) for temperature–this profile yields a disk mass $\approx 0.03 M_\odot$ within 100 AU. The density and temperature profiles roughly agree with GH09, but the latter are not quite hydrostatic.

All radiation emanates from the origin of spherical polar coordinates. Our simulation domain does not cover the origin, and the rays are not attenuated before they reach the inner boundary. The source is isotropic, but those rays that reach the midplane region at the inner boundary are discarded (we also test not discarding those rays, finding negligible differences in the dissociation layer and in the wind). Each ray has four discrete energy bins, representing four important bands of photon energy: $h\nu = 7$ eV for FUV photons that do not interact appreciably with hydrogen molecules ("soft FUV"), 12 eV for Lyman-Werner ("LW") band photons, 25 eV for EUV photons, and 1 keV for X-ray photons (see also §1.1.1). Lyα photons are neglected (§2.2). The number of photons radiated in each energy bin per unit time follows the luminosity model described in GH08 and GH09: (1) a 9000 K black body spectral profile for FUV (6 eV $< h\nu <$ 13.6 eV) with total luminosity $L_{\rm FUV} = 10^{31.7}$ erg s^{-1}; (2) an additional EUV-photon emission rate $\Phi_{\rm EUV} = 10^{40.7}$ s^{-1}; (3) and an X-ray luminosity $L_X = 10^{30.4}$ erg s^{-1}.

Thermochemistry

The initial elemental abundances are determined by the values in Table 6.1 (wherein $n_{\rm H}$ is the number density of hydrogen nuclei). These choices generally follow a subset of those in GH08, with the additional assumption that elements appear in chemical compounds if possible. These initial abundances are uniform throughout the simulation domain.

Our assumptions about the dust turn out to be important for our results. GH08 and GH09 treated two populations of grains: (i) an MRN-type power-law distribution with a minimum grain radius of 50 Å, maximum of 20 μm, and a dust-to-gas ratio by mass of 10^{-2}; and (ii) PAH grains with abundance 8.4×10^{-8} per hydrogen nucleus. The first population has a total geometrical cross section of 2×10^{-22} cm^2 per hydrogen nucleus ($\sigma_{\rm dust}$/H). The authors do not state the radius of their PAH grains explicitly, but they refer to Li & Draine (2001), and we interpret this to mean that their PAHs can be approximated by spheres of radius 6 Å. It would follow that the contribution of their PAHs to the cross section is $\sigma_{\rm dust}/{\rm H} \approx 9.5 \times 10^{-22}\,{\rm cm}^2$, i.e. several times larger than that of their MRN population, although the contribution to the dust-to-gas mass ratio is only $\sim 10^{-4}$. As noted above, 3.A.3, the principal effects of dust, especially heating and absorption of radiation, are expected to be dominated by the smallest grains—PAHs.

For simplicity, we prefer to work with a single-sized grain population. We therefore neglect MRN grains and take the approximate relative abundance for our PAH-like grain species (Gr) as 10^{-7} per hydrogen atom, slightly greater than that of GH08, and a PAH radius of 5 Å, i.e. approximately 60 carbon atoms per PAH: see Weingartner & Draine 2001). The dust-to-gas mass ratio is then 0.7×10^{-4}, and $\sigma_{\rm dust}/{\rm H} = 8 \times 10^{22}$ cm^2.

Although variable dust abundance is fully allowed by our code, for the sake of simplicity we set the relative abundance of Gr to be uniform and assume that the dust comoves with the gas.

Simulation run

We run the simulation for 1.2×10^4 yr with microphysics enabled but the central radiation sources turned off until the disk structure is fully numerically relaxed, and the temperature profile converges to that set by the artificial heating profile (§3.A.3, which is sufficiently close to the initial profile). The chemical abundances do not change during this relaxation process except by passive advection. We confirm after this process that the disk is indeed in hydrodynamic equilibrium and has no outflow. Then, at $t = 1.2 \times 10^4$ yr, irradiation is turned on and remains on for the rest of simulation; this lasts $\gtrsim 500$ yr, sufficiently long compared to the radial flow timescale $\tau \sim (100 \text{ AU})/(30 \text{ km s}^{-1}) \approx 16$ yr so as to reach an approximate quasi-steady state.

The performance of the simulation code varies with algorithms, especially with the backend ODE solver:

- Using `CVODE` as the ODE solver backend, on Princeton University's local computer cluster `perseus`, 500 yr of simulated time takes ~ 100 hrs of wall-clock time on 128 CPU cores. About 95 per cent of the time is consumed by the thermochemical calculations for the fiducial model, the hydrodynamic and ray-tracing steps being relatively quick.

- Using the Rosenbrock ODE solver (see §2.3.1; see also Press et al. 2002, section 16.6), still with 128 CPU cores on `perseus`, 500 yr of simulated time takes ~ 10 hr wall-clock time.

- Using the GPU-optimized solver (§2.3.2), on a high-end personal computer up to the date of this thesis (CPU: AMD Ryzen 1800X, 16 logical cores on hyperthreading; RAM: 16 GB DDR4; GPU: Nvidia GTX 1080 TI with 11 GB graphics memory), 500 yr of simulated time takes ~ 11 hrs to complete, similar to the 128 CPU cores on the cluster using the Rosenbrock solver, and ~ 9 times faster than using the `CVODE` backend. We hence observe that the optimized thermochemistry solver solves the problem on a single desktop computer with GPU at a speed comparable to a 128-core sub-cluster.

3.2.2 Results

Overall hydrodynamic profiles

Fig. 3.1 displays meridional plots of the structure of our fiducial model averaged over the final 100 yr of the simulation. The white curves shown in the top row of panels are streamlines, the integral curves of the vector field $\rho \boldsymbol{v}_p$ ($\boldsymbol{v}_p$ is the poloidal velocity), spaced by constant mass-loss rate $10^{-10}\ M_\odot\ \text{yr}^{-1}$: that is to say, this is the mass flux between neighboring streamlines when integrated over azimuth and multiplied by two to include the reflection of the computational region below the equatorial plane. Streamlines that meet the outer boundary with a negative value of the Bernoulli parameter

$$\mathcal{B} \equiv \frac{v^2}{2} + \frac{\gamma p}{(\gamma - 1)\rho} + \Phi \ , \tag{3.1}$$

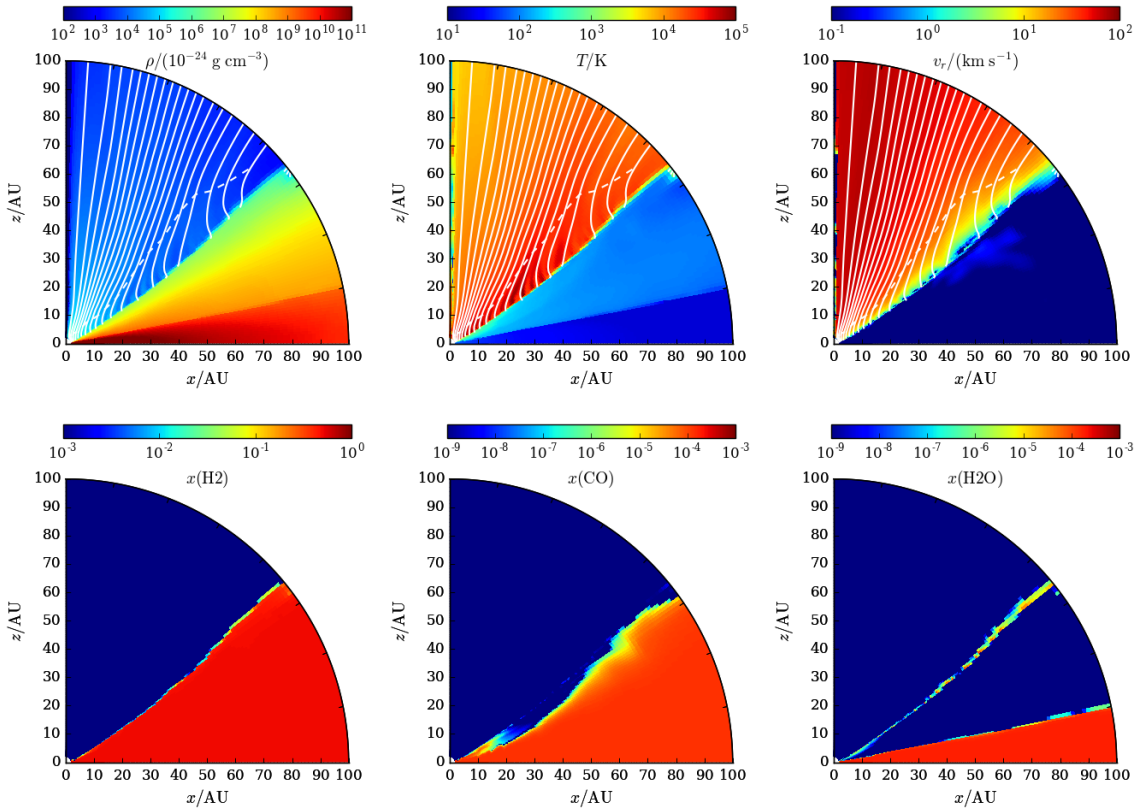


Figure 3.1 Meridional plots for the fiducial model (§3.2), averaged through the final 100 yr of the simulation. **Top row**: basic hydrodynamic profiles; left panel: mass density in units of 10^{-24} g cm^{-3}; middle panel: temperature in Kelvin; right panel: radial velocity in km s^{-1}. Panels in the top row are overlapped by streamlines (white solid lines), separated by 10^{-10} $M_\odot$ yr^{-1} wind mass loss rate (see §3.2.2 for details), and the locations of sonic points (white dashed line). **Bottom row**: relative abundance of different species [in units of $n(\mathrm{X})/n_\mathrm{H}$]; left panel: H_2; middle panel: CO; right panel: H_2O.

Table 3.1. Properties of the fiducial model

Item	Value
Radial domain	$2 \text{ AU} \leq r \leq 100 \text{ AU}$
Latitudinal domain	$0 \leq \theta \leq \pi/2$
Resolution	$N_{\log r} = 256$, $N_\theta = 128$
Stellar mass	$1.0\ M_\odot$
$M_{\rm disk}$	$0.03\ M_\odot$
Mid-plane density	$10^{10}(R/100 \text{ AU})^{-2.25}$ cm^{-3}
Mid-plane temperature	$20(R/100 \text{ AU})^{-0.5}$ K
Luminosities [photon s^{-1}]	
7 eV ("soft" FUV)	4.5×10^{42}
12 eV (LW)	1.6×10^{40}
25 eV (EUV)	5.0×10^{40}
1 keV (X-ray)	1.6×10^{39}
Initial abundances [$n_{\rm X}/n_{\rm H}$]	
H_2	0.5
He	0.1
H_2O	1.8×10^{-4}
CO	1.4×10^{-4}
S	2.8×10^{-5}
Si	1.7×10^{-6}
Fe	1.7×10^{-7}
Gr	1.0×10^{-7}
Dust/PAH properties	
$r_{\rm dust}$	5 Å
$\rho_{\rm dust}$	2.25 g cm^{-3}
$m_{\rm dust}/m_{\rm gas}$	7×10^{-5}
$\sigma_{\rm dust}$/H	8×10^{22} cm^2

are not plotted, and the outflow along such streamlines is omitted from the computation of the total mass-loss rate. Here v is the magnitude of fluid velocity vector, p the gas pressure, $\gamma \approx 5/3$ the adiabatic index, and Φ the gravitational potential. With this mask we get rid of (very slow) radial flows near the mid-plane: since the density there is six orders of magnitude higher than the wind, a tiny radial velocity fluctuation could otherwise give a spurious contribution to the mass-loss rate. As displayed in Fig. 3.1, the streamlines terminate on the disk at the surface where $\mathcal{B}$ becomes negative. We consider this surface to be the base of the wind. (As discussed in §3.4.2, this definition of the wind base differs from that of GH09.)

Thermodynamic profiles

Fig. 3.2 shows several flow variables along two representative streamlines originating from cylindrical radii $R \equiv r \sin\theta = 5$ AU and $R = 15$ AU.

The density and temperature profiles shown by Fig. 3.1 can be divided into three relatively distinct regions:

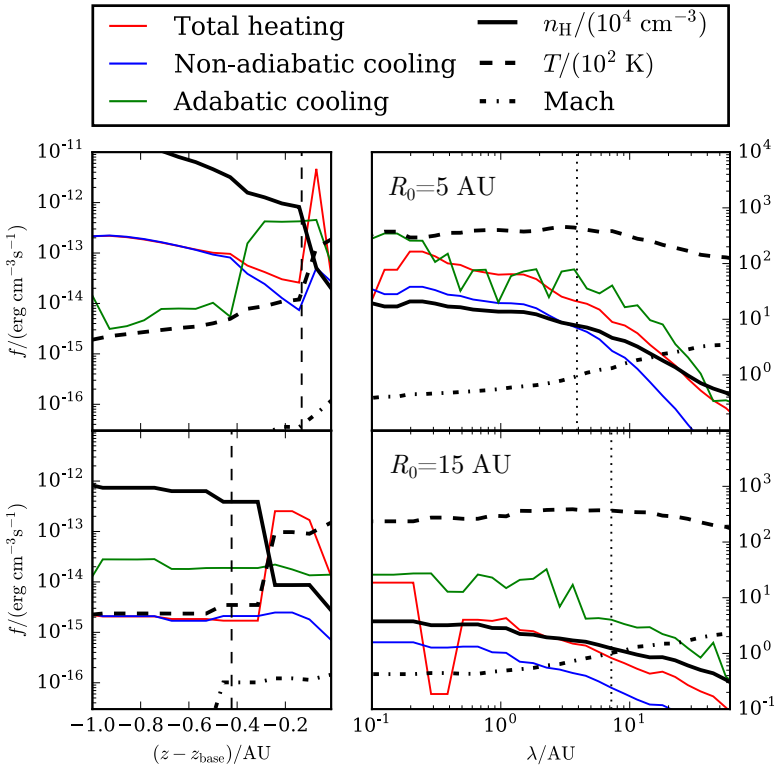


Figure 3.2 Cooling/heating rates (left ordinate) and fluid properties (right ordinate) along streamlines. $n_{\rm H}$ is the number density of hydrogen nuclei. In right column, horizontal axis is arc length (λ) measured from the wind base [where $\mathcal{B}=0$, eq. (3.1)]. Vertical dotted line marks sonic point. Left column present the profile *vertically below* wind base (i.e. $z-z_{\rm base}$). Vertical dashed line indicates wind base as defined by GH09. Upper row: streamline rooted at $R_0=5$ AU. Lower row: $R_0=15$ AU.

- Midplane layer: $0<(z/R)\lesssim 0.3$ ($R=r\sin\theta$ being cylindrical radius), $T<10^2$K. The structure here is basically unchanged from the initial conditions.
- Intermediate layer: $0.3\lesssim(z/R)\lesssim 0.6$, 10^{-19} g cm$^{-3}\lesssim\rho\lesssim 10^{-16}$ g cm^{-3}, $10^2\lesssim T\lesssim 10^3$ K. The total mass in this layer is $\sim 10^{-6}\ M_\odot$. EUV photons scarcely penetrate this region, whose properties are controlled by FUV and X-ray processes: photodissociation and photoelectric heating, as well as radiative cooling by collisionally excited molecular and/or atomic transitions. Most H_2 molecules and a lot of CO molecules survive in this region because of significant self- and cross-shielding of Lyman-Werner photons. Soft FUV photons that do not interact much with molecular hydrogen are relatively unshielded and pervade the intermediate layer, photodissociating OH and H_2O, penetrating to the bottom of the layer, or escaping through the outer radial boundary.
- Wind layer: $(z/R)\gtrsim 0.6$, $\rho\lesssim 10^{-19}$ g cm^{-3}, $T\gtrsim 10^4$ K. This region is filled with mostly ionized gas, flowing outwards at radial velocity $v_r\sim 30$ km s^{-1}.

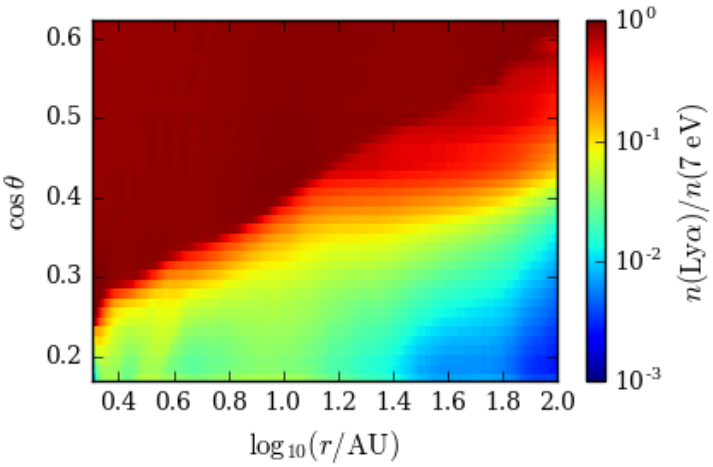


Figure 3.3 Ratio of local effective radiation flux (in $n_{\rm ph}c$) of Lyα to $h\nu = 7$ eV soft FUV, given that the luminosities in these two bands are identical.

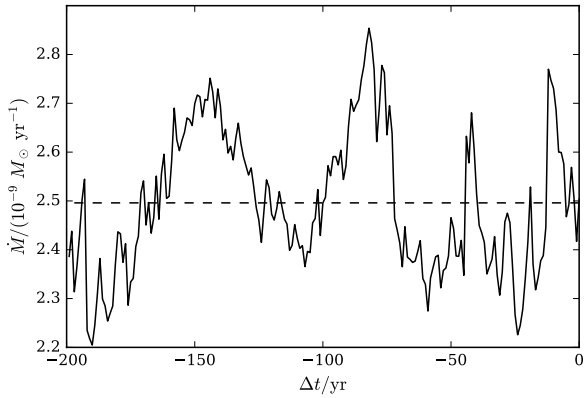


Figure 3.4 Variation of mass-loss rate measured at the $r = 100$ AU outer boundary of the fiducial model (Model 0). The dashed horizontal line shows the average of mass-loss rate over the last 200 yr.

> Photoionization heating and adiabatic expansion dominate the thermodynamics of this region.

We insert the hydrodynamic and thermochemistry profiles in our time-averaged fiducial simulation into the post-processing Monte Carlo transport code (§2.2.2) for Lyα photons. In Figure 3.3, we present the result: for the same luminosity in Lyα as in the 7 eV energy bin, the ratio of photon number density of Lyα to 7 eV is 10^{-1} to 10^{-3} in the intermediate layer.

Wind mass loss rate

If we integrate the $\mathcal{B}$-masked radial mass flux at the $r = 100$ AU boundary (and its reflection at $z < 0$) and average over the last 100 yr of our fiducial run, we obtain a

total mass-loss rate $\dot{M}_{\rm wind} \simeq 2.5 \times 10^{-9}\ M_\odot\ {\rm yr}^{-1}$, corresponding to a disk dispersal timescale $\sim 10^7$ yr. The mass-loss rate is lower than that of GH09 (see §3.4.2 for further discussion). However, our mass-loss rate undergoes significant fluctuations, and is uncertain to at least $\sim 10\%$. Fig. 3.4 plots the mass-loss rate for the last 200 yr of the (lower resolution) fiducial run (Model 0). These fluctuations correlate with what appears to be a thermal instability of the outer disk, whereby it swells vertically, intercepts more radiation, and then swells further but also migrates at a few km s^{-1} through the outer boundary, temporarily increasing $\dot{M}$. This behavior is smoothed over by the time averages used to make Fig. 3.1.

Wind thermochemistry: Why we need consistent microphysics

Swellings on the disk surfaces, being slower and denser than the general wind, partly shield themselves against photodissociation of some molecules, especially H_2 and CO, so that those molecules survive farther into the outflow than they would otherwise.

Even outside these swellings, there are also molecules surviving in regions with rather high temperature ($\sim 10^3$ K, or even up to $\sim 10^4$ K). H_2O and OH molecules exist at the surface of the intermediate layer, detached from the midplane (last panel of Fig. 3.1). The re-formation rates of H_2O and OH are comparable to photodissociation at that surface. At the cooler temperatures below it, inside the intermediate layer, reformation is less efficient but photodissociating FUV is still present. The wind region, on the other hand, does not have sufficient H_2 (reactions that are most efficient in forming H_2O and OH need H_2 as reactants, while the reactions that convert atomic H to OH and H_2O are very slow). Collisional destruction of OH and H_2O is not efficient below $\sim 5 \times 10^4$ K at these densities ($\lesssim 10^4 {\rm cm}^{-3}$).

In Fig. 3.5, we plot the distribution of CO, OH and H_2O in the wind region and intermediate layer, in the plane of by $\log_{10} T$ and v_r. The temperature T here represents the kinetic temperature of the local (mostly H & He) gas, not the vibrational or even rotational excitation temperature of the molecules. For those molecules, a tail on the high temperature ($T \sim 10^3$–10^4 K) and intermediate radial velocity ($v_r \sim 5$–10 km s^{-1}) end of the 2-D distribution indicate their survival at the bottom of the wind region. Such hot molecular gas would be less prominent had we assumed local thermochemical equilibrium. For the luminosity in the LW and EUV bands of our fiducial model, it can be estimated that the timescale of CO photodissociation is ~ 0.1 yr at $r \sim 10$ AU. Given the speed of photoevaporative outflow, this timescale is sufficient for some CO to survive $\sim 0.1 - 1$ AU into the hot wind. These timescales are sensitive to radial distance (from the radiation sources), to the way photodissociation is modeled (see §3.1.2), and to the LW and EUV band luminosity. Observational constraints on such molecules could be an important check on these models, and might diagnose the role of UV in driving PPD winds.

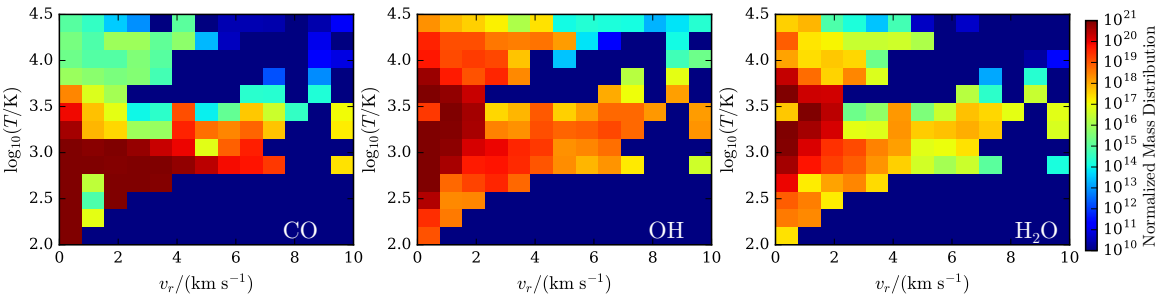


Figure 3.5 Distribution functions of key molecular species for the fiducial model in the two-dimensional space of $\{\log_{10} T\} \times \{v_r\}$ (common logarithm of temperature and radial velocity). The mass distribution function is normalized as $\mathrm{d}^2 m/[\mathrm{d}\log_{10}(T/\mathrm{K})\mathrm{d}(v_r/\mathrm{km\ s^{-1}})]$, i.e. mass of the species per dex-temperature per $(v_r/\mathrm{km\ s^{-1}})$.

3.3 Exploring the Parameter Space

To explore the effects of our input parameters, we have run a number of additional simulations, most differing from the fiducial run in one parameter. These models and some synoptic results are listed in Table 3.2. We discuss some of these models here, and others in §§3.4.2-3.4.3 in relation to the works by GH09 and OECA10.

3.3.1 Setup of Models

Luminosity in different radiation bands

In the fiducial model the luminosity in the Lyman-Werner band is tiny compared to that in soft ($h\nu < 11.3$ eV) FUV photons: around 0.35 per cent, using the 9000 K black body SED. However, as observed by e.g. Gullbring et al. (2000), the SED for FUV radiation is rather variable from object to object and often more luminous in the LW band than the black-body model adopted by GH08 and GH09. Hence we include a series of models, with 0 and 100 times the fiducial luminosity in the Lyman-Werner band, to cover this uncertainty. We also test 0 and 10 times EUV or X-ray luminosity to diagnose the impact of those photons that can ionize atomic hydrogen.

PAH abundance

For very small grains such as our PAHs, the grain absorption cross section for FUV and EUV photons depends on total grain mass rather than grain area. We have a much smaller grain mass than GH09. Model 9 in Table 3.2 has double the dust radius ($r_{\mathrm{dust}} = 10$ Å) and therefore eight times the dust mass at the same relative number density ($n_{\mathrm{Gr}}/n_{\mathrm{H}} = 10^{-7}$). According to the arguments in Geers et al. (2006); Tielens (2008); Woitke et al. (2016), our PAH abundance is roughly 4 times the ISM standard. The geometric dust cross section per hydrogen, which determines the thermal accommondation (§3.A.3), is also approximately 4 times bigger compared to GH09. Observations suggest that the PAH abundance in PPDs could be ~ 10 per

Table 3.2. Models exploring parameter space

No.	Description	$\dot{M}_{\rm wind}$ ($10^{-9} M_\odot$ yr^{-1})	$\dot{M}_{\rm GH}$ ($10^{-9} M_\odot$ yr^{-1})	Total heating (10^{30}erg s^{-1})	Efficiency	$\langle v_r \rangle$ (km s^{-1})
(1)	(2)	(3)	(4)	(5)	(6)	(7)
0	Fiducial	2.5 ± 0.2	11.6	4.4	0.67	39
1	No LW photons	2.5 ± 0.3	9.3	4.1	0.67	38
2	100× LW photons	17.6 ± 2.1	61.3	9.1	0.60	18
3	No "soft" FUV	1.1 ± 0.1	2.7	2.3	0.53	58
4	"Soft" FUV only	0.0	0.2	1.0	-	-
5	No EUV	0.0	3.7	1.6	-	-
6	10× EUV photons	9.4 ± 0.7	107.8	26.7	0.74	33
7	No X-ray	2.1 ± 0.2	6.9	2.6	0.80	38
8	10× X-ray photons	9.1 ± 0.4	55.6	14.1	0.42	24
9	$r_{\rm dust} = 10$ Å	2.8 ± 0.6	10.5	3.5	0.68	30
10	(1/40) dust	2.5 ± 0.4	12.1	3.5	0.75	41
11	OECA10 analog†	11.2 ± 4.2	105.0	0.8	0.54	5
12	Convergence test	2.7 ± 0.6	16.1	3.0	0.58	32

Note. — (1) Model identifier. (2) Parameter by which model differs from fiducial. (3) Wind mass-loss rate. The error quoted error is $\Delta\dot{M}_{\rm wind} = \langle[\dot{M}(t)]^2 - \langle\dot{M}\rangle^2\rangle^{1/2}$, where the time averages are taken over the last 100 yr. (4) Estimated wind mass-loss rate using GH09 scheme. (5) Total radiative plus thermal-accomodation heating of the gas (note that the accomodation heating can be negative). (6) Thermal-to-mechanical conversion efficiency: (heating − non-adiabatic cooling)/(heating). (7) Mean outflow velocity weighted by radial mass flux. †: Bernoulli parameter mask not applied; significant outflow occurs in the intermediate layer with $\mathcal{B} < 0$.

cent of the ISM. Model 10 covers this uncertainty by reducing the abundance of PAH by a factor of 40.

Convergence test

To test our truncation errors, we repeat the fiducial run at resolution 128×64, i.e. coarser by $\times 2$ in both latitude and radius. This convergence test is run for much longer time period (~ 2000 yr) to better characterize fluctuations around the mean state.

3.3.2 Results of Various Models

Fig. 3.6 illustrates the hydrodynamic structure of a few representative models. These plots are based on time averages over 100 yr, so that the flow field is in approximate steady state. In the runs with 100× LW photons (Model 2) or 10× X-ray photons (Model 8), a thick neutral atomic layer exists at the top of the intermediate layer. In this layer, the temperature and sound speed reach a local maximum with respect to height or latitude, and significant outflows may occur. This causes the jagged shape of the sonic curves in the third and fourth panels.

Figs. 3.7 and 3.8 show the vertical distributions of heating and cooling mechanisms at $R = 15$ AU, a typical location where the outflow streamlines originate. The three layer structure (§3.2.2) is obvious in most of the models. Details of those structures vary with model parameters, with implications for the mechanisms responsible.

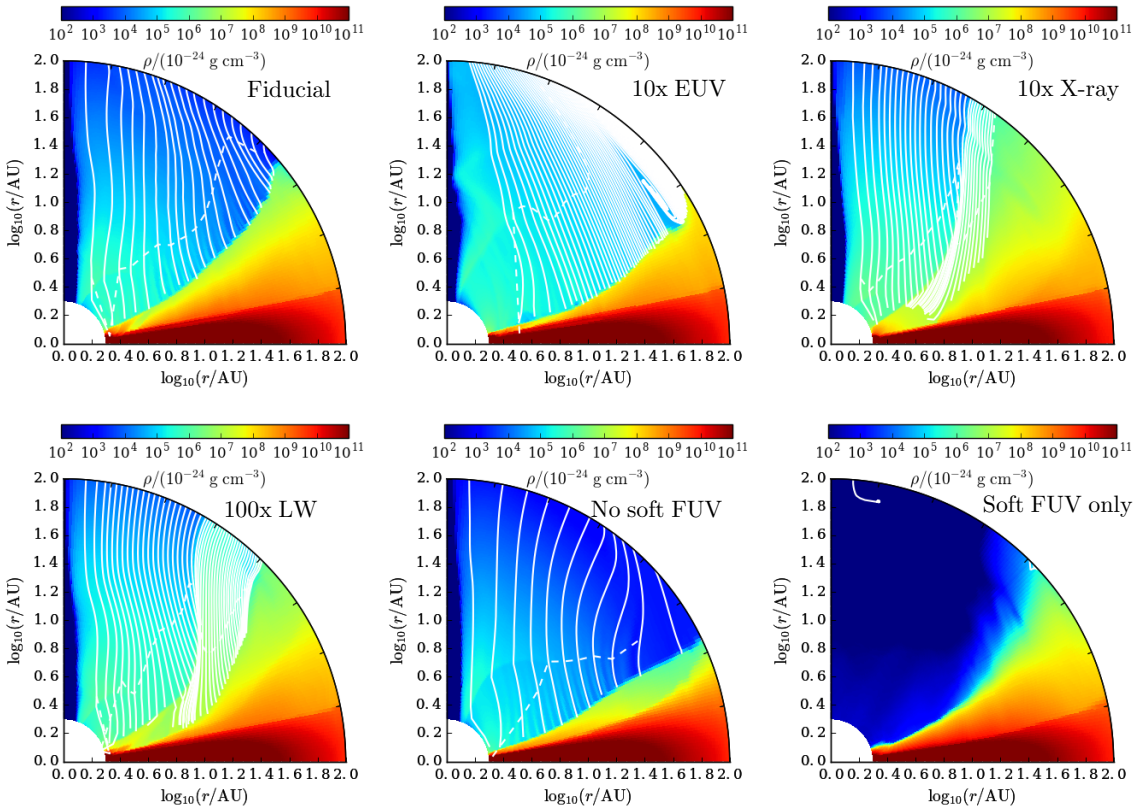


Figure 3.6 Selected plots of streamlines (based on 100 yr average), overlaid on density colormaps, that are relevant to the discussions in §3.3.2. The black curves, showing the streamlines, are separated by 10^{-10} $M_\odot$ yr^{-1} each. The white curves denote the location of sonic point of all streamlines plotted. Note that, for clearer presentation, the radial coordinates in all panels are $\log_{10}(r/\mathrm{AU})$.

The panels of Fig. 3.7 convey some general impressions about the heating mechanisms. The vertical heating profile usually has two peaks: one at the bottom of the intermediate layer, the other at the top of it. Photoionization heating by the harder (EUV and X-ray) photons dominates, unless these photons are absent or are overwhelmed by photons in other bands (e.g. Model 2, 100× LW photons; see discussions below). On the cooling side (Fig. 3.8), the OH and/or H_2O ro-vibrational transitions and S I 25 μm transition dominate at the bottom of intermediate layer, the Si II 35 μm and O I 63 μm transitions in the middle of that layer, and H_2 ro-vibrational cooling near the top. In the "wind" region, cooling and heating are dominated by recombination and the photoelectric effect. Using the integrated cooling rate, we have estimated some of the important line luminosities (Table 3.3).

Table 3.3. Approximate line luminosity

Model	O I 63 μm	O I 6300 Å	S I 25 μm	Si II 35 μm	H_2 ro-vib	OH/H_2O ro-vib	CO ro-vib
0	−4.31	−7.36	−4.00	−5.65	−4.67	−4.29	−3.89
1	−4.34	−8.17	−3.96	−5.73	−4.60	−4.36	−3.90
2	−3.75	−4.69	−4.17	−4.73	−4.11	−3.57	−3.91
3	−5.05	−7.72	−5.05	−6.48	−5.26	−3.61	−5.68
4	−5.05	-	−4.68	-	−5.61	−4.30	−4.26
5	−4.22	−7.31	−3.97	−5.58	−5.03	−4.63	−3.88
6	−4.43	−7.13	−3.88	−5.36	−3.65	−3.56	−3.78
7	−4.74	−8.02	−4.61	−6.30	−4.72	−4.26	−4.23
8	−3.57	−5.99	−3.11	−4.69	−4.15	−3.38	−3.37
9	−4.47	−4.94	−4.39	−5.94	−4.39	−4.07	−4.59
10	−4.50	−7.27	−4.60	−5.36	−4.77	−4.46	−4.30
11	−4.38	−6.88	-	−4.55	-	-	-
12	−4.49	−5.24	−4.32	−5.98	−4.79	−4.94	−4.83

Note. — All luminosities are presented in $\log_{10}(L/L_\odot)$.

3.4 Discussion

3.4.1 Roles of Different Bands of Radiation

Soft FUV

The heating and thickness of the intermediate layer is mainly attributable to photons that penetrate a radial column $\gtrsim 10^{21}$ cm^{-2} $\sim 10^8$ cm^{-3} $\times$ 10 AU, viz. soft FUV and X-rays. These two components penetrate to $n \sim 10^8$ cm^{-3}, which approximately defines the top of the midplane layer. For soft FUV photons, the radial optical depth contributed by dust grains is $\sim 10^{-4} - 10^{-3}$ at the wind base, and $\sim 10^0 - 10^1$ at the bottom of the intermediate layer. X-ray photons are mainly absorbed by molecules in the intermediate layer; their radial optical depth to the bottom of the intermediate layer is also $\sim 10^0 - 10^1$.

Heating processes inside the intermediate layer do not directly contribute to the outflows. This is suggested in Fig. 3.1 by the terminations of the streamlines, which mark the surface where $\mathcal{B} = 0$, at the top of the intermediate layer; and also by the mass-loss rates in Table 3.2, especially for models 5 (soft FUV only), 6 (no EUV photons), and and 3 (no soft FUV). The relatively high density in the bulk of the intermediate layer ($n \gtrsim 10^6$cm^{-3}) causes cooling processes to offset much of the radiative heating there. Nevertheless, the FUV photons, and in most cases the X-ray photons also, contribute indirectly to the mass-loss rate by thickening the intermediate layer, which exposes its upper surface to more intense EUV heating.

Lyman-Werner (LW) FUV

The LW photons play a more direct role. Due to self-shielding of H_2, heating by LW photons extends only slightly below the upper surface of the intermediate layer.

These photons contribute dramatically to the total outflow. Admittedly, this is not convincingly shown by Table 3.2 alone: compare Models 0 (fiducial), 1 (no LW photons) and 2 (10× LW photons). In these three cases, the luminosities in the LW band are smaller than the EUV component. But the corresponding panels of Fig. 3.7 reveal a clear trend of increasing heating by H_2 pumping (see §3.A.1). Model 2 (100× LW photons) clearly demonstrates that LW heating by interaction with H_2 can dominate the outflow when the LW luminosity is sufficient. It is worth noting that, for Model 2, the outflow velocity is approximately $\sim 1/3$ that of Models 0, 1, and 2: LW photons deposit less energy per reaction than EUV and X-ray (see also §3.1.2 and §3.A.1), thereby heating the gas to a lower temperature and hence accelerating the outflow to a lower velocity.

EUV

EUV photons are absorbed by a rather small column density ($\sim 10^{18}$ cm^{-2}) of neutral or molecular hydrogen. However, if they make their way to the surface of intermediate layer, EUV photons tend to dominate the photoevaporative outflow. This point is illustrated by comparison of Model 0 (fiducial) with 6 (no EUV) and 7 (10× EUV): Model 5 has its outflow almost totally shut down, while Model 6 has a dramatically increased mass loss rate and radial flow velocity. Because the EUV heating is concentrated in relatively little mass, it produces a high sound speed and therefore a relatively fast wind.

X-ray

Since the X-rays have considerably larger penetration than LW and EUV photons, in fact comparable to that of the softer FUV photons, they deposit most of their heat in the intermediate layer, where cooling mechanisms remove energy efficiently from the gas. The exception among the cases in Table 3.2 is Model 8 (10× X-ray), where X-rays drive a substantial wind by themselves. Note that the wind velocity is about half that of the fiducial model because the heating is distributed over a larger mass. X-ray driving is further discussed below in connection with the work of Owen et al. (2010a).

3.4.2 Comparison with GH09

Although we have modeled our fiducial case on that of GH09, our mass-loss rate is a few times smaller than theirs. GH09 did not simulate the hydrodynamic flow in two dimensions as we have done, but instead estimated $\dot{M}$ by analytically matching their heated disks onto a spherical Parker wind. The fourth column of Table 3.2 shows the rates that would be estimated by applying their prescription to our heated disks. For the fiducial case, this estimate matches GH09's results fairly well, as determined by integrating their radius-dependent mass-loss rate from 1 through 100 AU. The latter agreement suggests that our simplified thermochemical network is sufficient to predict the temperature, density, and flow, if not all of the trace species and line emission

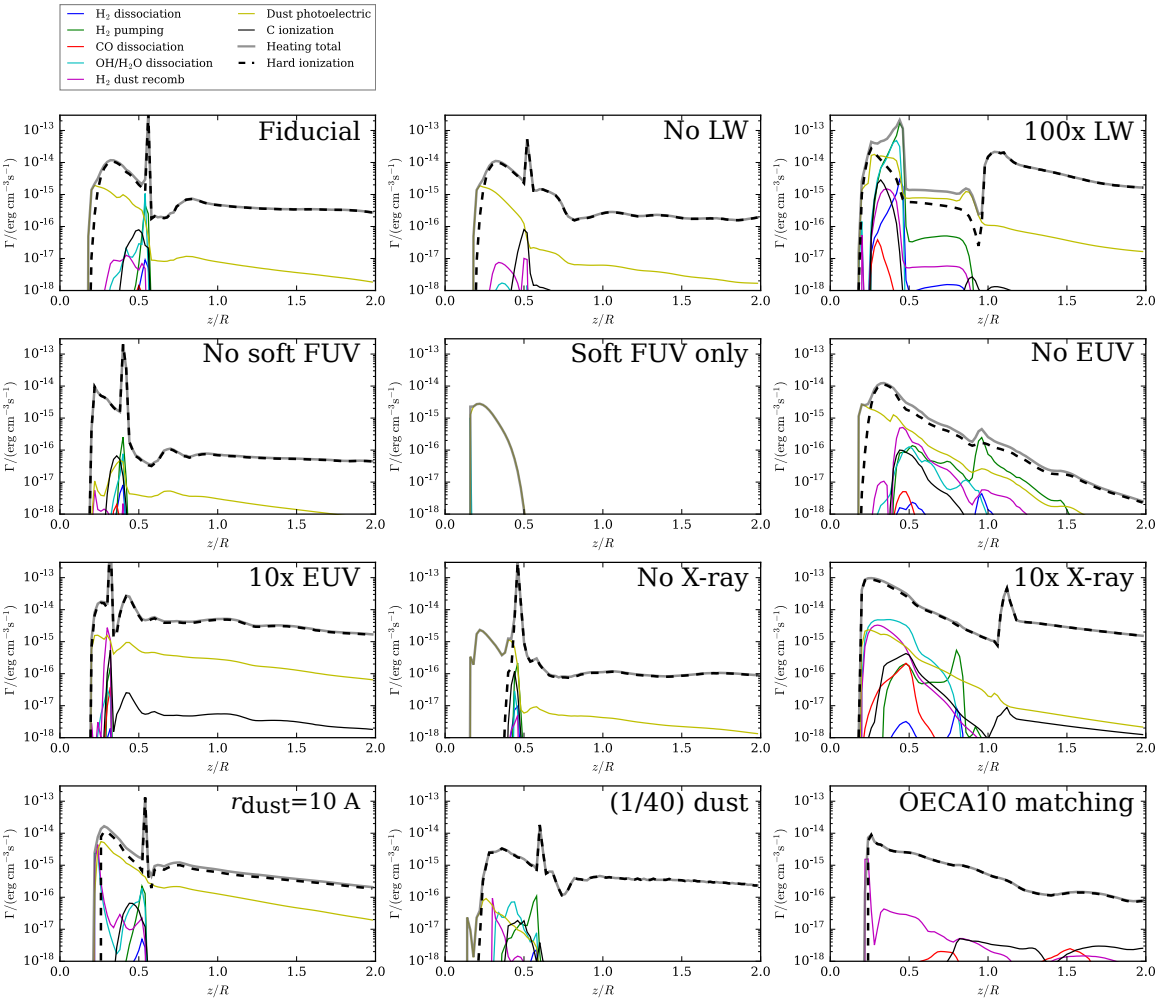


Figure 3.7 Profiles of heating mechanisms, in units of erg cm^{-3} s^{-1}, at $R = 15$ AU, for all models involved in this chapter. Heating mechanisms are distinguished by line shape and color as marked in the legend at the upper left.

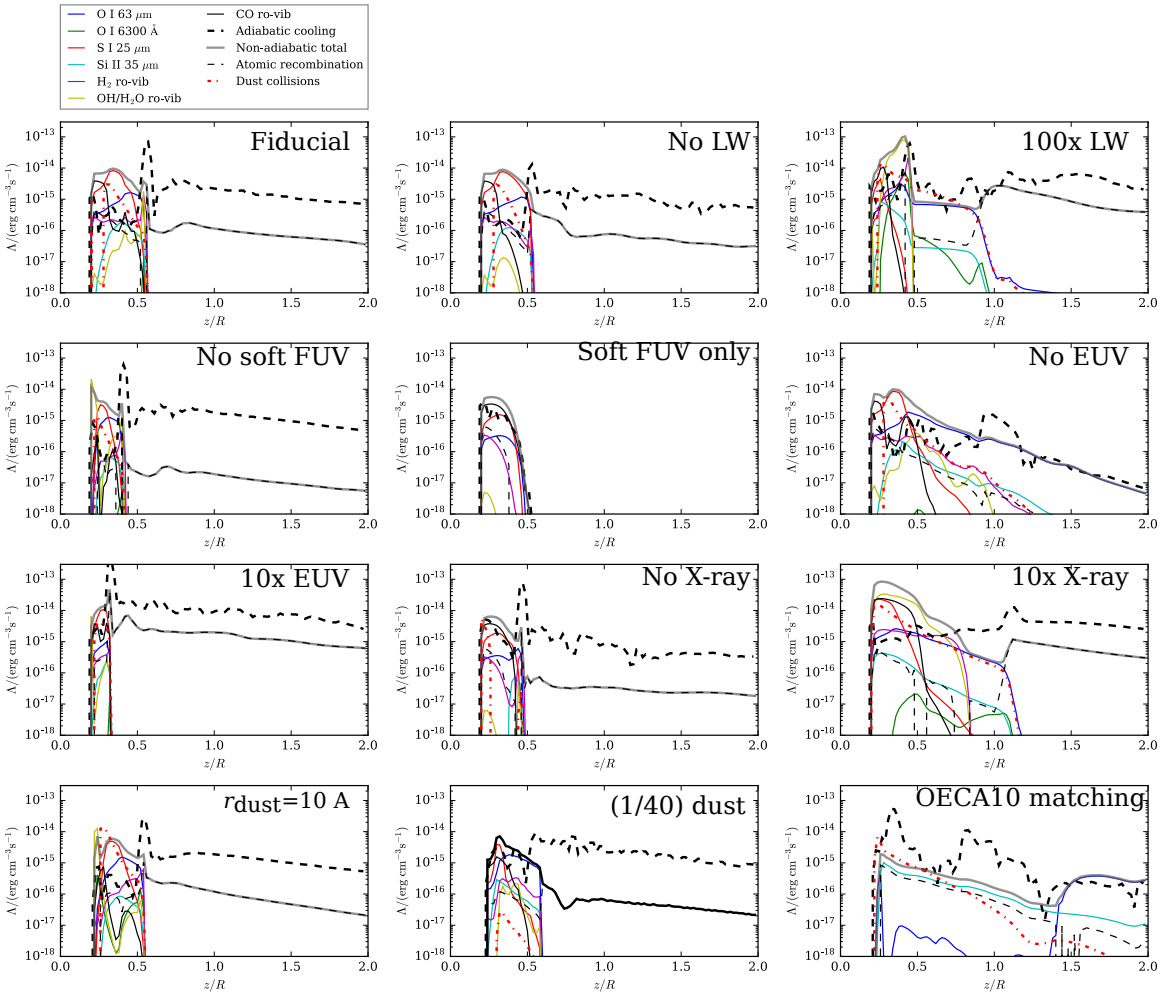


Figure 3.8 Same as Fig. 3.7, but shows profiles of different cooling mechanisms at $R = 15$ AU.

that one would like to compare with observations. The differences between the third and fourth columns point to the importance of modeling the hydrodynamics properly, however. Fig. 3.9 shows the radial profiles of the mass-loss computed in these two different ways, and also for GH09's original model disk. Note that the latter extended beyond 100 AU.

GH09's analytic prescription computes the mass-loss rate as if the disk atmosphere, which in their models is hydrostatic, belonged to a spherical Parker wind with constant sound speed, i.e. an adiabatic wind with an isothermal equation of state. For each cylindrical radius R, the matching point between the hydrostatic atmosphere and the isothermal wind is chosen at such an altitude as to maximize the imputed mass-loss rate. This is how GH09 determine the wind base, $z_{\rm b}(R)$. The sound speed of the wind is then the sound speed of the hydrostatic atmosphere at $z = z_b$. Note that $\dot{M}$—or rather $2\pi R^2\dot{\Sigma}(R)$—can be expected to have such a maximum with respect to the matching altitude z_b because of the strong vertical gradients of temperature and density within the atmosphere.

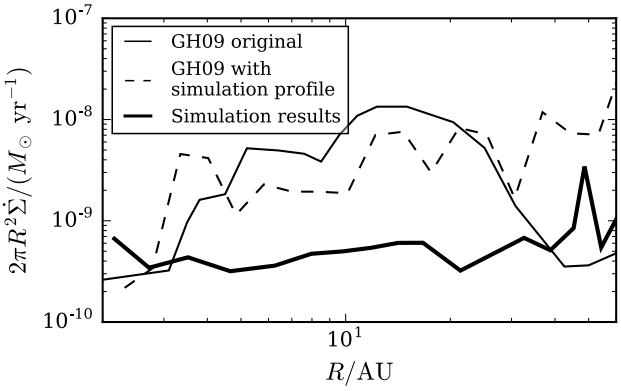


Figure 3.9 Radial profiles of the differential wind mass loss rate, $(2\pi R^2\dot{\Sigma})$, for the time-averaged fiducial simulation. Dashed curve is calculated by applying GH09's prescription to the density and temperature structure of our simulation, whereas solid curve is our actual mass-loss rate.

To understand better why our mass-loss rates differ from GH09's prescription, consider the streamline starting from $R_0 = 15$ AU in Fig. 3.1 (see also the lower panel of Fig. 3.2) . Using the density and temperature profiles obtained by our fiducial simulation, the density and temperature at the wind base (defined in the manner of GH09) read $n_{\rm H} \simeq 3.7 \times 10^6$ cm^{-3} and $T \simeq 0.7 \times 10^3$ K. These values are in good agreement with figure 1 in GH09. The corresponding isothermal sound speed is $c_{\rm s} \simeq 2.1$ km s^{-1}: the hydrogen is atomic and neutral, with mean mass per particle $\bar{m} \simeq 1.3 m_{\rm H}$. The implied sonic radius is then $r_s \simeq 78$ AU, and the predicted density there is $n_{{\rm H},s} \simeq 10^5$ cm^{-3}. The corresponding mass-loss rate for a spherical isothermal wind with these sonic-point parameters would be $\dot{M} \sim 2\pi r_s^2 \bar{m} n_{{\rm H},s} c_{\rm s} \simeq 7 \times 10^{-9}\ M_\odot$ yr^{-1}. This is identified with the local mass-loss rate per logarithmic radius at the surface of the disk, viz. $2\pi R^2\dot{\Sigma}$.

However, in the simulation, the actual sonic point on this streamline lies at $r_s \simeq 23$ AU. The actual density there is $n_{{\rm H},s} \simeq 1.2 \times 10^4$ cm^{-3}, and the temperature is nearly 3.6×10^4 K, so that the gas is largely ionized ($\bar{m} \simeq 0.64\ m_{\rm H}$). The isothermal sound speed based on this temperature and molecular weight is $c_{\rm s} \simeq 20$ km s^{-1}. The corresponding $\dot{M} \approx 0.8 \times 10^{-9}\ M_\odot$ yr^{-1} (again, this is indeed $2\pi R^2\dot{\Sigma}$). This is about one order of magnitude less than GH09's prescription.

In short, the actual mass-loss rate is smaller than GH09's prescription by approximately the reciprocal of the ratio of sound speeds (and hence flow velocities): 2.1 km s^{-1} vs. 20 km s^{-1}. The wind thrusts—momentum flux $2\rho_s c_{\rm s}^2$ times $4\pi r_s^2$—are nearly equal. The thrust is necessarily limited by the pressure of the gas at the wind base, since the disk must support the force exerted on it by the escaping wind. Although we and GH09 define the wind bases separately, the pressures are similar because the bases are separated vertically by only ~ 0.5AU out of ~ 9AU. An analogy can be made here with rocketry: at fixed thrust, the mass-flow rate in the rocket exhaust is inversely proportional to the exhaust velocity, or equivalently, to the specific impulse. By assuming a constant sound speed from their wind base upward, GH09's prescription fails to account for the increase in specific impulse due to the sharp rise

in temperature above the wind base, even though this rise is also seen in their own hydrostatic disk atmospheres (see Fig. 1 of GH08).

3.4.3 Comparison with OECA10

GH09 found that X-rays made a significant but not dominant contribution to the mass-loss rate. OECA10, on the other hand, modeled photoevaporation driven solely by X-rays, with a full axisymmetric hydrodynamic treatment similar to our own, though with a simplified prescription for the gas temperature. OECA10 assumed an X-ray luminosity close to that of our fiducial model, without FUV or EUV, but found a higher a wind mass-loss rate $\sim 1.4\times10^{-8}\ M_\odot\ \mathrm{yr}^{-1}$. Although our fiducial model has comparable X-ray and EUV luminosities, ($L_X = 10^{30.4}$ erg s^{-1}, $L_{EUV} = 10^{30.3}$ erg s^{-1}) EUV appears to dominate the mass loss. When we turn off the EUV, our mass-loss rate becomes less than $10^{-10}\ M_\odot\ \mathrm{yr}^{-1}$ (Model 5 in Table 3.2). We have investigated the causes of these large differences.

OECA10 prescribed the gas temperature as a function of the ionization parameter F_X/n_H, where F_X is the local X-ray flux, taking this relation from the hydrostatic models of Ercolano et al. (2008, hereafter EDRCO8), who took $L_X = 2\times10^{30}$ erg s^{-1} (very similar to ours), though with a slightly harder spectrum ($kT_X = 1.5$ keV). As shown by Fig. 3.10, a similar correlation holds for our fiducial model, though with some spread around the mean relation. Recall however that EUV and FUV are also present in this model, and the former dominates at $T \gtrsim 10^4$ K. At $T \approx 10^2$–10^3 K, the regime of the intermediate layer, our mean $\xi - T$ relation falls somewhat below that of OECA10 by $\sim$ 0.2–0.5 dex. We attribute this difference partially to the cooling mechanisms. The hydrostatic models of EDRC08 excluded cooling mechanisms by molecules and neutral atomic sulfur. In Table 3.3, we observe significant contribution to cooling by H_2O and neutral sulphur in the intermediate layer.

Adiabatic expansion also contributes to the differences between our ξ–T relation and that assumed by OECA10. Comparing the corresponding panels in Fig. 3.2 shows that adiabatic expansion removes around 3/4 to 1/3 (the ratio varies from location to location) of the internal energy injected by heating (converting it to kinetic energy); applying the the hydrostatic ξ–T relation to hydrodynamics assumes that this part of the energy still contributes to the gas temperature, and hence counts this part of the energy twice.

A significant difference between our model and that of EDRC08 involves the dust. Our recipes for thermal accommodation per gas-dust collision are identical to theirs (see §3.A.3). Our dust-to-gas ratio ($\sim 10^{-4}$) is smaller than theirs (6.5×10^{-4}). However, EDRC08 assumed an MRN size distribution of dust grains (Mathis et al., 1977). The present work assigns a very small radius to all grains (5 Å). This results in a dust surface area per gas mass that is ~ 10 times larger than in EDRC08, with a corresponding increase in the rate of cooling by thermal accomodation.

In support of the arguments here, we have run Model 11 (Table 3.2), in which all cooling processes related to molecules and neutral sulphur are disabled, the abundance of PAHs is lowered by $\times10^{-1}$, and X-rays are the only hard photons (no EUV or

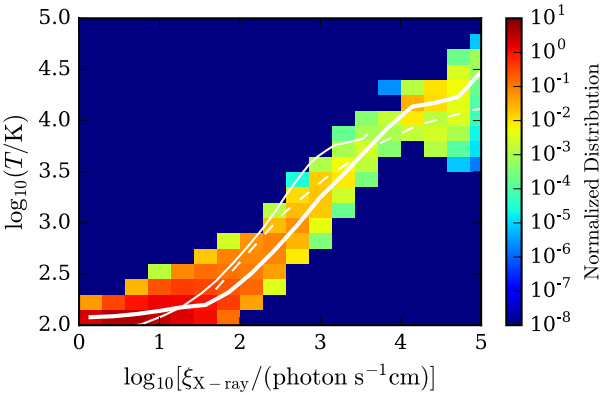


Figure 3.10 Distribution function of gas in the space spanned by $\{\log_{10} T\} \times \{\log_{10} \xi_{\mathrm{X-ray}}\}$, measured for the fiducial model. X-ray ionization parameter $\xi_{\mathrm{X-ray}}$ is defined as F_X/n_{H}, viz. photon number flux density divided by the number density of hydrogen nuclei. Heavy white curve indicates the $\log_{10}\xi$–$\langle\log_{10} T\rangle$ relation based on our colormap histogram (the average of $\log_{10} T$ is weighted by the mass of gas), while the thin white curves indicate the hydrostatic ξ–T relations adopted in OECA10 (solid: inner-hole disks; dashed: primordial disks; note that the definition of ξ is different in OECA10, which is converted here to the defintion in this chapter).

FUV, hence the total heating rate is small). This model yields a mass-loss rate of $\sim 1.1 \times 10^{-8}\ M_\odot\ \mathrm{yr}^{-1}$, fairly close to the results in OECA10.

3.5 Chapter Summary

In summary, this work combines hydrodynamics with consistent ray-tracing radiative transfer and thermochemistry to study the photoevaporation mechanisms of protoplanetary disks.

Irradiated by the FUV, EUV and X-ray radiation from the central source, the disk develops a three-layer structure; ordered by increasing latitude, these are a cold midplane region ($T < 10^2$K), a warm intermediate layer ($T \sim 10^2$–10^3K) and a hot tenuous ionized wind ($T \gtrsim 10^4$K). The initial structure of the disk, the abundances and chemistry, and the amount and size of the dust, broadly follow GH09, but the time-averaged wind mass-loss rate is somewhat lower, $\dot{M}_{\mathrm{wind}}(< 10\ \mathrm{AU}) \approx 2.5 \times 10^{-9}\ M_\odot\ \mathrm{yr}$, and the typical radial velocity is higher $\sim 30\ \mathrm{km\ s^{-1}}$, due in part at least to our explicit multidimensional modeling the hydrodynamics. Our solutions never reach a complete steady state, but show fluctuations ~ 10 per cent in $\dot{M}_{\mathrm{wind}}$, which correlate with what appears to be an instability in the response of the upper part of the intermediate layer to irradiation. (The fluctuations might be smaller in three-dimensional simulations due to azimuthal averaging.)

By varying the various hard-photon luminosities, we find that the main determinant of $\dot{M}_{\mathrm{wind}}$ is the total heating by radiation that interacts strongly with molecular and/or atomic hydrogen, viz. EUV and Lyman-Werner photons. Abundant soft FUV

photons and X-rays also help in launching the wind by increasing the thickness of the intermediate layer, causing its upper surface to intercept more of the EUV.

By comparison with previous work on PPD photoevaporation, we find that mass-loss estimates are sensitive to the fidelity of both the hydrodynamics and thermochemistry. Mass loss is also sensitive to intrinsically uncertain physical parameters, notably the dust abundance and size distribution. Some molecules, including OH, H_2O and CO, persist in the lower wind at higher temperatures and intermediate velocities than would be expected from equilibrium chemistry, as a consequence of comparable hydrodynamic and (photo-)chemical timescales.

Appendix

3.A Details of Key Thermochemical Processes

3.A.1 FUV induced reactions of H_2

When a 13.6 eV $> h\nu >$ 11.3 eV photon (the "Lyman-Werner" band, or LW for short) encounters hydrogen molecules, this photon can be absrobed by a H_2 molecule, and excite the H_2 molecule into an excited electronic state. This state can spontaneously decay into different ro-vibrational states, hence we have to include the excited $H_2{}^*$ as a representative for excited molecular hydrogen. Such photo-pumping of H_2 is also subject to self-shielding effects. We follow Draine & Bertoldi (1996) for the shielding factor.

As summarized by TH85, about 10 per cent of the excited hydrogen molecules result in photo-dissociation; we hereby simplify this reaction channel by adding a branch to the main photo-excitation channel, namely,

$$\mathrm{H_2} + h\nu(\mathrm{LW}) \rightarrow \begin{cases} 2\mathrm{H}\ , & \sim 10 \text{ per cent}\ ; \\ \mathrm{H_2}^*\ , & \sim 90 \text{ per cent}\ . \end{cases}$$

$H_2{}^*$ molecules may also be directly photo-dissociated; the reaction cross section of TH85 is adopted. We take 0.4 eV as the amount of energy deposited in the gas as heat per FUV dissociation of H_2 (Gong et al. 2016; see also Hollenbach & McKee 1979).

At gas densities relevant here, the majority of excited hydrogen molecules are de-excited by collisions with other particles, especially H_2 or H. The de-excitation rate (with the $v = 6$ vibrational state as a proxy for all excited $H_2{}^*$), is estimated by (see also TH85),

$$\begin{aligned} k_{\mathrm{de}}(\mathrm{H}) &\simeq 1.8 \times 10^{-13}\ \mathrm{cm^3\ s^{-1}} \times \left(\frac{T}{\mathrm{K}}\right)^{1/2} \exp\left(-\frac{1000\ \mathrm{K}}{T}\right)\ ; \\ k_{\mathrm{de}}(\mathrm{H_2}) &\simeq 2.3 \times 10^{-13}\ \mathrm{cm^3\ s^{-1}} \times \left(\frac{T}{\mathrm{K}}\right)^{1/2} \exp\left(-\frac{18000\ \mathrm{K}}{T + 1200\ \mathrm{K}}\right)\ . \end{aligned} \tag{3.2}$$

Each collisional de-excitation deposits ~ 2.6 eV of heat into the gas (see also TH85). The rate for spontaneous radiative de-excitation of $H_2{}^*$ is taken to be $A(H_2{}^*) \simeq 2 \times 10^{-7}$ s^{-1} (TH85).

3.A.2 FUV induced reactions of H_2O and OH

Photodissociation of H_2O and OH is not drastically affected by self-/cross-shielding due to line overlap. For the photodissociation cross sections of these two species as functions of photon energy, we adopt Fig. 1 of AGN14. These reactions also heat the gas. Here we adopt the estimate in AGN14 that about $\sim 0.5(h\nu - E_{\rm diss})$ of heat is deposited into the gas per reaction, where $E_{\rm diss}(H_2O) \simeq 5.13$ eV, and $E_{\rm diss}(OH) \simeq 4.41$ eV. Photodissociation of OH may result in oxygen atoms in the ^1D state, denoted by O*, which spontaneously decays to the ^3P state while emitting a photon at 6300 Å. Due to the uncertainty or variability of the FUV spectrum, we adopt the crude approximation that ~ 55 per cent of the OH dissociated results in O* (van Dishoeck & Dalgarno, 1984; Woitke et al., 2011). This seems not to be significant for hydrodynamics; nevertheless, as the [O I] 6300 Å radiation is an important diagnostic of PPDs winds, we expect this to be useful in our incoming analysis of comparison between simulation results and observations.

3.A.3 Dust and PAH

Dust-assisted H_2 formation

The reaction rate of H_2 formation on dust surface directly follows Bai & Goodman (2009), except for the efficiency of formation, for which we adopt the scheme of AGN14,

$$\eta \sim \begin{cases} 1 \ , & T_{\rm dust} < 25 \text{ K} \ ; \\ 0.6 \ , & 25 \text{ K} < T_{\rm dust} < 80 \text{ K} \ ; \\ 0.33 \ , & 80 \text{ K} < T_{\rm dust} < 900 \text{ K} \ ; \\ 0 \ , & T_{\rm dust} > 900 \text{ K} \ ; \end{cases} \tag{3.3}$$

where $T_{\rm dust}$ is the dust temperature, which may be significantly different from the gas temperature T. A typical formation rate is $R \simeq 7.5 \times 10^{-17}$ cm^3 s^{-1} at 100 K, which is comparable to the value in photodissociation regions (PDRs) given the geometric dust cross section 8×10^{-22} cm^2 per hydrogen nucleus (see §31.2 in Draine, 2011b). The formation of each H_2 molecules deposits ~ 1.5 eV of heat into the gas, the remaining recombination energy being radiated (AGN14). We take this effect into account.

Dust-assisted recombination and photoelectric effect

Dust-assisted recombination is implemented by including the following two processes:

$$\text{Gr}^+ + e^- \to \text{Gr} \ ; \quad \text{Gr} + e^- \to \text{Gr}^- \ .$$

The efficiency of Gr and Gr^+ capturing free electrons follows the fitting formulae for electrostatic focusing in Draine & Sutin (1987) and the sticking probability evaluated by Weingartner & Draine (2001). The following two kinds of reactions close the cycle of dust-assisted neutralization:

$$Gr^- + X^+ \rightarrow X + G \ ; \quad Gr + X^+ \rightarrow X + Gr^+ \ .$$

Here X represents H, He, C, O, S, Si, or Fe. The rates of these reactions are evaluated using the same method as in Bai & Goodman (2009), using the desorption temperature summarized by Ilgner & Nelson (2006a).

Photoelectric reactions of neutral and negatively charged dust grains are included,

$$Gr + h\nu \rightarrow Gr^+ + e^- \ ; \quad Gr^- + h\nu \rightarrow Gr + e^- \ .$$

The majority of the radiation absorbed is converted to dust thermal energy (which is in balance with thermal radiation of dust), but some is carried off by the photoelectrons. Following GH08 and GH09, the cross sections for photon absorption, as functions of photon energy and grain size, are evaluated for each photon energy based on the recipes in Li & Draine (2001) [eqs. (4)-(12) and Table 1 therein]. The photoelectric yield per photon absorption is calculated with recipes in Weingartner & Draine (2001) (elaborated in their §2). The work function is assumed to be $W \simeq 4.4$ eV (Weingartner & Draine, 2001) for carbonaceous grains. The energy deposited into the gas per reaction is estimated by $(h\nu - W)$. Ideally, our treatment should involve the valence band ionization potential (Weingartner & Draine, 2001), which differs from W by ~ 2 eV for $r_{\rm dust} = 5$ Å particles (this difference is smaller for larger grains). However, for simplicity and because our very small grains are proxies for grains of all sizes, we omit this refinement.

Dust-gas energy transfer and artificial heating term

Near the midplane, the gas acquires energy and maintains temperature through the energy transfer with dust. The gas-dust energy transfer rate is estimated following Goldsmith (2001):

$$\Lambda_{\rm dust} = \sum_s n_s \left(\frac{8k_{\rm B}T}{\pi m_s}\right)^{1/2} \sigma_{\rm dust}\alpha \times 2k_{\rm B}(T - T_{\rm dust}) \ , \tag{3.4}$$

where the subscripts "s" range over species, T is the gas temperature, $T_{\rm dust}$ the dust temperature, $\sigma_{\rm dust}$ is the geometric dust cross section, $\alpha \sim 0.5$ is the efficiency of gas-dust energy transfer (typically referred as the *accommodation coefficient*). It is possible that $\Lambda_{\rm dust}$ can be negative, indicating a heating instead of cooling process.

We further assume that the energy-transfer process does not affect the dust temperature profile. We do not evaluate the radiative transfer of diffuse infrared radiation iniside the disk, which should properly determine the temperature of dust. In order to have a reasonable estimate of $T_{\rm dust}$ profile, we assume local equilibrium, and adopt the simplest dual-temperature profile proposed by Chiang & Goldreich (1997), using

the following equation,

$$0 = \frac{\mathrm{d}\epsilon_{\rm dust}}{\mathrm{d}t} = \max\left[4\sigma_{\rm B}T_{\rm ah}^4(R)\sigma_{\rm dust}q(T_{\rm dust})\ ,\ \sum_{h\nu}F_{\rm eff}(h\nu)\sigma(h\nu)\right] - 4\sigma_{\rm B}T_{\rm dust}^4\sigma_{\rm dust}q(T_{\rm dust})\ , \tag{3.5}$$

where $\sigma_{\rm B}$ is the Stefan-Boltzmann constant, $T_{\rm ah}$ the desired artificial heating temperature as a function of R (e.g. Chiang & Goldreich 1997, figure 4), $\sigma_{\rm dust}$ the geometric cross section of dust, and $q(T_{\rm dust})$ the Planck-averaged emission efficiency as a function of black-body radiation field temperature [we evaluate this value with eq. (24.16) in Draine 2011b], $F_{\rm eff}(h\nu)$ the local effective irradiative radiation flux at photon energy bin $h\nu$ (see eq. 2.14), and $\sigma(h\nu)$ the effective absorption cross section (see §3.A.3).]

Optical photons ($h\nu \lesssim 4.5$ eV), which we have not included in our simulations, should also affect dust temperature in the regions that those photons penetrate. Although the optical luminosity is generally ~ 100 times greater than all other bands combined, the dust temperature is rather insensitive to the inclusion of optical radiation because the thermal emission per grain $\propto T_{\rm dust}^6$ (emissivity $q \propto T_{\rm dust}^2$). We have conducted a test that includes an optical photon-energy bin with luminosity 2.34 $L_\odot$ (see GH09), to find that the dust temperature in the intermediate layer rises by ~ 40 per cent, while the gas temperature there is almost invariant (as gas thermodynamics is dominated by processes not related to dust in the intermediate layer). As a result, the mass loss rate is unaffected by optical photons.

3.A.4 Other Molecular and Atomic Cooling Processes

Molecular ro-vibrational line cooling

Based on Neufeld & Kaufman (1993), ro-vibrational cooling caused by collisionally excited CO, OH, H_2O and H_2 are evaluated using interpolation tables. All of those cooling rate calculation schemes require the optical depth parameter $\tilde{N}_{\rm X}$ defined in Neufeld & Kaufman (1993), as a measure of escape probability of photons that remove energy from the gas, where X is the species interested, and $\tilde{N}_{\rm X}$ is the local $Gn({\rm X})/|\nabla v|$, where v is the local characteristic velocity, and G is a geometric factor at the order of 1; note that $\tilde{N}$ has units of time/volume. Here we use $\tilde{N}_{\rm X} \sim n({\rm X})/(v_{\rm th}/h)$ to estimate $\tilde{N}$, where h is the local scale height, and $v_{\rm th} \simeq [2k_{\rm B}T/m({\rm X})]^{1/2}$ is the thermal speed of the species X: $n({\rm X})h$ is a reasonable estimate of vertical column density integrated from $z = \infty$. In the regions where molecular cooling is important, the magnitude of the vertical gradient in the flow velocity is $\lesssim 10^{-1}$ km s^{-1} AU^{-1}. This is comparable to but smaller than $v_{\rm th}/h$, which is typically 10^{-1}–10^{0} km s^{-1} AU^{-1} at the molecular weights and typical kinetic temperatures of relevant species. For simplicity, we use only the thermal speed for the optical depth parameter.

Atomic cooling processes

Collisionally excited atoms may decay radiatively, removing heat from the gas. In this work, we evaluate the cooling rate of atoms as follows. For each kind of atoms, we assume that they are in local statistical equilibrium and calculate the population fraction on the "upper levels" of transitions by taking collisional (de-)excitation, photon or chemical pumping, and spontaneous decay into account, by solving detailed balance equations. With the population number of excited coolants obtained, the cooling rate is calculated by $\Lambda = \beta n^*_{\rm coolant} A$, where $n^*_{\rm coolant}$ is the number density of the desired coolant on the excited state, A the Einstein A coefficient, and β the escape probability. According to previous research work such as Kwan & Krolik (1981) β is a function of line-center optical depth τ_0,

$$\beta \simeq \begin{cases} \left[\tau_0 \pi^{1/2} \left(1.2 + \dfrac{\sqrt{\ln \tau_0}}{1+\tau_0/10^5}\right)\right]^{-1} , & \tau_0 \gtrsim 1 \ ; \\ \dfrac{1-\exp(-2\tau_0)}{2\tau_0} , & \tau_0 \lesssim 1 \ . \end{cases} \tag{3.6}$$

We estimate τ_0 as a function of local thermal velocity, vertical column density (estimated by $n_{\rm tot} h$, where h is the local scale height), line center wavelength, and oscillator strength (which can be directly inferred from A), as given by eq. (9.10) of Draine (2011b). In this work, we include these atomic coolants: Ly-α, [C II] 158 μm, [O I] 63 μm, O I 6300 Å (note that the excited state of oxygen atom for this transition is treated separately; see §3.A.2), [S I] 25 μm, [Si II] 35 μm, [Fe I] 24 μm, and [Fe II] 26 μm. We adopt the data in table 4 of TH85 for those transitions.

Chapter 4

Transitional PPDs: Chemistry and Accretion

This chapter applies the chemistry solver onto a *hydrostatic* grid with a fixed temperature profile, to examine the ionization inside a special type of PPDs, namely transitional disks, and attempts to explain fast accretion of transitional disks through the wind-launching mechanism (§1.1.2). §4.1 summarizes the observational evidence for rapid inflow and the theoretical reasons for expecting wind-driven accretion to be transsonic, in which we also review the importance of ambipolar diffusion, at least under laminar conditions, for allowing the gas to accrete without overly concentrating the magnetic flux. This leads to a calculation in §4.2 of the expected degree of ionization and ambipolar coupling of the gas to the field in the cavity regions. It is found that wind-launching accretion with ambipolar diffusion is plausibly neither so rapid as to undercut the magnetic wind torque on the neutrals, nor so slow as to cause the field to be accreted with the gas. A simple semi-analytic model of dynamics is also constructed to illustrate such plausibility. Further discussions on the issue of radial flux advection are presented in §4.3. The chapter is summarized in §4.4.

4.1 The Accretion Puzzle in TDs

4.1.1 TD Accretion in General

Transitional protostellar disks (transitional disks; hereafter TDs) are deficient in mid-infrared emission ($\lambda \lesssim 10\mu$m), implying a dearth of small dust grains interior to a few to several tens of AU (Strom et al., 1989; Skrutskie et al., 1990; Espaillat et al., 2014, and references therein). TDs are often supposed to represent an evolutionary stage intermediate between classical T Tauri systems, which have full disks, and weak-lined T Tauri systems, which have little or none [1].

[1] There is another type of *pre-transitional* disks, defined as those whose spectral energy distributions are deficient relative to full disks at wavelengths $\sim 10\mu$m, like TDs, but resemble full disks at near-infrared wavelengths ($\lambda \lesssim 5\mu$m: Espaillat et al. 2014).

TDs tend to accrete less than full disks of comparable mass by factors ∼3-10 (Najita et al., 2015). The abundance of small dust in the disk cavity is suppressed by much larger factors (van der Marel et al., 2015). Some TDs, however, have accretion rates entirely comparable to those of full disks despite inner gaps of tens of AU (Manara et al., 2014). Evidently gas somehow crosses the gap between the outer disk and the star. Indeed, gas is detected within dust cavities of accreting TDs via H_2 fluorescence (Ingleby et al., 2009; Gorti et al., 2011) and rovibrational CO emission (Pontoppidan et al., 2008; Salyk et al., 2009). In both cases the emission appears to correlate with $\dot{M}$. Owen (2016) suggests that there are two types of TDs: (1) those that are faint at submillimeter wavelengths, have cavities $\lesssim$ 10AU, and accrete at $\dot{M} \lesssim 10^{-9}\ M_\odot\ \mathrm{yr}^{-1}$; (2) those that are bright in the submillimeter, have cavities $\gtrsim$ 20AU, and accrete at $\sim 10^{-8}\ M_\odot\ \mathrm{yr}^{-1}$. The first type is consistent with expectations for photoevaporating disks, he suggests, whereas the latter is not. This chapter pertains mainly to class (2)—TDs that accrete rapidly despite large cavities.

The persistence of accretion suggests that within TD dust cavities either the ratio of small dust to gas is reduced, or the velocity of accretion is increased (implying a lower surface density for a given $\dot{M}$). A third possibility is that there is a reservoir of accreting gas at radii $\lesssim$ 1AU, separated from the outer disk by gap of $\gtrsim$ 10AU. Morishima (2012) finds that such structure can result if dead zones—regions of low viscosity near the midplane—are included in viscous photoevaporative disk models. Such models would seem to be better candidates for pre-transitional rather than transitional disks. Since quantitative measures of the gaseous surface density within TD cavities are sparse, many theoretical explanations for TDs have focussed on the former possibility, i.e. on mechanisms for altering the abundance of small grains per unit gas mass, such as photophoresis (Krauss & Wurm, 2005), radiation pressure (Chiang & Murray-Clay, 2007), pressure-induced dust filtering (Paardekooper & Mellema, 2006; Rice et al., 2006; Zhu et al., 2012), or grain coagulation (Tanaka et al., 2005).

Alternatively or in combination with modified dust, mechanisms for increasing the radial speed of accretion (v_{acc}) within TD cavities have been proposed. These include enhanced MRI turbulence (Chiang & Murray-Clay, 2007; Suzuki et al., 2010), and planetary or stellar torques (Varnière et al., 2006; Zhu et al., 2011; Rosenfeld et al., 2014; Casassus et al., 2015). At $\dot{M} \sim 10^{-8}\ M_\odot\ \mathrm{yr}^{-1}$, MRI alone cannot reduce the surface density below a few $\mathrm{g\,cm}^{-2}$ at relevant radii, which does not render the disk optically thin with standard ISM dust and would appear also to violate direct constraints on the gas column in some systems (§4.1.2). Planetary-torque models, even with multiple planets, have difficulty opening wide and clean gaps in the gas while still maintaining high accretion rates (Crida & Morbidelli, 2007; Zhu et al., 2011; Dong & Dawson, 2016).

4.1.2 Inflow Speed of TD Accretion

Constraints from observations

If the surface density of gas in a TD dust cavity were known, then the inflow speed could be estimated from the observed accretion rate on the assumption of steady

state. While gas has been detected in a number of TD cavities, the amount of gas has not often been reliably quantified. Bruderer (2013) has argued that CO should survive photodissociation even if the gas and dust surface densities are suppressed by several orders of magnitude. Rotational transitions trace the total gas content more reliably than rovibrational ones because of the lower excitation temperatures and critical densities of the former. ALMA has now made it possible to resolve TD cavities in CO rotational transitions. In a recent study, van der Marel et al. (2016, hereafter vdM16) have applied this method to four TDs, using multiple isotopologues of carbon monoxide (^{12}CO, ^{13}CO, C^{18}O) to correct for optical depth and photodissociation. Three of their four systems have quoted accretion rates $> 10^{-9}\ M_\odot\ \mathrm{yr}^{-1}$. Of these, DoAr44 is particularly interesting because the gas surface density (Σ) within 16AU is inferred to be no more than $\sim 10^{-4}$ of an extrapolation from the outer disk. Specifically, in vdM16's model, $\Sigma(r) \lesssim 5\times10^{-3}\ r_{16}^{-1}$ g cm^{-2} for $r_{16}\equiv r/(16\mathrm{AU}) < 1$. Yet $\dot{M} = 9\times10^{-9}\ M_\odot\ \mathrm{yr}^{-1}$. The implied accretion speed is

$$v_{\rm acc} = \frac{\dot{M}}{2\pi r\Sigma} \gtrsim 0.8\mathrm{km\ s}^{-1}. \tag{4.1}$$

This is comparable to the sound speed if the hydrogen is molecular and its temperature is in equilibrium with the radiation field of the star ($T_{\rm eq} \simeq 100\, r_{16}^{-1/2}$K): $c_{\rm s} \simeq 0.7 r_{16}^{-1/4}$km s^{-1}. Unless Σ is much less than vdM16's upper bound, the accretion speed (4.1) is much less than free fall speed, $v_{\rm ff} \simeq 12\, r_{16}^{-1/2}$km s^{-1}. On the other hand, it is much larger than can be explained by "viscous" accretion mechanisms: the implied Shakura-Sunyaev viscosity parameter would have to be $\alpha = \dot{M}\Omega/3\pi c_{\rm s}^2\Sigma \gtrsim 8$. Similar conclusions follow for the other two of van der Marel et al. (2016)'s systems that show appreciable accretion, viz. HD135344B & IRS48: the accretion speed is superviscous ($\alpha > 1$) but consistent with being subsonic or transsonic.

The inference of hydrogen gas masses from observations of trace species is fraught with difficulties, and it is not yet clear whether CO is a reliable mass indicator even when isotopologues are used to correct for optical depth and photodissociation effects (Manara et al., 2016; Miotello et al., 2016; McClure et al., 2016). Drabek-Maunder et al. (2016) model HCO+ emission in LkCa15 and find the gas in the cavity of that transitional disk to be suppressed by no more than a factor of 10 below extrapolation from the outer disk. Although LkCa15 was not studied by van der Marel et al. (2016), the inference that accretion *must* proceed transonically in TD cavities should be viewed as provisional until the extreme reduction in gas density can be confirmed.

Radial speed of magnetized wind-driven accretion

Following our arguments in §1.1.2, eq. (1.3), with the usual symmetry $[B_R, B_\phi, B_z]_{z=h} = [-B_R, -B_\phi, B_z]_{z=-h}$, the accretion speed is estimated by

$$v_{\rm acc} \simeq -\frac{B_z B_\phi^+}{\pi\Sigma\Omega}\ . \tag{4.2}$$

If all three components of the field are comparable, one gets $v_{\rm acc} \simeq v_{\rm A}^2/\Omega h$, where $v_{\rm A}^2 = B_z^2/4\pi\rho_0$ is the Alfven speed based on conditions at the midplane, and $h \equiv \Sigma/2\rho_0$ is the effective half thickness of the disk. If this thickness is determined by a balance between gas pressure and the tidal field, then $\Omega h \sim c_{\rm s}$, so that the Mach number of accretion is $\sim (v_{\rm A}/c_{\rm s})^2$. Hence winds with near-equipartition fields should drive transsonic accretion.

In the semi-analytic wind models developed by Königl (1989), Wardle & Königl (1993), and Li (1996), $v_{\rm acc}$ is in fact typically comparable to the sound speed, or even a few times larger.[2] This is also true of numerical simulations that treat the disk structure explicitly and approach a steady state (Casse & Keppens, 2002; Zanni et al., 2007b; Tzeferacos et al., 2009b).

4.1.3 Radial Advection of Magnetic Flux

In steady state, matter accreting through the disk must be able to cross field lines so that magnetic flux is not dragged with it. Otherwise, the radial concentration of flux will exert an outward force on the disk, producing subkeplerian rotation and possibly choking off the accretion or at least slowing it down (Bisnovatyi-Kogan & Ruzmaikin, 1976; Narayan et al., 2003). Indeed, the tendency to subkeplerian rotation might prevent the formation of protostellar disks in the first place (Li et al., 2014, and references therein). The wind models of Königl and collaborators invoke ambipolar diffusion to separate the accreting neutral gas from the magnetic flux. This process is characterized by the ambipolar Elsasser number, i.e. ratio of the neutral-ion collision time to the orbital time,

$$\mathrm{Am} \equiv \frac{\tau_{\rm ni}^{-1}}{\Omega} \simeq 0.56 \left(\frac{n_e}{\mathrm{cm}^{-3}}\right)\left(\frac{r}{16\ \mathrm{AU}}\right)^{3/2}\left(\frac{M_*}{M_\odot}\right)^{-1/2} . \tag{4.3}$$

Here we have evaluated the parameter Am for the surface-density profile fitted by vdM16 to DoAr44. It will be shown in §4.2 that the electron density at the midplane within the disk cavity is plausibly such that $\mathrm{Am} \sim 1 - 10$.

The ambipolar drift velocity between the neutral and charged species when the latter are tied to the field is

$$\mathbf{v}_{\rm drift} \simeq \mathrm{Am}^{-1} \frac{\mathbf{B}\times(\nabla\times\mathbf{B})}{4\pi\rho\Omega} , \tag{4.4}$$

and $v_{\rm drift} \simeq v_{\rm acc}$ if the field is stationary. The reduction in orbital velocity due to magnetic force is, with $\hat{\mathbf{e}}_r$ a radial unit vector,

$$\Delta v_\phi \simeq \hat{\mathbf{e}}_r \cdot \frac{\mathbf{B}\times(\nabla\times\mathbf{B})}{8\pi\rho\Omega} . \tag{4.5}$$

[2]The horizontal components of field, which vanish at the midplane, compress the thickness h to less than its tidal value, strengthening the conclusion of the previous paragraph.

Hence $v_{\mathrm{drift},r}/\Delta v_\phi \simeq 2\mathrm{Am}^{-1}$. In order that $v_{\mathrm{drift},r} \sim c_\mathrm{s}$ while $\Delta v_\phi \ll \Omega r$, it is therefore necessary that $\mathrm{Am} \ll 2\Omega r/c_\mathrm{s} \sim 20$. On the other hand, $\mathrm{Am} \gtrsim 1$ is needed for adequate coupling. We are not aware of a feedback mechanism to ensure that this rather narrow parameter range is realized at the midplane in the cavity.

4.2 Physical State of the Cavity Gas

The wind-launching accretion picture of TDs requires the ambipolar parameter Am to stay in the desired range . A reasonable estimate of the Am profile must take into account multiple chemical species in addition to hydrogen, including a simplified treatment of dust grains, and far-UV (FUV) as well as X-ray ionization. Such estimations are described in this section.

4.2.1 Model Setup

The calculations are done in spherical polar coordinates, dividing the gas into 100 radial zones spaced logarithmically in *cylindrical* radius from $r = 1$AU to $r = 50$AU, and 20 latitudinal zones spaced linearly from $\theta = 0$ (midplane) to $\theta = 0.2$. Radiative transfer of the ionizing photons is calculated by integrating along radial rays, so that the calculations are effectively one-dimensional, except for some implicit scattering of the X-rays after they strike the disk surface. The surface mass density within the cavity is taken as $\Sigma \sim 5 \times 10^{-3}\ r_{16}^{-1}$ g cm^{-3} following §4.1.2. To allow for a finite angle between the ionizing rays and the disk surface [e.g. Perez-Becker & Chiang (2011a)], we consider a flared disk with $h \propto r^{5/4}$ and $h = 0.1r$ at $r = 16$AU ($r_{16} = 1$). Hydrogen nuclei are distributed as

$$n_\mathrm{H}(r,z) = n_0 r_{16}^{-2.25} \exp[-(r\tan\theta)^2/(2h^2)]\ ,$$

with $n_0 = 10^8\mathrm{cm}^{-3}$. The gas is assumed vertically isothermal with radial temperature profile $T = T_0 r_{16}^{-1/2}$ and $T_0 = 100$ K, 30 K or 300 K. Note that the temperature in our chemical calculations is prescribed rather than selfconsistently determined from heating and cooling.

Ionizing photons emanate from the origin $r = 0$ with total luminosities in two discrete energy bins: X-ray $L_X = 10^{30}$ erg s^{-1} with $h\nu = 3$ keV, and $L_\mathrm{FUV} = 10^{30}$ erg s^{-1} with $h\nu = 12$eV. EUV photons ($h\nu > 13.6$eV) are ignored on the grounds that their penetration depths are insufficient for them to enter the mid-plane of transitional disks. Even FUV photons have rather little effect on the ionization balance at depth in the disk because of our restriction to purely radial propagation: the radial column density that must be crossed to reach the midplane at $r \gtrsim 1$AU is $N_{\mathrm{H}_2} \sim 10^{24}$ cm^{-2}, falling to $\sim 10^{22}$ cm^{-2} at $z \sim 1 - 2h$ off the plane.

Nine abundant elements (H, He, O, C, N, S, Si, Mg, and Fe) are included at IN06 abundances together with compounds totalling 175 species (following Table A.1 of Ilgner & Nelson, 2006b, with H^+ added). We use the thermochemical module with `CVODE` backend (§2.3.1) to solve for the steady states of chemical networks in each cell,

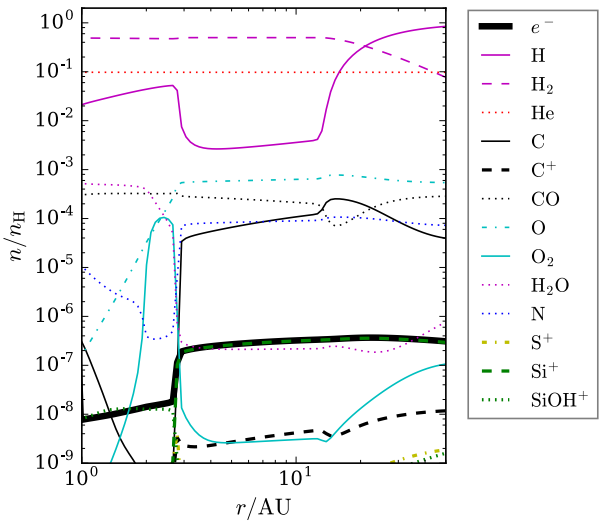


Figure 4.1 Relative abundance of significant neutral ($n/n_{\rm H} > 10^{-5}$) and ionic ($n/n_{\rm H} > 10^{-8}$) species at the midplane. The relative abundance of electrons is shown by the heavy black curve; other species as noted in the legend.

but we nontheless fix the prescribed temperature profile, as consistent calculations of temperatures will require full MHD simulations. The basic set of chemical network is obtained by (1) taking two-body reaction data from the `UMIST` (McElroy et al., 2013); (2) taking all other reactions into account via the same route as §3.A.

4.2.2 Results

Figure 4.1 plots the abundance at the midplane ($\theta = 0$) of major species relative to hydrogen for the fiducial model, in which $L_X = L_{\rm FUV} = 10^{30}$ erg s^{-1}, $n_0 = 10^8$ cm^{-3}, $T_0 = 100$ K, and $r_{\rm dust} = 10^{-3}$ μm. The electron abundance depends depend rather weakly on radius, while the dominant positive ions are Si^+ and $SiOH^+$. Photoionization of helium and oxygen are competitive with that of molecular hydrogen as a source of free electrons.

For the fiducial case, the timescale on which n_e equilibrates is at least one order of magnitude shorter than the local accretion timescale $\tau_{\rm acc} \equiv r/v_{\rm acc}$ based on eq. (4.1), justifying our neglect of advection. This is not always true, however, especially in cases without dust.

We calculate seven additional models, each differing from the fiducial one in one parameter (Table 4.1). Following eq. (4.3), Fig. (4.2) exhibits the profiles of Am in the rz plane for all eight models.

The electron abundance and therefore Am increase as X-ray luminosity increases, and as density decreases: the latter is contrary to the trend for radiative hydrogen recombination and is due to molecular ions. The dependence on temperature is relatively complicated and subtle, as temperature affects the rates of radiative, dissociative and dust-assisted recombination in different ways. Comparison between

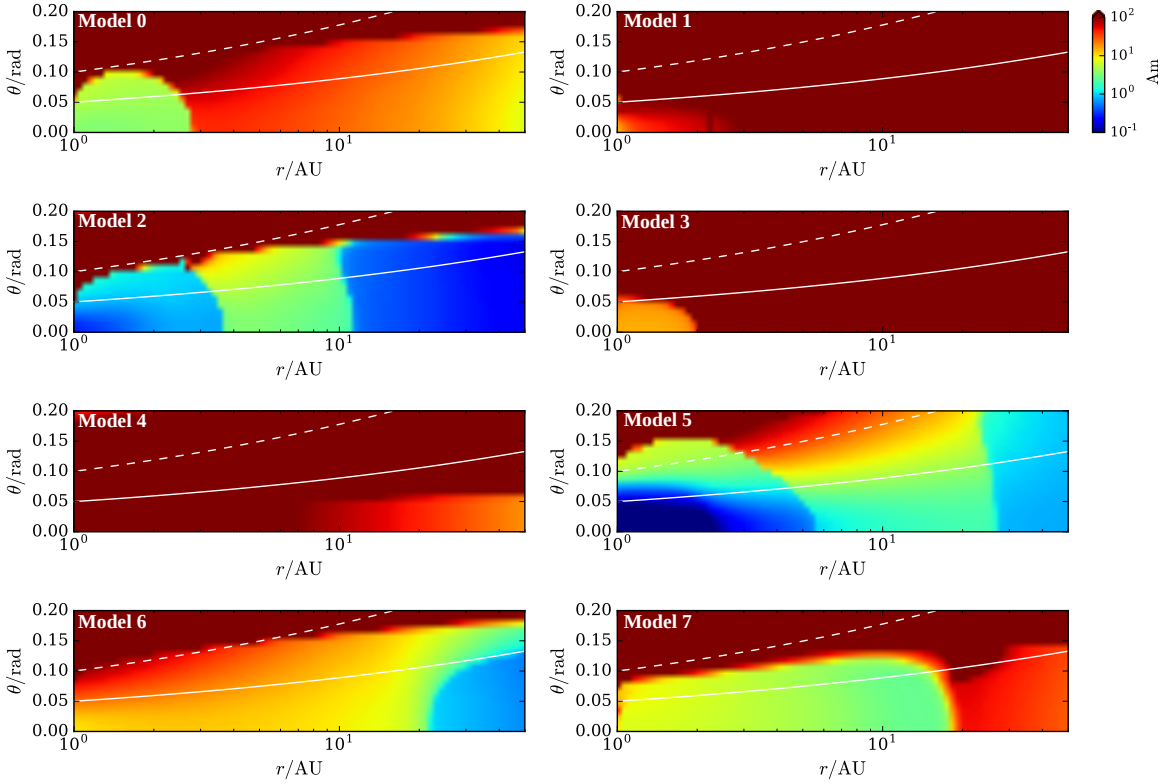


Figure 4.2 Ambipolar parameter Am vs. cylindrical radius r and latitude θ. Each panel corresponds to one of the models in Table 4.1, as marked. White curves are loci of constant gaussian scale height: h (solid), and $2h$ (dashed).

Table 4.1. Properties of the fiducial model

Model No.	Description
0	Fiducial
1	No dust
2	$L_X = 10^{29}$ erg s^{-1}
3	$L_X = 10^{31}$ erg s^{-1}
4	$n_0 = 10^7$ cm^{-3}
5	$n_0 = 10^9$ cm^{-3}
6	$T_0 = 30$ K
7	$T_0 = 300$ K

Models 0 and 1 illustrates the importance of small dust. Eliminating dust-assisted recombination raises the electron density by one to two orders of magnitude.

The fiducial model has a relatively low-Am region that extends radially to $\sim$ 3 AU, and vertically to 1-2 scale heights (h). Similar regions exist in Models 2, 5 and 7, and less clearly in Models 1 and 3. The exponential attenuation of X-rays with increasing column density actually lowers the ionization parameter $\xi \equiv \zeta/n_{\rm H}$ at smaller radii. The boundary of the low-Am regions corresponds to a transition in the dominant ion from Si^+ at relatively high n_e, to $SiOH^+$ (which has a larger dissociative-recombination cross section) at lower n_e.

We have used these results for the physical state of the gas to recompute the local wind model of Wardle & Königl (1993, hereafter WK93). Following these authors, we match the local solutions to the pressureless selfsimilar models of Blandford & Payne (1982, hereafter BP82) to obtain approximate global wind solutions. As already noted, WK93's model requires Am $\sim 10^0$ near the midplane, so that the coupling of the neutrals to the magnetic field is efficient enough to drive a wind but not so perfect as to accrete the magnetic flux. Fig. (4.2) shows that $0.3 \lesssim {\rm Am} \lesssim 30$ at $r \lesssim 10$AU in most of our models, excepting those with rather high ionization parameter or without dust. Quantitatively, we find that the radial velocity of the neutral gas at the midplane varies from $\sim 10^{-1} c_s$ to $\sim c_s$, and the accretion rate from 10^{-9} to $10^{-8}\ M_\odot$/yr, consistent with observed accretion rates in transitional disks.

An example of such a wind model is illustrated in Fig. 4.3. Gas parameters are taken from our fiducial model at $r = 2$AU: midplane density $n_0 = 6.4 \times 10^9$ cm^{-3}, temperature $T = 283$ K), and ambipolar parameter Am = 5. The vertical component of magnetic field is set to $B_0 = 4.45 \times 10^{-2}$ G. The corresponding values of WK93's dimensionless parameters are: $a = 1.03$ (midplane Alfvén velocity over sound speed), $\epsilon = 0.95$ (midplane radial velocity over sound speed), $\sigma_s = 10^{-3}$ (density at slow magnetosonic point over midplane density), $\epsilon_B = \beta_{i0}^{-1} = 0$ (radial drift speed of magnetic field over sound speed, and reciprocal of ion Hall parameter). These parameters are such that the solution passes smoothly through the sonic point, and at the base of the wind—defined where v_r reverses sign—matches a BP82 solution with parameters, in their notation, $\xi_0' = 1.30$ (= B_r/B_z projected to midplane), $\kappa = 0.0145$ (dimensionless mass flux), and $\lambda = 14.5$ (dimensionless specific angular momentum). The total vertical column density of this model is $\Sigma \simeq 6.8 \times 10^{-3}$ g cm^{-2}, and the accretion rate is $\dot{M} \simeq 3.6 \times 10^{-9}\ M_\odot$ yr^{-1}, while the mass-loss rate of the wind is smaller by a factor $\lambda^{-1} \simeq 0.068$.

4.3 Discussion

Following the methods presented in §4.2.1, "fiducial" values of the radiation field and other physical parameters do indeed suggest that Am is in the desired range indicated in §4.1.3, or at least close to it. However, this is likely not to be the last word on the subject because of the complex microphysics involved in the calculation and its sensitivity to input parameters such as the X-ray flux and dust abundance. *A priori*, if Am lies outside the desired range, it seems more likely to be too large than too

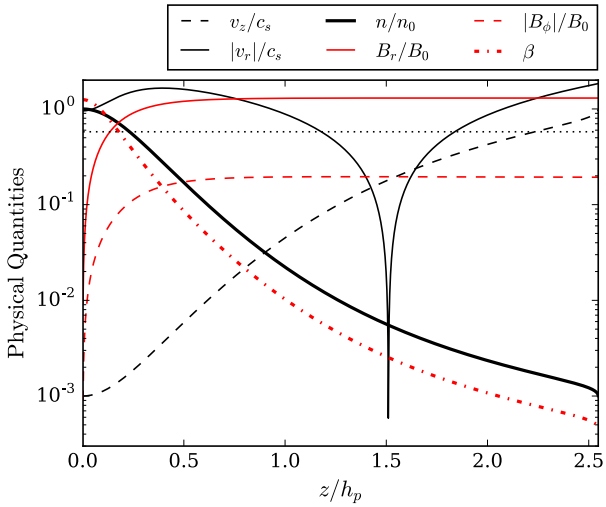


Figure 4.3 Example of a WK93-type wind. Physical quantities are plotted in dimensionless forms (note that here $c_s = 1.4$ km s^{-1}, $n_0 = 6.4 \times 10^9$ cm^{-3}, and $B_0 = 4.45 \times 10^{-2}$ G) against vertical coordinate z in units of thermal scale height $h_p \equiv c_s r/v_K = 0.13$ AU. The model is shown from the midplane through the sonic point. Wind base is at $z/h_p \simeq 1.5$, where v_r changes its direction. Physical quantities are marked by line color and shapes (as indicated in the legend). Note that velocities v_z and v_r pertain to the *neutral* component. β is the plasma beta, viz. the ratio of gas pressure to magnetic pressure. Intersection of solid red and horizontal dotted line marks $B_r/B_0 = 1/\sqrt{3}$, the critical field inclination for launching a cold BP82 wind from the midplane.

small on the grounds that (1) surely Am $\gtrsim 1$ in the active layers of full disks and the outer parts of transitional disks, else no magnetic mechanism, whether relying on MRI or winds, could be effective in driving accretion there; and (2) the lower surface density of the cavity gas and greater proximity to the sources of ionization might be expected to raise Am.

The problem of accretion of magnetic flux in ideal MHD is not new. When accretion is assumed to be driven by turbulent "viscosity", the concern is often opposite to that expressed here: namely, that turbulent diffusivity might allow the poloidal flux to escape too easily (van Ballegooijen, 1989; Lubow et al., 1994; Spruit & Uzdensky, 2005). In steady-state wind models based on near-ideal MHD, just enough turbulent diffusivity is invoked to allow the flux to be stationary as the gas accretes (Blandford & Payne, 1982; Ferreira & Pelletier, 1995a; Zanni et al., 2007c, and references therein). The questions then become (1) What is the origin of the turbulence? (2) How is the turbulent diffusivity regulated so that the magnetic flux neither accretes nor escapes?

A possible answer to question (1) above is MRI, whose turbulent diffusivity has been measured by several authors (Lesur & Longaretti, 2009; Guan & Gammie, 2009; Fromang & Stone, 2009). But MRI tends to be inhibited or suppressed by poloidal fields as strong as are found in many wind models (Salmeron et al., 2007; Bai &

Stone, 2013b; Gressel et al., 2015b). If the field were to become too strong to allow MRI, it is unclear what instability would arise to cause that field to reconnect or diffuse so as to allow MRI to return: that is, we lack an answer to question (2) above. Nonaxisymmetric interchange instabilities are possible but should occur only if $\mathrm{d}(B_z/\Sigma)/\mathrm{d}r < 0$, (Spruit et al., 1995; Stehle & Spruit, 2001; Igumenshchev, 2008), and while the interchange instability can rearrange the radial profile of B_z, it does not by itself alter B_z/Σ in a lagrangian sense. It may not be effective in reconnecting the horizontal components of magnetic field. More promising in this regard is the recently much-discussed plasmoid instability of current sheets (Loureiro et al., 2007; Loureiro & Uzdensky, 2016), but this instability has not yet been studied in the presence of a field component perpendicular to the sheet (B_z here).

4.4 Chapter Summary

We have seen that magnetized winds can rather naturally explain the combination of low gas and dust surface density and relatively robust accretion in transition-disk cavities. From a theoretical point of view, the suggestion is all the more natural because of previous work demonstrating the likelihood of *photoevaporative* winds on the one hand (Hollenbach et al., 1994b; Clarke et al., 2001; Alexander et al., 2006b; Owen et al., 2010b), and the need for net poloidal magnetic flux to sustain magnetorotational turbulence in the minimally ionized parts of protostellar disks, on the other (Fleming et al., 2000; Oishi & Mac Low, 2011; Flock et al., 2012; Bai & Stone, 2011a; Simon et al., 2013d,b). A thermally-driven outflow threaded by magnetic lines is bound to exert a torque on the gas remaining in the disk and drive some accretion, though just how much will require detailed modeling of a sort not attempted in the present work.

If the whole vertical column of the disk were to accrete at $v_{\rm acc} \sim c_{\rm s}$, then the surface density corresponding to observed accretion rates would be much less than what is inferred observationally, e.g. from submillimeter observations (Beckwith & Sargent, 1993; Andrews et al., 2013). Thus in the parts of TDs exterior to their cavities, as well as in full (non-transitional) T Tauri disks, either accretion is driven turbulently (and hence relatively slowly), or else it is again driven by a magnetized wind, but one that couples to only a small fraction of the vertical column where FUV and X-ray photons sufficiently ionize and heat the gas (Bai, 2016b).

Not addressed here is the *cause* of the transition between slow/layered accretion at large radii and fast, wind-driven, full-column accretion within the cavity. Perhaps, as proposed by Combet & Ferreira (2008), this has to do with a critical value of magnetization brought about by advection of poloidal flux. But as discussed in §4.3, the advection and diffusion of magnetic flux in a turbulent disk is an unsolved problem. Also, if this is the explanation, why aren't all T Tauri disks transitional? Perhaps indeed giant planets are implicated, but rather than producing the entire cavity by gravitational torques alone, such planets trigger a local change in the mass-to-flux ratio by stemming the inflow of gas near the midplane (which feels little magnetic torque) but not the inflow of the more ionized surface layers (which are more strongly

magnetically driven, whether by winds or MRI). In any case, one should entertain the possibility that transitional disks—or at least those that have accretion rates comparable to those of full disks—may not be an evolutionary phase that all disks pass through immediately before complete dispersal.

Chapter 5

Magnetized Wind of PPDs

This chapter explores magnetized winds of PPDs. §5.1 briefly summarizes the physical recipes we adopt for our simulations, some of whose details are further elaborated in the Appendix §5.A. §5.2 states the fiducial model of our simulation and explains the underlying physics, along with §5.3 presenting and discussing the main results of numerical calculations for this model. §5.4 explores the parameter space to understand the impact of different physical assumptions. In §5.5 we compare our results to those in B17 and Chapter 3, and discuss prospective connection to observations. The whole chapter is concluded and summarized in §5.6.

5.1 MHD with Magnetic Diffusivities

Without specific notices, we assume axisymmetry (and hence 2D), and with reflective symmetry over the equatorial ($\theta = \pi/2$) plane, for all of our models. All dependences on ϕ are negleted, but v_ϕ and B_ϕ are still included in our simulations. For convenience, we also occasionally use cylindrical coordinates (R, z), defined as $R \equiv r\sin\theta$, and $z \equiv r\cos\theta$. The HLLD Riemann solver and piecewise linear reconstruction are employed in all our simulations.

In CGS units, the MHD equations with magnetic diffusivities, which `Athena++` solves, read

$$\begin{aligned}
&\partial_t \rho + \nabla\cdot(\rho\mathbf{v}) = 0 \ ; \\
&\partial_t(\rho\mathbf{v}) + \nabla\cdot\left(\rho\mathbf{v}\mathbf{v} - \frac{\mathbf{B}\mathbf{B}}{4\pi} + P_{\rm tot}\mathbf{I}\right) = -\nabla\Phi \ ; \\
&\partial_t\mathbf{B} = \nabla\times(\mathbf{v}\times\mathbf{B} - c\mathbf{E}') \ ; \\
&\partial_t\epsilon + \nabla\cdot\left[(E + P_{\rm tot})\,\mathbf{v} - \frac{(\mathbf{B}\cdot\mathbf{v})\mathbf{B}}{4\pi} + \mathbf{S}'\right] = 0 \ ,
\end{aligned} \tag{5.1}$$

where ρ, $\mathbf{v}$ and p are the gas density, velocity and gas thermal pressure respectively, $P_{\rm tot} \equiv p + B^2/(8\pi)$ the total pressure, $\epsilon \equiv p/(\gamma-1) + \rho(v^2/2+\Phi) + B^2/(8\pi)$ the total

energy (γ is the adiabatic index)[1], Φ the gravitational potential, and $\mathbf{I}$ is the identity tensor. Thermodynamic processes that affect gas energy are calculated separately in an operator-splitting manner by solving the thermo-chemical system as a system in every simulation zone and timestep (see §(5.1.1)). The applied electric field due to non-ideal magnetic diffusion $\mathbf{E}'$ is given by,

$$\mathbf{E}' = \frac{4\pi}{c^2}\left(\eta_{\rm O}\mathbf{J} + \eta_{\rm H}\mathbf{J}\times\mathbf{b} + \eta_{\rm A}\mathbf{J}_\perp\right) \ , \tag{5.2}$$

where $\mathbf{b} \equiv \mathbf{B}/B$ is a unit vector along the local direction of magnetic field, $\mathbf{J} = c\nabla\times\mathbf{B}/4\pi$ is the electric current density, and $\mathbf{J}_\perp \equiv \mathbf{b}\times(\mathbf{J}\times\mathbf{b})$ is the component of $\mathbf{J}$ perpendicular to the local magnetic field. The Poynting flux associated to $\mathbf{E}'$ reads $\mathbf{S}' = c\mathbf{E}'\times\mathbf{B}/(4\pi)$. In this paper, we keep the Hall effect off ($\eta_{\rm H} = 0$). The remaining two diffusivities, $\eta_{\rm O}$ and $\eta_{\rm A}$ for Ohmic resistivity and ambipolar diffusion (AD hereafter) respectively, are calculated using the thermochemistry calculation results described in §5.1.1. This approach is clearly an improvement over previous works, where diffusivities are set as constants over the whole simulation domain, or calculated with pre-calculated interpolation table (e.g. B17).

5.1.1 Radiative Transfer and Thermochemistry

The set of chemical species and reactions largely follow Chapter 3, with some updates so that, based on our tests, the ionization in the intermediately ionized regions can be calculated with relatively good accuracy while the cost of computation is minimized. Compared to Chapter 3, the key updates are:

- There are 28 chemical species: e^- (free electrons), H^+, H, H_2, $H_2{}^*$ [using the $v = 6$ vibrational state as a proxy for H_2 in all excited states, see Tielens & Hollenbach 1985, (TH85)], He, He^+, O, O^+, OH, OH^+, H_2O, C, C^+, CO, HCO^+, CH^+, S, S^+, HS^+, Si, Si^+, SiO, SiO^+, $SiOH^+$, Gr, Gr^+, Gr^-. Here Gr and $Gr^\pm$ denote neutral and singly-charged dust grains, respectively. Such thermochemical network is tuned to properly capture the important reactions relevant to regions near wind bases and in the winds. It does not necessarily give realistic ionization profiles in the bulk disk. As this work primarily focuses on wind launching and its kinematics, we are satisfied with the performance of this network as long as it does not yield abnormal behaviors around the midplane region, which is the case as we will see.

- Ionization by diffuse high energy photons and radioactive decay becomes important. Similar to Chapter 4, we adopt the approach of Igea & Glassgold (1999), while details in estimating such effects are stated in §5.A.1.

[1] As a general equation of state (with variable γ) is not yet implemented in the current version of Athena++, we adopt an ideal equation of state with constant $\gamma = 5/3$. Admittedly γ should increase from $\gamma = 1.4$ in the molecular bulk disk to $\gamma = 5/3$ in regions where molecules are dissociated. We will further address this issue in §5.4.

- Self-/cross-shielding effects of photoionization/photodissociation processes are evaluated by Heays et al. (2017) (see also §5.A.2).
- A "pre-absorption" scheme is added to ray tracing so that unphysical conditions of radiation near the inner radial boundary are prevented (§5.A.3).
- The mid-plane temperature profile of artificial heating reads $T_{\rm ah} = 280\ {\rm K} \times (R/{\rm AU})^{-0.5}$.

5.1.2 Non-ideal MHD Diffusivities

Non-ideal MHD diffusivities are determined by the abundances of charge carriers, which are computed while the thermochemical networks are evolved. The general expressions for the three diffusivities read (e.g. Wardle, 2007; Bai, 2011b),

$$\eta_{\rm O} = \frac{c^2}{4\pi}\left(\frac{1}{\sigma_{\rm O}}\right)\ , \quad \eta_{\rm H} = \frac{c^2}{4\pi}\left(\frac{\sigma_{\rm H}}{\sigma_{\rm H}^2+\sigma_{\rm P}^2}\right)\ , \quad \eta_{\rm A} = \frac{c^2}{4\pi}\left(\frac{\sigma_{\rm P}}{\sigma_{\rm H}^2+\sigma_{\rm P}^2}\right) - \eta_{\rm O}\ , \tag{5.3}$$

Here $\sigma_{\rm O}$, $\sigma_{\rm H}$ and $\sigma_{\rm P}$ are Ohmic, Hall, and Pederson conductivities. These conductivities are calculated by,

$$\sigma_{\rm O} = \frac{ec}{B}\sum_j n_j Z_j \beta_j\ , \quad \sigma_{\rm H} = \frac{ec}{B}\sum_j \frac{n_j Z_j}{1+\beta_j^2}\ , \quad \sigma_{\rm P} = \frac{ec}{B}\sum_j \frac{n_j Z_j \beta_j}{1+\beta_j^2}, \tag{5.4}$$

summing over all charge carriers $\{j\}$, with n_j and Z_j being the number density and charge (in unit charge) of the jth charged species. The Hall parameter β_j represents the ratio between the gyrofrequency and neutral-collision frequency of such species,

$$\beta_j = \frac{Z_j e B}{m_j c}\frac{1}{\gamma_j \rho}\ ; \quad \gamma \equiv \frac{\langle\sigma v\rangle_j}{\langle m\rangle_n + m_j}\ , \tag{5.5}$$

where m_j is the species' mass, $\langle m\rangle_n$ is the mean molecular mass of the neutrals, and $\langle\sigma v\rangle_j$ is the rate of collisional momentum transfer between the jth species and the neutrals, given by (e.g. Draine, 2011a; Bai, 2011a, $T_2 \equiv (T/10^2\ {\rm K})$, m_p is the mass of proton),

$$\begin{aligned} \langle\sigma v\rangle_e &\simeq 8.3\times10^{-9}\ {\rm cm^3\ s^{-1}} \times \max\{T_2^{1/2}, 1\}\ , \\ \langle\sigma v\rangle_i &\simeq 2.0\times10^{-9}\ {\rm cm^3\ s^{-1}} \times \left(\frac{\langle m\rangle_n m_i/m_p}{\langle m\rangle_n + m_i}\right)^{-1/2}\ , \end{aligned} \tag{5.6}$$

for electrons and ions, respectively. As our dust grains are tiny, their collisional momentum transfer rate $\langle\sigma v\rangle_{\rm g}$ can be approximated by the rate of ions (but their conductivities are still calculated specifically using eqs. (5.4), (5.5)) using particle mass of dust grains). Although all three diffusivities are calculated, $\eta_{\rm H}$ is not actually adopted in this paper, as the Hall effect is turned off.

Regarding the accuracy of calculating diffusivities directly from chemistry, we test our thermochemical network under the same magnetic, thermodynamic and radiation conditions as the figure 5 in Xu & Bai (2016), in a hydrostatic grid and prescribed temperature. It gives no more than $\sim 10\%$ error in Elsasser numbers Am and $\Lambda_{\rm Ohmic}$ at higher altitudes ($z/H \gtrsim 2\ h_{\rm mid}$, $h_{\rm mid}$ is the fluid scale height at the equatorial plane), and no more than one order of magnitude in the mid-plane regions.

Real-time evaluation of diffusivities would have issues in two kinds of regions, both of which have huge $\eta_{\rm A}$ and makes simulation timesteps prohibitively small. First, near the polar axis, high energy photons can freely stream through and the gas is highly ionized ($x_{\rm e} \gtrsim 10^{-1}$), and the one-fluid treatment of magnetic diffusivity simply fails. Second, in the regions unreachable by high energy photons, ionization is extremely weak ($x_e \lesssim 10^{-11}$). In practice, we set a cap for $\eta_{\rm A}$, as $\eta_{\rm A,cap} = [10 c_{s,\rm mid} h_{\rm mid}]_{r=r_{\rm in}}$, where $c_{s,\rm mid}$ denotes the adiabatic sound speed at the equatorial plane, respectively (similar schemes capping diffusivity were also adopted in e.g. Bai & Stone 2013a; Gressel et al. 2015a, B17). Such diffusivity cap indeed does not harm our simulations, because (1) in highly ionized regions, the plasma is already in the ideal MHD regime, and (2) in regions with very weak ionization, fields are already decoupled from the fluids, and magnetic diffusivity is dominated by Ohmic resistivity.

5.1.3 Diagnostics of MHD Wind Models

This subsection briefly discusses major diagnostics, which are applied to analyze simulation results.

Magnetic diffusivities

As the Hall effect is turned off, diagnostics of non-ideal MHD effects focus on these two dimensionless Elsasser numbers,

$$\Lambda_{\rm Ohmic} \equiv \frac{v_{\rm A}^2}{\eta_{\rm O}\Omega_{\rm K}}\ , \quad {\rm Am} \equiv \frac{v_{\rm A}^2}{\eta_{\rm A}\Omega_{\rm K}}\ , \tag{5.7}$$

where $v_{\rm A} = (B^2/4\pi\rho)^{1/2}$ is the Alfven speed, and $\Omega_{\rm K}$ is the local Keplerian angular frequency. Magnetic diffusions are considered to be strong if either Elsasser number is at the order of unity or less. In general, $\Lambda_{\rm Ohmic} \lesssim 1$ is sufficient to supress MRI (e.g. Turner et al., 2007; Ilgner & Nelson, 2008). For Am, (Bai & Stone, 2011b) found that $\beta \lesssim \beta_{\rm min}({\rm Am})$ is also able to damp or suppressed MRI, where $\beta_{\rm min}$ is empirically found to be,

$$\beta_{\rm min}({\rm Am}) = \left[\left(\frac{50}{{\rm Am}^{1.2}}\right)^2 + \left(\frac{8}{{\rm Am}^{0.3}+1}\right)^2\right]^{1/2}\ . \tag{5.8}$$

Wind kinematics and dynamics

Following B17, we take the FUV front as the wind base, defined as where the radial absorption optical depth in the soft FUV band becomes unity. Near and above wind

bases, the mechanism that drives outflows is concerned. Following Bai et al. (2016) and B17, we project the specific force of a local fluid element onto the field line, and decompose the force into three terms,

$$\begin{aligned} &\left(\frac{\mathrm{d}v_\mathrm{p}}{\mathrm{d}t}\right)_s = f_\mathrm{gas} + f_\mathrm{ine} + f_\mathrm{mag} \ ; \\ &f_\mathrm{gas} \equiv -\frac{\mathrm{d}p}{\mathrm{d}s} \ ; \quad f_\mathrm{ine} \equiv \frac{v_\phi^2}{R}\frac{\mathrm{d}R}{\mathrm{d}s} - \frac{\mathrm{d}\Phi}{\mathrm{d}s} \ ; \quad f_\mathrm{mag} = -\frac{B_\phi}{4\pi\rho R}\frac{\mathrm{d}(RB_\phi)}{\mathrm{d}s} \ , \end{aligned} \tag{5.9}$$

where, along a field line, f_gas and f_mag are accelerations due to gas and magnetic pressure gradients respectively, and t f_ine is the net inertial acceleration (combining centrifugal force and gravitational force). Comparing these three terms helps us understand the mechanism of wind launching.

Wind mass loss rate $\dot{M}_\mathrm{wind}$ provides the most important diagnostics of disk dispersal. We characterize $\dot{M}_\mathrm{wind}$ by the local wind mass loss rate per logarithmic radius,

$$\frac{\mathrm{d}\dot{M}_\mathrm{wind}}{\mathrm{d}\ln R} = 4\pi R^2 \langle \rho v_z \rangle|_{z_\mathrm{wb}} \ , \tag{5.10}$$

and the cumulative wind mass loss rate that integrates $\partial_{\ln R}\dot{M}$ over logarithmic radius from $R = r_\mathrm{in}$.

Similar to B17, we use the following quantities that would be conserved along magnetic field lines in steady winds in the ideal MHD regime,

$$\begin{aligned} &k \equiv \frac{4\pi\rho v_\mathrm{p}}{B_\mathrm{p}} \, , \quad \omega \equiv \frac{v_\phi}{R} - \frac{kB_\phi}{4\pi\rho R} \, , \quad l \equiv v_\phi R - \frac{RB_\phi}{k} \, ; \\ &k_0 \equiv \frac{4\pi\rho_\mathrm{mid} v_\mathrm{K}}{B_{z0}} \ , \quad \omega_0 \equiv \Omega_\mathrm{K}(R_\mathrm{wb}) \ , \quad l_0 \equiv \Omega_\mathrm{K}(R_\mathrm{wb}) R_\mathrm{wb}^2 \ . \end{aligned} \tag{5.11}$$

Here subscripts "p" denote the "poloidal components", v_K is the Keplerian speed, and R_wb is the cylindrical radius of the wind base along the same field line. k, ω and l stand for poloidal mass flux per magnetic flux, angular velocity of magnetic flux surface, and specific angular momentum. k_0, ω_0 and l_0 are their corresponding normalizations, respectively.

Wind versus accretion: Angular momentum transfer

In order to analyze mass loading and angular momentum transfer along field lines, poloidal Alfven radius R_A is defined as the cylindrical radius of the point along the field line where the poloidal velocity v_p equals the poloidal Alfven velocity $v_\mathrm{A,p} \equiv B_\mathrm{p}/(4\pi\rho)^{1/2}$. At R_A, steady state accretion rate and mass flow rate are related by (e.g. Ferreira & Pelletier, 1995b; Bai et al., 2016)

$$\xi \equiv \left(\frac{1}{\dot{M}_\mathrm{acc}}\right)\left(\frac{\mathrm{d}\dot{M}_\mathrm{wind}}{\mathrm{d}\ln R}\right) = \frac{1}{2}\frac{1}{(R_\mathrm{A}/R_\mathrm{wb})^2 - 1} \ , \tag{5.12}$$

where $R_{\rm wb}$ denotes cylindrical radius of the point where the fluid originates from. The quantity $(R_{\rm A}/R_{\rm wb})^2$ is referred to as the magnetic lever arm ratio, and ξ is usually called the "ejection index".

Transport of angular momentum is mediated by magnetic stresses in steady states, which can be further decomposed into two components,

$$\frac{\dot{M}_{\rm acc} v_{\rm K}}{4\pi} = \frac{\partial}{\partial R}\left(R^2 \int_{-z_{\rm wb}}^{z_{\rm wb}} {\rm d}z \ \langle T_{R\phi}\rangle_{t,\phi} \right) + R^2 \langle T_{z\phi}\rangle_{t,\phi}\Big|_{-z_{\rm wb}}^{z_{\rm wb}} \ . \tag{5.13}$$

Here $\dot{M}_{\rm acc} \equiv -2\pi R \int_{-z_{\rm wb}}^{z_{\rm wb}} {\rm d}z \ \rho v_R$ is the radial accretion rate at radius R, $T_{ij} \equiv -B_i B_j/(4\pi)$ are components of the Maxwell stress tensor (not to be confused with gas temperature), and angle brackets stand for time and azimuthal averaging. Eq. (5.13) assumes that azimuthal velocities are close to local Keplerian speed. The first term in eq. (5.13) resembles a viscosity, which represents the radial component of angular momentum transport, which can be characterized by the classic dimensionless α parameter (Shakura & Sunyaev, 1973),

$$\alpha \equiv \left[\int_{-z_{\rm wb}}^{z_{\rm wb}} {\rm d}z \ p \right]^{-1} \times \int_{-z_{\rm wb}}^{z_{\rm wb}} {\rm d}z \ \langle T_{R\phi}\rangle \ . \tag{5.14}$$

The second term in eq. (5.13) represents the vertical component of angular momentum transfer. Comparison of these two terms reveals which type of angular momentum transport mechanism dominates in the disk.

5.2 Fiducial Model Setup

5.2.1 Geometries of the Simulation Domain

The simulation domain has axisymmetry, spanning the radial range $(r/{\rm AU}) \in [1, 100]$ and colatitude range $\theta \in [0.035, \pi/2]$; all dependence on ϕ is ignored. Reflective symmetry about the equatorial plane is imposed; all global quantities (e.g. wind mass loss rate, accretion rate) include the contribution of $\theta > \pi/2$ regime. The standard resolution is 384 radial by 128 latitudinal. The radial zones are spaced logarithmically. The latitudinal zones have grid spacing $\Delta\theta$ decreasing by a constant factor from pole to mid-plane, so that $\Delta\theta$ at mid-plane is 1/6 as zones near the pole. As the mid-plane scale height is roughly $h_{\rm mid} \sim 0.05 - 0.10R$, such grid geometry gives $20 - 25$ latitudinal zones per $h_{\rm mid}$ at the disk mid-plane.

5.2.2 Central Protostar and Radiation Sources

The gravitational field is provided by a 1 $M_\odot$ point source located at the origin. Radiation source is co-centered at the origin and radiate rays isotropically into the simulation domain. In order to appropriately approximate attenuation of radiation from the source so that the mid-plane region is not irradiated near the inner boundary, we adopt a "pre-absorption" recipes that is elaborated in Appendix 5.A.3. This

recipes will help us avoid instabilities caused by unphysical high ionization rate due to unattenuated rays reaching the mid-plane near the inner boundary. Note that, for the fiducial model, the EUV bin is *turned off*, for a better comparison to B17. The number of photons radiated in soft FUV and LW FUV bands per unit time follows a 9000 K black body spectral profile in the photon energy range 6 eV $< h\nu <$ 13.6 eV, with total luminosity $L_{\rm FUV} = 10^{31.7}$ erg s^{-1} (see also Gorti & Hollenbach 2009). The X-ray luminosity is $L_X = 10^{30}$ erg s^{-1}, mathcing B17 but approximately half of the value in Chapter 3.

5.2.3 Initial and Boundary Conditions

The initial disk density and temperature profiles are set using the steady state solution in Nelson et al. (2013): we set the mid-plane density as $\rho = 2.38 \times 10^{14}\ m_p\ {\rm cm}^{-3}\ (R/{\rm AU})^{-\alpha}$ and temperature $T = 280\ {\rm K}\ (R/{\rm AU})^{-q_T}$, with the negative radial power indices $\alpha = 2.25$ (not to be confused with the Shakura-Sunyaev α in eq. 5.14) for density and $q_T = 0.5$ for temperature (note that, at the mid-plane, such initial temperature profile is identical to the prescribed dust temperature profile). The disk mass is $\simeq 0.033\ M_\odot$ within 50 AU. Such hydrodynamic initial conditions generally follow B17; compared to , this disk has $\sim 1.5\times$ scale height near the mid-plane.

The initial abundances of chemicals are set according to Table 6.1 ($n_{\rm H}$ is the number density of hydrogen nuclei). The abundances of elements generally follow a subset of those in Gorti & Hollenbach (2009), with the additional assumption that elements appear in chemical compounds if possible. These initial abundances are uniform throughout the whole simulation domain before any thermochemical evolution applies.

These initial poloidal fields are described by a vector potential $\mathbf{A} \equiv A_\phi \hat{\phi}$ ($\hat{\phi}$ is the unit vector along azimuthal coordinates), and A_ϕ reads (Zanni et al., 2007a),

$$A_\phi = \frac{B_0 r_0}{4 - \alpha - q_T} \left(\frac{R}{r_0}\right)^{1-\frac{\alpha+q_T}{2}} \left[1 + (m \tan\theta)^{-2}\right]^{-5/2} , \tag{5.15}$$

where α and q_T are the negative mid-plane power indices for density and temperature, r_0 is some reference radius (we use $r_0 = 1$ AU), B_0 is the field intensity at the equator of r_0, controlled by the plasma β_0. Following B17, we choose $\beta_0 = 10^5$ for the fiducial model, which approximately yields disk accretion rate $\sim 10^{-8}\ M_\odot\ {\rm yr}^{-1}$. Such power-law dependence on R yields mid-plane poloidal field,

$$B_{\rm p}(\theta = \pi/2) = B_0 \left(\frac{R}{r_0}\right)^{-\frac{\alpha+q_T}{2}} , \tag{5.16}$$

which in turn sets β_0 a constant at the equatorial plane for all R. m is the control parameter that describes the bending of these initial poloidal fields; here we choose $m = 1$ (similar to B17, we verified that this m does not affect the outcome of the final quasi-steady state).

The boundary conditions deserves special attention, in order to avoid unphysical results. As the innermost domain of $r < 1$ AU is not included by our simulations, any fluxes (fluid, magnetic) emerging from the inner radial boundary should not affect the simulation domain. Otherwise, the standard outflow boundary conditions could violate causality and make the system unstable. We therefore adopt boundary conditions similar to B17, so that the impact on the main simulation domain is minimized. Within the "ghost zones" for the inner boundary, the density and velocity are set according to the steady state solution used for the initial conditions, while the gas temperature and relative abundances of chemical species copy the values in the innermost radial zone. The magnetic fields are copied and modified from the innermost radial zone assuming $B_r \propto r^{-2}$, $B_\phi \propto r^{-1}$, and B_θ being unchanged. Inside the simulation domain we also set a radial buffer zone, $r \in [r_{\rm in}, 1.5r_{\rm in}]$, in which the MHD diffusivities are linearly suppressed to zero as the radius decreases to $r_{\rm in}$, and the poloidal velocity is damped at the local orbital timescale. This buffer zone damps disk evolution and hence helps stablizing our simulations near the inner radial boundary. On the outer radial boundary, outflow boundary conditions (with inflow inhibitor) applies to the fluids, while the scheme for magnetic fields is the same as the inner radial boundary. The latitudinal boundaries are reflective.

5.2.4 Simulation Run

Setting up the model along the time axis generally follows B17. We run the simulation for 2000 yr, from $t = -2000$ yr to $t = 0$ with hydrodynamics (MHD disabled), radiation and thermochemistry included, letting the bulk of the disk to fully relax to its hydrodynamic steady state. Instantaneously, at $t = 0$, MHD with non-ideal effects is turned on, and an external poloidal magnetic field described by eq. (5.15) is applied to the system. After that, this model is evolved all the way to $t = 2000$ yr, and is confirmed to reach its quasi-steady state by then.

5.3 Fiducial Model Results

For the fiducial model (Model 0), Figure 5.1 exhibits meridional plots averaging through the final 50 yr (from $t = 1950$ yr to 2000 yr) in the simulation. Black solid curves in the top and bottom row are streamlines of fluids, the integral curves of the poloidal vector field $\rho v_{\rm p}$ spaced by constant wind mass loss rate $10^{-9}\ M_\odot\ {\rm yr}^{-1}$. White solid curves in the bottom row are magnetic field lines spaced by constant poloidal magnetic flux 5×10^{25} G cm^2. Mass fluxes between neighboring stream lines integrate over azimuth and are multiplied by two, to include azimuthal and reflective symmetry (about the equatorial plane) of the computational region. Fluid streamlines are masked out below the wind bases.

We find that for a stream/field line that originates from the disk at cylindrical radius $R_0 > 50$ AU, it may not reach its poloidal Alfvenic point before it leaves the simulation domain at $r = 100$ AU. Furthermore, if we consider that sa part of MHD structures has to evolve at least 5 times dynamical timescale to reach (quasi-)steady

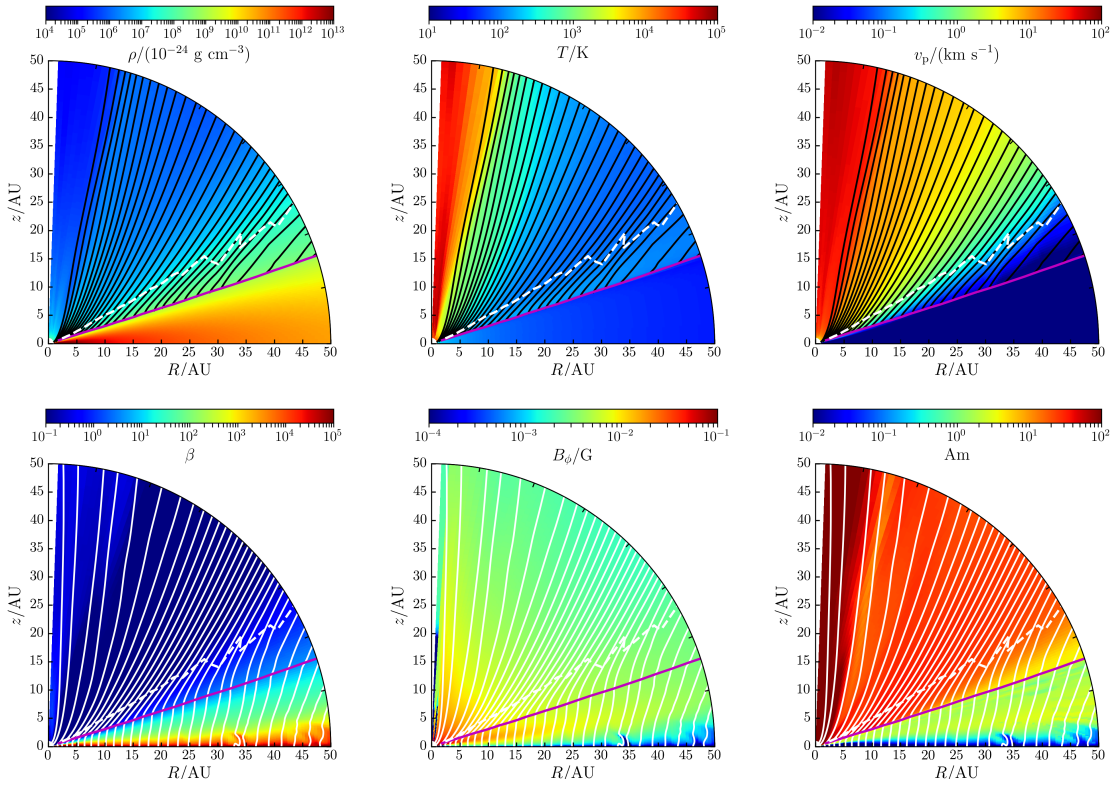


Figure 5.1 Meridional plots for the fiducial model (Model 0; §5.2), showing the innermost 50 AU averaging through the final 50 yr of the simulation. **Top row** presents basic hydrodynamic profiles: left panel: mass density in units of 10^{-24} g cm^{-3}; middle panel: temperature in Kelvin; right panel: poloidal velocity in units of km s^{-1}. **Bottom row** shows MHD-related profiles: left panel: plasma β (dimensionless); middle panel: toroidal magnetic field in units of Gauss; right panel: ambipolar Elsasser number Am (dimensionless). Panels are overlapped by poloidal streamlines separated by 10^{-9} $M_\odot$ yr^{-1} wind mass loss rate (top row, in black solid lines) or poloidal magnetic field lines (bottom row, in white solid lines). In addition, the locations of poloidal Alfvenic points (in white dashed line), and wind bases (in magenta solid line) are overlaid on all panels.

Table 5.1. Properties of the fiducial model

Item	Value
Radial domain	$1 \text{ AU} \leq r \leq 100 \text{ AU}$
Latitudinal domain	$0.035 \leq \theta \leq \pi/2$
Resolution	$N_{\log r} = 384$, $N_\theta = 128$
Stellar mass	$1.0\ M_\odot$
$M_{\rm disk}(1 \text{ AU} \leq r \leq 100 \text{ AU})$	$0.033\ M_\odot$
Initial mid-plane density	$2.38 \times 10^{14} (R/\text{AU})^{-2.25}\ m_p\ \text{cm}^{-3}$
Initial mid-plane plasma β	10^5
Initial mid-plane temperature	$280 (R/\text{AU})^{-0.5}$ K
Artificial heating profile	$280 (R/\text{AU})^{-0.5}$ K
Luminosities [photon s^{-1}]	
7 eV ("soft" FUV)	4.5×10^{42}
12 eV (LW)	1.6×10^{40}
25 eV (EUV)	0
3 keV (X-ray)	2.1×10^{38}
Initial abundances [$n_{\rm X}/n_{\rm H}$]	
H_2	0.5
He	0.1
H_2O	1.8×10^{-4}
CO	1.4×10^{-4}
S	2.8×10^{-5}
SiO	1.7×10^{-6}
Gr	1.0×10^{-7}
Dust/PAH properties	
$r_{\rm dust}$	5 Å
$\rho_{\rm dust}$	$2.25\ \text{g cm}^{-3}$
$m_{\rm dust}/m_{\rm gas}$	7×10^{-5}
$\sigma_{\rm dust}$/H	$8 \times 10^{22}\ \text{cm}^2$

states, we also have to exclude the $r \gtrsim 50$ AU region (where the orbital timescale for the disk is ~ 350 yr), as our simulation is conducted for 2000 yr. Therefore, in what follows, our analyses will only be conducted for $r < 50$ AU regime.

The quasi-steady state has apparent mass outflows, which quickly becomes super-Alfvenic (hence the outflow is a wind, rather than a sub-Alfvenic breeze; in what follows we will use the terms "wind"/"outflow" interchangeably unless specially noted). If we integrate the radial outflow above wind bases at $r = 50$ AU (all streamlines emanating from the inner radial boundary are also excluded), we obtain a total wind mass loss rate of $\dot{M}_{\rm wind} \simeq 2.9 \times 10^{-8}\ M_\odot\ \text{yr}^{-1}$. Mean radial velocity of outflow (weighted by radial mass flux) is $\langle v_r \rangle \simeq 4.6\ \text{km s}^{-1}$. In the mid-plane, radial accretion rate is almost constant along different radius, varying slightly within the rage of $1.3 - 2.1 \times 10^{-8}\ M_\odot\ \text{yr}^{-1}$.

For the same set of data averaging through the final 50 yr, Figure 5.2 displays important MHD profiles along three representative different magnetic field lines that originate from cylindrical radii at the equatorial plane $R_0 = 2$ AU, 10 AU and 30 AU, respectively. Along each field line, the bottom ordinate of each column reads vertical

heights z, and the top ordinate reads cylindrical radii R, both normalized to R_0. Profiles are distinguished by line shape and color, as marked by the legend on the right of each row. In each panel, the vertical dash-dotted, dotted and dashed lines in black indicate the mid-plane scale height ($h_{\rm mid}$), the wind base ($z_{\rm wb}$, defined as the soft FUV front; §5.1.3), and the poloidal Alfvenic point, respectively. The first row presents: gas partial number density n, Elsasser numbers of Ohmic resistance ($\Lambda_{\rm Ohmic}$) and Ambipolar diffusion (Am), and temperature T (T should read the right ordinate). The second row: poloidal (B_p) and toroidal (B_ϕ) components of the magnetic field (normalized to the poloidal field strength at the equatorial plane along the current field line, $B_{\rm mid}$), and poloidal ($v_{\rm p}$) and toroidal (v_ϕ) components of fluid velocity (normalized to the Keplerian velocity at the *local* cylindrical radius, $v_{\rm K} \equiv \sqrt{GM_*/R}$). The third row: gas pressure ($p_{\rm gas}$), magnetic pressure ($p_{\rm mag}$) and (R,ϕ) component of Maxwell stress tensor ($T_{R\phi} \equiv -B_R B_\phi/4\pi$), normalized by $p_{\rm mid} \equiv p_{\rm gas}|_{z=0}$.

Physical processes in these simulation results are discussed in the rest of this section.

5.3.1 Magnetohydrodynamics of Disk and Wind

Wind launching and kinematics

How is the disk wind launched? In contrast to the wind, before applying the poloidal magnetic field at $t = 0$, the fiducial simulation has been run for 2000 yr (§5.2.4), during which no appreciable outflow is observed ($\dot{M}_{\rm wind} < 10^{-11}\ M_\odot\ {\rm yr}^{-1}$)–similar to the model without EUV in Chapter 3. Obviously magnetic fields are crucial to disk wind launching.

Figure 5.3 illustrates the decomposed specific poloidal force along the field line originating from $R_0 = 10$ AU, which we find representative for field lines at all radii. We note that $f_{\rm ine}$ (the net inertial acceleration along field lines) is always negative at different altitudes. In fact, toroidal velocity v_ϕ is always sub-Keplerian in both the bulk disk and the wind (see the second row of Figure 5.2). Magnetic fields with $\beta \gtrsim 10^{-1}$ inside the wind is too weak to overcome gas inertia and enforce co-rotation, which is the key of magnetocentrifugal mechanisms (see also discussions in Bai et al., 2016). Instead, at the wind bases, magnetic pressure gradient starts to take over gas pressure gradient to support the fluids against gravity; the sum of gas and magnetic pressure gradients begins to overwhelm $f_{\rm ine}$, launching the outflow. Such mechanism should be described as "magneto-thermal" within the nomenclature suggested by B17.

Analyzing the energy budget of the wind can also help us confirm the conclusion. Per unit time, within the $1 - 50$ AU effective simulation domain:

- The power carried by outflow, in kinetic energy $\dot{E}_k \simeq 6.4 \times 10^{29}$ erg s^{-1}, and in total energy (including magnetic and gas internal energy) $\dot{E}_{\rm tot} \simeq 9.1 \times 10^{29}$ erg s^{-1}.
- Cooling power: $L_{\rm cool} \simeq 6.2 \times 10^{29}$ erg s^{-1}.

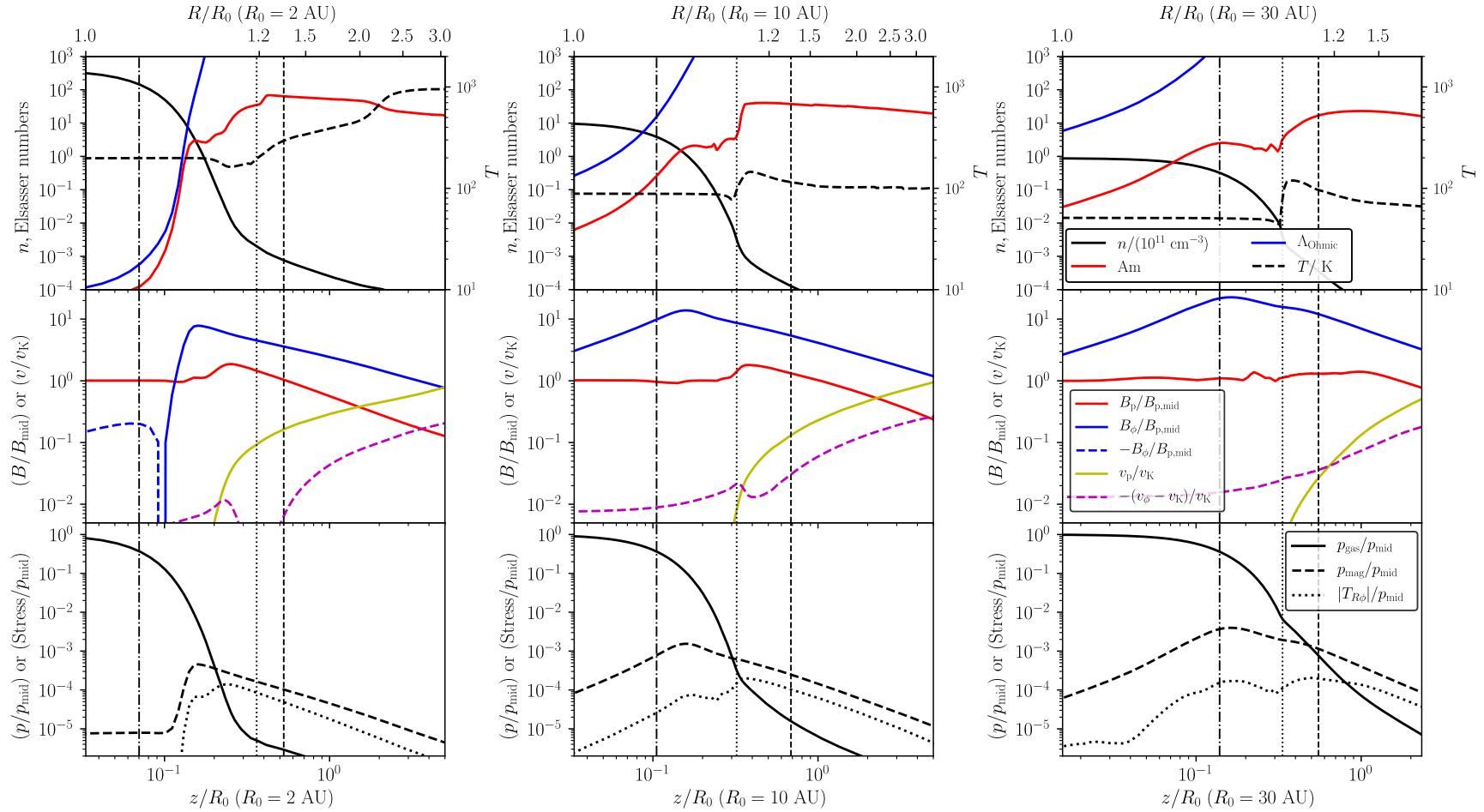


Figure 5.2 MHD profiles of the fiducial model (Model 0), showing the results averaging through the final 50 yr of simulation. The profiles are plotted along three different magnetic field lines, which intercept the equatorial plane at cylindrical radii $R_0 = 3$ AU (left column), $R_0 = 10$ AU (middle column), and $R_0 = 30$ AU (right column), respectively. Detailed descrption of this figure is found in §5.3.

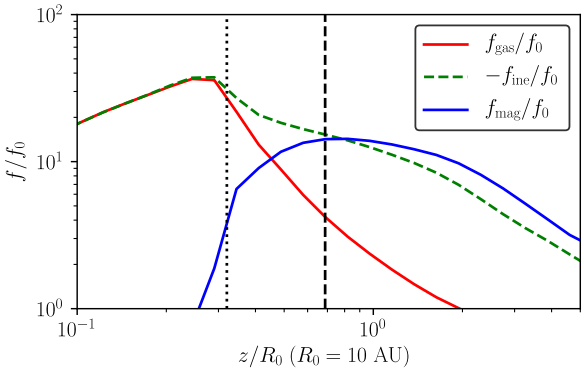


Figure 5.3 For Model 0 (averaged throught the final 50 yr), decomposed poloidal specific forces along the field line anchoring the equatorial plane at $R_0 = 10$ AU, showing the contributions of gas pressure gradient $f_{\rm gas}$, magnetic pressure gradient $f_{\rm mag}$, and net inertial force $f_{\rm ine}$ (see eq. 5.9). All forces are normalized to $f_0 \equiv p_{\rm mid}/(R_0\rho_{\rm mid})$. Vertical dotted and dashed lines in black indicate the locations of wind base and the poloidal Alfvenic point, respectively.

- Luminosity of high energy photon radiated by the central star is $L_{\rm tot} \simeq 5.2 \times 10^{31}$ erg s^{-1}, in which $L_{\rm abs} \simeq 6.0 \times 10^{30}$ erg s^{-1} is actually absorbed. For most populated soft FUV and LW photons, most of the absorbed photon energy is consumed by photodissociation, photoionization and photoelectric processes; less than 10 % of photon energy is eventually thermalized (see also §3.A). The actual radiative heating power by those high energy photons is only $L_{\rm heat} \simeq 2.6 \times 10^{29}$ erg s^{-1}.

- The heating power of non-ideal MHD effects (see also eq. 5.2) is 8.8×10^{29} erg s^{-1}.

Obviously the sum of power consumption by winds and by cooling photons exceeds radiative heating, indicating that the major source of wind energy in Model 0 cannot be high energy radiation–instead, it must directly come from the magnetic field, and eventually from the mechanical (kinetic and gravitational) energy of the bulk disk. We note that the heating power by non-ideal MHD effects is significantly greater than radiation. Pertinent discussions is postponed to §5.3.2.

Above wind bases, toroidal fluid velocities start to appreciably deviate from the local $v_{\rm K}$, and poloidal components becomes important, increasing to $v_{\rm p} \sim 10^{-1} v_{\rm K}$. With Figure 5.4 we examine along the $R_0 = 10$ AU field line, as an representative, for those diagnostic quantities eq. (5.11). Those quantities are mostly but not strictly conserved, illustrating the fact that the wind approximately operates as ideal MHD but still allows non-ideal behaviors (e.g. field lines deviating from fluid streamlines, as is seen in Figure 5.1). We notice that the specific angular momentum l is approximately 1.7 $\Omega_{\rm K}(R_0)R_0^2$: a fluid element on this field line takes only ~ 0.7 times of extra angular momentum away as it flies to infinity, implying that the local wind mass loss rate should be comparable to the accretion rate.

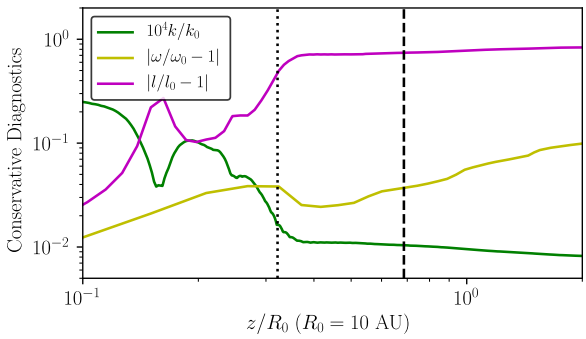


Figure 5.4 Three diagnostic quantities along the field line anchoring the disk at $R_0 = 10$ AU (k, ω and l, with normalizations k_0, ω_0 and l_0; see eq. 5.11) of Model 0 (averaged throught the final 50 yr). Vertical dotted and dashed lines in black indicate the locations of wind base and the poloidal Alfvenic point, respectively.

Magnetic field profiles

The fiducial model presents poloidal fields whose field lines thread through the bulk of the disk in the mid-plane almost vertically. Although the mid-plane diffusivity is not captured very accuratly, such profile is still well-behaved and largely consistent with B17. Above the mid-plane in the wind, stronger field-fluid coupling bends the field lines radially outwards with outflows.

Toroidal component B_ϕ dominates field strengths at almost all radii and altitudes. This component should change sign across the equatorial plane due to physical symmetry. Such flip is in principle guaranteed by the MHD boundary conditions at the equatorial plane. However, because the level of ionization varies with radius in the mid-plane (see also §5.3.2), B_ϕ behaves differently in the mid-plane region, as we can observe from the second row in Figure 5.2. Mid-plane at relatively large radii ($R \gtrsim 3$ AU) has sufficient charge carriers to conduct electric current therein, allowing relatively big vertical gradient of B_ϕ. At small radii ($R \lesssim 2$ AU), abundances of charge carriers are extremely low near the equator, prohibiting large vertical gradient of fields. As a result, $|B_\phi|$ must decrese to rather small magnitudes (during which B_ϕ may already change sign) before the ionization level gets too low at $|z| \lesssim h_{\rm mid}$, then reaches the equator with a rather flat profile. Those behaviors of toroidal fields are qualitatively consistent with B17.

Angular momentum budget and accretion

In Figure 5.5 we relate disk wind to accretion by presenting radial profiles of local and cumulative wind mass loss rate, and compares the accretion rate driven by different angular momentum transport mechanisms (eq. 5.13). Clearly, vertical transport of angular momentum by a magnetized disk wind overwhelms radial transport by a significant factor. We find that local wind mass loss rate is always comparable to accretion rate throughout all radii, as we already discussed in §5.3.1.

Laminar Maxwell stress is also charachterized by the equivalent α (eq. 5.14), which is measured in the simulation as small as $\alpha \lesssim 3 \times 10^{-4}$ throughout the whole

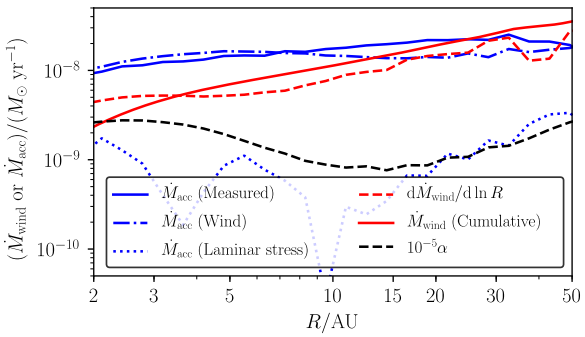


Figure 5.5 Radial profiles of mass dispersal rates of the fiducial model (Model 0; averaged throught the final 50 yr). Accretion rates contributed by wind and laminar Maxwell stress are estimated by eq. (5.13). The radial profile of Shakura-Sunyaev α parameter for radial angular momentum transport (see eq.5.14) is also presented as $10^{-5}\alpha$ for reference.

radial range of simulation. At small radii ($R \lesssim 20$ AU), we find $R_{\rm A}/R_{\rm wb} \simeq 1.4$ and $\xi \simeq 0.5$. Lever arm decreases to $R_{\rm A}/R_{\rm wb} \sim 1.15 \pm 0.02$ at larger radii, corresponding to bigger $\xi \simeq 1$. These ratios are verified by Figure 5.5. These magnetic levers extract angular momentum from the disk and lead to accretion.

Figure 5.6 further exhibits vertical profiles of radial mass flux of two representative cylindrical radii, $R = 2$ AU and 10 AU. Accretion flows center at the mid-plane at $R = 10$ AU. They occur at $|z| \simeq 1.5h_{\rm mid}$ above/below the equatorial plane at $R = 2$ AU, while there are no obvious accretion within the very weakly ionized mid-plane zone. Dashed curves in the figure indicate radial mass flux profiles predicted by taking the vertical gradient of $T_{z\phi}$ stress. These predictions are consistent with with direct measurements of simulation, verifying that vertical transport of angular momentum (and hence wind launching) mediated by the $T_{z\phi}$ stress is indeed the predominant mechanism that drives disk accretion. There is a layer of radial outflow above the accretion layer and below wind bases. This outflow, similar to the accretion inflow, is driven by the $B_\phi B_z$ magnetic stress, but with opposite sign on the vertical gradient. Such outflow is always subsonic and sub-Alfvenic; within the simulation domain, it does not become magnetic dominant, nor does the flow actually join the wind. In order to distinguish it from the wind, we describe this layer as "decretion" in what follows. Total fluid flux in the decretion layer is only $\lesssim 15\%$ of the accretion. This decretion layer is a generic feature that is also present below the wind base in the Hall-free simulations of B17. However, as discussed in B17, the flow structure in wind-driven accretion disks depends on the gradient of B_ϕ, which is sensitive to the diffusivity profiles within the disk. In this work, our diffusivity profile is not necessarily realistic near the mid-plane (§5.1.2), thus we generally do not treat the flow structures near midplane as exact results.

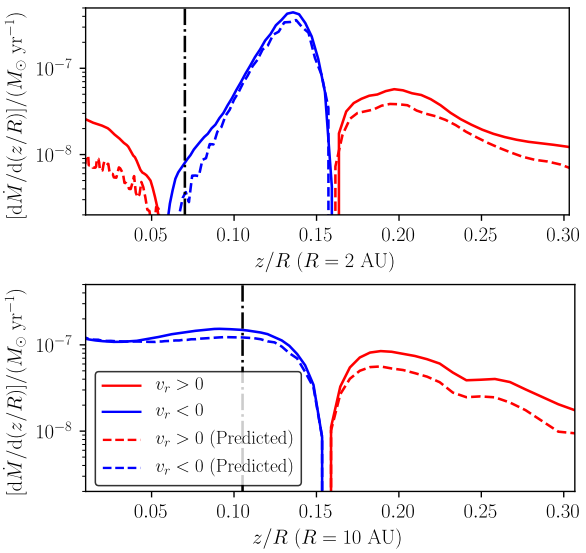


Figure 5.6 Vertical profile of local mass flux [in $M_\odot$ yr^{-1} per (z/R)] at $R = 2$ AU and $R = 10$ AU of Model 0 (averaged throught the final 50 yr), plotted below the wind bases. Blue and red colors indicate accretion and decretion/outflow, respectively. Solid lines are measured directly from the simulation, while dashed curves are values predicted by taking vertical gradients of $T_{z\phi}$ magnetic stress. Vertical dash-dotted line in black indicates the locations of $h_{\rm mid}$, the scale height at the mid-plane.

5.3.2 Thermochemistry and Radiation

The interaction between magnetic fields and fluids is determined by radiation and thermochemical processes. These microphysics is analyzed in this subsection for three different layers: mid-plane (§5.3.2), wind-launching region (§5.3.1), and the wind (§5.3.2). In addition to Figure 5.2, thermodynamic budgets and radiation fluxes along a typical field line originating from $R_0 = 10$ AU are exhibited in Figure 5.7. As a reference, we define the flow timescale of fluids along this field line as,

$$\tau_{\rm flow} \equiv \left| v_{\rm p} \frac{\mathrm{d} \ln \rho}{\mathrm{d}s} \right|^{-1} , \tag{5.17}$$

where the derivate with respect to curve arc length s is taken along the field line. The upper panel of Figure 5.2 clearly shows that $\tau_{\rm flow}$ is always comparable to the heating/cooling timescales at all altitudes: this fact emphasizes the necessity of consistent thermochemical calculations for these MHD simulation of PPD winds.

Mid-plane region

Being unable to be reached by photons directly radiated from the centroid and decoupled from the magnetic field, the mid-plane region is not appreciably affected from photoionization/photodissociation heating or non-ideal MHD heating. Gas temperature here is almost vertically isothermal: this is maintained by heat accommodation

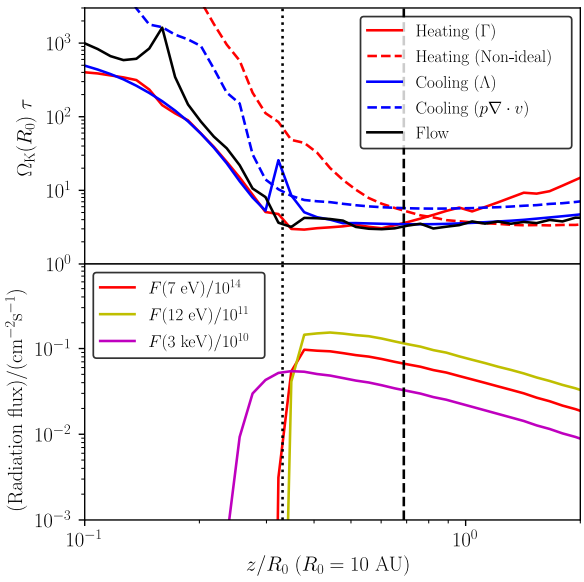


Figure 5.7 For Model 0 (averaged throught the final 50 yr), along the field line anchoring the disk at $R_0 = 10$ AU. **Upper panel**: Heating/cooling timescales, normalized by the Keplerian angular velocity $\Omega_{\rm K}$ at $R_0 = 10$ AU, due to different heating/cooling mechanisms ("Γ" and "Λ" are the heating/cooling terms in eq. 2.17). A black solid line, showing the flow timescale along the current field line (eq. 5.17), is plotted for reference. **Lower panel**: Local radiation flux in (photon cm^{-2} s^{-1}). Vertical dotted and dashed lines in black indicate the locations of wind base and the poloidal Alfvenic point, respectively.

between gas and dust, where the dust temperature is also vertically isothermal within the mid-plane. Dust heat accommodation perfectly offsetting cooling processes, as is shown in Figure 5.7. The charge carriers therein are predominantly positively and negatively charged dusts.

At small radii ($R \lesssim 2$ AU), we observe that ionization is very weak near the equatorial plane: the vertical column above is too massive for diffuse sources of ionization (scattered X-ray photons and cosmic rays) to penetrate. The Elsasser numbers are therefore tiny, Am $\ll \Lambda_{\rm Ohmic} \lesssim 10^{-4}$ at $R = 2$ AU. Eased penetration at relatively larger radii raises the level of ionization, and Elsasser numbers also rise accordingly (at 10 AU, $\Lambda_{\rm Ohmic} \sim 10^0$ and Am $\gtrsim 10^{-2}$ at the equator). Radial variation of ionization also leads to the change of magnetic field morphology, as we discussed in §5.3.1.

Wind-launching region

At higher altitudes, the transition from a poloidally static mid-plane layer to an appreciable outflow takes place near the wind base within a layer with $\sim h_{\rm mid}$ thickness ($3h_{\rm mid} \lesssim z \lesssim 4h_{\rm mid}$).

Density of fluids here is $\sim 10^{-4}$ to 10^{-5} lower, compared to the equatorial plane. Penetration is eased for cosmic ray and scattered X-ray ionization, and especially, for high energy photons directly radiated from the centroid. Thanks to those processes,

the gas temperature raises to ~ 2 times higher than the mid-plane region vertically beneath. Those ionizing photons also yield considerably higher level of ionization. As the absolute abundance of charge increases to $\sim 10^{0\pm1}$ cm^{-3} (relative charge abundance $\sim 10^{-7\pm1}$), the ambipolar Elsasser number Am reaches the order of unity. We find that the dominant charge carriers are S^+ and Si^+, while carbon is almost neutral since photoionization processes of CO and C are more susceptible to cross-/self-shielding effects of ionizing photons, especially by cross-shielding of H_2.

Wind region

The physics is relatively straightforward inside the outflow. Fluids are continued to be accelerated by magnetic pressure gradient all the way through the Alfvenic point. Attenuated gas allows more ionizing photon to get in, hence ambipolar Elsasser number reaches $30 \lesssim \mathrm{Am} \lesssim 10^2$. Such Am still allows some extent of drifts between charged and neutral particles, therefore field lines and streamlines are not perfectly overlapped.

Thermodynamics in the wind is determined by the balance between non-ideal MHD heating (as the leading heating mechanism), and adiabatic expansion (for outflow launched from the inner disk) and/or atomic/molecular cooling (for outflow launched by the outer disk). Radiative heating is relatively ineffective because of tiny interaction cross section of X-ray, excessive cross-shielding of LW, and depetion of susceptible chemical species for soft FUV. At relatively large radii, gas temperature drops slightly as fluids move outwards, since the sum of adiabatic expansion and cooling mechanisms exceeds non-ideal MHD heating (see Figures 5.2, 5.7).

From Figure 5.8 we observe distributions of different chemical species in spaces of configuration, velocity and temperature. We notice a prominent tail of neutral atomic/molecular species inside the wind, located at relatively high temperature ($T \gtrsim 10^3$ K) and intermediate poloidal velocity ($v_\mathrm{p} \sim 15$ km s^{-1}). Note that abundances of those species cannot be correctly calculated if we assume local thermochemical equilibrium instead of evolving thermochemical networks in real-time, as the flow timescale τ_flow (eq. 5.17) is comparable to some reaction timescales. In Table , we present the mass loss rate in different species. The magneto-thermal wind is perdominantly molecular, thanks to inefficiency of FUV and X-ray in photoionization, and to self-/cross-shielding effects of photodissociation/photoionization processes (Appendix 5.A.2). Most of the H_2O/OH molecules, however, are dissociated by soft FUV photons as their photodissociation is not susceptible to shielding.

Carbon-related species indicate the interaction between fluids and LW photons. LW-susceptible CO molecules survive by a significant fraction in the wind. while we also noticed that ionized carbon exists therein. We attribute such co-existence of CO and C^+ to shielding effects: in LW band, CO photodissociation is more sensitive to self-shielding and especially to cross-shielding by H_2, compared to photoionization of CO and C. As a result, although LW photons penetrate deeply near the wind base, CO still exists there.

H_2O and OH molecules are mainly dissociated by the continuum represented by the soft FUV band, hence they are not sensitive to shielding effects and do not

Table 5.2. Mass loss rate in different species for Model 0.

Species	$\dot{M}$ ($M_\odot$ yr^{-1})	$\dot{M}/\dot{M}_{\rm wind}$
H_2	1.91×10^{-8}	6.97×10^{-1}
H	5.64×10^{-10}	2.06×10^{-2}
H^+	2.56×10^{-14}	9.34×10^{-7}
He	7.81×10^{-9}	2.85×10^{-1}
He^+	1.90×10^{-14}	6.93×10^{-7}
H_2O	9.01×10^{-13}	3.29×10^{-5}
OH	2.21×10^{-12}	8.07×10^{-5}
CO	5.38×10^{-11}	1.96×10^{-3}
O	6.67×10^{-11}	2.43×10^{-3}
O^+	7.80×10^{-17}	2.84×10^{-9}
C	9.02×10^{-12}	3.29×10^{-4}
C^+	7.00×10^{-13}	2.55×10^{-5}
S	1.07×10^{-11}	3.89×10^{-4}
S^+	6.84×10^{-12}	2.49×10^{-4}

survive by a appreciable fraction in the wind. Instead, oxygen exist mostly in neutral atoms, characterizing the typical wind poloidal velocity (~ 15 km s^{-1}). It is worth noting that, at high latitudes, proper temperature ($T \sim 10^3$ K) and density ($n \sim 10^{6-7}$ cm^{-3}) result in re-formation rates of H_2O and OH that could be important compared to photodissociation rates (perdominantly by soft FUV). For example, at $r = 5$ AU inside the wind in our fiducial model, the major destruction mechanism of OH molecules is photodissociation by soft FUV photons, whose rate per OH molecule is $\xi \simeq 3 \times 10^{-5}$ s^{-1} (absorption ignored). If, at some latitude at $r = 5$ AU, the temperature is $T \simeq 10^3$ K and the number density of H_2 is $n(H_2) \simeq 10^7$ cm^{-3}, the rate at which an oxygen atom re-forms OH is approximately (according to the `UMIST` database; see McElroy et al. 2013) 3×10^{-6} s^{-1}, via the most important reaction channel of OH re-formation, $O + H_2 \rightarrow OH + H$. As a result, ~ 10 % of oxygen there will stay in OH molecules. As such conditions of re-formation is usually satisfied at the top of winds, those H_2O/OH molecules mainly appear at very high latitudes and intermediate radial velocity ($v_r \sim 10 - 40$ km s^{-1}). Distribution of these molecules could be checked observationally and used as constraints on wind models.

5.4 Parameter Study

To explore the effects of our input parameters and more physical possibilities, a number of additional simulations are conducted, each modifying one parameter based on the fiducial model. These simulations are described in §5.4.1, and summarized by Table 5.3 (also lists wind mass loss rate of each model).

5.4.1 Setup of Models

Models 0^- test the convergence of our simulations, repeating the fiducial run on a 192×64 grid, i.e. 2 times coarser in both latitudinal and radial zones. Another

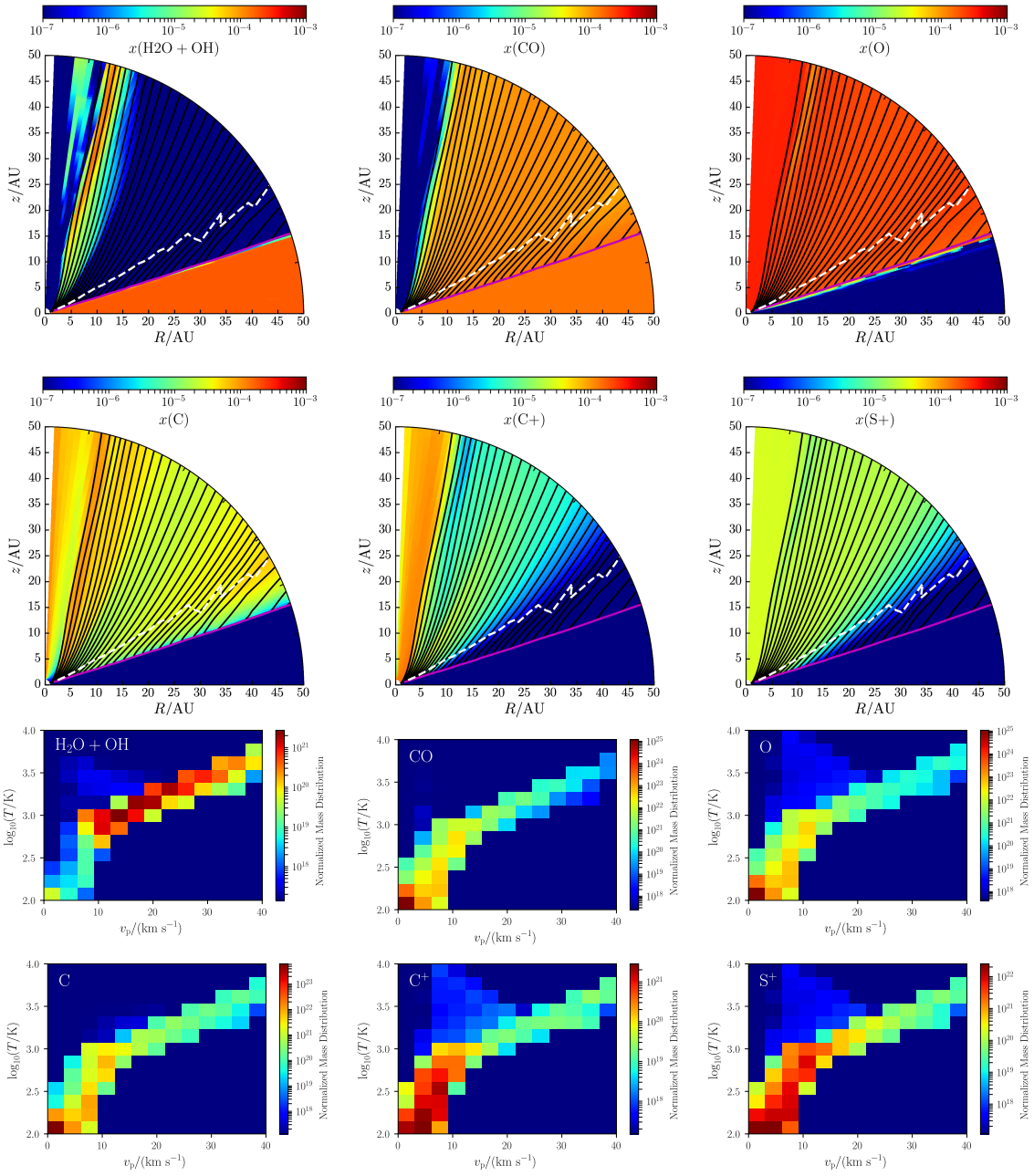


Figure 5.8 In Model 0 (averaged throught the final 50 yr), distribution of key species: H_2O/OH, CO, O (atomic oxygen), C (atomic carbon), C^+ (ionized carbon), and S^+ (ionized sulfur). Top two rows show their spatial distribution, while bottom two row presents their distribution funtions in the two-dimensional space subtended by poloidal velocity magnitude v_p and logarithm of temperature $\log_{10}(T/\mathrm{K})$. The mass distribution function is normalized as $\mathrm{d}^2m/[\mathrm{d}\log_{10}(T/\mathrm{K})\mathrm{d}(v_\mathrm{p}/\mathrm{km\ s^{-1}})]$, i.e. mass of the species (in g) per dex-temperature per $(v_\mathrm{p}/\mathrm{km\ s^{-1}})$. Stream lines, wind bases and Alfvenic surfaces are indicated in the top two rows in the same way as Figure 5.1.

Table 5.3. Various models for parameter study

Model	$\dot{M}_{\rm acc}$(10 AU) ($10^{-8}\ M_\odot$/yr)	$\dot{M}_{\rm wind}$ ($10^{-8}\ M_\odot$/yr)	$\langle v_r \rangle$ (km s^{-1})
(1)	(2)	(3)	(4)
0 (Fiducial)	1.7 ± 0.3	2.9 ± 0.2	4.6 ± 0.4
0^- (Convergence test)	1.9 ± 0.5	2.7 ± 0.4	4.0 ± 0.3
0^γ ($\gamma = 1.4$)	1.3 ± 0.3	2.7 ± 0.2	4.4 ± 0.6
1 (Non-ideal heating off)	1.7 ± 0.3	2.8 ± 0.3	4.7 ± 0.3
2 (0.1× X-ray)	1.2 ± 0.4	2.7 ± 0.3	6.0 ± 0.3
3 (0.1× Soft FUV	1.7 ± 0.4	2.4 ± 0.3	5.5 ± 0.7
4 (0.1× LW)	1.6 ± 0.3	2.6 ± 0.2	5.0 ± 0.5
5 ($\Phi_{\rm EUV} = 10^{40.7}$ s^{-1})	1.5 ± 0.4	1.6 ± 0.1	8.5 ± 0.6
6 ($\beta_0 = 10^4$)	17.1 ± 1.5	16.6 ± 3.3	6.7 ± 0.7
7 (0.1× Dust grains*)	7.4 ± 0.8	5.1 ± 1.5	3.4 ± 4.5

Note. — (1) Model identifier and description (parameter by which model differs from fiducial). (2) Accretion rate measured at $R = 10$ AU. (3) Wind mass-loss rate. (4) Mean outflow velocity (weighted by mass flux). Statistics are conducted through the final 50 yr of simulations. Errors estimate time variation by 2× standard deviation.
∗: The model exhibits instabilities; see §5.4.6

test involves the variation of adiabatic index γ; in Model 0^γ, we simulate the fiducial model specifically with $\gamma = 1.4$.

Our analyses in §5.3.2 shows that heating by non-ideal MHD effects could be important in at least some regions of the wind-launching system. By shutting down all heating by non-ideal MHD effects (with applied electric field eq. 5.2), Model 1 further studies this impact by turning off such heating process while keeping the rest of simulation identical to fiducial.

According to Chapter 3, the SED of high energy radiation is substantial in shaping photoevaporative outflows in absence of magnetic fields. One major concern here is how different bands of radiation are going to affect the MHD outflows. Specifically, the fiducial model totally shuts down EUV radiation for comparison with B17, which may not be realistic as EUV may still reach the top of the MHD outflows. Models 2 through 5 will try to examine the importance of radiation, especially EUV, by varying the luminosities in each energy band.

Magnetic field plays a central role in transporting angular momentum and hence disk dispersal. Model 6 examines the impact of increased magnetization by setting mid-plane plasma $\beta_0 = 10^4$.

Models 7 emphasizes the abundance of dust grains. According to Geers et al. (2006); Tielens (2008); Woitke et al. (2016), the PAH abundance is roughly 4 times the ISM standard in Chapter 3 and also here. Arguments in Geers et al. (2006); Tielens (2008); Woitke et al. (2016) suggest that our PAH abundance is roughly 4 to 10 times the ISM standard. Although we use PAH as a proxy for all dust grains, this uncertainty is still covered by Model 7, reducing the abundance of PAH by a factor of 10.

5.4.2 Verification of the Fiducial Model

Model 0^- shows almost identical MHD profiles and consistent wind mass loss rates to fiducial, which successfully verifies the convergence of our model. This result is consistent with our knowledge towards the system, that such wind-launching accretion process is dominated by angular momentum transfer mediated by magenetic fields.

According to Bai et al. (2016), wind mass loss rates should be relatively insensitive to the adiabatic index. Similar comparison applies to this work: with different adiabatic index $\gamma = 1.4$, Model 0^γ confirms our conjecture that the uncertainty in adiabatic γ index does not substantially affect the wind structure and mass loss rate. There are still caveats regarding complicated interactions between the thermodynamics affected by γ and MHD. For example, accretion inside the disk decreases by $\sim 20\%$ in Model 0^γ. Fully detailed and consistent treatment of this issue goes beyond the scope of this paper and is left to future works.

5.4.3 Heating, ionization, diffusivity and dynamics

Multiple microphysics may affect MHD wind in multiple subtle ways. Qualitative behaviors in Models 1 through 4 do not show appreciable difference from fiducial; they only yield different wind mass loss rates.

Model 1 keeps the whole wind launching system almost intact by turning off heting from non-ideal MHD effects; quantitative results are almost identical to fiducial within their errorbars. This is naturally explained by Figure 5.7: non-ideal MHD heating is important in the wind only at relatively high altitudes, where the wind is already super-Alfvenic. At high latitudes in the wind ($0.3 \lesssim \theta \lesssim 0.6$), nevertheless, absence of non-ideal MHD heating lowers the gas temperature to $T \sim 300$ K, compared to $T \sim 10^3$ K in the fiducial model. Garcia et al. (2001) suggested that ambipolar heating might be important in PPD wind structures, while our models show that, at least in the parameter space that interest us in mangeto-thermal wind scenario, such heating is important in thermodynamics of the gas, rather than dynamics of the wind.

Models 2 through 4, with reduced luminosity in different photon energy bands, have $\sim 10 - 20\%$ lower wind mass loss rates than the fiducial model. Interestingly, Model 2 has $\sim 30\%$ smaller accretion rate ($1.2 \times 10^{-8}\ M_\odot\ \mathrm{yr}^{-1}$ at $R = 10$ AU), while Models 3 and 4 have accretion rates mostly the same as Model 0 ($1.7 \times 10^{-8}\ M_\odot\ \mathrm{yr}^{-1}$ at $R = 10$ AU, see Table 5.3).

What is the underlying reason of decreased mass loss rate? The winds are launched by the combination of thermal and magnetic pressure gradients (see Figure 5.3), thus one can reduce wind mass loss by two mechanisms. We illustrate our arguments below with Figure 5.9.

The first factor is fluid-field coupling being reduced. This mechanism applies to all three models, but especially to Model 2. The top panel of Figure 5.9 shows that X-ray mainly contribute to ionization of $z \lesssim z_{\rm wb}$ (due to reduced ionization rate of diffuse X-ray photons): in Model 2, Am below the wind base is reduced by $\sim 2 - 3$ times. Weaker field-fuild coupling generates weaker toroidal fields as disk rotates due

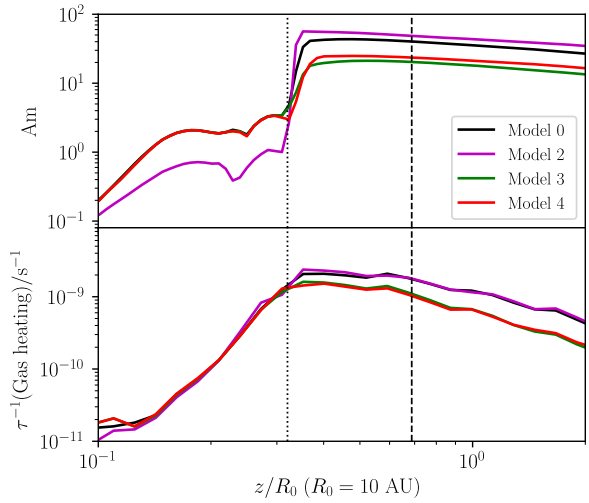


Figure 5.9 Ambipolar Elsasser number (top panel) and inverse of heating times scale (bottom panel) of Models 0, 2, 3, 4, plotted along the field lines anchoring the equatorial plane at $R_0 = 10$ AU in each model. Vertical dotted and dashed lines in black indicate the locations of wind base and the poloidal Alfvenic point of Model 0, respectively.

to increased dissipation. In the accretion layer at $R = 10$ AU, $|B_\phi|$ of Model 2 is typically $\sim 15-20$ % smaller than Model 0. With weaker $B_\phi B_z$ stress, less accretion is driven. As a result, reducing X-ray luminosity allows less wind mass loss because of angular momentum conservation.

The second is reducing heating during wind launching. Along field lines originating at $R_0 = 10$ AU between wind base and Alfvenic point, heating timescales by photons of Models 3 and 4 are $\sim 1.5-3$ times longer compared to the fiducial model. These effects generally raise wind bases to regions with higher altitudes and hence lower density, which enhances the magnetic lever arm (see also discussions in Bai et al., 2016). These models have relatively bigger lever arm ratio than fiducial at relatively large radii (e.g. at $R_{\rm wb} = 30$ AU, $R_{\rm A}/R_{\rm wb} \simeq 1.2$ for Models 3 and 4, compared to $R_{\rm A}/R_{\rm wb} \sim 1.12$ for fiducial) at relatively small radii ($R \lesssim 8$ AU), allowing them to drive the same accretion rate with lower wind mass loss rate.

5.4.4 EUV Hybrid Wind

Behavior of EUV photons is different from FUV and X-ray: they interact with hydrogen and helium, and hence can only penetrate a radial column of $\sim 10^{18}$ cm^{-2} $\sim 10^5$ cm$^{-3}\times 10$ AU, depositing their energy very efficiently at rather low radial columns. With the impact of EUV, Models 5 shows interesting fluid structures, compared to the fiducial model. The mid-plane is still unreachable and remains the same as Model 0, and the wind is still launched by magnetic pressure gradient of toroidal fields. Inside the magnetized wind, however, EUV photons could inject their energy at higher altitudes and change the wind structures substantially.

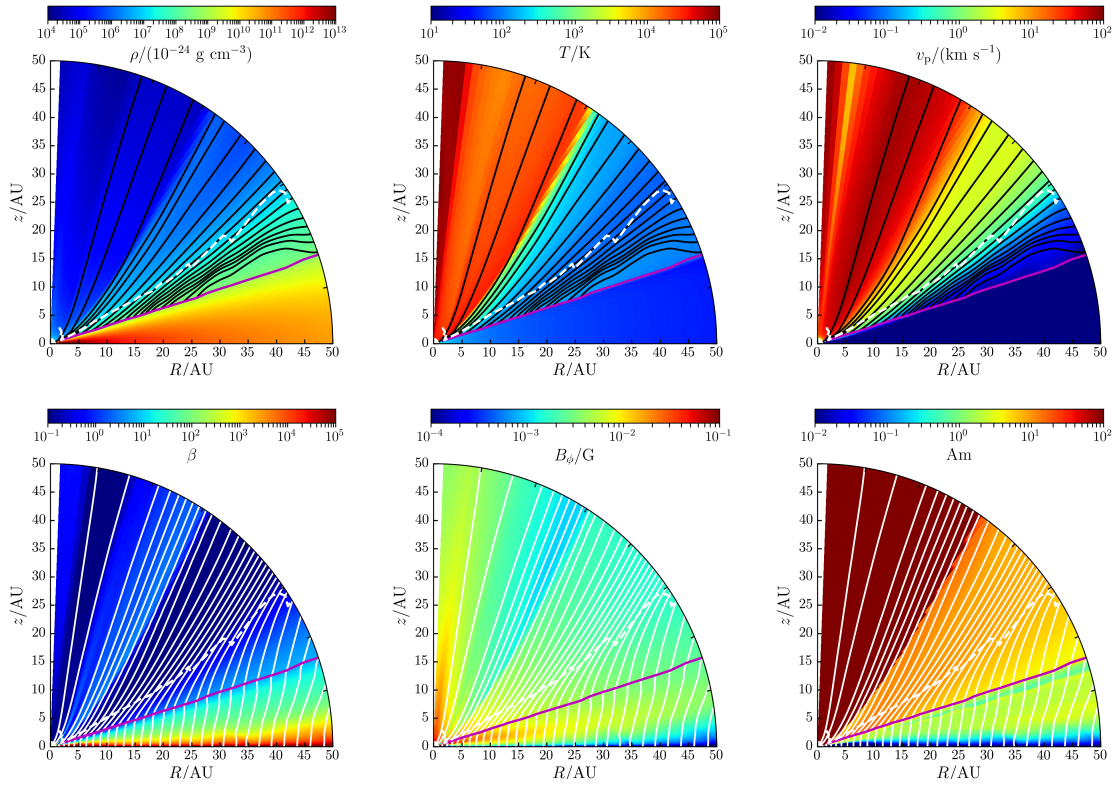


Figure 5.10 Same as Figure 5.1, but plotted for Model 5.

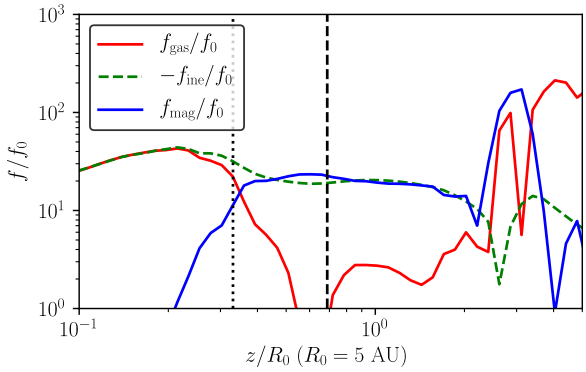


Figure 5.11 Decomposition of force along the field line emanating from $R_0 = 5$ AU, for Model 5 (averaged throught the final 50 yr). Denotations of lines are the same as Figure 5.3.

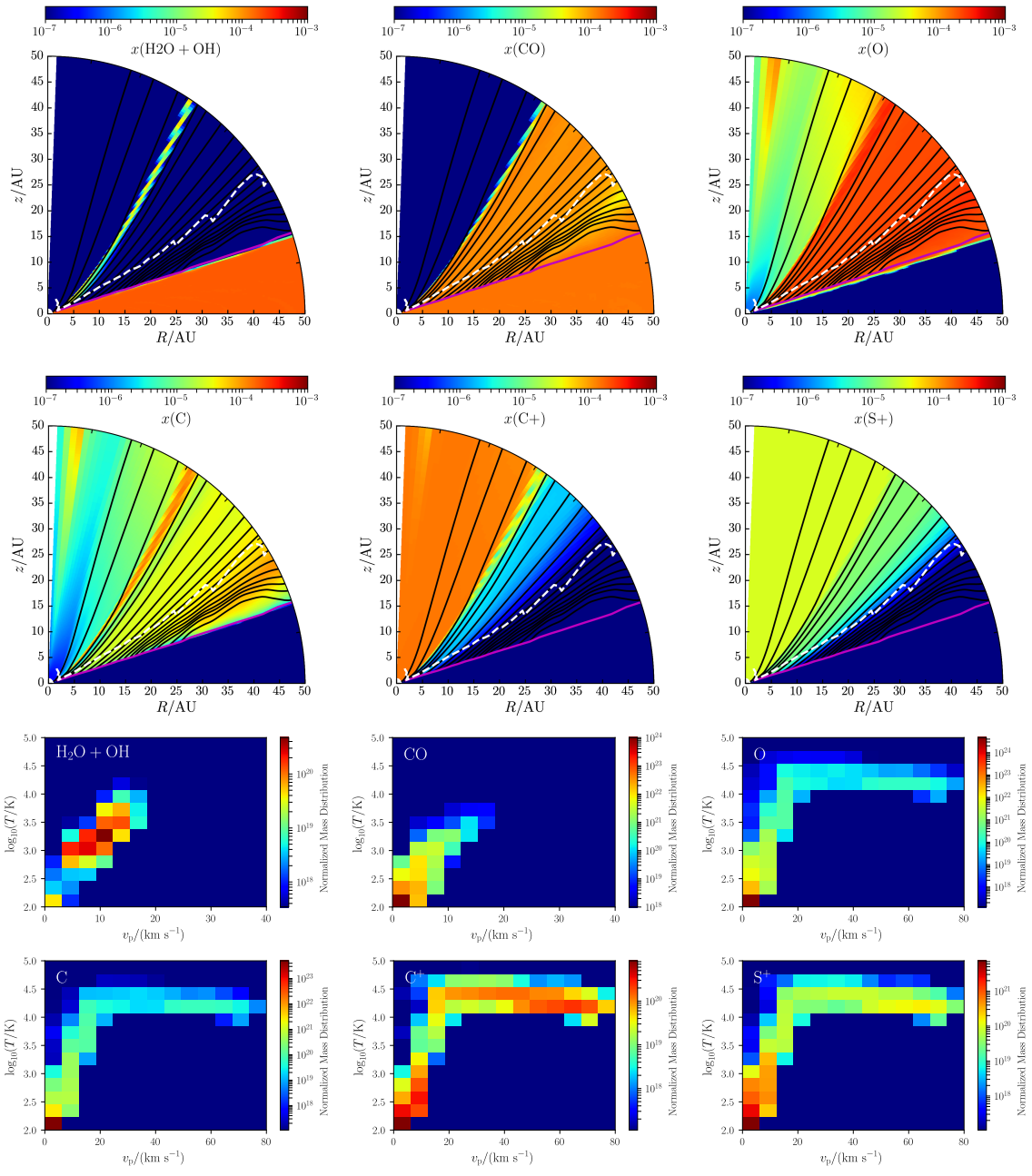


Figure 5.12 Same as Figure 5.8 but for Model 5. Note that the ranges of distribution in temperature and velocity are different.

We present meridional plots of its characteristic profiles in Figure 5.10. The most prominent feature is that the outflow is the hybrid of two components. Above the magneto-thermal wind layer that is qualitatively similar to non-EUV models, there is a fast EUV wind layer, where gas temperature raises to $T \sim 2 \times 10^4$ K and poloidal velocities reaches $v_{\rm p} \sim 40-80$ km s^{-1}. This fast wind "stoles" $\sim 0.26 \times 10^{-8}\ M_\odot$ yr^{-1} from the magneto-thermal wind beneath.

Figure 5.11 illustrates the force decomposition along the field line emanating from $R_0 = 5$ AU, in which we can easily recognize the EUV wind base at $z/R_0 \simeq 4$. The contribution of magnetic pressure gradient $f_{\rm gas}$ and gas pressure gradient $f_{\rm mag}$ are comparable in launching this wind. Obviously $f_{\rm gas}$ is directly yielded by EUV heating. In the mean time, the fast wind advects magnetic field away rapidly, causing an abrupt decrease in magnetic field strength (see also lower-middle panel of Figure 5.10) and thus creating significant $f_{\rm mag}$.

The energy balance of Model 5 is also qualitatively different from the fiducial. The power of radiation heating and cooling reads respectively $L_{\rm heat} \simeq 2.9 \times 10^{30}$ erg s^{-1}, and $L_{\rm cool} \simeq 1.7 \times 10^{30}$ erg s^{-1}. In the mean time, non-ideal MHD heating becomes relatively unimportant, only 4.6×10^{29} erg s^{-1}. Thanks to significant wind acceleration by EUV, the kinetic power carried by wind is much higher than fiducial, increases to $\dot{E}_k \simeq 2.3 \times 10^{30}$ erg s^{-1}, and the total energy power also raises to $\dot{E}_{\rm tot} \simeq 3.1 \times 10^{30}$ erg s^{-1}. Contribution by radiation turns to be much more prominent, though, in the energy budget, magnetic energy still takes a substantial share.

Launching of the fast EUV wind exerts vertical pressure on gas below the EUV front, as we can recover from the plasma β profile. This pressure in turn makes the magneto-thermal outflow denser than the fiducial case by a about one order of magnitude. Higher densities lead to higher rates of recombination and more absorption to ionizing photons, resulting in poorer field-fluid coupling (indicated by smaller Am) and reduced heating near wind bases. Similar to our discussions in §5.4.3, these cause the decline in wind mass loss rates, and even lower wind speed: $v_{\rm p} \simeq 1$ km s^{-1} in this layer.

Table 5.4, compared to its counterpart for Model 0 (Table 5.2), clearly illustrates that the EUV-dominated layer contributes a perdominantly ionized flux to the total outflow. Inspecting Figure 5.12, the distribution functions on the $\{\log_{10} T\} \times \{v_{\rm p}\}$ plane of CO and H_2O/OH molecules are similar to the fiducial model on the lower-left (low temperature, low $v_{\rm p}$). Spatial location of H_2O/OH molecules has lower altitudes than fiducial; proper condition of sufficient H_2O/OH re-formation against photodissociation (see also discussions in §5.3.2) is satisfied in a thin layer dividing magnetic-thermal wind and hot EUV wind. EUV ionization eliminates these molecules in the EUV-dominated hot wind, where the temperature reaches $T \gtrsim 10^4$ K and poloidal velocity $v_{\rm p} \gtrsim 15$ km s^{-1}. Atomic species features much higher velocity and temperature. Figure 5.12 shows that an relatively important amount of neutral O and C atoms still exist within the EUV hot wind layer. In the $\{\log_{10} T\} \times \{v_{\rm p}\}$ space, they present arounc temperature $\sim 10^4$ K and poloidal velocity $v_{\rm p} \gtrsim 40$ km s^{-1}, similar to C^+ and S^+ ions. These relatively high velocity tails prospectively distinguish the EUV models from the fiducial one in terms of observational diagnostics.

Table 5.4. Mass loss rate in different species for Model 5.

Species	$\dot{M}$ ($M_\odot$ yr^{-1})	$\dot{M}/\dot{M}_{\rm wind}$
H_2	1.07×10^{-8}	6.11×10^{-1}
H	5.95×10^{-10}	3.41×10^{-2}
H^+	1.37×10^{-9}	7.83×10^{-2}
He	4.46×10^{-9}	2.56×10^{-1}
He^+	5.48×10^{-10}	3.15×10^{-2}
H_2O	6.15×10^{-15}	3.53×10^{-7}
OH	5.59×10^{-14}	3.21×10^{-6}
CO	2.84×10^{-11}	1.63×10^{-3}
O	4.14×10^{-11}	2.37×10^{-3}
O^+	6.75×10^{-12}	3.87×10^{-4}
C	6.30×10^{-12}	3.62×10^{-4}
C^+	2.55×10^{-12}	1.46×10^{-4}
S	8.41×10^{-12}	4.83×10^{-4}
S^+	2.82×10^{-12}	1.62×10^{-4}

5.4.5 Disk Magnetization

Model 6, with initial β_0, is also qualitatively similar to Model 0, featured by its accretion rate $\sim 10\times$ higher, which is almost proportional to β_0^{-1}: the accretion is mostly driven by magnetic stresses. In the mean time the wind mass loss rate is only $\sim 6\times$ higher. Poloidal wind speed is slightly higher (~ 6.7 km s^{-1}), and the lever arm ratio is $R_a/R_{\rm wb} \sim 1.5$ at all radii, yielding smaller ejection index $\xi \sim 0.5$. The mass density of the wind increases; such increase is yet sufficient prohibit FUV and X-ray from reaching the wind bases as the radial column is $\sim 10^{22}$ cm^{-2} from the centroid (close to $\sim 10^{23}$ cm^{-2} penetration of FUV and X-ray; see Appendix 5.A.3), but X-ray and LW ionization becomes comparably important at wind bases. Toroidal motion in the wind is super-Keplerian in most places, but the net centrifugal force projected onto field lines are still negative.

5.4.6 Dust: Chemistry and MHD Instability

Models 7 is rather special: it do not have a well-defined quasi-steady state; instead, it develops instabilities rather quickly in the simulation run.

Dust grains are crucial factors in the ionization balance of disks, especially near the mid-plane. In general, they assist recombination by adsorbing charged particles. If their abundance is reduced, regions with weaker magnetization become more ionized, which could make the system more vulnerable to MRI. For Model 7, the MRI criteria in eq. (5.8) is satisfied in the layer of accretion. This is illustrated in Figure 5.13, showing the snapshots for $\beta/\beta_{\rm min}$ and magnetic field lines when the instability occurs ($t \sim 60$ yr). Thanks to increased Am, field lines in the accretion layer is better coupled with inward-moving gas, forming "spikes" pointing inward. We further exclude the possibility of shear instabilities by confirming that (r, ϕ) component of magnetic stress

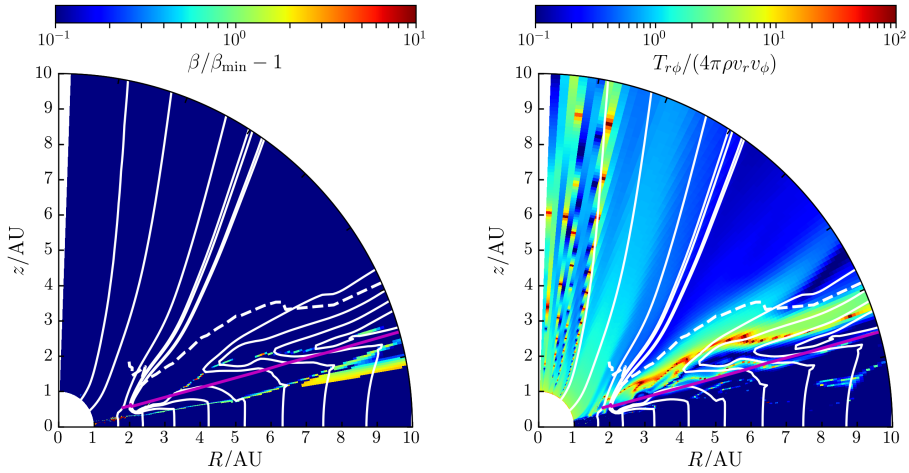


Figure 5.13 Meridional plots of Model 7 for $(\beta/\beta_{\rm min}-1)$ (upper panel, see eq. 5.8) and $|T_{r\phi}/(\rho v_r v_\phi)|$ (lower panel, see eq. 5.18), showing a snapshot immediately after instabilities are developed ($t\sim 60$ yr). Denotations of overlaid lines are identical to Figure 5.1.

overwhelms fluid stress, i.e.

$$\left|\frac{T_{r\phi}}{\rho v_r v_\phi}\right| = \left|\frac{B_\phi B_r}{4\pi\rho v_\phi v_r}\right| \gg 1\ . \tag{5.18}$$

For the unstable Model 7, we find that within the layer of instabilities $|T_{r\phi}/(\rho v_r v_\phi)| \gtrsim 10$ (see also Figure 5.13). In contrast, for Modle 0, such ratio is always smaller than unity. As axisymmetric 2.5-D simulations cannot deal with saturation of MRI properly, however, we choose not to over-trust the results, and simply marking this "unstable".

5.5 Discussions

5.5.1 Comparison with B17

As a key improvement over B17, this work is featured by the introduction of real-time consistent calculations of radiation and thermochemistry. How does these improvements modify the physical pictures of magneto-thermal wind mechanism?

The local mass loss rate here is $\sim 3-8$ times smaller through the range of cylindrical radii concerned, and the integrated mass loss rate through the radial range $1<R/{\rm AU}<20$ is $2.1\times10^{-8}\ M_\odot\ {\rm yr}^{-1}$ versus B17's $7.5\times10^{-8}M_\odot\ {\rm yr}^{-1}$. In the mean time, the accretion rate throught the same radial range is only lower by no more than a factor of 1.5. Angular momentum wind mass loading, reflected by the typical lever arm ratio, becomes the apparent difference. The underlying reason of such difference should thus mainly be attributed to thermodynamics and diffusivity profiles. Near

the wind bases, gas temperature and Am rise more sharply within the prescription of B17 than in this work (see Figures 5.2, 5.9), and shallower gradients will thus deliver less significant outflow.

In addition to wind mass loss rates, there are more observations comparing results herein and those in B17. We compare different components of force along field lines in Figure 5.3, showing that the contribution of gas pressure gradient $f_{\rm gas}$ is greater than magnetic pressure gradient $f_{\rm mag}$ at wind bases, and $f_{\rm gas}$ remains comparable to $f_{\rm mag}$ before the wind becomes super-Alfvenic. B17, in contrast, had $f_{\rm gas}$ making much smaller or even negative contribution to wind launching near wind bases and above. Another interesting comparison involves Model 6 herein and the corresponding model with $\beta_0 = 10^4$ (namely model B40). In B17 the model B40 features FUV front at higher altitudes than the Alfvenic surface; FUV photons are completely shielded from the deep of the wind. Our Model 6, however, still has FUV photons penetrating down to the wind bases. Those deep-penetrating FUV photons are partially the reason that Model 6 has greater wind mass loss rate than Model 0 by a factor of 6, while in B17 the same factor is only 3. This difference emphasizes the necessity of consistent calculation of microphysics in non-ideal MHD simulations.

5.5.2 Comparison with Chapter 3

Even with different disk profile, before applying poloidal field at $t = 0$, our Model 5 exhibits $\dot{M}_{\rm wind} \simeq 2.2 \times 10^{-9}\ M_\odot\ {\rm yr}^{-1}$ mass loss rate in the $1 < (r/{\rm AU}) < 50$ radial range, thanks to EUV radiation. Such $\dot{M}_{\rm wind}$ is comparable to Chapter 3 results in the $2 < (r/{\rm AU}) < 100$ radial range.

In terms of spatial structure in the magnetized steady state, we stil find major similarities in Model 5 to Chapter 3, that the vertical structure can also be described as having three layers: (1) a relatively cold mid-plane that is intact by high energy radiation, (2) a warm ($T \sim 10^2 - 10^3$ K) "intermediate layer", and (3) a hot ($T \sim 10^4$ K), fast ($v_{\rm p} \gtrsim 40$ km s^{-1}) EUV-dominated wind. In fact, if we measure the mass flux only in the fast wind, we obtain a wind mass loss rate ($2.6 \times 10^{-9}\ M_\odot\ {\rm yr}^{-1}$, integrating through $1 - 50$ AU) very similar to the pure hydrodynamic simulation results in Chapter 3 ($2.5 \times 10^{-9}\ M_\odot\ {\rm yr}^{-1}$, integrating through $2 - 100$ AU). Flow structures in the EUV-dominated wind is also similar to Chapter 3, in which gas pressure overwhelms magnetic pressure (plasma $\beta \sim 10$; see Figure 5.10 and 5.11).

Nevertheless, including MHD effects drives the intermediate layer outwards with magneto-thermal mechanism, in contrast to Chapter 3 which had radially static intermediate layers. Gas outflow inside this intermediate layer is approximately $1.4 \times 10^{-8}\ M_\odot\ {\rm yr}^{-1}$, in which the gas is still perdominantly molecular. Therefore, as indicators of this layer, molecules here exhibit higher poloidal velocities than Chapter 3. For example, distribution function of H_2O/OH molecules extend to ~ 15 km s^{-1} poloidal velocity (see Figure 5.12), compared to ~ 10 km s^{-1} maximum (see figure 4 in Chapter 3). Moreover, without MHD, shutting down EUV in Chapter 3 totally eliminates all outflows, in clear contrast to our fiducial model in this work.

In addition, as toroidal fields provide more pressure, the outflowing "intermediate layer" is more inflated than Chapter 3, which gives more solid angle to intercept EUV

photons and provides fast wind with higher initial specific energy. As a result, the FUV outflow has slightly higher velocity and density than Chapter 3.

5.5.3 Implications of Observables

A major advantage of real-time consistent evolution of thermochemical network is that molecular/atomic signals are directly connected to the kinematics and dynamics of disk outflows, revealing the underlying physics of PPD dispersal.

One important possibility is to distinguish PPD outflows driven by MHD effects from photoevaporation. Pure photoevaporative mechanism in Chapter 3 yields molecules whose poloidal motion traces only the thin layer near EUV wind bases, and toroidal motion is almost Keplerian. Magneto-thermal winds, on the other hand, hold major fractions of molecules with prominent poloidal motion. At high altitudes, the molecular winds deviate significantly and systematically from Keplerian. With ALMA data, Flaherty et al. (2018) constrained the amplitude of turbulence inside the disk of TW Hya (which suggested very small upper limit of $\alpha < 0.007$). This result confirms the wind-launching accretion mechanism, and further suggests the capability of spectral and spatial resolution that could help us understand wind kinematics with proper transitions in different species. In addition to accretion mechanism, we expect in the future that similar observations will be conducted to constrain the distribution of molecules at higher temperature inside the wind.

Careful syntheses of molecular spectra, starting from thermochemical environments, kinematics, and proper treatments of radiative transfer of molecular lines, will eventually help us put useful constrains on the dynamics of PPD winds based on the non-ideal MHD models herein.

5.6 Chapter Summary

In summary, this work studies PPD outflows by conducting 2.5-dimensional axisymmetric global simulations, combining non-ideal MHD with consistent ray-tracing radiative transfer and thermochemistry. Focusing on the effects of Ohmic and ambipolar diffusion, we turn off the Hall effect in our simulations, and evaluate diffusivities of the former two by using the results of radiation and thermochemical calculations in real-time. Our fiducial model, whose parameters broadly follows B17, features a warm ($T \sim 10^2 - 10^3$ K), predominantly molecular (except H_2O and OH) magneto-thermal wind, filling most of the coronal latitudes over the top of the cold ($T \lesssim 10^2$ K) midplane, driven by the gradient of toroidal magnetic pressure. Such wind has mostly sub-Keplerian toroidal motion, with typical radial velocity $\langle v_r \rangle \simeq 4.6$ km s^{-1} and mass loss rate $\dot{M}_{\rm wind} \simeq 2.9 \times 10^{-8}\ M_\odot$ yr^{-1}. By varying luminosities of high energy photons in various energy bands, we find that the wind mass loss is directly related to the status of ionization near wind bases, which is in turn affected by high energy (especially soft FUV and Lyman-Werner band) photons that can reach wind bases. Adding EUV photons changes the overall kinematics of the wind, in which a fast ($v_{\rm p} \gtrsim 50$ km s^{-1}), hot ($T \gtrsim 10^4$ K), ionized wind is launched above the warm magneto-thermal wind,

whose wind pressure squeezes the magneto-thermal wind layer, decreases the fraction of ionization therein, and thus lowers the total wind mass loss rate by about a half. Alternating the abundances of dust grains may raise ionization near the wind base and cause instabilities, revealing the fact that structures and dynamics of magneto-thermal winds may well depend sensitively on subtle details of thermochemistry.

Appendix

5.A Additional Details in Radiation and Thermochemistry

This appendix provides the details of some thermochemical and radiation processes. Only major upgrades compared to Chapter 3 are listed.

5.A.1 Ionization by Diffuse High Energy Photons and Radioactive Decay

We follow the recipes in Bai & Goodman (2009), the effective ionization rate by diffuse source of ionization, $\xi^{\rm eff}$, formally reads,

$$\xi^{\rm eff} = \xi^{\rm eff}_{\rm X-ray} + \xi^{\rm eff}_{\rm CR} + \xi^{\rm eff}_{\rm SLR} \ . \tag{5.19}$$

The first term $\xi_{\rm X-ray}$, representing the ionization processes by down-scattered X-ray photons at $h\nu = 3$ keV, is approximately given by the fitting formula based on Igea & Glassgold (1999),

$$\begin{aligned} \xi^{\rm eff}_{\rm X-ray} = & \left(\frac{R}{\rm AU}\right)^{-2.2} \left(\frac{L_{\rm X}}{10^{29}\ {\rm erg\ s^{-1}}}\right)^2 \\ & \times \left\{ \xi_1 \left[{\rm e}^{-(N_{\rm H1}/N_1)^\alpha} + {\rm e}^{-(N_{\rm H2}/N_1)^\alpha} \right] + \xi_2 \left[{\rm e}^{-(N_{\rm H1}/N_2)^\beta} + {\rm e}^{-(N_{\rm H2}/N_2)^\beta} \right] \right\} \ . \end{aligned} \tag{5.20}$$

The first square bracket in the parenthes describes the scattering penetration from the from the closest disk surface, and the second square bracket stands for scattering penetration from the other side. Here $L_{\rm X}$ is the X-ray luminosity (in our simulations, $L_{\rm X}$ is measured by the luminosity in the 3 keV energy band), $N_{\rm H1}$ and $N_{\rm H2}$ are the vertical column densities of hydrogen nucleus measured above and below the point of interest, $\xi_1 = 4.0 \times 10^{-12}$ s^{-1}, $\xi_2 = 2.0 \times 10^{-15}$ s^{-1}, $N_1 = 1.5 \times 10^{21}$ cm^{-2}, $N_2 = 7.0 \times 10^{23}$ cm^{-2}, $\alpha = 0.5$, and $\beta = 0.65$. For the sake of simplicity, instead of doing vertical integration, we use such a simplified estimation of $N_{\rm H\,1,2}$ up to ~ 20

per cent error, assuming that the vertical density profile is Gaussian,

$$N_{\mathrm{H}\,1}(z) = n_{\mathrm{H}}(z) \int_{z}^{+\infty} \mathrm{d}z' \ \mathrm{e}^{(z^2-z'^2)/2h^2} \sim h n_{\mathrm{H}}(z) \ ,$$
$$N_{\mathrm{H}\,2}(z) = n_{\mathrm{H}}(z) \int_{-\infty}^{+\infty} \mathrm{d}z' \ \mathrm{e}^{(z^2-z'^2)/2h^2} - N_{\mathrm{H}\,1}(z) \sim 2.5h \ \mathrm{e}^{z^2/2h^2} n_{\mathrm{H}}(z) - N_{\mathrm{H}\,1}(z) \ , \tag{5.21}$$

where h is the local disk scale height, and n_{H} the local number density of hydrogen nucleus. The cosmic ray term, $\xi_{\mathrm{CR}}^{\mathrm{eff}}$, can be approximated by, using the updated recipes in Umebayashi & Nakano (1981)

$$\xi_{\mathrm{CR}}^{\mathrm{eff}} = 10^{-17} \ \mathrm{s}^{-1} \times \left(\mathrm{e}^{-N_{\mathrm{H1}}/N_{\mathrm{CR}}} + \mathrm{e}^{-N_{\mathrm{H2}}/N_{\mathrm{CR}}} \right) \ , \tag{5.22}$$

where $N_{\mathrm{CR}} = 5.7 \times 10^{25}$ cm^{-2}. The contribution of short-lived radioactive nuclei is presumably a constant, $\xi_{\mathrm{SLR}}^{\mathrm{eff}} = 6.0 \times 10^{-19}$ s^{-1}. The effective ionization rate is distributed onto three channels, effectively,

$$\begin{aligned} \mathrm{H_2} \rightarrow \mathrm{H} + \mathrm{H^+} + e^- \ , \quad \xi = \xi^{\mathrm{eff}} \ ; \\ \mathrm{H} \rightarrow \mathrm{H^+} + e^- \ , \quad \xi = 0.50 \ \xi^{\mathrm{eff}} \ ; \\ \mathrm{He} \rightarrow \mathrm{He^+} + e^- \ , \quad \xi = 0.84 \ \xi^{\mathrm{eff}} \ ; \end{aligned} \tag{5.23}$$

Admittedly those are rather rough estimate, however, the focus of this paper is in the disk atmosphere and wind zone. It is hence acceptable that our chemical network is not accurate for the bulk part of the disk interior with a less accurate estimate of ionization by those diffuse source.

5.A.2 Self-/Cross-Shielding and Absorption of FUV Photons

Some photoreactions, especially those photoionizations and photodissociations by absorption lines (e.g. photoreactions by photons in the LW band), are subject to self-/cross-shielding effects. For the dominant species in the intermediate zone, $\mathrm{H_2}$, we adopt the scheme in Chapter 3, which treats the photo-pumping $\mathrm{H_2} + h\nu(\mathrm{LW}) \rightarrow \mathrm{H_2}^*$ with the self-shielding recipes in Draine & Bertoldi (1996). Such photo-pumping is the starting point of some important subsequent processes, including collisional heating, dissociation, and spontaneous decay. For other species, we adopt the tabulated self-shielding and cross-shielding coefficients (by $\mathrm{H_2}$ and by C if applicable) obtained by Heays et al. (2017) for the photoreactions of the following species: C, CO, S, Si, and SiO.

5.A.3 Pre-absorption of Radiation at the Inner Radial Boundary

As our simulations exclude the central zone, ionizing radiation is not attenuated by the flaring outflow in the $r < r_{\mathrm{in}}$ regime. At low latitudes in the predominantly

neutral outflow near the inner radial boundary, this absence of attenuation could cause unphysical high ratio of ionization, which affects the credibility and even stability of our simulations. We therefore use a "pre-absorption" scheme to account for estimating such attenuation: for each energy bin, the absorption optical depth of a ray at co-latitude θ from the central source to the inner boundary $r_{\rm in}$, $\tau_{\rm in}(h\nu,\theta)$, should be estimated. We assume that the ratio $\tau_{\rm out}(h\nu,\theta)/\tau_{\rm in}(h\nu,\theta)$ ($\tau_{\rm out}(h\nu,\theta)$ is the absorption optical depth from $r_{\rm in}$ to the outer radial boundary at $r_{\rm out}$) equals to $\zeta^{-1}r_{\rm in}/r_{\rm out}$, where ζ is the proportionality coefficient. Based on this assumption we obtain,

$$\tau_{\rm in}(h\nu,\theta) \simeq \zeta\frac{r_{\rm in}}{r_{\rm out}}\tau_{\rm out}(h\nu,\theta)\ ; \quad \tau_{\rm out}(h\nu,\theta) = \ln\left[\frac{F_{\rm in}(h\nu,\theta)}{F_{\rm out}(h\nu,\theta)}\right]\ , \tag{5.24}$$

where $r_{\rm out}$ is the radius of, and $F_{\rm in}(h\nu,\theta)$ and $F_{\rm out}(h\nu,\theta)$ are the photon fluxes of the same ray at $r_{\rm in}$ and $r_{\rm out}$ respectively. $F_{\rm in}$ and $F_{\rm out}$ are measured with the previous step of simulation (for the initial step in simulation, $F_{\rm in}$ and $F_{\rm out}$ are also calculated for each ray specifically). We tested several ζ from 10^{-1} to 10^{1}, confirming that the results of simulations are not sensitive to ζ. For convenience we choose $\zeta = 1$ throughout this work.

Chapter 6

Photoevaporation of Planetary Atmosphere

This chapter discuss the dispersal of planetary atmosphere, with the help of our `Athena++`-based simulation code coupled with thermochemical and radiation. §6.1 presents the static atmosphere model without any irradiation as the initial conditions of our numerical simulations, and discusses the implications of those hydrostatic models. §6.2 presents the setup and results of the fiducial model. In §6.3 we explore and elaborate the effects of different physical parameters. §6.4 discusses the implications and applications of our photoevaporation models. §6.5 concludes and summarizes the chapter. Appendix §6.B provides necessary details about thermochemistry calculations.

6.1 Hydrostatics of Planet Atmosphere

The hydrostatic structures of planet atmospheres are discussed in this section, as the initial condition and inner boundary conditions of our further numerical explorations on photoevaporation. In what follows, we will use the terms "atmosphere" and "envelope" interchangeably.

We start with a solid core as the inner supporter and the source of gravity of the atmosphere. Compared to the host star, the gravity of planets dominates within the Hill radius,

$$r_{\rm H} \simeq a \left(\frac{M_c}{3M_*}\right)^{1/3} \simeq 235 R_\oplus \times \left(\frac{a}{\rm AU}\right) \left(\frac{M_c}{M_\oplus}\right)^{1/3} \left(\frac{M_*}{M_\odot}\right)^{-1/3}, \tag{6.1}$$

where a is the semi-major axis of planet orbit, M_c the planetary core mass, and M_* the hos star mass. Since all phenomena discussed in this chapter take place well within such radii, it is safe to ignore the gravity of host stars and orbital motion of planets.

The mass-radius relation approximately obeys $M_c \propto R_c^4$ (see also Lopez & Fortney, 2014). We adopt the terrestrial mean density at 1 $M_\oplus$, $\rho(M_c = M_\oplus) = 5.5$ g cm^{-3}, unless specially noted. Outside the solid core lies the atmosphere. The atmosphere of

a planet has two segments: an adiabatic, convective interior and an (approximately) isothermal, radiative exterior (e.g. Rafikov, 2006; Owen & Wu, 2016; Ginzburg et al., 2016). Due to incident radiation from the central star at bolometric luminosity L_*, the temperature of the roughly isothermal exterior for a planet at semi-major axis a satisfies,

$$T \simeq T_{\rm eq} = 886 \text{ K } \left(\frac{L_*}{L_\odot}\right)^{1/4} \left(\frac{a}{0.1 \text{ AU}}\right)^{-1/2} . \tag{6.2}$$

Transition from adiabatic to isothermal occurs when eq. (6.2) is equated to the temperature in eq. (6.3), marked by subscript "rcb" (short for "radiative-convective boundary") attached to pertinent physical quantities.

6.1.1 Convective (Adiabatic) Interior

The adiabatic equation of state (EoS) of gas reads $p = K\rho^\gamma$, where p is the gas pressure, ρ the mass density, γ the adiabatic index, and K a constant related to the specific entropy. We neglect the self gravity of the envelope. The temperature and density profiles in the adiabatic layer are given by,

$$\begin{aligned} &T = T_0 \left[1 + \beta_{\rm ad}\left(\frac{R_c}{r} - 1\right)\right] \ ; \ \rho = \rho_0 \left(\frac{T}{T_0}\right)^{1/(\gamma-1)} ; \\ &\beta_{\rm ad} \equiv \nabla_{\rm ad} \left(\frac{GM_c\mu}{R_c k_{\rm B} T_0}\right) \ ; \quad \nabla_{\rm ad} \equiv \left(\frac{\gamma-1}{\gamma}\right) . \end{aligned} \tag{6.3}$$

Here μ is the (dimensional) mean molecular mass, G the gravitational constant, M_c and R_c the mass and radius of the solid core beneath the atmosphere respectively, T_0 and ρ_0 temperature and density at the bottom of adiabatic atmosphere ($r = R_c$) respectively. $\nabla_{\rm ad}$ is the adiabatic gradient, and $\beta_{\rm ad}$ measures gravitational binding energy against gas energy: the adiabatic inner envelope is gravitationally unbounded if $\beta_{\rm ad} \leq 1$, which is not discussed in this chapter.

As the total mass of isothermal layer is ill-defined (and practically small compared to the mass in the adabatic layer; see §6.1.2), we characterize the envelope mass by the mass of the adiabatic segment, by integrating from $r = R_0$ to $r_{\rm rcb}$,

$$\begin{aligned} M_{\rm ad} = 4\pi \int_{R_c}^{r_{\rm rcb}} \rho r^2 {\rm d}r = 4\pi R_c^3 \rho_{\rm rcb} &\left[\nabla_{\rm ad}\left(\frac{GM_c\mu}{R_c k_{\rm B} T_{\rm eq}}\right)\right]^{\frac{1}{\gamma-1}} \left(\frac{\beta_{\rm ad}}{\beta_{\rm ad}-1}\right)^{\frac{3\gamma-4}{\gamma-1}} \\ &\times \ \mathcal{B}\left[\left(\frac{\beta_{\rm ad}-1}{\beta_{\rm ad}}\right) x; \ \frac{3\gamma-4}{\gamma-1}, \frac{\gamma}{\gamma-1}\right]_{x=1}^{x=r_{\rm rcb}/R_c} , \end{aligned} \tag{6.4}$$

where

$$\mathcal{B}(x; \, a, b) \equiv \int_0^x {\rm d}t \ t^{a-1}(1-t)^{b-1} , \tag{6.5}$$

is the incomplete beta function.

6.1.2 Radiative (Isothermal) Exterior and Model Calibration

The isothermal layer the density profile is given by,

$$\rho = \rho_{\rm rcb} \exp\left[\beta_{\rm iso}\left(\frac{r_{\rm rcb}}{r} - 1\right)\right] \geq \rho_{\rm rcb}\, {\rm e}^{-\beta_{\rm iso}} \ ; \quad \beta_{\rm iso} = \frac{GM_c\mu}{r_{\rm rcb}k_{\rm B}T_{\rm eq}} \ . \tag{6.6}$$

ρ converges to a finite constant at $r \to \infty$; the integration of gas mass diverges at infinite radius. We setup the initial atmosphere of a planet by comparing gas pressure at infinite radius in the isothermal layer to the ambient pressure of e.g. stellar wind, nominally ($\tilde{p}$ is the reference parameter characterizing the magnitude of ambient pressure),

$$p_{\rm amb} \simeq \tilde{p} \times 10^{-8}\ {\rm dyn\ cm^{-2}}\ \left(\frac{a}{0.1\ {\rm AU}}\right)^{-2} \ . \tag{6.7}$$

If $p_\infty \equiv (k_{\rm B}T_{\rm eq}\rho_{\rm rcb}{\rm e}^{-\beta_{\rm iso}}/\mu) < p_{\rm amb}$, the pressure in the isothermal segment is matched to the ambient pressure at a finite radius. In this case, the mass of the isothermal region, estimated from $r = r_{\rm rcb}$ to where $p = p_{\rm amb}$, is generally $\lesssim 10^{-1}$ of $M_{\rm ad}$, and characterizing the mass of atmosphere with $M_{\rm ad}$ is well-defined. If $p_\infty > p_{\rm amb}$, the isothermal envelope evaporates at a very short timescale by hydrodynamic mechanisms that are irrelevant to photoevaporation (see e.g. Owen & Wu, 2016). The latter will be discussed in §6.1.3, and the former case is the focus of §6.2 and §6.3.

The radiative nature of the isothermal layer helps us to calibrate the model parameters. Given M_c and R_c, a pair of (ρ_0, T_0) uniquely determines the hydrostatics of atmosphere, but those quantities are difficult to map directly onto the physics. In order to express those crucial parameters more explicitly, here we follow the scheme in OW17 with some simplifications. At the radiative-convective boundary, the adiabatic gradient of $\ln T$ is related to the luminosity of cooling by continuum of the planet L,

$$\left.\frac{{\rm d}\ln T}{{\rm d}r}\right|_{r_{\rm rcb}} = -\frac{GM_c\mu}{k_{\rm B}T_{\rm eq}r_{\rm rcb}^2} = -\left(\frac{L}{4\pi r_{\rm rcb}^2}\right)\left(\frac{3\kappa\rho_{\rm rcb}}{16\sigma T_{\rm eq}^4}\right) \ , \tag{6.8}$$

where σ here is the Stefan-Boltzmann constant, and κ is the Rosseland mean opacity. We adopt the fitting formula of κ, as a function of ρ and T (obtained by Rogers & Seager 2010, based on Freedman et al. 2008),

$$\begin{aligned} &\kappa \simeq \kappa_0 \times \tilde{\kappa}\left(\frac{p}{\rm dyn\ cm^{-2}}\right)^{\alpha}\left(\frac{T}{\rm K}\right)^{\beta} \ ; \\ &\kappa_0 \equiv 10^{-7}\ {\rm cm^2\ g^{-1}} \ , \quad \alpha \equiv 0.45 \ , \quad \beta \equiv 0.68 \ . \end{aligned} \tag{6.9}$$

Our ignorance about L, as well as the uncertainty in the dimensionless opacity parameter $\tilde{\kappa}$, are absorbed into a parameter with the dimension of time,

$$\tau_{\rm KH} \equiv \frac{GM_cM_{\rm ad}}{R_cL\tilde{\kappa}} \ . \tag{6.10}$$

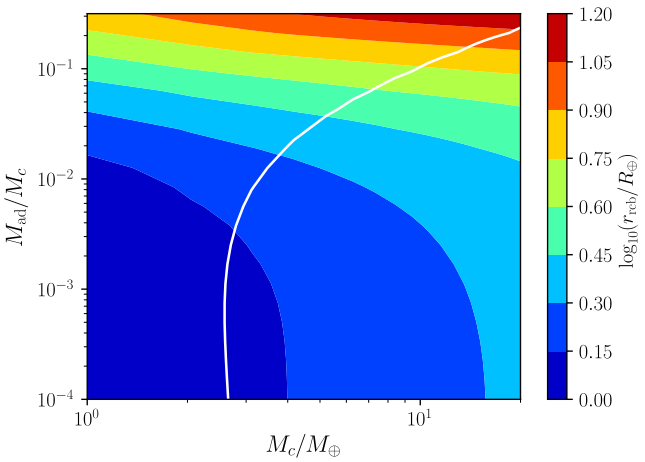


Figure 6.1 Radius of the radiative-convective boundary $r_{\rm rcb}$, which roughly resembles the *observed* radius of planets, presented as a function of solid core mass M_c and envelope mass fraction characterized by $M_{\rm ad}/M_c$ ($M_{\rm ad}$ is the mass of the adiabatic atmosphere). The white curve overlaid indicates the limit at which the ambient pressure can marginally confine a hydrostatic atmosphere. The region on its upper left consists of models that would rapidly disperse their envelopes due to Parker wind. Note the critical core mass that occurs at $M_c \sim 3\ M_\oplus$, which depends logarithmically on the luminosity of the host star, the core composition, and the ambient pressure.

This $\tau_{\rm KH}$ is indeed the Kelvin-Helmholtz timescale of planet atmosphere with $\tilde{\kappa}$ absorbed. From eq. (6.8) we have,

$$\begin{aligned} M_{\rm ad} &= \frac{64\pi\mu\sigma T_{\rm eq}^3 R_c \tau_{\rm KH}}{3k_{\rm B}(p_{\rm rcb}/{\rm dyn\ cm^{-2}})^\alpha \kappa_0 (T_{\rm eq}/{\rm K})^\beta \rho_{\rm rcb}}\ ; \\ \left(\frac{\rho_{\rm rcb}}{10^{-3}\ {\rm g\ cm^{-3}}}\right)^{\alpha+1} &= \left[10^{-1-3\beta}(3.51\times10^7)^{1-\alpha}\right] \times \left(\frac{M_{\rm ad}}{0.104\ M_\oplus}\right)^{-1} \\ &\quad \times \left(\frac{R_c}{R_\oplus}\right)\left(\frac{\tau_{\rm KH}}{10^8\ {\rm yr}}\right)\left(\frac{\mu}{2.35\ m_p}\right)^{\alpha+1}\left(\frac{T_{\rm eq}}{10^3\ {\rm K}}\right)^{3-\alpha-\beta}. \end{aligned} \tag{6.11}$$

For fixed M_c and R_c, we first take $M_{\rm ad}$ and $\tau_{\rm KH}$ as input parameters, then use eq. (6.11) to find out $\rho_{\rm rcb}$, before inserting those quantities into eq. (6.4) to solve for $\beta_{\rm ad}$ numerically, utilizing eq. (6.3). Those steps allows us to determine atmospheric profiles of the planet as a function of envelope mass fraction and the Kelvin-Helmholtz timescale.

6.1.3 Mass Loss with Unbalanced Ambient Pressure

We present examples of hydrostatic models in Figure 6.1. Model parameters are: $\tau_{\rm KH} = 10^8$ yr, $T_{\rm eq} = 886$ K, $\mu = 2.35\ m_p$ (m_p is the mass of proton), and $\tilde{p} = 1$. Note the overlaid white curve indicating the critical conditions of pressure balancing, above which the models have $p_\infty > p_{\rm amb}$ and thus the atmosphere is expected to lose

mass rapidly. The approximate mass loss rate by Parker wind mechanism, assuming sufficient energy supply to maintain an isothermal outflow, is estimated by (subscript "s" denotes the sonic surface; for estimating $\rho_{\rm s}$ see e.g. Parker 1958),

$$\dot{M}_{\rm Parker} = 4\pi R_{\rm s}^2 \rho_{\rm s} c_{\rm s} \ ; \ R_{\rm s} = \frac{GM_c}{2c_s^2} \ ; \ \rho_{\rm s} \sim \rho_{\rm rcb} \exp\left[-\frac{R_s}{r_{\rm rcb}} \left(1 - \frac{r_{\rm rcb}}{R_{\rm s}} \right)^2 \right] \ . \qquad (6.12)$$

On the other hand, the rate of energy injection by the bolometric luminosity L_* of the host star (not to be confused with photoevaporation by high energy photons, $L_{\rm HE}$) is also limiting hydrodynamic mass loss rate. The energy-limited mass loss rate $\dot{M}_{\rm ene}$ is approximately (note that $\pi r_{\rm rcb}^2$ is roughly the area of intercepting stellar radiation in optical and infrared, and a is the semi-major axis of the planet orbit),

$$\dot{M}_{\rm ene} \sim \left(\frac{L_*}{4\pi a^2} \right) \pi r_{\rm rcb}^2 \left(\frac{c_s^2}{2} \right)^{-1} \ ; \quad \dot{M} \sim \min\{ \dot{M}_{\rm Parker}, \dot{M}_{\rm ene} \} \ . \qquad (6.13)$$

The evaporation timescale of the adiabatic atmosphere is approximately $t_{\rm evap} \equiv M_{\rm ad}/\dot{M} \gtrsim 10^2$ yr for planets with $M_{\rm ad}/M_c \gtrsim 10^{-2}$ (detailed calculations of such $t_{\rm evap}$ are postponed to §6.4.1, Figure 6.7). Envelope of a planet evaporates until it reaches the curve if M_c is greater than the critical value $M_{\rm crit} \sim 2.5\ M_\oplus$, or otherwise totally loses its adiabatic segment of envelope. For rocky-core planets, we varied $\tilde{p}$ by ± 4 orders of magnitude to confirm that the value of $M_{\rm crit}$ varies within the range of $2 \lesssim (M_{\rm crit}/M_\oplus) \lesssim 3$, which depends on the logarithm (thus very insensitively) of $\tilde{p}$ and $T_{\rm eq}$, as one can infer from eq. 6.7. We refer the reader to §6.4.3 for examples of evaporation timescale in this region.

This critical mass quantitatively agrees with the observed absence of massive H/He planetary atmosphere for less massive planets with $M \lesssim 3\ M_\oplus$ (e.g. Rogers, 2015; Zeng et al., 2016; López-Morales et al., 2016). We hence suggest that the inability of low mass planets to have its atmosphere pressure balanced by the ambient would be possible to result in those observation constraints. Similar mechanisms are also suggested in Owen & Wu (2016) to shape a similar limit.

This would suggest that planets with $M_c \lesssim 3\ M_\oplus$ would lose its primordial H/He atmosphere quickly after the disk disperses (after 10^{6-7} yr). In other words, planets in this mass range will not have a substantial H/He envelope ($< 10^{-4}$ by mass) unless subsequent outgassing is significant. Owen & Wu (2016) reached a similar conclusion but did not offer an quantitative prediction on the threshold. We will show in §6.4, that observational test of this prediction is more complicated. This is because planets with core masses between $\sim 3\ M_\oplus$ to $\sim 6\ M_\oplus$ (the upper boundary is more sensitive to the specific choices of parameters) may be stable to Parker Wind outflow but still susceptible to photoevaporation. On a $\sim 10^8$ yr timescale, these planets will also lose their primordial H/He envelope photoevaporatively. Observationally, the $6\ M_\oplus$ (or $\sim 1.6\ R_\oplus$) threshold was pointed out by Dressing et al. (2015) and Rogers (2015). We admit that "super-puff" objects recently discovered (e.g. Masuda, 2014; Jontof-Hutter et al., 2016) seem to be in conflict with the discussions herein. Detailed discussions

Table 6.1. Properties of the fiducial model

Item	Value
Radial domain	$r_{\rm in} \le r \le 10\ r_{\rm in}$ ($r_{\rm in} \simeq 2.448\ R_\oplus$)
Latitudinal domain	$0 \le \theta \le \pi$
Resolution	$N_{\log r} = 128$, $N_\theta = 128$
Planet core	
M_c	$5\ M_\oplus$
R_c	$1.495\ R_\oplus$
Planet Atmosphere	
$M_{\rm ad}$	$10^{-2}\ M_c$
$T_{\rm eq}$	886 K
$\tau_{\rm KH}$	10^8 yr
Radiation flux [photon cm $^{-2}$ s^{-1}]	
7 eV (Soft FUV)	2×10^{15}
12 eV (LW)	5×10^{13}
25 eV (EUV)	5×10^{14}
1 keV (X-ray)	1.3×10^{13}
Initial abundances [$n_{\rm X}/n_{\rm H}$]	
H_2	0.5
He	0.1
H_2O	1.8×10^{-4}
CO	1.4×10^{-4}
S	2.8×10^{-5}
Si	1.7×10^{-6}
Fe	1.7×10^{-7}
Gr	1.0×10^{-7}
Dust/PAH properties	
$r_{\rm dust}$	5 Å
$\rho_{\rm dust}$	2.25 g cm^{-3}
$\sigma_{\rm dust}$/H	8×10^{22} cm^2

of these outliers, however, are beyond the scope of this chapter, which focuses on photoevaporation instead.

6.2 Fiducial Model

In this section we describe the setup and results of the fiducial model, which is the reference point of all further numerical explorations. As a direct product of planet formation that takes place in protoplanetary disks (PPDs), the *primordial* atmosphere of planets are expected to involve thermochemical processes similar to PPDs. We hence inherit the thermochemical network and recipes from Chapter 3. The main properties of our fiducial model is summarized in Table 6.1.

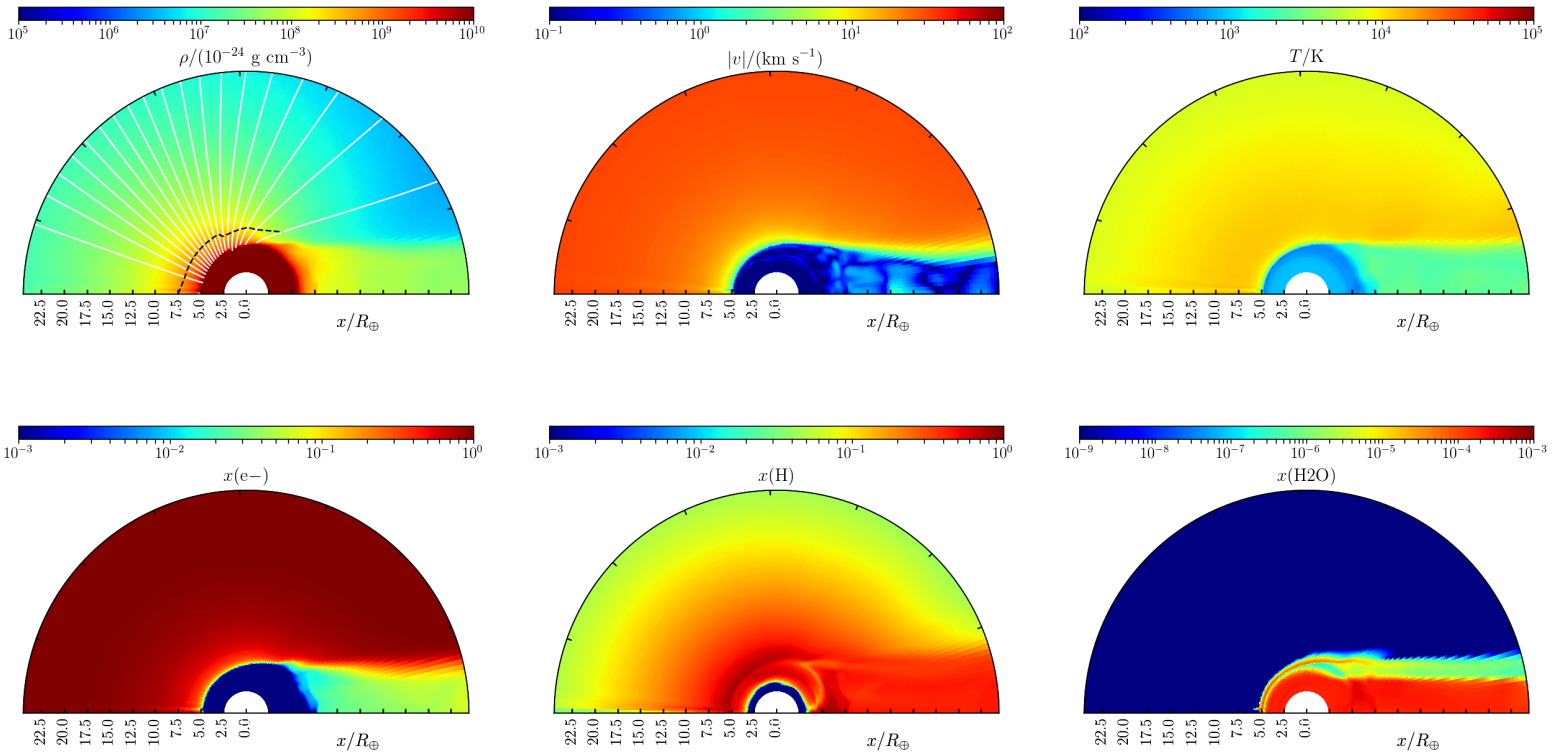


Figure 6.2 Meridional slice plot of the fiducial model at steady state, averaged through the final 0.05 yr of the fiducial simulation. The top row presents fluid properties, including mass density ρ (upper left panel; colormap saturated for $\rho > 10^{-10}$ g cm^{-3} to present the wind better), magnitude of velocity $|v|$ (upper middle), and temperature T (upper right). The bottowm row exhibits the relative abundances of important chemical species, including electons (lower left), neutral hydrogen (lower middle), and water (lower right). The streamlines (white solid curves; separated by 2×10^{-11} $M_\oplus$ yr^{-1} mass loss rate) and transonic surface (black dashed curve) are overlaid in the density panel. Regarding the way of presentation in this figure, rays for radiative transfer are injected from the left, and all rays travel horizontally across the simulation domain. Note the hydrostatic "tail" on the night side over the planet; see §6.2.2.

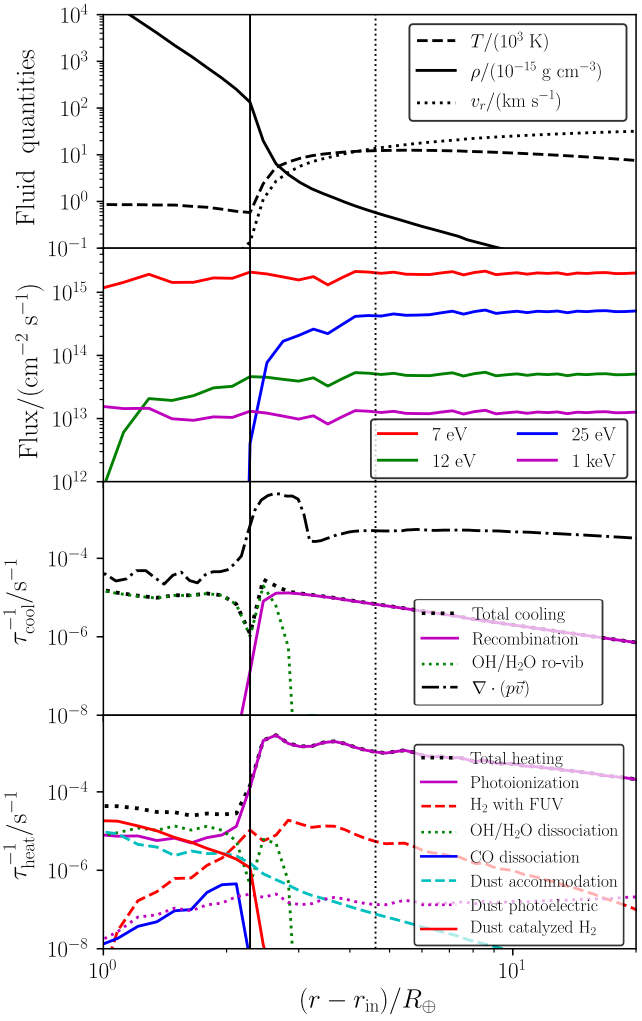


Figure 6.3 Radial profiles at $\theta = 0.4$ of the time-averaged fiducial model. Fluid mechanics profiles (ρ, v_r and T, upper left panel), radiation flux in four energy bins (lower left), inverse cooling timescale ($\tau_{\mathrm{cool}}^{-1}$, upper right), and inverse heating timescale ($\tau_{\mathrm{heat}}^{-1}$, lower right) in four panels, respectively. Denotation of curve shapes and colors are indicated in each individual panel. Vertical solid lines show the wind base, while vertical dotted lines indicate the sonic point.

6.2.1 Fiducial Model Setup

We setup the simulation in an axisymmetric spherical polar grid; dependence on the azimuthal coordinate (ϕ) is ignored. The symmetry axis points to the host star, from which the radiation comes as parallel rays. The grid extends from $r_{\rm in}$ to 10 $r_{\rm in}$ in radius (r) and 0 to π in co-latitude (θ). $r_{\rm in}$ is defined as the radius at which the static density equals to a reference value $\rho_{\rm in}$, which can be smaller than $\rho_{\rm rcb}$ since photoevaporation only affects the outermost part of isothermal layer. In this chapter we choose $\rho_{\rm in} = 10^{-7}$ g cm^{-3} unless specifically noted. For the fiducial model, $r_{\rm in} = 2.448\ R_\oplus$, which guarantees that all relevant dynamical, radiative and thermochemical processes are taking places inside the simulated domain.[1] Outflow boundary conditions with a radial flow limiter are imposed at $r = 10\ r_{\rm in}$, and reflecting boundary conditions at $r = r_{\rm in}$, while $\theta = 0$ and $\theta = \pi$ are polar boundaries. The resolution is 128 radial by 128 latitudinal; the radial zones being logarithmically spaced, and the latitudinal zones equally spaced. Rays of high energy radiation are injected at the $r = 10\ r_{\rm in}$ boundary in the θ range $0 < \theta < \pi/2$, carrying uniform flux density in each energy bin. All rays are parallel to the symmetric axis.

The fiducial model has a $M_c = 5\ M_\oplus$ rocky core, whose radius is therefore $R_c \simeq 1.495\ R_\oplus$ (see §6.1). The gravitational field is set according to the core; self-gravity of the atmosphere is ignored. Outside the core, we set an adiabatic envelope with $M_{\rm ad} = 10^{-2}\ M_c$, surrounded by an isothermal layer characterized by $T_{\rm eq} = 886$ K (eq. 6.2). The initial density profile is set according to the discussions in §6.1, with $\tau_{\rm KH} = 10^8$ yr (see eq. 6.10). This fiducial model has $\beta_{\rm ad} = 3.94$ and $\rho_{\rm rcb} = 1.1 \times 10^{-2}$ g cm^{-3}. The specific entropy in the adiabatic atmosphere is $\sim 8.3\ k_{\rm B}$ per baryon.

Host star luminosities in high energy photon are calibrated as $L_{\rm EUV} + L_{\rm X} = 10^{30}$ erg s^{-1} (e.g. Owen & Jackson 2012; OW17). In each energy bin the luminosity is set according to the $t < 0.1$ Gyr SED concluded in Ribas et al. (2005), which approximately reads $L(7\text{ eV}) = L(25\text{ eV}) = L(1\text{ keV}) = 0.5 \times 10^{30}$ erg s^{-1}, and $L(12\text{ eV}) = 0.5 \times 10^{29}$ erg s^{-1}. Those luminositis are converted into fluxes at $a = 0.1$ AU, assuming that the stellar radiation is isotropic. The initial abundance of chemicals is the same as the fiducial model in Chapter 3, which is a subset of Gorti & Hollenbach (2008), defined by the values in Table 6.1 (where $n_{\rm H}$ is the number density of hydrogen nuclei).

Dust (including PAH) is one of the most important mechanisms that maintain the temperature in the isothermal region: in optical and infrared bands where the radiation from the central star is most energetic, dusts provide most of the opacity. The abundances of PAH in exoplanet atmospheres, however, are still unconstrained due to difficulties in observation. Observations within the solar system suggest that relatively high concentration of PAH is possible (e.g. López-Puertas et al. 2013 shows that the mass fraction in PAH is $\sim 2 \times 10^{-3}$ in the fully evolved nitrogen-rich atmosphere of Titan, with ~ 34 carbon atoms per PAH particle on average). Similar to Chapter 3, we use the PAH at 5 Å as a proxy of all dusts, with abundance 10^{-7} per hydrogen atom. The dust-to-gas mass ratio is then 0.7×10^{-4}, and $\sigma_{\rm dust}/{\rm H} = 8 \times 10^{22}$ cm^2 for

[1] For the fiducial model, we vary the value of $\rho_{\rm in}$ by ± 1 orders of magnitude for different $r_\in$, to confirm that the mass loss rate is invariant up to $\sim 5\%$.

the geometric cross section. We note that, under the planetary gravity, PAH particles fall at a terminal speed, at which gas drag balances gravity. As is elaborated in §6.B.1, however, this terminal speed might be negligible compared to upward motion of gas at sufficiently high wind mass loss rate. For the fiducial model, we presumably ignore PAH precipitation, and revisit this issue once $\dot{M}$ is obtained.

Instead of calculating the radiative transfer of optical and infrared radiation, we set the dust temperature $T_{\rm dust} = T_{\rm eq}$ everywhere in the simulation for simplicity. The emission power per dust surface area is proportional to approximately the sixth power of dust temperature considering dust emissivity (see e.g. Draine, 2011a); slight deviation of $T_{\rm dust}$ from $T_{\rm eq}$ will result in rapid restoration of $T_{\rm dust}$ back to $T_{\rm eq}$.

The fiducial model is run through $\sim 10^{-1}$ yr to guarantee that the system reaches quasi-steady state, especially that the photospheres of high energy radiation in four bins do not move. We confirm that the system is already steady after only $\sim 5 \times 10^{-3}$ yr: the dynamical timescale across the simulation domain is at the order of $t_{\rm dyn} \sim 40\ R_\oplus/v_r \sim 10^{-4}$ yr, and the quasi-steady state is established after only a few $t_{\rm dyn}$.

6.2.2 Fiducial Model Results

The meridional plots, showing the structure of the fiducial model in the quasi-steady state, are displayed in Figure 6.2. The flow structure is shown by white streamlines overlaid on the mass density panel (upper left), separated by constant mass loss rate $2 \times 10^{-11}\ M_\oplus\ {\rm yr}^{-1}$ (integrated through the polar and azimuthal region between neighbor streamlines). Streamlines are only plotted in regions with positive "Bernoulli parameter", defined as

$$\mathcal{B} \equiv \frac{v^2}{2} + \frac{\gamma p}{(\gamma-1)\rho} + \Phi\ , \tag{6.14}$$

where v is the magnitude of velocity vector, and Φ is the gravitational potential. The surface where the streamlines terminate is considered as the base of photoevaporation outflow, which is located at $r \simeq 5\ R_\oplus$. In Table 6.2 we present several radii as characteristic locations of different physical processes. Note that $R_{\rm EUV}$ is the radius of EUV photosphere, defined as where $F_{\rm EUV}$ drops to 10^{-2} of the unattenuated value, which also defines the wind base in our following analyses. [2] [t]

Radial profiles of thermodynamics

Along a typical radial column at co-latitude $\theta = 0.4$ (where the streamline is almost radial), the hydrodynamical and microphysical profiles are shown in Figure 6.3. Only important mechanisms of heating and cooling are included in the lower two panels, where the inverses of heating/cooling timescales are defined as internal energy density divided by the cooling/heating rate, $\tau^{-1}_{\rm cool,heat} \equiv \epsilon/f({\rm cool,\ heat})$ (ϵ is the interal energy density of the gas; not to be confused with the Kelvin-Helmholtz timescale

[2] by numerical experiments, we find that this criteria result in an almost invariant ρ at $R_{\rm EUV}$ for different physical parameters.

Table 6.2. Characteristic radii of the fiducial model

Item	Value
$R_c/R_\oplus$	1.50
$r_{\rm rcb}/R_\oplus$	1.91
$r_{\rm in}/R_\oplus$	2.45
$R_{\rm EUV}/R_\oplus$	4.78
$R_s/R_\oplus$	7.24

Note. — The fiducial model is defined in Table 6.1.

in 6.1.2). The term $\nabla \cdot (p\vec{v})$, as another kind of "cooling", consists of adiabatic expansion and radial acceleration and characterizes the rate at which thermal energy is converted into kinetic energy. The heating curve marked by "H_2 with FUV" includes photodissociation and FUV pumping processes by LW FUV photons (see also §3.A.1).

Below the wind base, there is a small dip in temperature, thanks to dramatic expansion as the gas is accelerated. Inside the isothermal layer where EUV photons cannot reach, $|\nabla \cdot (p\vec{v})|$ of the gas creeping outwards at relatively very high density and very slow speed consumes the majority of injected energy, at a rate about three times the dissipation by ro-vibrational cooling of H_2O and OH. Spatial locations of the peaks in cooling rate by H_2O/OH agree with the spatial distribution of water molecules (see Figure 6.2). Note that there is a layer of H_2O detached to the bulky molecular atmosphere, where the re-formation rate of H_2O exceeds the photodissociation and thermal collisional destruction rate. Cooling mechanisms via recombination and Lyα , in contrast, are negligible. On the heating side, photoionization brought by X-ray and LW photons, photodissociation of H_2O and OH, re-formation of H_2 on dust surface, and photoelectric effect of dust grains, are the four comparable mechanisms that are major heating sources.

From the profiles presented by Figure 6.2, we observe that the day hemisphere has a clear outflow above the isothermal layer. The outflow becomes supersonic at the black dashed curve (marking the sonic points), which confirms that it is a wind rather than a "breeze". As is seen in Figure 6.3, in the subsonic part of wind, the thermodynamics of gas is dominated by photoionization and $\nabla \cdot (p\vec{v})$. Beyond the sonic point, radial acceleration almost vanishes, and $|\nabla \cdot (p\vec{v})|$ gradually surpasses photoionization heating, which causes a slight ddecreasedrop in temperature.

Neutral hydrogen and planet size in Lyα

We notice that neutral hydrogen atmos still exist at a considerable fraction in the wind, thanks to the capability of dealing with non-equilibrium thermochemical processes[3]. The timescale of hydrogen photoionization is roughly $(F_{\rm EUV}\sigma)^{-1} \sim 0.5$ hr,

[3]We confirm that the existence of neutral hydrogen in the wind does not affect the structure of photoevaporating atmosphere by a test run, whose outer boundary is set at $r = 10^2\ r_{\rm in}$ and the

allowing a fluid element in the wind to travel $\sim 8.4\ R_\oplus$ before its fraction of neutral hydrogen decreases by one e-fold. The low ionization fraction prohibits the propagation of Lyα into the isothermal layer: the line-center optical depth is $\sim 10^{6-7}$, which allows us to ignore Lyα radiative transfer safely. Meanwhile, neutral hydrogen in the wind makes the observed size of planet in Lyα much bigger than other bands. The dimensionless equivalent width on a wide Lyα profile denoted by $\phi(u)$, is estimated as (here u is the line-of-sight velocity),

$$W = \left[\int \mathrm{d}u\ \phi(u)\right]^{-1} \times \left[\int \mathrm{d}u\ \phi(u)(1 - \mathrm{e}^{-\tau(u)})\right] \ . \tag{6.15}$$

We assume that $\phi(u)$ is a Gaussian profile with FWHM $\sim$ 200 km s^{-1}, and that $\tau(u)$ is another Gaussian with FWHM $\sim$ 50 km s^{-1}, combining the bulk and thermal motion of the outflow. By integrating τ and then W along different lines of sight, we find that $W \sim (1 - \mathrm{e}^{-1})$ at an impact parameter $b \sim 11\ R_\oplus$, which roughly indicates the observed size in Lyα during transits. The excess of obsereved size of planets in Lyα compared to optical is readily observed in Jupiter-size objects (e.g. Lecavelier Des Etangs et al., 2010). According to our simulations, the same holds true for sub-Neptune planets.

Flow structures and the mass loss rate

Above the night hemisphere, where no high energy photons can ever reach, there exists a roughly isothermal "tail" at $\rho \sim 10^{-15} - 10^{-16}$ g cm^{-3} and $T \sim 2 \times 10^3$ K. The tail is almost static; the velocity magnitude is roughly below 10^{-1} km s^{-1}. The streamline structures and the evolution history both reveal that the tail is brought about by the gas flowing along the streamline originating from $\theta \simeq \pi/2$, similar to the Bernoulli effect for isenthalpic flows. Existing works of planet atmosphere suggest much larger tails (outside the Roche lobe of the planet) which are typically attributed to ram pressure of stellar wind or radiation pressure of the central star (e.g. Christie et al., 2016; Bourrier et al., 2016), while the tail here comes from the thermal wind of the planet itself. The fate of this "smaller" tail, however, has to be studied with full three-dimensional simulations in order to include the effects of planet orbital motion, which we will tackle in future works.

By integrating the mass flux through the outer boundary of r, we obtain a mass loss rate $\dot{M} \simeq 4 \times 10^{-10}\ M_\oplus$ yr^{-1}. Such mass loss rate is $\sim 13\times$ greater than $\dot{M}_{\rm eq}$ (eq. 6.23, §6.B.1), which is sufficient to keep $r_{\rm dust} = 5$ Å PAH particles in the quasi-isothermal atmosphere, confirming the assumption to ignore PAH precipitation. For the fiducial case alone, multidimensionality does not contribute to the mass loss rate appreciably. Multiplying the radial mass flux at $\theta = 0$ (at the substellar point) by 2π (the solid angle of day hemisphere), the estimated mass loss rate is only ~ 3 % bigger than the value measured from simulation. The dimensional effects (i.e. 2.5

radial number of zones is doubled so that the mesh configuration in the innermost 10 $r_{\rm in}$ is identical to the fiducial run.

Table 6.3. Models exploring the parameter space

Model Series	Variable	Values
(1)	(2)	(3)
	Microphysics parameters	
E	Energy bin turned off (eV)	$\{7,\ 12,\ 25,\ 10^3\}$
G	Dust grain abundance	$\{10^{-8},\ 10^{-9},\ 0\}$
D	Depleted species	{CO, H_2O, CO & H_2O}
	Atmosphere parameters	
KH	$\tau_{\rm KH}/(10^8$ yr)	$\{0.3,\ 3,\ 10\}$
TE	$T_{\rm eq}$/K	$\{411,\ 518, 703\}$
X	$M_{\rm ad}/M_c$	$[10^{-4}, 0.02]$
	Planet and stellar properties	
W	$p_{\rm ram}/($dyn cm$^{-2})$	$\{10^{-4},\ 10^{-3},\ 10^{-2}\}$
C	Core composition	{Iron, Water}
M	M_c	$[3, 20]$
F	Relative high energy flux	$[1/30, 30]$

Note. — (1) Model series identifier. (2) Description of the varied quantity in the model series. (3) Sets of values of the variable. Squared brackets $[l, u]$ denote that the variable will take several different values between lower limit l and upper limit u, while braces "{}" indicate that the variable will select one of the discrete values in the braces at a ime.

dimensions with axisymmetry) are nonetheless manifested by models with strong stellar wind ram pressure (see §6.3.1).

6.3 Exploring the Parameter Space

We have run serieses of simulations to explore the effects of different parameters. To manifest the impact of each parameter more clearly, each run in this subsection differs from the fiducial model by only one parameter unless specifically stated. Table 6.3 lists the model serieses [indicated by "Model(s) Y" for the model series Y in what follows] with brief descriptions.

6.3.1 Stellar Wind Ram Pressure and the Effects of Multi-dimensions

For a typical radial column above the day hemisphere, in which the flow is virtually radial, we derive the total pressure of outflow (including thermal pressure and fluid ram pressure), from conservation of momentum (here $v_{r,\infty}$ is the terminal radial velocity of outflows),

$$p_{\rm tot} \simeq 10^{-3}\ {\rm dyn\ cm^{-2}} \times \left(\frac{\dot{M}}{10^{-10}\ M_\oplus\ {\rm yr^{-1}}}\right)\left(\frac{v_{r,\infty}}{34\ {\rm km\ s^{-1}}}\right)\left(\frac{r}{5\ R_\oplus}\right)^{-2} . \quad (6.16)$$

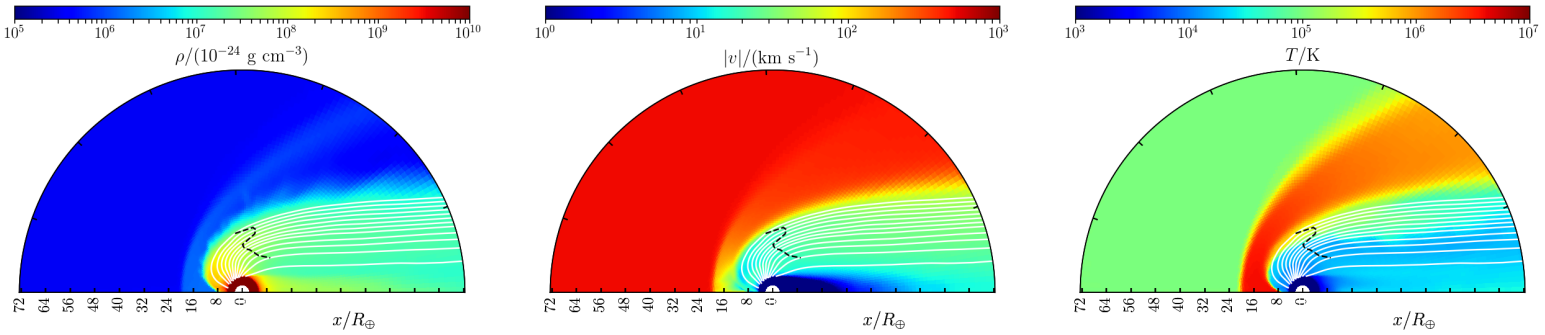


Figure 6.4 Meridional slice plot of the $p_{\rm ram} = 10^{-3}$ dyn cm^{-2} case in Models W (left panel: mass density ρ; middle panel: magnitude of velocity $|v|$; right panel: temperature T), where a strong stellar wind ram pressure is included. The colormap exhibits the mass density ρ, showing the time-averaged results for the final 10^{-2} yr of quasi-steady states. The denotation of overlays in this figure are identical to the upper left panel of Figure 6.2. See §6.3.1 for the details of simulation setup.

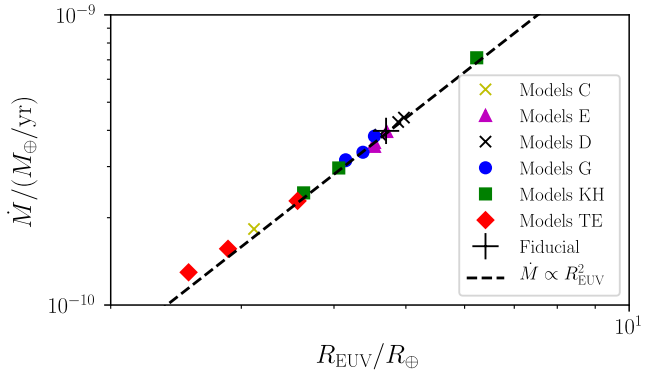


Figure 6.5 Scattered plots showing the $\dot{M}$-R_{EUV} relations for Models E, G, KH, TE, and C, as well as the fiducial model. Makers of each model series are indicated by the legend. The simple relation $\dot{M} \propto R_{\mathrm{EUV}}^2$ is shown by a dashed line.

This pressure is typically much greater than ambient pressure (eq. 6.7), which allows us to safely ignore the ambient constraints once photoevaporation outflow is launched. If the model is 1D and spherical symmetric, when the ram pressure exerted by the stellar wind p_{ram} is comparable to the total pressure near the sonic point (namely $p_{\mathrm{tot},s}$), one would expect that the supersonic outflow is quenched while only a subsonic breeze is possible (see also M-CCM09).

However, considering the multidimensional reality, it is more likely that the supersonic planetary winds would divert to the night hemisphere instead of being totally chocked. We hence compute simulation Models W, in which we setup significant inflow at the outer r-boundary, in the range $0 < \theta < \pi/2$ (the boundary condition is the same as fiducial in $\pi/2 < \theta < \pi$). The inflow is parallel to the radiation fluxes, at velocity $v = 500\,\mathrm{km\ s^{-1}}$, and temperature $T = 10^5$ K. Mass density of the inflow is the variable that controls p_{ram} in Models W: $\rho = 4 \times 10^{-19}\ \mathrm{g\ cm^{-3}} \times (p_{\mathrm{ram}}/10^{-3}\ \mathrm{dyn\ cm^{-2}})$. Three different ram pressures are tested respectively, $(p_{\mathrm{ram}}/\mathrm{dyn\ cm^{-2}}) \in \{10^{-4},\ 10^{-3},\ 10^{-2}\}$, compared to the total outflow pressure at the sonic point $p_{\mathrm{tot,s}} \simeq 1.8 \times 10^{-3}\ \mathrm{dyn\ cm^{-2}}$ for the fiducial model. The outer boundary is 30 r_{in} so that all important hydrodynamic features are correctly included in the simulation domain, and the number of radial zons is adjusted accordingly in order to keep the resolution of the innermost region identical to the fiducial one.

In their quasi-steady states, all cases in Models W still have significant supersonic outflows originating from the day hemisphere flowing to the night side. Although the flow morphology changed dramatically, the mass loss rate is comparable to the fiducial model. Previous one-dimensional calculations carried out by M-CCM09 could not capture the multidimensional effects, thus incorrectly predicted the quenching of supersonic photoevaporative outflow when ram pressure becomes significant. For each individual model:

- The $p_{\mathrm{ram}} = 10^{-3}\ \mathrm{dyn\ cm^{-2}}$ case has mass loss rate $\dot{M} \simeq (3.0 \pm 1.1)\ M_\oplus\ \mathrm{yr^{-1}}$ (the uncertainty here is the standard deviation over the final 10^{-2} yr, reflecting the variation amplitude of the outflow). In Figure 6.4, we present meridional

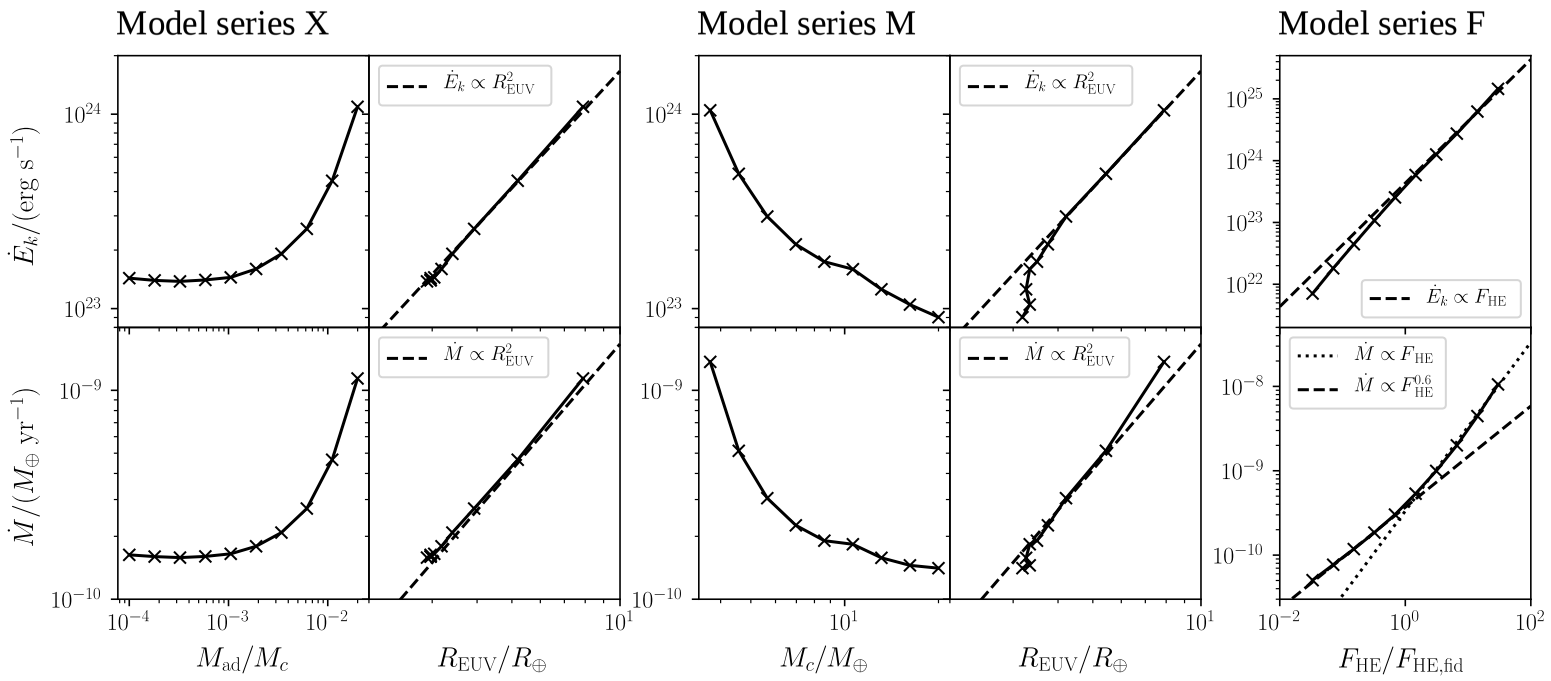


Figure 6.6 Simulation results of model serieses X (varying envelope mass fraction; left block), M (varying core mass; central block), and F (varying high energy flux, right block). Each data point, representing a model in its quasi-steady state, is indicted by a cross ("×"). In some panels, dashed or dotted lines present simple power-laws (indicated by legends in the panels) to help the reader recognize the general trend of variation. Panels related to $R_{\rm EUV}$ are not shown for model series F as $R_{\rm EUV}$ does not vary appreciably in the series. y-axes of the panels on the top-row all present $\dot{E}_k$ (the kinetic energy carried by the outflow, in erg $\rm s^{-1}$), while those of the bottom-row panels present $\dot{M}$ (the mass loss rate, in $M_\oplus$ $\rm yr^{-1}$).

plots of fluid properties with streamlines overlaid for this case, based on the time-averaged results during the final quasi-steady state (10^{-2} yr) of the simulation. Although the outflows are suppressed by the post-shock external wind near the substellar point, they still find their ways out on the night side and become supersonic. The discontinuity surface is rather turbulent thanks to Kelvin-Helmholtz instability (as the fluid speed behind the bow shock is still $\sim 10^2$ km s^{-1}), which in turn affects the shape of the shock as the post-shock flow is subsonic. Therefore we do not observe sharp transitions for the bow shock and the discontinuity in Figure 6.4.

- The $p_{\rm ram} = 10^{-4}$ dyn cm^{-2} case also has turbulent supersonic outflow, with mass loss rate $\dot{M} \simeq (3.3 \pm 1.0)\ M_\oplus$ yr^{-1}.
- The test case $p_{\rm ram} = 10^{-2}$ dyn cm^{-2} still has $\dot{M} \simeq (3.1 \pm 0.1)\ M_\oplus$ yr^{-1} mass loss rate, even when the ram pressure is one order of magnitude greater than the fiducial total pressure at the sonic surface $p_{{\rm tot},s}$. The supersonic outflow becomes fairly laminar in this case.

6.3.2 Different Bands of Radiation

Models E, varying the SED of incident high energy radiation by turning off one band of radiation at a time, help us to understand in which band is the high energy photons most relevant to photoevaporation. Simulation results reveal that only the EUV photons have primary impact on the mass loss rate. By turning off the EUV flux, the mass loss rate drops to $\dot{M} \lesssim 10^{-12}\ M_\oplus$ yr^{-1}, while the gas is creeping outwards at a radial velocity $v_r \lesssim 10^{-1}$ km s^{-1}. This is understood by comparing the depth of gravitational potential well, which is roughly ~ 1 eV per proton for a $5\ M_\oplus$ planet core at $r \sim 3\ R_\oplus$, to the energy per particle deposited by high energy photons.

When an EUV photon is absorbed by a hydrogen atom/molecule, photoionization processes deposit roughly 10 eV per reaction of energy to the post-interaction particle. LW photons, in comparison, deposit-es only ~ 0.5 eV of energy into each hydrogen atom by dissociating a H_2 molecule (e.g. Hollenbach & McKee, 1979), which is marginally sufficient to free it from the potential well. As EUV photons interact with the most abundant elements (hydrogen and helium), the energy injected is not considerably diluted. In contrast, energy injected by soft FUV and X-ray photons, which interact predominantly with species at relatively low abundance (especially water and dust grains), experiences significant dilution. Soft FUV and X-ray photons penetrate to higher depths where the number densities of hydrogen nuclei are rather high ($\sim 1 \times 10^{14}$ cm^{-3} for soft FUV and $\sim 3 \times 10^{14}$ cm^{-3} for X-ray). At those high densities, energy deposited by those photons is easily transferred to coolants or accommodated by dusts, and then re-radiated as infrared photons that are not efficient in heating the gas at all.

Meanwhile, when bands other than EUV are turned off, the mass loss rate is only secondarily affected: being responsible to modifying the temperature in quasi-isothermal layer, turning off a non-EUV band of radiation leads to (a) slight shrinking

of the quasi-isothermal layer and hence EUV photosphere, and (b) survival of more coolants. As a result, the mass loss rate decreases by $\sim 5\%$ (LW off) or $\sim 15\%$ (X-ray or soft FUV off).

6.3.3 Configuration of Atmospheres

An important substance maintaining temperature in the isothermal layer as they are, dust grains (which we use PAH as the proxy) have nonetheless highly uncertain abundances (see §6.2.1). In Models G, we confirm that the abundance of Gr affects $\dot{M}$ by competing with the cooling mechanisms in the quasi-isothermal region and then setup the location and structure at the EUV photosphere. Two models reducing the Gr abundance by one or two orders of magnitude results in a $\sim 10\%$ or $\sim 20\%$ decrease in $\dot{M}$ respectively.

The additional model in Models G has zero PAH abundance. Temperature of the quasi-isothermal layer is maintained by these mechanisms:

- An extra band of radiation is added, with photon energy $h\nu = 2$ eV. The incident flux is 4.25×10^{19} cm^{-2} s^{-1}, which corresponds to the photon flux 0.1 AU from a protostar with $L_* = L_\odot$ in this band.
- Opacity for this band is $\kappa = 0.1$ cm^2 g^{-1} (roughly the Thomson opacity). We assume that such opacity converts all absorbed photons into heat.

This model results in a shrinked $R_{\rm EUV}$, and $\sim 25\%$ lower $\dot{M} \simeq 3.1 \times 10^{-10}\ M_\oplus\ {\rm yr}^{-1}$. We note that such $\dot{M}$ is still $\sim 10\times$ greater than the equilibrium mass loss rate $\dot{M}_{\rm eq}$ discussed in §6.B.1, being sufficient to keep PAH particle in the isothermal region even if PAH is absent.

Although it is a resonable guess that planetary atmospheres inherit chemical species from PPDs, there could still be significant difference thanks to planet formation processes. For example, observations of transmission spectra of some "hot Jupiters" suggest the possibility that H_2O and/or CO could be depleted in the atmospheres. Such uncertainty is covered by Models D, in which we assume that the abundances of CO and/or H_2O are zero in the initial atmospheres (MacDonald & Madhusudhan, 2017). Removal of these two species, as the major molecular coolants, yields greater $R_{\rm EUV}$ due to the shifted equilibrium of atmospheric hydrostatics, hence $\sim 5\%$ (with CO or H_2O depleted) to 10% (with CO *and* H_2O depleted) greater $\dot{M}$.

Covering the uncertainties in the hydrostatics of planet atmosphere, we setup Models KH and TE. $\tau_{\rm KH}$ and $T_{\rm eq}$ together characterize the specific entropy and hence the density profile of the atmosphere (see §6.1.2). Models C, varying the core density by assuming an iron or water core below the atmosphere (using the mass-radius relation in Lopez & Fortney 2014 for different core components), also modify the atmospheric density profile dramatically.

It is worth noting that almost all models discussed above obey the simple relation, $\dot{M} \propto R_{\rm EUV}^2$, as $R_{\rm EUV}^2$ is proportional to the effective area for the planet to intercept EUV photons. We exhibit this scaling relatino in Figure 6.5.

6.3.4 Envelope Mass Fraction and the Planet Core

Models X, varying the envelope mass fraction, also clearly presents the dependence $\dot{M} \propto R_{\rm EUV}^2$, as is seen in the left column in Figure 6.6. This relation is almost invariant when the wind starts from different depth in the gravitational potential well: the kinetic energy at $v_{\rm wind} \simeq 32$ km s^{-1} overwhelms the gravitational potential (escape velocity is only ~ 11 km s^{-1} at $r = 5\ R_\oplus$ for a 5 $M_\oplus$ core) and other energy balance as a fluid element escapes. The kinetic energy carried by the outflow, $\dot{E}_k$, also follows the same proportionality. Thermal energy carried by the outflow is only $\sim 10^{-1}$ of $\dot{E}_k$, hence does not affect our discussions.

When the core mass varies in the Models M, the physics becomes slightly different (see the middle column in Figure 6.6). If $M_c \gtrsim 10\ M_\oplus$, $R_{\rm EUV}$ varies much slower with M_c, but the depth of the potential well starts to become significant. In the hypothetical case with $M_c = 20\ M_\oplus$, $v_{r,\infty}$ drops to ~ 26 km s^{-1}, as the gas spent part of its energy against gravitational potential well when escaping.

6.3.5 High Energy Photon Flux and "Cooling Limited"

In Models F (see the right column in Figure 16.6), $R_{\rm EUV}$ does not vary appreciably with the luminosity. When the high energy fluxes are weak ($F_{\rm HE} \lesssim F_{\rm HE,fid}$), the mass loss rate scales as $\dot{M} \propto F_{\rm HE}^{0.6}$ (shallower than linear), while the kinetic energy of outflow drops faster than linear. Considering the proportionalities $\dot{M} \propto r^2 \rho v_r$ and $\dot{E} \propto r^2 \rho v_r^3$, this clearly indicates that the outflow speed drops drastically at low luminosities, which in turn increases the efficiency of converting energy into outflow. In fact, for $F_{\rm HE}/F_{\rm HE,fid} = 1/30$, we have $v_{r,\infty} \simeq 12$ km s^{-1}. At high fluxes, $\dot{M}$ has linear dependence on $F_{\rm HE}$

Interestingly, M-CCM09 claimed that $\dot{M} \propto F_{\rm HE}^{0.6}$ at high $F_{\rm HE}$ due to increasing rate of recombination cooling, and that $\dot{M} \propto F_{\rm HE}^{0.9}$ otherwise. They concluded that recombination cooling at high $F_{\rm HE}$ is the limiting factor ("recombination limited"). Our models confirmed the power index 0.6 when cooling is the major limit. However, involving detailed thermochemistry reveals that the dominant coolants are the molecules via ro-vibrational transitions, while recombination is indeed impossible to remove injected heat at considerable amounts near the wind base (see discussions in §6.A.3). At lower $F_{\rm HE}$, the abundances of molecular coolants are higher. We hence summarize the mass loss rate at low $F_{\rm HE}$ with a more general term, "cooling limited", instead.

6.4 Discussions

6.4.1 Grid Data of Photoevaporative Model and Evaporation Timescale

In order to understand the general trend of $t_{\rm evap}$ varying with different planet configurations, we run a grid of simulations with parameters in the space where $p_\infty < p_{\rm amb}$

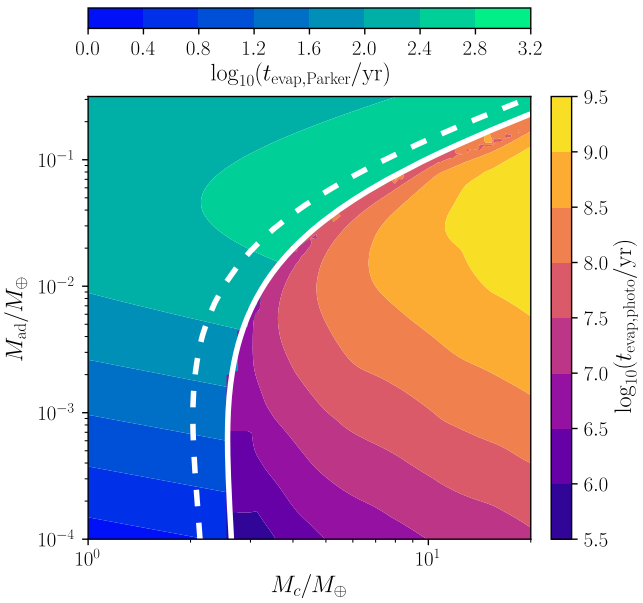


Figure 6.7 Evaporation timescale of planet atmosphere. The heavy white curve is the critical curve above which the isothermal layer pressure cannot be balanced by the ambient ($p_\infty < p_{\rm amb}$, see §6.1.3), and the white dashed curve indicates $\rho_\infty \simeq 10^{-13}$ g cm^{-3}, above which the pressure balance by outflow is no longer valid (see also discussions in §6.4.1). $t_{\rm evap}$ in the region with unbalanced ambient pressure above the solid white white curve is calculated with eqs. (6.12) and (6.13), which should read the blue-green color map indicated on the top. $t_{\rm evap}$ based on simulation results, presented by the region below the critical curve, should read the purple-yellow color map on the right.

(parameters unspecified are identical to the fiducial model),

$$\begin{aligned}&\{M_c/M_\oplus,\ M_{\rm ad}/M,\ F_{\rm HE}/F_{\rm HE,fid}\}\\ &\in \{[3,20]\otimes[10^{-4},10^{-0.5}]\otimes[10^{-2},1]\}\cap\{p_\infty < p_{\rm amb}\}\ .\end{aligned} \tag{6.17}$$

The resolution is 10 logarithmically-spaced grid points along M_c, 10 logarithmic along $M_{\rm ad}/M_c$, and 3 logarithmic along $F_{\rm HE}$. After excluding $p_\infty > p_{\rm amb}$ points 261 simulations in total have been integrated to at least 10^2 $t_{\rm dyn}$. Figure 6.7 plots $t_{\rm evap}$ the grid at $F_{\rm HE}/F_{\rm HE,fid} = 1$, where data in the region $p_\infty > p_{\rm amb}$ (above the heavy white curve) present the timescale of mass loss through Parker wind (§6.1.3).

When the envelope of a planet starts evolution in the Parker wind region, it is expected to be dispersed rapidly, at timescale shorter than 10^3 yr, until it becomes a "bare" planet ($M_c \lesssim 3\ M_\oplus$), or reaches the photoevaporation region ($M_c \gtrsim 3\ M_\oplus$), as we already discussed in §6.1.3. This scenario is slightly changed when high energy radiation fluxes exist. Compared to the ambient, outflows exert much greater pressure confinement onto the internal static atmosphere at wind bases (see eq. 6.16). However, this kind of "confinement" does require the isothermal atmosphere to allow EUV photons penetrate. Inspecting the location of EUV photosphere in various

models, $R_{\rm EUV}$ is always found at radii where $\rho \sim 10^{-13}$ g cm^{-3} (also see discussions in M-CCM09); if $\rho_\infty \gtrsim 10^{-13}$ g cm^{-3}, EUV photons are unlikely to penetrate, and this mechanism (pressure balance by outflow) is not valid either. In Figure 6.7 we present this criterion by a white dashed curve. The region between two type of pressure balancing is rather narrow. Therefore, in practice, adopting the ambient pressure balancing criterion will not significantly change the story, which is what we will do in the followings.

Planets in the photoevaporative domain disperse their envelopes at much longer timescales. In particular, the timescale peaks at $M_{\rm ad}/M_c \sim 10^{-2}$, $t_{\rm evap} \gtrsim 10^8$ yr for $M_c \gtrsim 5\ M_\oplus$. At the same M_c, planets with $M_{\rm ad}/M_c$ above this peak have rather puffy envelope, and $R_{\rm EUV}^2$ increases dramatically faster than $M_{\rm ad}$. The power injected by intercepting EUV photons per $M_{\rm ad}$ hence increases, shortening $t_{\rm evap}$ as a result. Below that peak, $R_{\rm EUV}$ does not shrink appreciably, especially when $M_{\rm ad}/M_c \lesssim 10^{-3}$. $\dot{M}$ is almost constant, thus $t_{\rm evap} \propto M_{\rm ad}$ becomes shorter and shorter as a planet loses its envelope mass. Qualitatively those are similar to the mechanisms proposed in OW17 which are probably responsible of the bimodal distribution of observed planet radius. We will discuss this with more details in §6.4.3. We particularly noticed that, for planets with core mass $M_c \lesssim 6\ M_\oplus$, evaporation timescales of their envelopes will be shorter than ~ 300 Myr everywhere. In other words, under fiducial set of parameters, photoevaporation prevents us from finding rich H/He envelopes on those low mass planets in evolved systems. This is not a hard limit, since the photoevaporation conditions vary from system to system, while $t_{\rm evap}$ depends on those conditions rather sensitively. Nevertheless, observations show the decline in number of planets with rich atmospheres (see also Dressing et al., 2015; Rogers, 2015). We thus suggest that this decrease can be attributed to photoevaporation.

6.4.2 Scaling Relations of the Mass Loss Rate

Based on the simulation grid as well as the explorations in §6.3, in almost all cases already tested, the relation $\dot{M} \propto R_{\rm EUV}^2$ holds very well (except for $M_c \gtrsim 10\ M_\oplus$, where the depth of potential well begins to make a difference). We notice that, in M-CCM09 and OW17, the mass-loss rate is scaled to an expression proportional to $r_{\rm rcb}^3$. The third power implies two assumptions, if the efficiency is nearly constant:

1. Terminal specific energy of the outflow is proportional to the depth of gravitational potential well at the wind base.

2. The radius of EUV photosphere (approximately the same as wind base) is proportional to $r_{\rm rcb}$.

Assumption 1 disagrees with our simulations, which indicate that the specific energy of outflow at infinity is almost invariant in most cases as it is much greater than the depth of potential well at wind bases. It is obvious that assumption 2 does not hold either. The $\dot{M} \propto R_{\rm EUV}^2$ scaling is the same as the "photon-limited" case discussed in Owen & Alvarez (2016), which assumes that each ionizing photon frees one hydrogen atom into the wind, and the depth of planetary graviational potential

well is negligible compared to heating. Photons in other energy bands (FUV and X-ray), as well as coupling of thermochemistry and hydrodynamics, subtly affect the results: our simulation indicate that ~ 3 hydrogen atoms are freed into the wind per EUV photon absorbed.

By observing our grid of photoevaporation models, we confirm that in each model $R_{\rm EUV}$ is always located at $\rho \sim 10^{-13}$ g cm^{-3}. This threshold density is relatively well-defined and constant: gas heating processes by EUV photons concentrate in a relatively thin layer due to low penetration of EUV photons in neutral gas. Using eq. (6.6), we estimate by assuming that EUV photons penetrate to where $\rho \sim 10^{-13}$ g cm^{-3},

$$R_{\rm EUV} \simeq r_{\rm rcb} \left[1 + \tilde{\beta}_{\rm iso}^{-1} \ln \left(\frac{10^{-13}\ {\rm g\ cm^{-3}}}{\rho_{\rm rcb}} \right) \right]^{-1} , \tag{6.18}$$

where $r_{\rm rcb}$ and $\rho_{\rm rcb}$ can be determined analytically using eqs. (6.4) and (6.11). Clearly $R_{\rm EUV}/r_{\rm rcb}$ is not constant. $\tilde{\beta}_{\rm iso}$ here should be estimated using a different μ from the one used for the adiabatic layer, as hydrogen molecules in the upper part of the isothermal layer are partially dissociated by LW and X-ray photons. We find that $\mu \simeq 1.88\ m_p$ fits $R_{\rm EUV}$ all models in the simulation grid and §6.3 with errors $\lesssim 10$ % (mostly within 5 %).

According to §6.3.5, the dependence of $\dot{M}$ on incident high energy flux is linear if $F_{\rm EUV} \gtrsim F_{\rm EUV,fid}$, and $\dot{M} \propto F_{\rm EUV}^{0.6}$ otherwise. Calibrated at the fiducial model, we propose a semi-empirical formula for mass loss rate that reads,

$$\begin{aligned} &\dot{M} \simeq 4.5 \times 10^{-10}\ M_\oplus\ {\rm yr^{-1}} \times \left(\frac{R_{\rm EUV}}{5\ R_\oplus} \right)^2 \times \max\{\mathcal{F}, \mathcal{F}^{0.6}\}\ \min\{1, \mathcal{M}^{-0.5}\}\ ; \\ &\mathcal{F} \equiv \frac{F_{\rm EUV}}{F_{\rm EUV,fid}}\ ; \quad \mathcal{M} \equiv \frac{M_c}{10\ M_\oplus}\ . \end{aligned} \tag{6.19}$$

With $R_{\rm EUV}$ given by eq. (6.18), we test the mass loss rate fitting by setting up 100 simulations with random (but reasonable) combinations of all parameters, confirming that the error of eq. (6.19) is $\lesssim 20$ % for most simulation runs, or $\lesssim 50$ % at worst [most of the worst cases have relatively large $R_{\rm EUV}$ ($R_{\rm EUV} \gtrsim 20\ R_\oplus$) that cannot be accurately estimated by eq. (6.18)].

6.4.3 Mass and Radius Evolution of Planet Atmosphere

Evolution of sample planets

Equipped with eqs. (6.19) and (6.18), we can model the evolution tracks of planet models by setting up initial conditions and then integrate the ODE ${\rm d}M_{\rm ad}/{\rm d}t = \dot{M}$ for each model planet.

Figure 6.7 implies that, even the external conditions and the initial conditions are nearly the same, two planets would experience substantially different tracks of evolution if they have different core masses. Such systems are suggested by observations, but the most clear detection is Kepler-36, whose two planets circulate it at

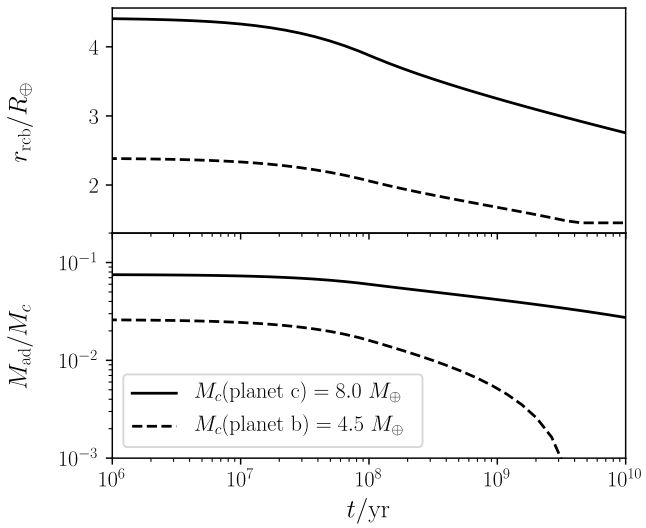


Figure 6.8 Evolution of model planet atmospheres, resembling the conditions of the two planets in Kepler-36, showing $r_{\rm rcb}$ and envelope mass fraction. Note that the two planets start from the same initial envelope mass fraction, but the less massive one (corresponding to Kepler-36b) has already evaporated most of its envelope via Parker wind before $t = 10^6$ yr. See §6.4.3 for detailed discussions.

similar orbital radius (~ 0.12 AU) but have different core masses and observed radii (Kepler-36b: 4.5 $M_\oplus$, 1.49 $R_\oplus$; Kepler-36c: 8 $M_\oplus$, 3.7 $R_\oplus$; see also Carter et al. 2012). Here we setup two model planets according to Kepler-36. For other parameters, we set Kelvin-Helmholtz timescale $\tau_{\rm KH} = 10^8$ yr , isothermal layer temperature $T_{\rm eq} = 850$ K, and a evolving high energy luminosity with initial value one order of magnitude lower than the fiducial, $L_{\rm HE}(t) = 10^{-4.5}\ L_\odot \times \min\{1, (t/10^8\ {\rm yr})^{-1.5}\}$ (for the time-depence see the discussions in §6.4.3). Both planets have initial envelope mass fraction $M_{\rm ad}/M_c = 2 \times 10^{-1}$ (as both models will lose their atmosphere rapidly until they reach the pressure balance line, this parameter is not sensitively depended upon), and are integrated along the evolution tracks to 10^{10} yr. Figure 6.8 show their fate: at the age of Kepler-36, (~ 7 Gyr), the more massive planet still has a relatively rich atmosphere ($M_{\rm ad}/M_c$ is few per cent), while the other has already evaporated all its atmosphere. Considering the $\sim (+0.5\ R_\oplus)$ correction applied to the more massive planet for the observed radius (given its $r_{\rm rcb}$ and core mass, e.g. Lopez & Fortney 2014), the bigger one should have $\sim 3.6\ R_\oplus$ observed radius, while the other is a $\sim 1.5\ R_\oplus$ "bare" planet. We thus conclude that the diverged evolution tracks due to photoevaporation agrees with observation semi-quantitatively (similar conclusion has also been reached by e.g. Lopez & Fortney 2013; Owen & Morton 2016).

Planet ensembles

This subsection extends the calculation in §6.4.3 to a relatively big ensemble of planets. We start by setting up the initial and input conditions for the ensemble.

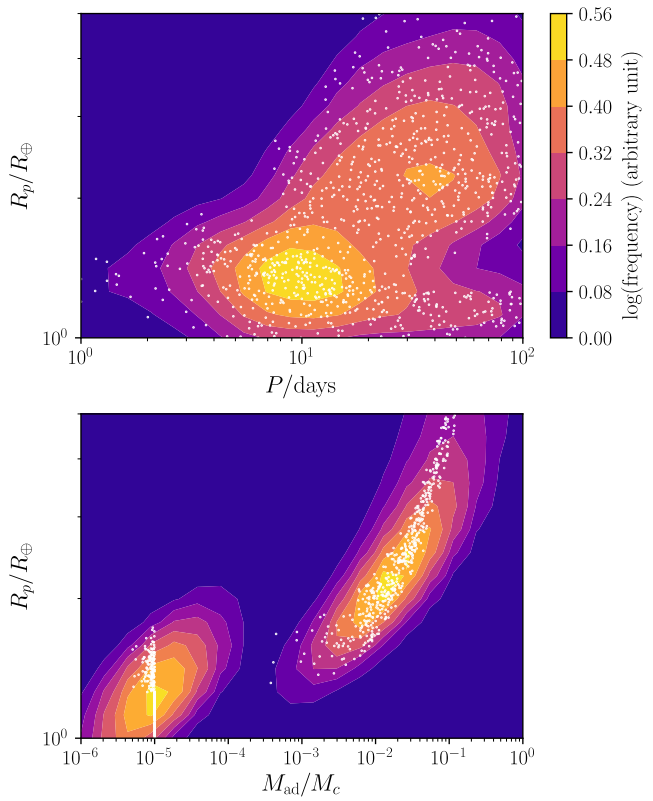


Figure 6.9 Bimodal distribution of evolved model planets. Scattered white dots present a sub-sample of simulated planet atmosphere evolution results (10^3 out of 10^4; for clearer presentation). The color-mapped contour is the estimated distribution function with Gaussian kernel, scaled to frequency per $\{\log_{10} P \times \log_{10} R_p\}$ (upper panel), and $\{\log_{10} M_{\rm ad}/M_c \times \log_{10} R_p\}$ (lower panel), using the results of the whole ensemble.

The distribution in orbital period is well-constrained by Kepler observations. We adopt the recipes of OW17, based on the observation results in Fressin et al. (2013), $\mathrm{d}N/\mathrm{d}\ln P \propto \min\{(P/7.6\ \mathrm{days})^{1.9},\ 1\}$, in the range $(P/\mathrm{days}) \in [1, 10^2]$. The orbital periods are translated into orbital radii assuming the host stellar mass being $M_\odot$. At each orbital radius, $T_{\rm eq}$ and $F_{\rm HE}$ are set accordingly. The core mass distribution function is a Rayleigh function, $\mathrm{d}N/\mathrm{d}M_c \propto M_c\ \exp[-M_c^2/(2\sigma_M^2)]$ with $\sigma_M \sim 3\ M_c$ and $(M_c/M_\oplus) \in [1, 12]$ (see also Marcy et al., 2014). We assume that the core of all model planets are rocky. The initial distribution of envelope mass fraction, however, is impossible to directly determine. We hence assume that the distribution function of $\ln(M_{\rm ad}/M_c)$ is uniform in $(M_{\rm ad}/M_c) \in [10^{-2}, 10^{-0.5}]$, and zero elsewhere. All those distributions are assumed to be independent to each other.

When evolving the planet envelopes, we integrate the mass loss process to 10^9 yr or until $M_{\rm ad}/M_c \leq 10^{-5}$. Ribas et al. (2005) suggested that the high energy luminosity of a young star drops as power-law, whose power indices vary from band to band. Here for simplicity, we assume that the power index is the same $L \propto \min\{1,\ (t/10^8\ \mathrm{yr})^{-1.5}\}$ in all bands, before totally shutting down radiation at 10^9 yr. For those planet en-

velopes in the Parker wind zone in Figure 6.7, we assume that it drops vertically down to the photoevaporative region immediately before evolving them photoevaporatively if $M_c > 3\ M_\oplus$, or that it loses all envelope otherwise.

One possible caveat is the evolution of specific entropy in the adiabatic interior of planet atmosphere, characterized by the Kelvin-Helmholtz timescale, $\tau_{\rm KH}$. OW17 suggested that $\tau_{\rm KH} = \max\{10^8\ {\rm yr},\ t\}$ at time t during the evolution process. Intuitive as it seems, we realize that this recipes overestimates the overall energy loss of planet envelopes after 10^8 yr, by comparing the evolution of planet radii under OW17 scheme to the detailed simulations, e.g. Howe & Burrows (2015). Hence we simply assume $\tau_{\rm KH} \simeq 10^8$ yr for all planets at all times. This may overestimate observed planet radii at the same $M_{\rm ad}$ after evaporation, but the post-evaporation $M_{\rm ad}$ may be underestimated by having a bigger $R_{\rm EUV}$ during the evolution, partially offsetting the former overestimation.

By evolving the ensemble with 10^4 model planets, we obtain the frequency of evolved planet models on the $\{\log_{10} P \times \log_{10} R_p\}$ plane (upper panel; here R_p is characterized by $r_{\rm rcb}$) and $\{\log_{10} M_{\rm ad}/M_c \times \log_{10} R_p\}$ plane (lower panel), presented in Figure 6.9. The distribution is bimodal. One cluster is centered at $R_p \sim 2.5\ R_\oplus$, $P \sim 30$ days. This cluster corresponds to those planets whose mass loss timescales are longer than the evolution time, and the peak $M_{\rm ad}/M_c \sim 2\%$ is in good accordance with the longest photoevaporation timescales indicated in Figure 6.7. The other cluster centers at $R_p \sim 1.4\ R_\oplus$, $P \sim 10$ days. Note that $M_{\rm ad}/M_c$ for this peak is concentrated at 10^{-5}, which is the terminal envelope mass fraction of our revolution recipes and simply indicates those planets having lost almost all of their atmospheres. Locations of these two peaks agree semi-quantitatively with observation results in e.g. Fulton et al. (2017); Dong et al. (2017). Similar to OW17, this bimodality is attributed to the peak in evolution timescales at $M_{\rm ad}/M_c \sim 10^{-2}$, which is hereby confirmed in detailed simulations with hydrodynamics, radiative transfer and thermochemistry involved. The observations also confirm the lack of objects at the upper left corner in the plot, which is a direct result of photoevaporation (e.g. Lundkvist et al., 2016).

6.5 Chapter Summary

In conclusion, this chapter studies the photoevaporation processes of planet atmosphere by combining 2.5-dimensional axisymmetric full hydrodynamic simulations with consistent thermochemistry and ray-tracing radiative transfer.

As the initial conditions of photoevaporation, static planet envelopes require the atmospheric pressure at large radii being balanced by the ambient; otherwise, the envelopes may lose mass rapidly through Parker wind. We find that for planet core mass $M_c \lesssim 3\ M_\oplus$, such balancing is almost impossible to achieve by ambient pressure, which suggests that they may not hold substantial H/He envelopes.

Numerical simulations of photoevaporation reveal that the wind escapes at 32 km s^{-1} with the "standard" high energy radiation prescribed by Ribas et al. (2005) and OW17, for a planet with a 5 $M_\oplus$ rocky core and envelope mass fraction 10^{-2}. Such a model planet loses its envelope mass at $\dot{M} \simeq 4 \times 10^{-10}\ M_\oplus\ {\rm yr}^{-1}$. While

the outflow is fairly close to radial on the day hemisphere, there exists a static tail on the other side, shaped hydrodynamically by the flows near $\theta = \pi/2$. We emphasize the importance of multidimensionality by models whose supersonic outflows still survive under strong stellar windram pressure, with comparable mass loss rate to the fiducial case. By turning off radiation flux in different bands, we find that the main determinant of mass loss rate is the EUV photons, which interact with most abundant species, $H/H_2/He$. Other bands of radiation assists the EUV photons by enlarging the effective interception area of EUV and destroying molecular and atomic coolants. Varying the planet and atmosphere properties confirm that the size of EUV photosphere is the most relevant factor. By setting different incident high energy fluxes, we find that the mass loss rate drops sub-linearly and the kinetic energy super-linearly at low irradiation flux, where the mechanism limiting the outflow is molecular ro-vibrational cooling rather than recombination. Our numerical grid of planet models suggests that the decrease of occurrence in rich planetary atmospheres with core mass $M_c \lesssim 6\ M_\oplus$ is likely to be attributed to photoevaporation. We also semi-quantitatively reproduce the bimodal distribution of Kepler planet on the $\{\log_{10} P \times \log_{10} R_p\}$ plane by evolving such an ensemble, owing to the longest $t_{\rm evap}$ for envelope mass fraction around 10^{-2}.

Appendix

6.A Semi-analytic Models

In this appendix we describe an analytic model with minimum (but adequate) hydrodynamics, radiative transfer and thermochemistry, to help us understand the process of photoevaporation. The procedures are similar to (but still subtly different from) M-CCM09.

6.A.1 Governing physics and equations

We consider a spherically symmetric model with external gravity set by the co-centered solid core. The hypothetical configuration of stellar radiation is characterized by radiation flux $\vec{F} = -\hat{r}F_0$ in absence of absorption. For simplicity we still only take the ionization and recombination of atomic hydrogen into account. With the set of dimensionless parameters defined in eq.(2.26), the governing equations are different from eq.(2.27) only by geometry,

$$\begin{aligned}
&\partial_\lambda \varrho = (\mu\delta)^{-1}\left[(\gamma-1)\Sigma_E - 2\mu^3\varrho/\lambda + \Gamma\mu\varrho/\lambda^2\right]\ ;\\
&\partial_\lambda \mu = -(\varrho\delta)^{-1}\left[(\gamma-1)\Sigma_E - 2\mu\epsilon/\lambda + \Gamma\mu\varrho/\lambda^2\right]\ ;\\
&\partial_\lambda \epsilon = \delta^{-1}\gamma\left[(\gamma-1)\mu\Sigma_E - 2\mu^2\epsilon/\lambda + \Gamma\epsilon/\lambda^2\right]\ ;\\
&\partial_\lambda x_e = \mu^{-1}\Sigma_I\ ;\quad \partial_\lambda\varphi = -\tau_0\varrho(1-x_e)\varphi\ ;\\
&\Sigma_E \equiv C_1\varphi\varrho(1-x_e)\zeta_0 - C_2\Theta^{\kappa+1}x_e^2\varrho^2\xi_0\ ;\quad \Sigma_I \equiv C_3\varphi(1-x_e) - C_4\Theta^\kappa x_e^2\varrho\ .
\end{aligned} \tag{6.20}$$

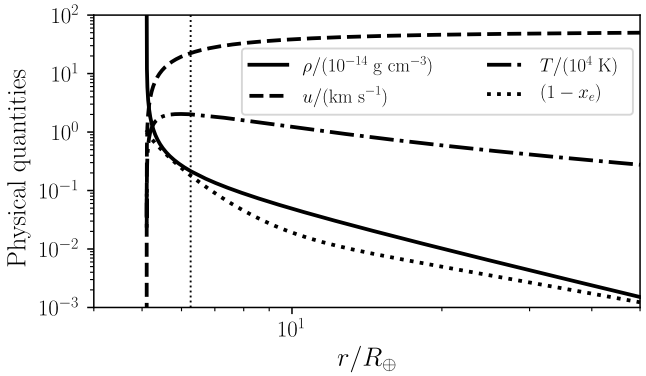


Figure 6.10 The radial profile of various quantities in the spherically symmetric analytical solution of a 5 $M_\oplus$, 10^{-2} envelope mass fraction at 0.1 AU, presented in §6.A.1. Mass density ρ, radial velocity u, temperature T, and neutral fraction $(1-x_e)$ profiles are presented in different line styles, which are indicated in the legend. The vertical thin dotted line indicates the location where the flow is transonic.

6.A.2 Critical and boundary conditions

The ODEs eqs. (6.20) are singular at $\delta = 0$, i.e. the radial velocity becomes transonic. Physically feasible solutions (eigen solutions) must pass through the sonic surface regularly by also having vanishing numerators for $\partial_\lambda \varrho$, $\partial_\lambda \mu$ and $\partial_\lambda \epsilon$. It is straightforward to prove that numerators of those derivatives vanish simultaneously if one of them approaches zero as $\delta \to 0$. Near the sonic surface the approximated derivatives are obtained by the l'Hospital rule. Also, $\mu \to 0$ leads to singularity where Σ_E is still finite. We construct the solution by starting at a finite radius $\lambda_{\rm ini} = (r_{\rm ini}/l_0)$, then integrate both inwards to $\lambda_{\rm min} = (r_{\rm min}/l_0)$, defined as the wind base, where the dimensionless radiation flux $\varphi = 10^{-4}$, and outwards to $\lambda_{\rm max} = (r_{\rm max}/l_0) = 10\lambda_{\rm ini}$. The dependent variables at $r_{\rm ini}$ are adjusted, so that the solution (a) is regular at the sonic surface; (b) satisfies $\varphi = 1$ at $r_{\rm max}$ by setting F_0 the incident EUV flux; and (c) matches ρ and T of the given isothermal hydrostatic profile at $r_{\rm min}$ (see also eq. 6.6).

We are not matching x_e at the inner boundary $\lambda_{\rm min}$, as we do not prescribe the ionization profile in the static region, while x_e drops rapidly to zero near and below $\lambda_{\rm min}$. Comparing the number of effective constraints (ρ and T at $r_{\rm min}$, $\varphi = 1$ at $r_{\rm max}$, and regularity at the sonic point; 4 constraints in total) to the number of dependent variables (ϱ, μ, ϵ, x_e, and φ; 5 dependent varialbes in total), the ODEs are actually *underdetermined* with one degree of freedom: with identical internal isothermal profile and external radiation, a series of solutions (that are regular at transonic points) can match the isothermal profile at different $r_{\rm min}$. This mathematical consideration actually has its physical implication, as is elaborated in §6.A.3.

In Figure 6.10, we present an example of semi-analytic solutions. Following the construction procedures in §6.A, this solution is matched (a) inwards to a $T_{\rm eq} = 886$ K isothermal layer outside an $M_{\rm ad} = 10^{-2}\ M_c$ adiabatic envelope at $r_{\rm min} = 5.11\ R_\oplus$ (where $\rho = 0.98 \times 10^{-13}$ g cm^{-3}), surrounding an $M_c = 5\ M_\oplus$, $R_c = 1.5\ R_\oplus$ core (assuming envelope cooling timescale 10^8 yr), and (b) outwards to an

$F_0 = 10^{15}$ cm^{-2} s^{-1} outer boundary (this is the radiation flux at $a = 0.1$ AU with EUV luminosity $10^{-3.5}$ $L_\odot$ at $h\nu = 25$ eV). Considering the effective solid angle of intercepting EUV irradiation being π, the mass loss rate is estimated by $\dot{M} \sim (\pi r^2 \rho u)_{r_{\max}} \simeq 1.3 \times 10^{-9}$ $M_\oplus$ yr^{-1}, thus $t_{\rm evap} \sim 40$ Myr.

6.A.3 Steady versus static: Caveats and necessity of a consistent model

Straightforward as it may seem, the semi-analytic solution presented in the previous section still has caveats. To be mathematically rigorous, a steady state outflow solution has no hope to be *fully* matched to a static interior: the radial mass flux, being a finite constant in the steady outflow, must vanish in the static region. Typically this mismatch is interpreted by assuming that the static region quickly relaxes to new configurations as the gas at the wind base is removed by the outflow. The new configurations are almost identical to the original one as long as the evolution time $t \ll t_{\rm evap}$, so that the location and hydrodynamic conditions of the wind base can be treated as invariant.

However, the equilibrium conditions beneath the wind base are impossible, with only hydrogen ionization and recombination processes included. Since $\langle E_{\rm pe} \rangle \sim (k_{\rm B} \times 10^5$ K) is much greater than $\langle E_{\rm rr} \rangle \lesssim (k_{\rm B} \times 10^3$ K), in case of $S_I = 0$ (ionization equilibrium), the local energy balance S_E is always appreciably positive (see also eqs. 2.23, 2.24). Lyα cooling, suggested by M-CCM09, is indeed negligible at the temperature and density beneath the wind base for our low-mass planet models. As a result, the timescale at which a fluid element in the static region doubles its temperature is estimated by $t_{\rm heat,static} \sim 10$ s $\times [F/(10^{15}$ cm^{-2} s$^{-1})]^{-1}$, which is merely one day even if the EUV flux F is suppressed by 4 orders of magnitude compared to the unattenuated flux F_0. As soon as a fluid element is heated, it expands and allows more EUV radiation to come in, which in turn speeds up the heating process before this fluid element finally migrates into the wind. As a result, the eroded static layer never recovers its original configuration; instead, the location of wind base moves inwards in a relatively short period of time compared to $t_{\rm evap}$. The wind base shrinks until it reaches a very high density so that the speed of erosion is comparable to $t_{\rm evap}$. In fact, using the code described in Chapter 2 in spherically symmetric configuration and identical thermochemistry, we figure out that the wind base moves from $\rho \sim 10^{-13}$ g cm^{-3} to $\rho \sim 10^{-6}$ g cm^{-3} within $t \lesssim 0.1$ yr, while the mass loss rate roughly halves as the effective area of intercepting EUV radiation shrinks (the mass of isothermal layer in the range of 10^{-13} g cm$^{-3} < \rho < 10^{-6}$ g cm^{-3} is only $\sim 10^{-10}$ $M_\oplus$). At each instant the wind region can still be perfectly fit by a semi-analytic solution (mathematically thanks to the extra degree of freedom; note that the timescales for a wind configuration to relax is $r_{\max}/v_{\rm wind} \sim 10^4$ s, which is still tiny compared to the erosion timescale).

In summary, the assumption of quasi-invariant static region matching a steady state wind with hydrogen only leads to contradictions. Therefore we need numerical

models where detailed microphysics are coupled consistently with full hydrodynamics, preferably in multiple dimensions.

6.B Additional Details of Thermochemistry

6.B.1 Precipitation of PAH

PAH falls downwards relative to gas due to planetary gravity in the atmosphere. This is not a concern in the adiabatic internal atmosphere due to convection, but may still affect PAH spatial distribution in the isothermal region.

As gas drag force increases monotonically with the magnitude of relative velocity, PAH falling speed converges to a constant (nominally the terminal speed) in steady states so that gas drag force balances gravity. At gas temperature T, gas molecule number density n and mean molecular mass μ, the force equilibrium condition reads (Baines et al., 1965; Draine, 2011a)

$$\begin{aligned}\frac{GM_c}{r^2}\left(\frac{4\pi}{3}r_{\rm dust}^3\rho_{\rm dust}\right)s = F_{\rm drag} &\simeq 2\pi r_{\rm dust}^2 k_{\rm B}Tn\left[\frac{8s}{3\pi^{1/2}}\left(1+\frac{9\pi s^2}{64}\right)^{1/2}\right] \\ &> 2\pi r_{\rm dust}^2 k_{\rm B}Tn\frac{8s}{3\pi^{1/2}}\ ,\end{aligned} \tag{6.21}$$

where $s \equiv (\mu v_{\rm term}^2/2k_{\rm B}T)^{1/2}$, and $v_{\rm term}$ is the terminal speed of PAH particles. Solving the inequality gives,

$$\begin{aligned}v_{\rm term} < 3.84\ {\rm m\ s^{-1}} &\times \left(\frac{M}{M_\oplus}\right)\left(\frac{r}{R_\oplus}\right)^{-2}\left(\frac{r_{\rm dust}}{10\ {\rm \AA}}\right) \\ &\times \left(\frac{\rho_{\rm dust}}{3\ {\rm g\ cm^{-3}}}\right)\left(\frac{n}{10^{12}\ {\rm cm^{-3}}}\right)^{-1}\left(\frac{T}{10^3\ {\rm K}}\right)^{-1/2}\left(\frac{\mu}{m_p}\right)^{-1/2}\ .\end{aligned} \tag{6.22}$$

As the upper limit of $v_{\rm term}$ is proportional to $r^{-2}n^{-1}$, we then define an equilibrium wind mass loss rate $\dot{M}_{\rm eq}$, at which the uplifting speed of gas equals to $v_{\rm term}$. The upper limit of $\dot{M}_{\rm eq}$ is,

$$\begin{aligned}\dot{M}_{\rm eq} \equiv 4\pi r^2 n\mu v_{\rm term} < 1.8\times10^{-11}\ M_\oplus\ {\rm yr^{-1}} &\\ \times \left(\frac{M}{M_\oplus}\right)\left(\frac{r_{\rm dust}}{10\ {\rm \AA}}\right)\left(\frac{\rho_{\rm dust}}{3\ {\rm g\ cm^{-3}}}\right)\left(\frac{T}{10^3\ {\rm K}}\right)^{-1/2}&\left(\frac{\mu}{m_p}\right)^{1/2}\ .\end{aligned} \tag{6.23}$$

If $\dot{M} \gg \dot{M}_{\rm eq}$, at every radius in a steady state planet atmosphere, $v_r \gg v_{\rm term}$. In this case, precipitation of PAH due to planetary gravity is always replenished by upward motion of gas, hence can be neglected.

Chapter 7

Conclusions

This thesis features the consistent combination of thermochemistry, radiation and (magneto-)hydrodynamics. Simulations incorporating such a combination are usually costly in computation, but we have managed to implement and optimize pertinent algorithms, assisted by computation power of the GPUs. These costly simulations reward us with better understanding towards the dispersal processes of PPDs and planetary atmospheres.

Photoevaporation simulations figure out that full hydrodynamic simulations might be crucial in obtaining correct structures of PPD photoevaporation (as compared to e.g. GH09) and planetary atmospheres. Such simulations recognize that EUV photons ($h\nu > 13.6$ eV) are most relevant to photoevaporation in both scenarios (PPD and planets): photons in other energy bands either have too much penetration and deposit energy into high density regions where their heating is quickly dissipated by cooling, or simply do not inject sufficient amount energy per gas particle during photoionization/photodissociation processes. They also reveal the importance of cooling processes by collisional excitation of atoms and molecules, with which the estimated wind mass loss rates are significantly lower than previous works that have ignored such cooling (e.g. OECA10).

MHD simulations, studying the magneto-thermal wind, find that the mass loss rate is $\sim 10^{-8}\ M_\odot\ \mathrm{yr}^{-1}$ when magnetization drives a comparable accretion rate. Such simulations investigate the EUV-irradiated magnetized winds, which show a hybrid of photoevaporation and magneto-thermal wind launching. In addition, they also emphasize the subtlety of thermochemical networks that can determine the grand structures of magnetized PPD winds by drastically affecting the coupling between fluids and magnetic fields.

7.1 Future Works

Admittedly the research works in this thesis are far from perfect. Numerous approximations and computational recipes are still adopted for viable computations. Some important topics closely related to those works are also temporarily skipped. This

section discusses our expectations of future improvements and explorations based on the findings we have obtained in this thesis.

7.1.1 Extensions on Disk Wind Models

Hall effect and mid-plane thermochemistry

We expect to explore several other aspects of problems as natural extensions to this work. Adding Hall effect to the MHD models will likely substantially reshape the flow structure, and magnetic flux transport in the bulk disk mediated by Hall effect may also affect wind launching (Bai & Stone 2017, B17). This in turn requires better treatment of mid-plane thermochemistry. In addition to magnetic diffusivities, adsorption and desorption of volatile species on surfaces of dust grains also take place inside the bulk disk, which may change the thermochemical conditions at wind bases and in turn affect the wind dynamics and chemistry. Consistent treatment of this effect requires implementation of adsorption and desorption processes, as well as the kinetics of dust grains shaped by the interaction between dust particle, gas, and magnetic fields. Better modeling of scattered/re-emitted photons (especially in infrared and in X-ray), instead of simplified recipes, may also be required for more accurate knowledge towards the thermochemical environments in wind-launching regions.

Instabilities and turbulence

Some parts of the parameter space show signs of instabilities, which should be properly studied by 3-dimensional global simulations. The advection and diffusion of magnetic flux in a turbulent disk is an unsolved problem. Eventually, modeling the molecular and atomic lines using simulation results based on the paradigm of coupled non-ideal MHD and consistent microphysics will help us to connect those theoretical findings to observations and improve our understanding towards the dispersal process of PPDs.

Line diagnostics and predictions of observations

Now that we have the temperature, density, and velocity structure, it should be possible to model molecular and atomic lines, including trace species not important for heating and cooling, and explicitly treating the level populations and optical depths of CO, O, C, C^+, etc. These lines and their profiles will be used to confront our models with observations, e.g. Carr et al. (2004); Carr & Najita (2008); Bast et al. (2011); Brown et al. (2013); Simon et al. (2016), and may well help us shed more light upon the disk wind launching mechanism: photoevaporative wind, magneto-thermal wind, or the combination of these two.

7.1.2 Photoevaporative Planetary Atmospheres: One Dimension Up

A lot of restrictions on our about planetary atmosphere dispersal is introduced by dimensionality: 2.5-dimensional setup disables explorations on the impact of non-axisymmetric effects, especially interactions with planetary orbital motion.

§6.1.3 conceded the inability of the current hydrodynamic photoevaporative model in explaining the existence of "super-puff" planetary objects. We also hope to explore the problem using models with consistent thermochemistry, and probably with magnetic fields (requiring full 3D simulations as well), which may introduce further dissipation in the adiabatic interior atmosphere, and/or change the structure of outflows.

After leaving the planet, photoevaporative outflow is subject to modulations by orbital motion. Orbital centrifugal force and the Coriolis force, which are expected to play a role even within the Hill sphere of a planet in the co-rotational frame, break the axisymmetry assumed in the 2.5-dimensional models in this chapter. Specifically, three dimensional models will help us understand the behavior of the tail, which is particularly interesting as similar structures are already found in observations (e.g. Ehrenreich et al., 2015; Lavie et al., 2017). Moreover, three dimensional simulations will enable us to explore the interaction of photoevaporative outflow with planet spin and even magnetic field, leading to insights on more interesting physics therein.

Bibliography

Ádámkovics, M., Glassgold, A. E., & Najita, J. R. 2014, ApJ, 786, 135, **(AGN14)**

Adams, F. C., Hollenbach, D., Laughlin, G., & Gorti, U. 2004, ApJ, 611, 360

Alexander, R. D., Clarke, C. J., & Pringle, J. E. 2006a, MNRAS, 369, 216

—. 2006b, MNRAS, 369, 216

—. 2006c, MNRAS, 369, 229

Andrews, S. M., Rosenfeld, K. A., Kraus, A. L., & Wilner, D. J. 2013, ApJ, 771, 129

Armitage, P. J. 2000, A&A, 362, 968

—. 2011, ARA&A, 49, 195

Bai, X.-N. 2011a, ApJ, 739, 50

—. 2011b, ApJ, 739, 51

—. 2013, ApJ, 772, 96

—. 2016a, ApJ, 821, 80

—. 2016b, ApJ, 821, 80

—. 2017, ApJ, 845, 75, (**B17**)

Bai, X.-N., & Goodman, J. 2009, ApJ, 701, 737

Bai, X.-N., & Stone, J. M. 2011a, ApJ, 736, 144

—. 2011b, ApJ, 736, 144

—. 2013a, ApJ, 769, 76

—. 2013b, ApJ, 769, 76

—. 2017, ApJ, 836, 46

Bai, X.-N., Ye, J., Goodman, J., & Yuan, F. 2016, ApJ, 818, 152

Baines, M. J., Williams, I. P., & Asebiomo, A. S. 1965, MNRAS, 130, 63

Balbus, S. A., & Hawley, J. F. 1991, ApJ, 376, 214

Bast, J. E., Brown, J. M., Herczeg, G. J., van Dishoeck, E. F., & Pontoppidan, K. M. 2011, A&A, 527, A119

Beckwith, S. V. W., & Sargent, A. I. 1993, in Protostars and Planets III, ed. E. H. Levy & J. I. Lunine, 521–541

Bethell, T. J., & Bergin, E. A. 2011, ApJ, 739, 78

Bisnovatyi-Kogan, G. S., & Ruzmaikin, A. A. 1976, Ap&SS, 42, 401

Blandford, R. D., & Payne, D. G. 1982, MNRAS, 199, 883, (**BP82**)

Bourrier, V., Lecavelier des Etangs, A., Ehrenreich, D., Tanaka, Y. A., & Vidotto, A. A. 2016, A&A, 591, A121

Brown, J. M., Pontoppidan, K. M., van Dishoeck, E. F., et al. 2013, ApJ, 770, 94

Bruderer, S. 2013, A&A, 559, A46

Carr, J. S., & Najita, J. R. 2008, Science, 319, 1504

Carr, J. S., Tokunaga, A. T., & Najita, J. 2004, ApJ, 603, 213

Carroll-Nellenback, J., Frank, A., Liu, B., et al. 2017, MNRAS, 466, 2458

Carter, J. A., Agol, E., Chaplin, W. J., et al. 2012, Science, 337, 556

Casassus, S., Marino, S., Pérez, S., et al. 2015, ApJ, 811, 92

Casse, F., & Keppens, R. 2002, ApJ, 581, 988

Chiang, E., & Murray-Clay, R. 2007, Nature Physics, 3, 604

Chiang, E. I., & Goldreich, P. 1997, ApJ, 490, 368

Christie, D., Arras, P., & Li, Z.-Y. 2016, ApJ, 820, 3

Clarke, C. J., Gendrin, A., & Sotomayor, M. 2001, MNRAS, 328, 485

Combet, C., & Ferreira, J. 2008, A&A, 479, 481

Crida, A., & Morbidelli, A. 2007, MNRAS, 377, 1324

Dong, R., & Dawson, R. 2016, ApJ, 825, 77

Dong, S., Xie, J.-W., Zhou, J.-L., Zheng, Z., & Luo, A. 2017, ArXiv e-prints, arXiv:1706.07807

Drabek-Maunder, E., Mohanty, S., Greaves, J., et al. 2016, ArXiv e-prints

Draine, B. T. 2011a, Physics of the Interstellar and Intergalactic Medium (Princeton University Press)

—. 2011b, Physics of the Interstellar and Intergalactic Medium (Princeton University Press)

Draine, B. T., & Bertoldi, F. 1996, ApJ, 468, 269

Draine, B. T., & Sutin, B. 1987, ApJ, 320, 803

Dressing, C. D., Charbonneau, D., Dumusque, X., et al. 2015, ApJ, 800, 135

Ehrenreich, D., Bourrier, V., Wheatley, P. J., et al. 2015, Nature, 522, 459

Ercolano, B., Drake, J. J., Raymond, J. C., & Clarke, C. C. 2008, ApJ, 688, 398, **(EDC08)**

Ercolano, B., & Owen, J. E. 2016, MNRAS, 460, 3472

Espaillat, C., Muzerolle, J., Najita, J., et al. 2014, Protostars and Planets VI, 497

Fatuzzo, M., & Adams, F. C. 2008, ApJ, 675, 1361

Ferreira, J. 1997, A&A, 319, 340

Ferreira, J., & Pelletier, G. 1995a, A&A, 295, 807

—. 1995b, A&A, 295, 807

Flaherty, K. M., Hughes, A. M., Teague, R., et al. 2018, ApJ, 856, 117

Fleming, T. P., Stone, J. M., & Hawley, J. F. 2000, ApJ, 530, 464

Flock, M., Henning, T., & Klahr, H. 2012, ApJ, 761, 95

Font, A. S., McCarthy, I. G., Johnstone, D., & Ballantyne, D. R. 2004, ApJ, 607, 890

Freedman, R. S., Marley, M. S., & Lodders, K. 2008, ApJS, 174, 504

Fressin, F., Torres, G., Charbonneau, D., et al. 2013, ApJ, 766, 81

Fromang, S., & Stone, J. M. 2009, A&A, 507, 19

Fulton, B. J., Petigura, E. A., Howard, A. W., et al. 2017, AJ, 154, 109

Garcia, P. J. V., Ferreira, J., Cabrit, S., & Binette, L. 2001, A&A, 377, 589

Geers, V. C., van Dishoeck, E. F., Visser, R., et al. 2007, A&A, 476, 279

Geers, V. C., Augereau, J.-C., Pontoppidan, K. M., et al. 2006, A&A, 459, 545

Ginzburg, S., Schlichting, H. E., & Sari, R. 2016, ApJ, 825, 29

Glover, S. C. O., Federrath, C., Mac Low, M.-M., & Klessen, R. S. 2010, MNRAS, 404, 2

Goldsmith, P. F. 2001, ApJ, 557, 736

Gong, M., Ostriker, E. C., & Wolfire, M. G. 2016, ArXiv e-prints, arXiv:1610.09023

Gorti, U., & Hollenbach, D. 2008, ApJ, 683, 287, (**GH08**)

—. 2009, ApJ, 690, 1539

Gorti, U., Hollenbach, D., Najita, J., & Pascucci, I. 2011, ApJ, 735, 90

Gressel, O., Turner, N. J., Nelson, R. P., & McNally, C. P. 2015a, ApJ, 801, 84

—. 2015b, ApJ, 801, 84

Guan, X., & Gammie, C. F. 2009, ApJ, 697, 1901

Gullbring, E., Calvet, N., Muzerolle, J., & Hartmann, L. 2000, ApJ, 544, 927

Haisch, Jr., K. E., Lada, E. A., & Lada, C. J. 2001, ApJ, 553, L153

Hartigan, P., Edwards, S., & Ghandour, L. 1995, ApJ, 452, 736

Haworth, T. J., Boubert, D., Facchini, S., Bisbas, T. G., & Clarke, C. J. 2016, MNRAS, 463, 3616

Haworth, T. J., Facchini, S., Clarke, C. J., & Cleeves, L. I. 2017, MNRAS, 468, L108

Haworth, T. J., & Harries, T. J. 2012, MNRAS, 420, 562

Heays, A. N., Bosman, A. D., & van Dishoeck, E. F. 2017, A&A, 602, A105

Hindmarsh, A. C., Brown, P. N., Grant, K. E., et al. 2005, ACM Transactions on Mathematical Software (TOMS), 31, 363

Hollenbach, D., Johnstone, D., Lizano, S., & Shu, F. 1994a, ApJ, 428, 654

—. 1994b, ApJ, 428, 654

Hollenbach, D., & McKee, C. F. 1979, ApJS, 41, 555

Howe, A. R., & Burrows, A. 2015, ApJ, 808, 150

Igea, J., & Glassgold, A. E. 1999, ApJ, 518, 848

Igumenshchev, I. V. 2008, ApJ, 677, 317

Ilee, J. D., Boley, A. C., Caselli, P., et al. 2011, MNRAS, 417, 2950

Ilee, J. D., Forgan, D. H., Evans, M. G., et al. 2017, MNRAS, 472, 189

Ilgner, M., & Nelson, R. P. 2006a, A&A, 445, 205

—. 2006b, A&A, 445, 205

—. 2008, A&A, 483, 815

Ingleby, L., Calvet, N., Bergin, E., et al. 2009, ApJ, 703, L137

Jin, S., & Mordasini, C. 2017, ArXiv e-prints, arXiv:1706.00251

Johnstone, D., Hollenbach, D., & Bally, J. 1998, ApJ, 499, 758

Jontof-Hutter, D., Ford, E. B., Rowe, J. F., et al. 2016, ApJ, 820, 39

Königl, A. 1989, ApJ, 342, 208

Königl, A., Salmeron, R., & Wardle, M. 2010, MNRAS, 401, 479

Krasnopolsky, R., Li, Z.-Y., & Blandford, R. D. 2003, ApJ, 595, 631

Krauss, O., & Wurm, G. 2005, ApJ, 630, 1088

Kuiper, R., Klahr, H., Dullemond, C., Kley, W., & Henning, T. 2010, A&A, 511, A81

Kwan, J., & Krolik, J. H. 1981, ApJ, 250, 478

Lammer, H., Selsis, F., Ribas, I., et al. 2003, ApJ, 598, L121

Lavie, B., Ehrenreich, D., Bourrier, V., et al. 2017, A&A, 605, L7

Lecavelier Des Etangs, A. 2007, A&A, 461, 1185

Lecavelier Des Etangs, A., Ehrenreich, D., Vidal-Madjar, A., et al. 2010, A&A, 514, A72

Lesur, G., Kunz, M. W., & Fromang, S. 2014, A&A, 566, A56

Lesur, G., & Longaretti, P.-Y. 2009, A&A, 504, 309

Li, A., & Draine, B. T. 2001, ApJ, 554, 778

Li, Z.-Y. 1995, ApJ, 444, 848

—. 1996, ApJ, 465, 855

Li, Z.-Y., Banerjee, R., Pudritz, R. E., et al. 2014, Protostars and Planets VI, 173

Lopez, E. D., & Fortney, J. J. 2013, ApJ, 776, 2

—. 2014, ApJ, 792, 1

López-Morales, M., Haywood, R. D., Coughlin, J. L., et al. 2016, AJ, 152, 204

López-Puertas, M., Dinelli, B. M., Adriani, A., et al. 2013, ApJ, 770, 132

Loureiro, N. F., Schekochihin, A. A., & Cowley, S. C. 2007, Physics of Plasmas, 14, 100703

Loureiro, N. F., & Uzdensky, D. A. 2016, Plasma Physics and Controlled Fusion, 58, 014021

Lubow, S. H., Papaloizou, J. C. B., & Pringle, J. E. 1994, MNRAS, 267, 235

Lundkvist, M. S., Kjeldsen, H., Albrecht, S., et al. 2016, Nature Communications, 7, 11201

MacDonald, R. J., & Madhusudhan, N. 2017, MNRAS, 469, 1979

Manara, C. F., Testi, L., Natta, A., et al. 2014, A&A, 568, A18

Manara, C. F., Rosotti, G., Testi, L., et al. 2016, A&A, 591, L3

Marcy, G. W., Isaacson, H., Howard, A. W., et al. 2014, ApJS, 210, 20

Masuda, K. 2014, ApJ, 783, 53

Mathis, J. S., Rumpl, W., & Nordsieck, K. H. 1977, ApJ, 217, 425

McClure, M., Bergin, T., Cleeves, I., et al. 2016, ArXiv e-prints

McElroy, D., Walsh, C., Markwick, A. J., et al. 2013, A&A, 550, A36

Mignone, A. 2014, Journal of Computational Physics, 270, 784

Miotello, A., van Dishoeck, E. F., Kama, M., & Bruderer, S. 2016, ArXiv e-prints

Morishima, R. 2012, MNRAS, 420, 2851

Murray-Clay, R. A., Chiang, E. I., & Murray, N. 2009, ApJ, 693, 23, (**M-CCM09**)

Najita, J. R., Andrews, S. M., & Muzerolle, J. 2015, MNRAS, 450, 3559

Narayan, R., Igumenshchev, I. V., & Abramowicz, M. A. 2003, PASJ, 55, L69

Nelson, R. P., Gressel, O., & Umurhan, O. M. 2013, MNRAS, 435, 2610

Neufeld, D. A., & Kaufman, M. J. 1993, ApJ, 418, 263

Oishi, J. S., & Mac Low, M.-M. 2011, ApJ, 740, 18

Owen, J. E. 2016, PASA, 33, e005

Owen, J. E., & Adams, F. C. 2014, MNRAS, 444, 3761

Owen, J. E., & Alvarez, M. A. 2016, ApJ, 816, 34

Owen, J. E., Ercolano, B., & Clarke, C. J. 2011, MNRAS, 412, 13, (**OEC11**)

Owen, J. E., Ercolano, B., Clarke, C. J., & Alexander, R. D. 2010a, MNRAS, 401, 1415, **(OECA10)**

—. 2010b, MNRAS, 401, 1415

Owen, J. E., & Jackson, A. P. 2012, MNRAS, 425, 2931

Owen, J. E., & Morton, T. D. 2016, ApJ, 819, L10

Owen, J. E., & Wu, Y. 2013, ApJ, 775, 105

—. 2016, ApJ, 817, 107

—. 2017, ArXiv e-prints, arXiv:1705.10810, (**OW17**)

Paardekooper, S.-J., & Mellema, G. 2006, A&A, 453, 1129

Parker, E. N. 1958, ApJ, 128, 664

Pascucci, I., & Sterzik, M. 2009, ApJ, 702, 724

Pascucci, I., Hollenbach, D., Najita, J., et al. 2007, ApJ, 663, 383

Perez-Becker, D., & Chiang, E. 2011a, ApJ, 735, 8

—. 2011b, ApJ, 727, 2

Plewa, T., & Müller, E. 1999, A&A, 342, 179

Pontoppidan, K. M., Blake, G. A., & Smette, A. 2011, ApJ, 733, 84

Pontoppidan, K. M., Blake, G. A., van Dishoeck, E. F., et al. 2008, ApJ, 684, 1323

Press, W. H., Teukolsky, S. A., Vetterling, W. T., & Flannery, B. P. 2002, Numerical recipes in C++ : the art of scientific computing (Cambridge University Press, Cambridge)

Pudritz, R. E., Rogers, C. S., & Ouyed, R. 2006, MNRAS, 365, 1131

Rafikov, R. R. 2006, ApJ, 648, 666

Ribas, I., Guinan, E. F., Güdel, M., & Audard, M. 2005, ApJ, 622, 680

Rice, W. K. M., Armitage, P. J., Wood, K., & Lodato, G. 2006, MNRAS, 373, 1619

Rigliaco, E., Pascucci, I., Gorti, U., Edwards, S., & Hollenbach, D. 2013, ApJ, 772, 60

Rogers, L. A. 2015, ApJ, 801, 41

Rogers, L. A., & Seager, S. 2010, ApJ, 712, 974

Rosenfeld, K. A., Chiang, E., & Andrews, S. M. 2014, ApJ, 782, 62

Salmeron, R., Königl, A., & Wardle, M. 2007, MNRAS, 375, 177

—. 2011, MNRAS, 412, 1162

Salyk, C., Blake, G. A., Boogert, A. C. A., & Brown, J. M. 2009, ApJ, 699, 330

Sanz-Forcada, J., Micela, G., Ribas, I., et al. 2011, A&A, 532, A6

Schneiter, E. M., Esquivel, A., D'Angelo, C. S. V., et al. 2016, MNRAS, 457, 1666

Shakura, N. I., & Sunyaev, R. A. 1973, A&A, 24, 337

Shull, J. M. 1978, ApJ, 224, 841

Simon, J. B., Bai, X.-N., Armitage, P. J., Stone, J. M., & Beckwith, K. 2013a, ApJ, 775, 73

—. 2013b, ApJ, 775, 73

Simon, J. B., Bai, X.-N., Stone, J. M., Armitage, P. J., & Beckwith, K. 2013c, ApJ, 764, 66

—. 2013d, ApJ, 764, 66

Simon, M. N., Pascucci, I., Edwards, S., et al. 2016, ApJ, 831, 169

Skrutskie, M. F., Dutkevitch, D., Strom, S. E., et al. 1990, AJ, 99, 1187

Spruit, H. C., Stehle, R., & Papaloizou, J. C. B. 1995, MNRAS, 275, 1223

Spruit, H. C., & Uzdensky, D. A. 2005, ApJ, 629, 960

Stehle, R., & Spruit, H. C. 2001, MNRAS, 323, 587

Strom, K. M., Strom, S. E., Edwards, S., Cabrit, S., & Skrutskie, M. F. 1989, AJ, 97, 1451

Suzuki, T. K., Muto, T., & Inutsuka, S.-i. 2010, ApJ, 718, 1289

Tanaka, H., Himeno, Y., & Ida, S. 2005, ApJ, 625, 414

Tian, F., Toon, O. B., Pavlov, A. A., & De Sterck, H. 2005, ApJ, 621, 1049

Tielens, A. G. G. M. 2008, ARA&A, 46, 289

Tielens, A. G. G. M., & Hollenbach, D. 1985, ApJ, 291, 722, **(TH85)**

Tripathi, A., Kratter, K. M., Murray-Clay, R. A., & Krumholz, M. R. 2015, ApJ, 808, 173

Turner, N. J., Fromang, S., Gammie, C., et al. 2014, Protostars and Planets VI, 411

Turner, N. J., Sano, T., & Dziourkevitch, N. 2007, ApJ, 659, 729

Tzeferacos, P., Ferrari, A., Mignone, A., et al. 2009a, MNRAS, 400, 820

—. 2009b, MNRAS, 400, 820

Umebayashi, T., & Nakano, T. 1981, PASJ, 33, 617

van Ballegooijen, A. A. 1989, in Astrophysics and Space Science Library, Vol. 156, Accretion Disks and Magnetic Fields in Astrophysics, ed. G. Belvedere, 99–106

van der Marel, N., van Dishoeck, E. F., Bruderer, S., et al. 2016, A&A, 585, A58

van der Marel, N., van Dishoeck, E. F., Bruderer, S., Pérez, L., & Isella, A. 2015, A&A, 579, A106

van Dishoeck, E. F., & Dalgarno, A. 1984, Icarus, 59, 305

Varnière, P., Blackman, E. G., Frank, A., & Quillen, A. C. 2006, ApJ, 640, 1110

Verner, D. A., Ferland, G. J., Korista, K. T., & Yakovlev, D. G. 1996, ApJ, 465, 487

Verner, D. A., & Yakovlev, D. G. 1995, A&AS, 109

Vidal-Madjar, A., Lecavelier des Etangs, A., Désert, J.-M., et al. 2003, Nature, 422, 143

Vidal-Madjar, A., Désert, J.-M., Lecavelier des Etangs, A., et al. 2004, ApJ, 604, L69

Visser, R., van Dishoeck, E. F., & Black, J. H. 2009, A&A, 503, 323

Wardle, M. 2007, Ap&SS, 311, 35

Wardle, M., & Königl, A. 1993, ApJ, 410, 218

Weingartner, J. C., & Draine, B. T. 2001, ApJS, 134, 263

White, C. J., Stone, J. M., & Gammie, C. F. 2016, ApJS, 225, 22

Williams, P., & Cieza, A. 2011, ARA&A, 49, 67

Woitke, P., Kamp, I., & Thi, W.-F. 2009, A&A, 501, 383

Woitke, P., Riaz, B., Duchêne, G., et al. 2011, A&A, 534, A44

Woitke, P., Min, M., Pinte, C., et al. 2016, A&A, 586, A103

Xu, R., & Bai, X.-N. 2016, ApJ, 819, 68

Yelle, R. V. 2004, Icarus, 170, 167

Zanni, C., Ferrari, A., Rosner, R., Bodo, G., & Massaglia, S. 2007a, A&A, 469, 811

—. 2007b, A&A, 469, 811

—. 2007c, A&A, 469, 811

Zeng, L., Sasselov, D. D., & Jacobsen, S. B. 2016, ApJ, 819, 127

Zhu, Z., Nelson, R. P., Dong, R., Espaillat, C., & Hartmann, L. 2012, ApJ, 755, 6

Zhu, Z., Nelson, R. P., Hartmann, L., Espaillat, C., & Calvet, N. 2011, ApJ, 729, 47

Zuckerman, B., Forveille, T., & Kastner, J. H. 1995, Nature, 373, 494